Full Wave 2D Modeling of Scattering and Inverse Scattering for Layered Rough Surfaces with Buried Objects

by

Chih-hao Kuo

A dissertation submitted in partial fulfillment
of the requirements for the degree of
Doctor of Philosophy
(Electrical Engineering)
in The University of Michigan
2008

Doctoral Committee:
- Associate Professor Mahta Moghaddam, Chair
- Professor Christopher Ruf
- Professor Kamal Sarabandi
- Professor Fawwaz T. Ulaby
- Assistant Professor Anthony Grbic

© Chih-hao Kuo 2008
All Rights Reserved

ACKNOWLEDGEMENT

First, I would like to thank my faculty advisor and committee chair, Professor Mahta Moghaddam for her guidance, support, and motivation during my Ph.D. years in the University of Michigan, Ann Arbor. I sincerely appreciate the opportunity she gave me for pursuing my doctoral degree under her supervision. She has been a wonderful faculty advisor who played an important role in my academic success over the course of my Ph.D. research. I also would like to thank my other committee members: Professor Kamal Sarabandi, Professor Fawwaz Ulaby, Professor Christopher Ruf, and Professor Anthony Grbic for agreeing to serve on my thesis committee and accepting to evaluate this dissertation work.

I would like to acknowledge and thank my colleagues at the Radiation Laboratory for their invaluable friendships. I especially like to thank Alireza Tabatabaeenejad, Dahan Liao, Jia-Shiang Fu, Meng-Hong Chen, Amy Buerkle, Yuriy Goykhman, Jackie Vitaz, and Xinen (Alfred) Zhu. Their support and encouragement over the past years have been a significant help in my Ph.D. journey.

Finally, I would like to express my deepest gratitude to my parents and my sister. Without their love and care, the completion of this dissertation would not have been possible.

Chih-hao Kuo

Dec. 27, 2007

TABLE OF CONTENTS

CHAPTER

LIST OF TABLES

Table

LIST OF FIGURES

Figure

CHAPTER 1

Introduction

1.1 Motivation

Efficient and accurate modeling of electromagnetic interaction between a buried object and layered rough surfaces finds a wide variety of applications ranging from detection of landmines and remote sensing of soil moisture content to retrieval of snow depth. Considerable research efforts have been focused on analyzing multiple scattering between objects and rough interfaces. Many analytical and numerical approaches have been developed to tackle various subsets of the problem. For rough surface scattering, analytical methods, such as the small perturbation method (SPM) [1, 2] or Kirchoff approximations (KA) [3] have been employed to solve the problem. The applicability of analytical methods is typically limited by their domains of validity for roughness of each layer interface [4]. On the other hand, numerical techniques, such as the Method of Moments (MoM) [5-9] and finite-difference time domain (FDTD) [10-12] offer the advantage of the capability of modeling electromagnetic scattering from rough surfaces with arbitrary roughness. However, they also present several drawbacks and modeling challenges. In MoM, the size of the impedance matrix is determined by the size of objects, the sample points per wavelength, and the number of scatterers. The computational cost becomes prohibitively high when the problem scenario involves multiple rough surfaces and a cluster of objects.

In MoM, the edge diffraction effect [13] caused by a truncated stack of layered rough surfaces also poses a problem since the tapered illumination source [14], if used, only remedies the edge diffraction effect due to the top rough surface, leaving that of subsurface rough surfaces untreated. In FDTD which is an attractive candidate for modeling inhomogeneous media, full-space discretization is required. FDTD also involves the delicate task of specifying absorbing boundary conditions to terminate the computational domain. Very fine grid spatial discretization is needed to resolve small-wavelength geometrical features. For low frequency radar applications, modeling even only slightly rough natural soil rough surfaces may result in very long solution times. Finally, for rough surface problem using FDTD, the cell-to-cell phase variation between corresponding points in different unit cells that arises from a plane-wave illumination source at oblique incidence renders time-domain implementation very challenging [15].

The intent of this dissertation is to develop an efficient and accurate solution to electromagnetic scattering from layered rough surfaces, which is not limited by the drawbacks of MoM and FDTD. This dissertation in the forward modeling development consists of three components: 1) the theoretical formulation of an efficient and coherent scattering solution for layered rough surfaces and a thorough feasibility evaluation and sensitivity study for remote sensing of subsurface soil moisture, 2) the study of the backscattering enhancement effect due to surface plasmon resonance from layered rough surfaces, and 3) the development of a novel scattering analysis for incorporating a buried object or a cluster of objects in layered rough surfaces. Following the development of a forward model, the last part of the dissertation focuses on inverse scattering from layered rough surfaces where the goal is to estimate the complex dielectric constants and layer depth of multilayer rough surfaces.

1.2 Applications and Previous Work

Forward electromagnetic modeling of scattering from buried objects in layered rough surfaces finds applications in optical probing of layer depth, remote sensing of subsurface soil moisture, detection of landmines, through-wall imaging, among many others. In the area of inverse modeling, we focus our attention on the application in the retrieval of the subsurface soil dielectric properties. In what follows, several applications of this thesis work are discussed in detail.

1.2.1 Remote Sensing of Subsurface Soil Moisture

Remote sensing of soil moisture is one of the major applications of radar technology where the objective is to map the distributions of soil moisture using radar backscattering coefficients. For observations of surface soil moisture fields, the use of L-band radars and radiometers has been long established as an effective means ([16-20]), and has led to community-wide support for the proposed Hydrosphere State (HYDROS) satellite soil moisture mission at L-band [20, 21], followed by the National Research Council's recommendation for the Soil Moisture Active/Passive (SMAP) mission. Complementary to surface soil moisture, the soil moisture profile to depths of tens of centimeters to meters (within the root-zone) is a key controlling variable of the hydrologic partitioning over terrestrial surfaces. The soil moisture depth gradients can undergo significant variations and are determined by the difference of surface hydrologic fluxes and deep moisture variations related to drainage and transpiration by deep-rooted grasses and trees. This gradient undergoes frequent reversals in response to wetting and drying periods, and hence its measurement, if possible, could enable proper characterization of the hydrologic fluxes involved.

With recent technology developments for radar systems at the VHF (e.g., 137 MHz) and UHF (e.g., 435 MHz) bands, the potential of probing deep soil moisture content has been enhanced due to the larger penetration depth afforded at these lower frequencies. Mission concept studies such as the Microwave Observatory of Subcanopy and Subsurface (MOSS) [22] and studies using actual airborne systems such as the NASA/JPL AIRSAR [23] have shown the technological and analytical feasibility of obtaining reliable radar data and subsurface soil moisture products at low frequencies. At VHF band, electromagnetic waves can penetrate well into the ground surface and scatter from subsurface interfaces. Both backscattering coefficients and co-polarized phase differences at low frequencies capture the effect of deep soil moisture well below the ground surface without detrimental attenuation [24].

Depth-dependent soil moisture gives rise to dielectric profiles which strongly depend on soil type, temperature profile, surface evaporation and moisture content. The real part of the dielectric constant at VHF ranges from 3 for dry soil to about 30 for wet soil. Therefore, backscattering coefficients at this frequency band could vary significantly depending on the ground moisture regime. Along with a non-uniform soil moisture function in depth, soil consists of different subsurface layers, which are typically rough. For example, there could exist sand, clay, and rock layers. These distinct layers could be of very different soil types and must be modeled as individual rough layers [25]. Fig. 1.1 shows an example of the cross section of layered soil media. Distinct layers are apparent from the picture taken at the Walnut Gulch Experimental Watershed (WGEW) in Arizona during a dry period.

Fig. 1.1: An example of layered soil profile in WGEW, showing the rough interfaces and visible moisture variations within each layer

Consequently, the presence of both inhomogeneous dielectric profiles as well as irregular soil layers necessitates the need for a model of layered soil media which accounts for both dielectric profiles and multilayer rough surfaces in the development of scattering models at low frequencies.

In [26], an analytical solution based on SPM to scattering from a slightly rough surface with inhomogeneous dielectric profiles is developed where the top ground surface is assumed to be slightly rough. There are also a few studies on the scattering of electromagnetic waves from multilayer homogeneous rough surfaces. Analytical solutions based on SPM to electromagnetic scattering from a rough surface covered by a homogeneous layer and also two-interface rough surfaces have been proposed and formulated recently in [27-29] and [1, 30, 31], respectively, and they are valid for surfaces with small roughness ($kh \ll 1$) and small slope approximation ($kl_c \sim 1$), where k is the free space wavenumber, h is the root-mean-squared height, and l_c is the correlation length. Numerical solution based on Method of Moments (MoM) also has been employed to solve the scattering problem for layered rough surfaces [7, 32]. MoM based on Steepest Descent Fast Multi-pole Method (SDFMM) is also investigated in [32]. Forward-backward method with spectral acceleration for scattering from layered rough surfaces is introduced in [7].

1.2.2 Backscattering Enhancement of Surface Plasmon Resonance from Layered Rough Surfaces

Backscattering enhancement is a phenomenon in rough surface scattering which manifests itself as a well-defined peak in the backscattering direction [33]. In a small roughness regime, backscattering enhancement is induced by the excitation of surface plasmon waves along a certain path followed by their retracing the same path in the reverse direction. Both theoretical [34, 35] and experimental [36] research efforts have been previously made to study backscattering enhancement effect of rough surfaces due to surface plasmon resonance. Backscattering enhancement of surface plasmon waves is important in various applications, including surface plasmon localization in rough-metal surfaces and ocean acoustic applications [33]. It is also an emerging area of interest in biological applications and has provided a new means to detect and image biological interfaces of thickness well below the diffraction limit [37].

Backscattering enhancement due to rough surface scattering can arise from two distinct mechanisms: multiple (double) scattering effect and surface plasmon resonance. When the rms height is close to a wavelength and the slope is also close to unity, waves scattered from the surface may interfere constructively in the backscattering direction, producing an enhanced peak. This type of backscattering enhancement is caused by the phenomenon of multiple (double) scattering [38] where constructive interference takes place between the direct scattered fields and their time-reversed reciprocal pairs within the valleys of rough surfaces. The formation of enhanced backscattering from very rough surfaces does not require the existence of surface plasmon modes [39]. This type of backscattering enhancement tends to result in broad angular width. The second type of backscattering enhancement is due to surface plasmon resonance. It occurs when the rms height is much smaller than a wavelength and the medium can support surface waves. When surface plasmon waves are excited and they traverse along the surface in opposite directions, they may constructively interfere with each other, producing an enhanced backscattered peak. The angular width of an enhanced peak due to surface plasmon resonance is typically narrow.

Surface plasmon resonance is a charge-density oscillation associated with surface plasmon waves at the interface which decay evanescently into both media and propagate along the interface. In a planar interface geometry, these surface plasmon waves stay bound to the surface. When the surface geometry becomes irregular, such as a periodic or rough surface, these surface plasmon waves become localized at protrusions and crevices of rough surface and they can couple into propagating modes and significantly enhance the scattered energy [40, 41]. For a planar interface between two media, backscattering enhancement can only be observed in TM (vertical) polarization because only the TM boundary conditions allow the surface plasmon waves to exist for nonmagnetic media. When the field is TE polarized, surface plasmon waves cannot be supported because the boundary condition cannot be satisfied if the TE wave decays exponentially on both sides of the interface. In fiber optic communications, the TM-only nature of the surface plasmon modes has been exploited to provide polarization selectivity [42]. However, when the scattering medium consists of a slab on a substrate, this guiding structure can support surface waves for both TE and TM polarizations. Depending on the layer thickness and the dielectric constant of slab, this waveguide can excite multiple surface plasmon waves, giving rise to backscattered enhanced peaks for both polarizations.

Previous work which discussed enhanced backscattering due to surface plasmon modes from a single metallic rough surface can be found in [34, 35]. In analyzing backscattering enhancement due to surface plasmon resonance, only coherent methods that can handle at least up to the 2nd order of scattering are useful. In [30], a theoretical development based on the higher-order SPM for backscattering enhancement from multilayer rough surfaces was presented. Numerical techniques such as extended boundary condition method (EBCM) also known as reduced Rayleigh method have been extensively employed to analyze backscattering enhancement. In [43], EBCM was employed in a numerical study of light scattered from a one-dimensional, randomly rough surface on a metal. It was also applied to analyze the case of a dielectric film with a randomly rough surface deposited on a planar metal surface in [44]. Similarly, the scenario of a rough metal surface coated with a planar dielectric film was studied using reduced Rayleigh method in [45]. In [45], the two-layer problem results in a pair of coupled matrix equations which need to be solved simultaneously. Computational cost increases exponentially as the number of layers increases. Finally, in [46, 47], the scattering and transmission of light from a film with two corrugated surfaces was solved using EBCM where the simulation in [46] was only carried out for a set of two deterministic periodic surface profiles. In [47], only normal incidence was investigated.

1.2.3 Landmine Detection

This area of research has attained prominence for the past decades and found applications in the detection of landmine and unexploded ordnance (UXO). Fig. 1.2 shows the human search for unexploded ordnance using ground penetrating radar (GPR).

Fig. 1.2: Detection and localization of unexploded ordnance (UXO) using ground penetrating radar (GPR)

Anti-personnel mines are typically buried at shallow/moderate depth. Low frequency radars with an improved signal depth penetration can potentially sense buried objects embedded in layered media. Therefore, it is especially important to account for the presence of subsurface rough interface for the low frequency radar application. The backscattered signal from the mine could be small compared with the primary backscattered signal due to rough surface scattering at the soil-air interface. The presence of a subsurface rough interface will further clutter the backscattered target response. When the solution is developed to analyze scattering from a buried object in layered rough surfaces, multiple scattering due to the interactions between an object and layered rough surfaces needs to be accounted for. Various methods have been developed to solve the scattering problem for a buried object underneath a rough surface.

Commonly, the solution to scattering from an object beneath a rough surface is based on MoM (e.g. [48-53]). In MoM, the rough interface of finite length is modeled in the simulation and a tapered incident field is used to avoid surface edge scattering effects. Due to the presence of both object and distributed source (the rough surface) scatterers, scattering coefficient depends on the rough surface area illuminated by the incident tapered wave. Rough surface effects become more likely to dominate object scattering effects when a large surface area is illuminated. Therefore, the concept of difference field cross sections is often applied to reduce the dependency on the tapered incident field (illumination area) [53]. Essentially, scattered fields are computed both for the combined object/rough surface problem and the rough-surface-only problem, and subtracted to yield “object minus no-object” fields. Tests have confirmed that difference field cross sections do not depend on the illumination area. To avoid the use of difference field cross sections, an infinitely extended incident waves needs to be applied in the simulation without causing edge diffractions. This can be accomplished through the use of periodic boundary condition which minimizes the effect of edge diffraction.

Another difficulty associated with MoM is to choose the proper value of the tapering parameter. This problem with edge diffractions is often complicated and amplified by an object located in a stack of truncated rough layers. Therefore, for numerical simulation, the length of each rough surface is often chosen to be very long in an attempt to eliminate edge diffractions using tapered incident wave. This in turn increases both computational time and memory requirements. The large size of the matrix in MoM often demands the use of computationally efficient methods for solving layered rough surface scattering problems.

1.2.4 Retrieval of Subsurface Soil Moisture in Layered Media

Tremendous research effort has been made to retrieve bare surface soil moisture from remote sensing data. Semi-empirical polarimetric backscattering models for bare soil surfaces have been developed and inverted directly to estimate both the volumetric soil moisture content and the rms surface height from multiple polarized radar observations [16, 17, 54]. A numerical inversion of the Integral Equation Method (IEM) model using a look-up table of IEM simulation results has been applied to retrieve soil moisture over bare soil surfaces from active microwave data in [55]. Furthermore, a Bayesian approach to the retrieval of soil moisture content using a priori information on soil moisture content and surface roughness has been devised in [56]. On the other hand, many attempts in inverting the dielectric profile of a layered soil medium also have been made. Using ground penetrating radar near-field data, mono-static pulse radar has been used to estimate permittivity profiles in a multilayer medium where the conductivity profile is assumed to be known in [57] and [58]. In those works, the radar operates at the normal-incidence mode and therefore any laterally scattered energy due to surface roughness is negligible.

Due to the nature of nonlinearity and non-uniqueness underlying the problem of subsurface inversion, the development of a reliable and accurate inversion algorithm for subsurface soil moisture becomes an extremely challenging task especially when the subsurface roughness statistics are the parameters to invert. Currently, an inversion method for the retrieval of subsurface soil moisture including both dielectric constants and roughness information using multi-frequency polarimetric backscattering radar data is still lacking. To probe subsurface soil moisture, there is more readily useful information contained in time-domain data (a broadband pulse) than magnitude and phase measurements at a single or just a few discrete frequencies. Each delay echo in the time history represents a reflection from an interface and the time difference between echoes is directly correlated with layer thickness. However, one of the major challenges underlying the acquisition of time-domain data at low frequencies is that it is very difficult to design and implement wideband radar systems at low frequencies. Step-frequency radar systems are an alternative solution to wideband low frequency radar systems. Step-frequency radar offers the advantage of both frequency-domain data collection and the realization of time-domain data. In addition, compared to impulse radar systems, step-frequency radar technology also has an improved signal-to-noise ratio, stable signal sources, and the availability of total source power at each measurement frequency [59]. Although the full realization of step-frequency radar system in [59] is not feasible from space, but from air, the systems such as GeoSAR [60-62] covering from 270 MHz to 430 MHz or LORA/CARABAS can be deployed to perform UHF/VHF multi-frequency measurements.

1.3 Thesis Objectives and Contribution

I developed a coherent technique for analyzing scattering from layered rough surfaces and embedded objects in two dimensions. The formulation of the approach is outlined in the following. The core of the proposed method for modeling electromagnetic scattering from layered rough surfaces lies in the use of the scattering matrix method (SMM). Layered rough surfaces consist of a stack of rough interfaces. The solution to scattering from each rough interface is sought independently based on the extended boundary condition method (EBCM) [9, 63-65], where the scattered fields of each rough interface are expressed as a summation of plane waves and then cast in terms of reflection and transmission matrices. To account for multiple scattering between multiple rough boundaries, SMM is employed to recursively cascade reflection and transmission matrices of each rough interface and obtain the composite reflection matrix from the overall scattering medium. This coherent scattering approach can be used to compute both backscattering coefficients and co-polarized phase difference, which are useful measured parameters for the inversion of dielectric properties and roughness statistics of layered rough surfaces.

One of the strengths of this method is its capability of incorporating a buried object in layered rough surfaces. The derivation of the transition matrix (T-matrix) for a circular dielectric cylinder can be found in [9]. A T-matrix relates the incident field to the scattered field of an object, both of which are expanded in terms of cylindrical harmonics in two dimensions. To perform mode matching between layered rough surfaces and a buried object, the cylindrical-to-spatial harmonics (plane wave) transformation is applied to the T-matrix of a buried object. This harmonic transformation is derived through the use of the recurrence formula and Fourier integral representation for Hankel functions and the expressions for the transformation matrices can be found in [66-70]. When the T-matrix of a buried circular cylinder is transformed into the reflection and transmission matrices, these matrices can then be cascaded with those of layered rough surfaces to account for electromagnetic interaction between a buried cylinder and layered rough interfaces.

Following the development of a forward model, I then set out to develop a multi-frequency inversion algorithm where dielectric properties and roughness statistics of ground surface are estimated using higher frequency information (L band) and subsurface probing capabilities are achieved using low frequency radar measurements (VHF and UHF). The main feature of the proposed inversion method is that it accounts for the existence of a rough subsurface layer in the development of the inversion algorithm by characterizing subsurface roughness as a statistical unknown to be estimated. The proposed inversion algorithm performs an inverse Cosine transform of radar measurements over the VHF- and UHF- frequency bands to obtain synthetic time-domain data and subsequently parameterizes individual delay echoes in time as a result of successive reflections upon different rough interfaces. These parameters are then used to invert subsurface geophysical parameters. The proposed inversion algorithm in this thesis is designed to complement a step-frequency radar system at the VHF- and UHF- bands.

No previous work exists regarding scattering from multilayer rough surfaces separated by arbitrary inhomogeneous dielectric profiles. Similarly, a coherent technique, which efficiently solves scattering from arbitrary N-interface rough surfaces with multiple scattering effect fully accounted for, has not previously been formulated. A unifying theory which systematically handles wave interactions between buried objects and rough surfaces is also lacking. In this dissertation, a hybrid analytical/numerical technique for analyzing scattering from layered rough surfaces based on EBCM/SMM is proposed. This rigorous technique coherently accounts for all multiple orders of scattering and multiple bounces due to wave interactions between rough interfaces. In addition, it does not suffer from any disadvantageous aspects of MoM and FDTD, including the rapid growth of matrix size with increasing number of scatterers (MoM), the effect of edge diffraction (MoM), very fine grid spatial discretization to resolve small-wavelength geometrical features (FDTD), difficulty in the implementation of an obliquely-incident plane wave source (FDTD), and the specification of absorbing boundary conditions (FDTD). The capability of the proposed forward modeling technique is also enhanced by demonstrating its ability to incorporate buried objects in layered media. The usefulness of the technique is further corroborated by employing the method to perform a sensitivity analysis for remote sensing of subsurface soil moisture, study backscattering enhancement effect from layered rough surfaces, and carry out numerical experiments for the landmine detection problem and volume scattering from discrete random media. It is important to point out the theoretical nature of this thesis work. Cross-validation with experimental data is subject of future work, where well-controlled experiments can be performed.

1.4 Dissertation Overview

This dissertation is composed of seven chapters. Chapter 2 defines the forward modeling problems and reviews the statistical properties and generation methodologies of random rough surfaces and discrete random media. The last section of Chapter 2 discusses SMM which serves as the basis for further advanced modeling, and outlines the scattering matrix solution to scattering from layered rough surfaces. Chapter 3 reviews EBCM, derives the scattering matrices of a rough surface, and formulates the scattering analysis for layered rough surfaces with stratified dielectric profiles. In Chapter 3, extensive analytical and numerical validations are presented and a benchmarking study of MoM and EBCM/SMM is performed. A thorough feasibility evaluation and sensitivity study are then conducted for remote sensing of subsurface soil moisture. In Chapter 4, the proposed hybrid method based on EBCM/SMM is applied to analyze multiple scattering processes by investigating the backscattering enhancement phenomenon for layered rough surfaces. The chapter examines backscattering enhancement due to surface plasmon resonance from two-interface rough surfaces and derives the wavenumbers for surface plasmon waves supported by a two-layer medium. Exhaustive numerical experiments are performed to study the backscattering enhancement effects for different sub-wavelength features, such as, subsurface roughness and layer thickness. Qualitative conclusions regarding mode conversion efficiencies of TE and TM surface waves are drawn. Chapter 5 enhances the proposed forward modeling solver by allowing a buried object or a cluster of objects to be incorporated in layered rough surfaces. Analytical validations and numerical examples are provided and discussed in Chapter 5. Particular attention is given to the investigation of the relative importance and sensitivity of various physical parameters of buried objects and layered rough surfaces to the overall backscattered response. In Chapter 5, the proposed technique is also generalized to analyze scattering from a cluster of cylinders (2D discrete random media) in layered rough surfaces. In Chapter 6, a multi-frequency polarimetric inversion algorithm for the retrieval of subsurface properties of layered soil media using VHF/UHF and L-band radar measurements is presented. In the proposed inversion method, synthetic time-domain data are constructed using multi-frequency measurements and the dielectric properties and roughness statistics are estimated using the pulse shape optimization for time delay echoes from dual-polarized VHF/UHF band radar measurements. At the end of this dissertation, Chapter 7 makes the concluding remarks and motivates future work.

CHAPTER 2

Problem Description and Background Theory

In this chapter, we define the forward scattering problems whose scattering solution will be sought in the following chapters. In section 2.1, three forward modeling problems are examined: scattering from layered rough surfaces with stratified dielectric profiles, scattering from a buried cylinder in layered rough surfaces, and finally scattering from discrete random media in layered rough surfaces. Following the description of forward modeling problems, the statistics and Monte Carlo generation of rough surfaces and discrete random media are discussed in section 2.2. Fundamental statistical properties associated with rough surfaces and discrete random media are reviewed. In section 2.3.1, the derivation of the scattering matrix method (SMM) is given. Upon obtaining the scattering matrix solution, the expressions for solving the forward scattering problems are provided in section 2.3.2.

2.1 Problem Definition

2.1.1 Multilayer Rough Surfaces

We consider scattering coefficients for a two-rough-interface geometry with arbitrary dielectric profiles modeled as fine stratifications. The top rough surface, f_1, separates free space from the medium of dielectric profile $\varepsilon_1(z)$ and $\mu_1 = \mu_0$. This medium fills a layer separated from another inhomogeneous stratified medium ($\varepsilon_2(z)$, $\mu_2 = \mu_0$) by another rough surface f_2. The geometry of the problem is illustrated in Fig. 2.1. The dielectric profiles arise due to spatially varying volumetric moisture content denoted by $m_v(z)$ also shown in Fig. 2.1. The inhomogeneous medium described by $\varepsilon_1(z)$ has mean layer thickness of d. The wave vector of the incident field lies in the x-z plane. The polarization is said to be TM or vertical when the magnetic field is directed along the y axis and TE or horizontal when the electric field is directed along the y axis. The technique developed in this dissertation can also handle the problem of general 2D geometry where there is any number of rough surfaces and profiles involved, or where every single interface is rough. The dielectric profiles between each two rough surfaces are modeled as finely stratified media (Fig. 2.1).

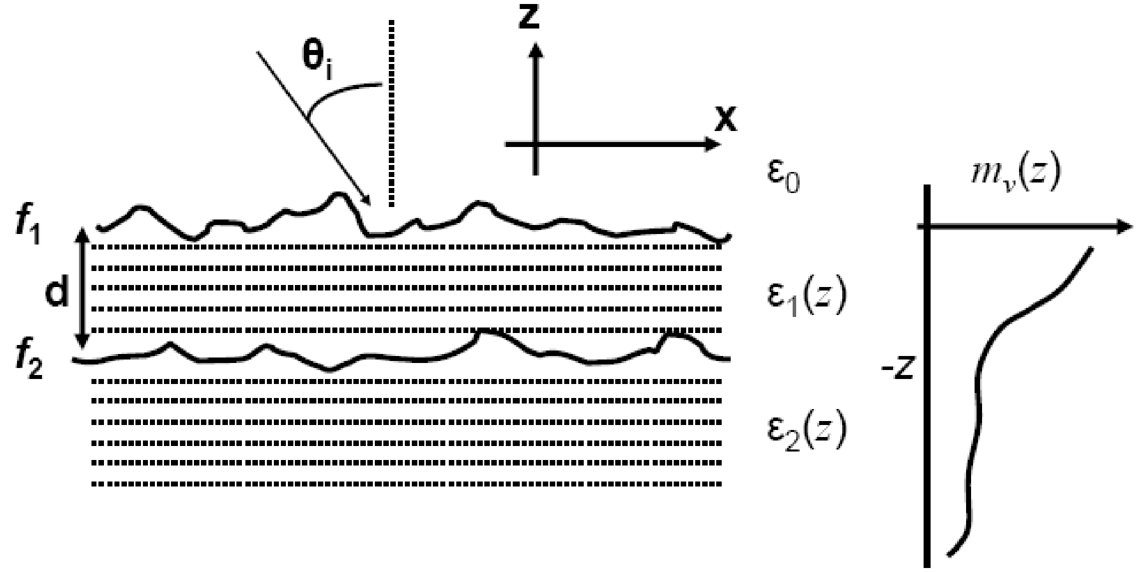

Fig. 2.1: Geometry of scattering from arbitrary profiles separated by multilayer rough surfaces

2.1.2 Buried Cylinder in Layered Rough Surfaces

We next consider bistatic scattering coefficients from two-interface rough surfaces bounding a dielectric cylinder of dielectric constant ε_c. The top rough surface, f_1, separates free space from a homogenous medium (ε_1, $\mu_1 = \mu_0$). This homogeneous medium fills a layer surrounding a homogeneous dielectric cylinder separated from the lower half space (ε_2, $\mu_2 = \mu_0$) by another rough surface f_2. The geometry of the problem is illustrated in Fig. 2.2. The axis of the cylinder is parallel to the y axis. The cylinder has radius *a* and is buried at a distance d_1 below the top rough interface and at a distance d_2 above the bottom rough interface. The cylindrical structure is assumed to be infinite along the y axis so the problem is a two-dimensional one. The wave vector of the incident field lies in the x-z plane. The polarization is said to be TM (with respect to the axis of the cylinder) or vertical when the electric field is directed along the y axis and TE or horizontal when the magnetic field is directed along the y axis. The technique developed in this dissertation can also handle the problem of general geometry where the cylinder could be situated anywhere in the layered structure, for example, a cylinder beneath both of the two rough interfaces.

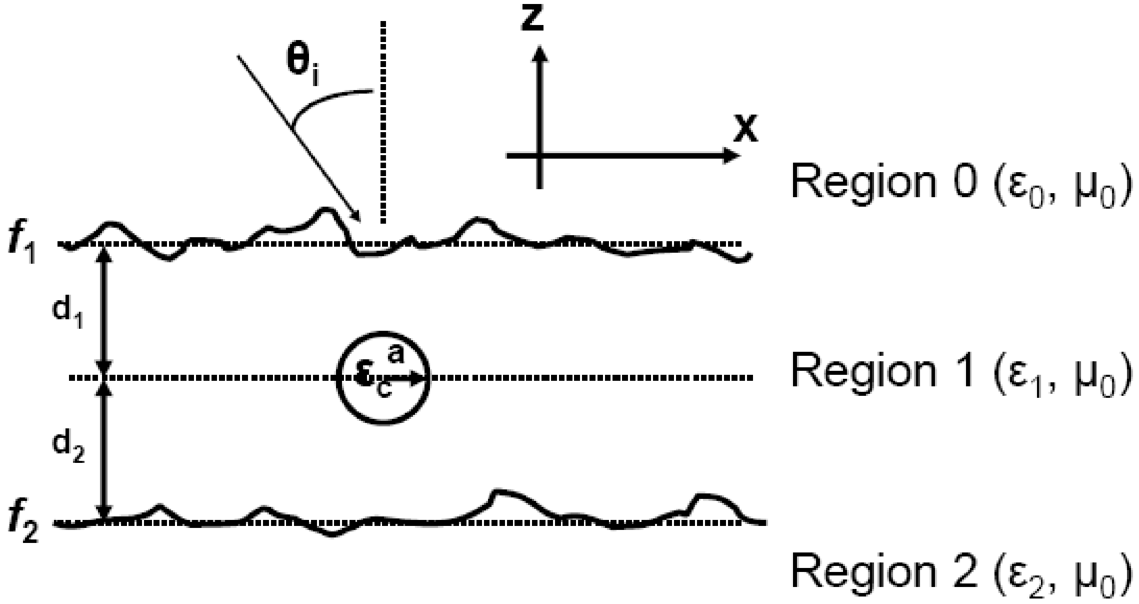

Fig. 2.2: Scattering from multilayer rough surfaces bounding a dielectric cylinder

2.1.3 Discrete Random Media

The last scattering problem considered in this thesis is the discrete random media problem with two-interface rough surfaces bounding a random distribution of dielectric cylinder of dielectric constant ε_c. The top rough surface, f_1, separates free space from a discrete random medium. This discrete random medium is a layer of background (host) material (ε_1) filled with a random discrete distribution of homogeneous dielectric cylinder (ε_c) separated from the lower half space (ε_2) by another rough surface f_2. The geometry of the problem is illustrated in Fig. 2.3. The axis of each cylinder of 2D discrete random media is parallel to the y axis and each cylinder is of radius *a*. The cylindrical structure is assumed to be infinite along the y axis so the problem reduces to a two-dimensional one. The wave vector of the incident field lies in the x-z plane. The polarization is said to be TM (with respect to the axis of the cylinder) or vertical when the electric field is directed along the y axis and TE or horizontal when the magnetic field is directed along the y axis.

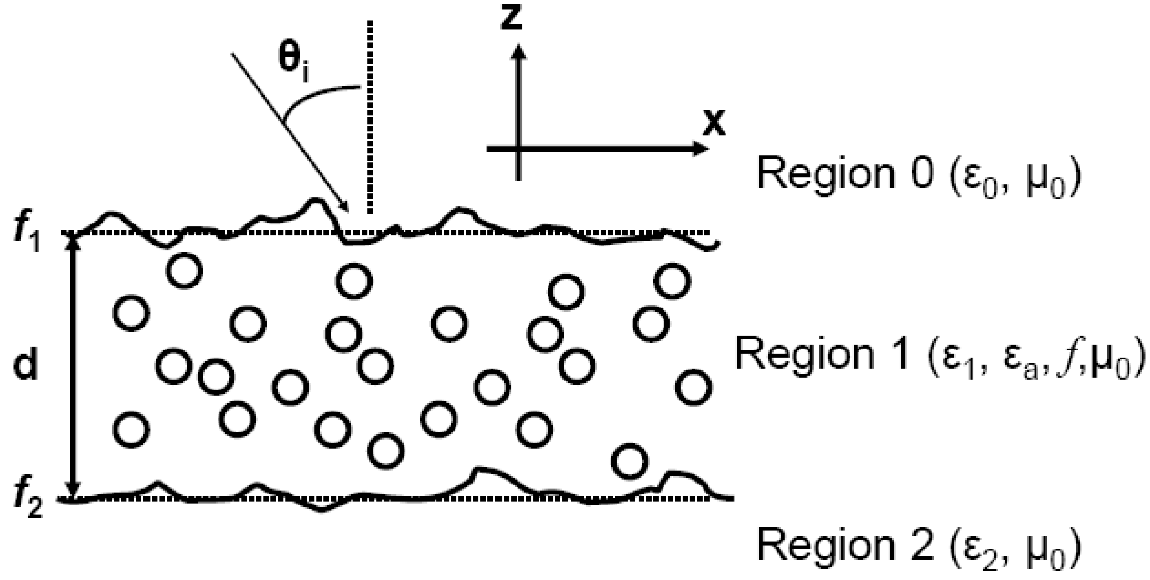

Fig. 2.3: Geometry of scattering from discrete random media in multilayer rough surfaces

2.2 Statistics of Random Media

2.2.1 Random Rough Surface

This section discusses the statistical properties of rough surfaces. Since this thesis deals with one dimensional (1D) rough surfaces, the statistics for 1D rough surface are outlined here. The following discussion is based on [9]. 1D random rough surface is represented by z=*f*(x), where *f*(x) is a real valued random rough height function of x with a zero mean.

$$\int_0^L xf(x)dx = < f(x) >= 0 \tag{2.1}$$

where L is the length of the random rough surface profile. The Fourier transform of the rough surface height function, *f*(x), is

$$F(k_x) = \frac{1}{2\pi}\int_{-\infty}^{\infty} f(x)e^{-ik_x x}dx \tag{2.2}$$

The mean of the rough surface height function in spectral domain is also zero. The process *f*(x) is called Gaussian if *f*(x_1), *f*(x_2), …, *f*(x_n) are jointly Gaussian for any n. The Gaussian process is described and characterized by its correlation function

$$< f(x_1)f(x_2) >= h^2C(x_1 - x_2) \tag{2.3}$$

with the assumption of stationarity where the rough surface height function is shift-invariant. The quantity *h* is called the root mean squared height (RMS) which is related to the standard deviation of the Gaussian samples of the rough surface height function. The Fourier transform of (2.3) is given by

$$h^2C(x_1 - x_2) = \int_{-\infty}^{\infty} dk_{1x}\int_{-\infty}^{\infty} dk_{2x}e^{i(k_{1x}x_1 - k_{2x}x_2)} < F(k_{1x})F^*(k_{2x}) > \tag{2.4}$$

Since the left hand side of (2.3) depends only on x_1-x_2 and *f*(x) is real,

$$< F(k_{1x})F^*(k_{2x}) >=< F(k_{1x})F(-k_{2x}) >= \delta(k_{1x} - k_{2x})W(k_{1x}) \tag{2.5}$$

where $W(k_{1x})$ is known as the spectral density. The Fourier transform of *$h^2C(x)$* is the spectral density $W(k_x)$

$$h^2C(x) = \int_{-\infty}^{\infty} dk_x e^{ik_x x}W(k_x) \tag{2.6}$$

This thesis primarily considers the Gaussian correlation function for rough surfaces with

$$C(x) = \exp(-\frac{x^2}{l^2}) \tag{2.7}$$

Its corresponding spectral density can be shown to be

$$W(k_x) = \frac{h^2 l}{2\sqrt{\pi}}\exp(-\frac{k_x^2 l^2}{4}) \tag{2.8}$$

where *h* is rms height, *l* is correlation length, and k_x is surface wavenumber. Another interesting statistical parameter associated with rough surfaces is the rms slope defined as

$$s = \sqrt{2}\frac{h}{l} \tag{2.9}$$

We then consider the surface profile *f*(x). Let *f*(x) be a periodic function of L, i.e., *f*(x)=*f*(x+*L*). Hence, *f*(x) can be represented using Fourier series.

$$f(x) = \frac{1}{L}\sum_{n=-\infty}^{\infty} b_n e^{i\frac{2\pi n}{L}x} \tag{2.10}$$

where b_n can be shown to be Gaussian random variables for Gaussian rough surfaces. From (2.3) and (2.10),

$$< f(x_1) f(x_2) >= \frac{1}{L^2}\sum_{n=-\infty}^{\infty}\sum_{m=-\infty}^{\infty} < b_n b_m^* > e^{i\frac{2\pi n}{L}x_1} e^{-i\frac{2\pi m}{L}x_2} \tag{2.11}$$

By comparing (2.3), (2.6), and (2.11)

$$< f(x_1) f(x_2) >= h^2 C(x_1 - x_2) = \int_{-\infty}^{\infty} dk_x e^{ik_x(x_1-x_2)} W(k_x) \tag{2.12}$$

Since b_n and b_m are independent, $< b_n b_m^* >= \delta_{nm} B_n$.

$$\int_{-\infty}^{\infty} dk_x e^{ik_x(x_1-x_2)} W(k_x) = \frac{1}{L^2}\sum_{n=-\infty}^{\infty} B_n e^{i\frac{2\pi n}{L}(x_1-x_2)} \tag{2.13}$$

Then, we sample k_x at K_n and let $\Delta k_x = \frac{2\pi}{L}$ and $K_n = \frac{2\pi n}{L} = n\Delta k_x$

$$\frac{2\pi}{L}\sum_{n=-\infty}^{\infty} e^{iK_n(x_1-x_2)} W(K_n) = \frac{1}{L^2}\sum_{n=-\infty}^{\infty} B_n e^{i\frac{2\pi n}{L}(x_1-x_2)} \tag{2.14}$$

This gives

$$B_n = 2\pi L W(K_n) =< |b_n|^2 > \tag{2.15}$$

When f(x) is real, Fourier series coefficients satisfy

$$b_n = b_{-n}^* \tag{2.16}$$

The orthogonality principle gives

$$< b_n b_{-n}^* >= 0 \tag{2.17}$$

Combining (2.16) and (2.17) results in

$$< b_n b_n >= 0 \tag{2.18}$$

We then represent b_n as the sum of its real and imaginary parts.

$$b_n = \mathrm{Re}\{b_n\} + i\,\mathrm{Im}\{b_n\} \tag{2.19}$$

From (2.18),

$$< (\mathrm{Re}\{b_n\})^2 >=< (\mathrm{Im}\{b_n\})^2 > \tag{2.20}$$

$$< \mathrm{Re}\{b_n\} >< \mathrm{Im}\{b_n\} >= 0 \tag{2.21}$$

Therefore, Re$\{b_n\}$ and Im$\{b_n\}$ are independent Gaussian random variables with zero mean and variance equal to half of that of $<|b_n|^2>$. Therefore, a Gaussian rough surface can be represented by a Fourier series with Gaussian distributed coefficients satisfying (2.15)-(2.21).

We further employ a discrete Fourier transform (DFT) version of (2.10). Let there be N points in both space and spectral domains, then the unit distance is $\Delta x = \frac{L}{N}$. Define

$$f(x_m) \triangleq f_m, \qquad x_m = m\Delta x \quad \text{for } m = -\frac{N}{2}+1,\ldots,0,1,\ldots,\frac{N}{2} \tag{2.22}$$

Then,

$$f_m = \frac{1}{L}\sum_{n=-\frac{N}{2}+1}^{\frac{N}{2}} b_n e^{i\frac{2\pi nm}{N}} \tag{2.23}$$

The DFT results in

$$b_n = \frac{L}{N}\sum_{m=-\frac{N}{2}+1}^{\frac{N}{2}} f_m e^{-i\frac{2\pi nm}{N}} \tag{2.24}$$

(2.23) and (2.24) can be computed using fast Fourier transform (FFT). Both f_m and b_n are periodic with period N.

$$b_{n+N} = b_n \tag{2.25}$$

$$f_{m+N} = f_m \tag{2.26}$$

From (2.25) and (2.16), we know

$$b_{-\frac{N}{2}} = b_{\frac{N}{2}} = b^*_{-\frac{N}{2}} \tag{2.27}$$

(2.27) yields both $b_{+\frac{N}{2}}$ and b_0 are real. Therefore, any periodic discrete function has DFT coefficients satisfying (2.25)-(2.27). Then, these symmetry properties are exploited to generate a Gaussian rough surface. The Matlab methodology for Gaussian rough surface generation is given below.

1. With a given seed, *N* Gaussian distributed random numbers with zeros mean and unit variance are generated using Matlab function randn. These *N* numbers are independent and they are not required to be grouped or arranged in any order. Let the numbers be labeled as r_1, r_2, r_3, … , r_N.

2. Then two real Gaussian numbers $b_{+\frac{N}{2}}$ and b_0 are computed as follows:

$$b_0 = \sqrt{2\pi W(0)}r_\alpha \tag{2.28}$$

$$b_{+\frac{N}{2}} = \sqrt{2\pi W(\frac{\pi N}{L})}r_\beta \tag{2.29}$$

where $\alpha \neq \beta$ and $\alpha, \beta \in \{1, 2, ..., N\}$.

3. (*N*/2-1) Gaussian numbers are then calculated using

$$b_n = \sqrt{2\pi W(|K_N|)}\left[\frac{1}{\sqrt{2}}(r_\sigma + ir_\xi)\right] \tag{2.30}$$

for $n = -\frac{N}{2} + 1, ..., -2, -1$ where σ, ξ are distinct indices selected from set $S = \{\{1, 2, ..., N\}/\{\alpha, \beta\}\}$.

4. Using $b_n = b^*_{-n}$, b_n for $n = 1, 2, ..., \frac{N}{2} - 1$ can be easily calculated.

5. Finally, using the inverse DFT relation in (2.31) with $X(n) = b_n$,

$$x(m) = \frac{1}{N} \sum_{n=-\frac{N}{2}+1}^{\frac{N}{2}} X(n) e^{i\frac{2\pi nm}{N}} \tag{2.31}$$

$x(m), m \in \{1, 2, ..., N-1\}$ is obtained. Extending $x(m)$ periodically, the rough surface profile can be generated as follows:

$$f_m = \frac{N}{L} x(m) \tag{2.32}$$

for $m = -\frac{N}{2} + 1, ..., \frac{N}{2}$.

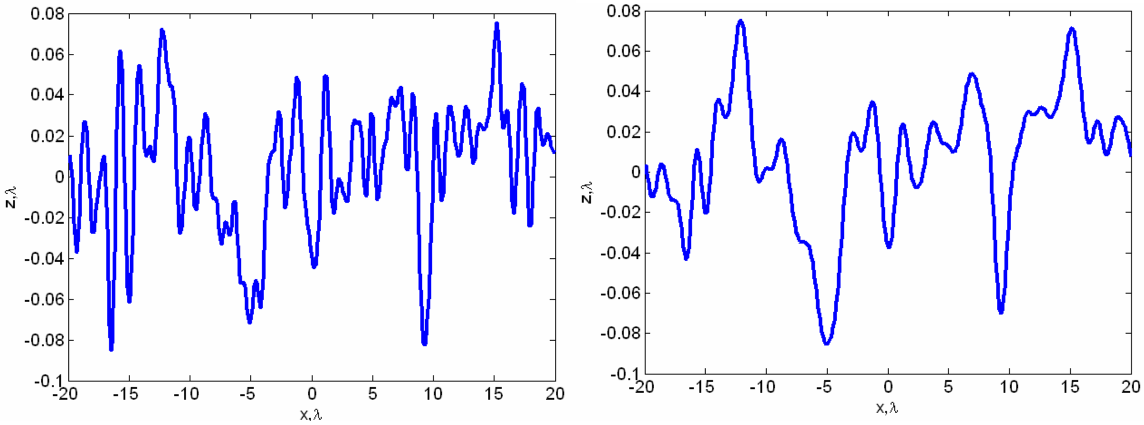

a) b)

Fig. 2.4: Two realizations of Gaussian rough surfaces with different correlation lengths: a) L=40λ, h=0.03λ, lc=0.5λ, b) L=40λ, h=0.03λ, lc=1λ

2.2.2 Discrete Random Media

Scattering from discrete random media depends on the positions of particles. A discrete random medium consists of discrete particles packed together which occupy some fractional volume *f*. This section consists of sub-sections from Chapters 8 and 9 in [9]. The probability density function (pdf) of particle positions $\rho(\bar{r}_i)$ is uniformly distributed. However, due to the finite size of particles, the joint probability density of two particle positions cannot be independent. Let $\rho(\bar{r}_i, \bar{r}_j)$ be the joint probability density function of two particles centered at $\bar{r}_i$ and $\bar{r}_j$ and $\rho(\bar{r}_i, \bar{r}_j) = 0$ for $|\bar{r}_i - \bar{r}_j|$ less than the minimum separation which is the diameter of a particle if the two particles are spheres of the same radius. The joint probability density function of two particles describes the pair distribution function. Let *N* be the number of particles. The particles are centered at $\bar{r}_1, \bar{r}_2, ..., \bar{r}_N$ and placed in a volume V. Then,

$$\rho(\bar{r}_i) = \frac{1}{V} \tag{2.33}$$

is the single particle pdf.

$$\rho(\bar{r}_i, \bar{r}_j) = \frac{g(\bar{r}_i, \bar{r}_j)}{V^2} \frac{N}{N-1} \tag{2.34}$$

is the joint pdf of two particles and *g* is the pair distribution function. In the limit of finite N, $\rho(\bar{r}_i, \bar{r}_j) \sim \frac{g(\bar{r}_i, \bar{r}_j)}{V^2}$. When the fractional area is not appreciable (i.e. less than 0.2), the hole-correction (HC) approximation can be applied to the pair distribution function where $g(\bar{r}) = 0$ for $r < b$ and $g(\bar{r}) = 1$ for $r \geq b$, where *b* is the diameter of the sphere. The HC approximation accounts for the fact that the particles do not interpenetrate each other. Neither the independent position approximation nor the HC approximation is accurate for appreciable fractional volume of scatterers. If we consider the opposite limit where the fractional volume of scatterers is unity and the entire volume *V* is occupied by scatterers, the pair distribution function, $g(\bar{r})$, will be zero for $r \neq mb$ where *m* is any nonzero integer. It consists of a train of delta functions at the positions of *r* equal to integer multiples of *b*. When $0 < f < 1$, the pair distribution function is of a form between the HC approximation and delta function trains. It is also worth noting that when the separation distance between particles approaches infinity, the particle positions become independent of each other and hence $\lim_{r \to \infty} g(\bar{r}) = 1$ for *f* not equal to maximum concentration. For $0 < f < 1$, the Percus-Yevick approximation [9] is often employed to obtain the analytical expression for pair distribution function. Let *b* be the diameter of the particle, with *b* = 2*a,* where *a* is the radius of the particle. Let *f* be the fractional area occupied by the particles. The value of *f* is related to *N* and *b* through the following expression:

$$f = \frac{\pi b^2 N}{4} \tag{2.35}$$

Equations (2.36) – (2.44) provide the expressions for the 2D pair distribution function with a random distribution of cylinders. Under the Percus-Yevick approximation,

$$c(x) = 1 \qquad for \qquad x > 1 \tag{2.36}$$

For $x \leq 1$, direct correlation *c(x)* assumes the following form,

$$c(x) = c(0)\left[1 - 4f + 4\omega_2\left(\frac{x}{2}\right) + s_2(f)x\right] \tag{2.37}$$

where

$$\omega_2(x) = \frac{2}{\pi}\left[\cos^{-1} x - x\sqrt{1-x^2}\right] \tag{2.38}$$

$$s_2(f) = \frac{3f^2}{8}\left[\frac{8(1-2p) + (25-9p)pf - (7-3p)pf^2}{1 + f + 3pf^2 - pf^3}\right] \tag{2.39}$$

$$c(0) = -\frac{1 + f + 3pf^2 - pf^3}{(1-f)^3} \tag{2.40}$$

$$p = \frac{7}{3} - \frac{4\sqrt{3}}{\pi} \tag{2.41}$$

Assuming isotropic correlation functions,

$$C(\bar{p}) = \frac{1}{2\pi}\int_0^{\infty} drc(r)J_0(\bar{p}r) \tag{2.42}$$

$$H(\bar{p}) = \frac{C(\bar{p})}{1 - n_0 4\pi^2 C(\bar{p})} \tag{2.43}$$

$$g(\bar{r}) = 1 + \int_{-\infty}^{\infty} d\bar{p}e^{i\bar{p}\cdot\bar{r}}H(\bar{p}) \tag{2.44}$$

To the first order Born or distorted Born approximation, the bistatic scattering intensity is proportional to the structure factor which is related to the Fourier transform of the pair distribution function. The study of pair distribution functions is an important subject in discrete random media problems. The next paragraph describes a Monte Carlo procedure for shuffling the positions of 2D random cylinders in a square area.

In what follows, a step-by-step procedure for Metropolis shuffling algorithm [9] is provided. We first need to define the statistical properties which characterize the discrete random media. Let there be *N* particles. For simplicity, let

$$N = N_1^2 \tag{2.45}$$

where N_1 is an integer. The particles are placed in a unit square of [0,1] x [0,1]. If n_o is the number of cylinders per unit area, then

$$n_o = N \tag{2.46}$$

Let *b* be the diameter of the cylinder with *b* = 2*a,* where *a* is the radius of the cylinder. Let *f* be the fractional area occupied by the cylinders. Thus, the diameter *b* is given by

$$b = \sqrt{\frac{4f}{\pi N}} \tag{2.47}$$

Inside the square, the cylinders are first placed periodically in both x and z directions with spacing given by

$$s = \frac{1}{N_1} \tag{2.48}$$

For example, the first row of N_1 particles have coordinates

$$\left(\frac{s}{2},\frac{s}{2}\right),\left(\frac{3s}{2},\frac{s}{2}\right),\left(\frac{5s}{2},\frac{s}{2}\right),\ldots,\left(\left(N_1-\frac{1}{2}\right)s,\frac{s}{2}\right) \tag{2.49}$$

To generate the 0th realization, we employ a shuffling method described as follows. N_{pass} passes are performed. For each pass, each cylinder is moved once even though the move may not be accepted. The move is dictated by Δ where

$$\Delta = c_{st} b \tag{2.50}$$

and c_{st} is an adjustable constant for the displacement. For a cylinder *j* with coordinates (x_j, z_j), we generate new coordinates $(x_j^{'}, z_j^{'})$ from two random numbers r_1 and r_2 which are uniformly distributed between -1 and 1. In Matlab, the function rand can be used to generate r_1 and r_2.

$$x_j^{'} = x_j + r_1\Delta \tag{2.51}$$

$$z_j^{'} = z_j + r_2\Delta \tag{2.52}$$

Next, we check whether the new coordinates, $(x_j^{'}, z_j^{'})$, are acceptable by ensuring they do not overlap with other particles. Note that the periodic boundary conditions are applied. Thus each particle has images in other squares. To check for overlap with particle *l*, (*l*=1,2,…,*N* and $l \neq j$), we calculate

$$r_x = x_l - x_j^{'} \tag{2.53}$$

If $r_x > 0.5$, then the image of x_l is closer to $x_j^{'}$. Thus we do the following

If $r_x > 0.5$, replace r_x by r_x-1
If $r_x \leq 0.5$, replace r_x by r_x+1

Do the same fo $r_y = z_l - z_j^{'}$ with the appropriate replacements. Then, the distance between cylinders *j* and *l* given by (2.54) is computed.

$$r_d = \sqrt{r_x^2 + r_z^2} \tag{2.54}$$

If $r_d \geq b$ for all $l \neq j$, then the move is accepted for cylinder *j*.

Replace x_j by $x_j^{'}$
Replace z_j by $z_j^{'}$

If $r_d < b$ for any $l \neq j$, then the move is rejected and the original coordinates (x_j, z_j) are kept. If $r_d > b$ for all $l \neq j$, we take $(x_j^{'}, z_j^{'})$ and temporarily call it the new coordinates $(x_j^{'}, z_j^{'})$. Before we finally accept the new $(x_j^{'}, z_j^{'})$, we need to make sure the cylinder *j* is within the unit square. If it is out of the unit square, it has become an image and we need to translate it back into the unit square. Thus, for the new x_j

$$\begin{aligned}&\text{If } x_j < 0\text{, replace } x_j \text{ by } x_j + 1\\ &\text{If } x_j > 1\text{, replace } x_j \text{ by } x_j - 1\end{aligned}$$

Do the same for z_j with the appropriate replacements. Then we accept (x_j, z_j) as the new position for cylinder *j*.

The process is applied to all the cylinders *j*=1,2,3,…,*N*. When the process is finished, one pass is completed. A new realization is generated after N_{pass} passes to make sure that the particles are sufficiently randomized. To get the 0th realization from the initial periodic configuration, it is better to do several times of N_{pass} passes. From the 0th realization, we generate new realizations for a total N_r realizations with each one created after N_{pass} passes. For each accepted new position for a cylinder, we count it as an accepted move. Let N_{acc} be the total number of accepted moves after N_r realizations. Then the acceptance rate is given by

$$accept \quad rate = \frac{N_{acc}}{N N_{pass} N_r} \tag{2.55}$$

If the displacement Δ is too small, then all the moves will be accepted and the realizations will be dependent on each other. On the other hand, if the displacement Δ is too large, then all the moves will be rejected. A good acceptance rate is between 30% and 70% by choosing an appropriate Δ through c_{st}. It is important to point out that Metropolis algorithm typically gives reasonable acceptance rate ranging from 40% to 75% when the volume fraction *f* is less than 0.4. For *f* > 0.4, overlapping rate is typically very high and acceptance rate is normally above 0.8. When discrete random media are rectangular whose length and depth are unequal (i.e., *d*=1λ and *L*=40 λ), good acceptance rates are only obtained when *f* < 0.2. Therefore, In Chapter 6 of this dissertation, only scattering from sparse random media will be investigated. For packing algorithms for a dense random media, the algorithm in [71] can be implemented. Fig. 2.5 shows the realizations of discrete random media whose computational domain is 40λ (L) by 1λ (d) for *f* = 0.1 and 0.2. The cylinder radius is set to be 0.1λ, which results in 127 cylinders for *f* = 0.1 and 254 cylinders for *f* = 0.2. The calculated acceptance rates for *f* = 0.1 in Fig 2.5 (a) and *f* = 0.2 in Fig. 2.5 (b) are 0.48 and 0.23.

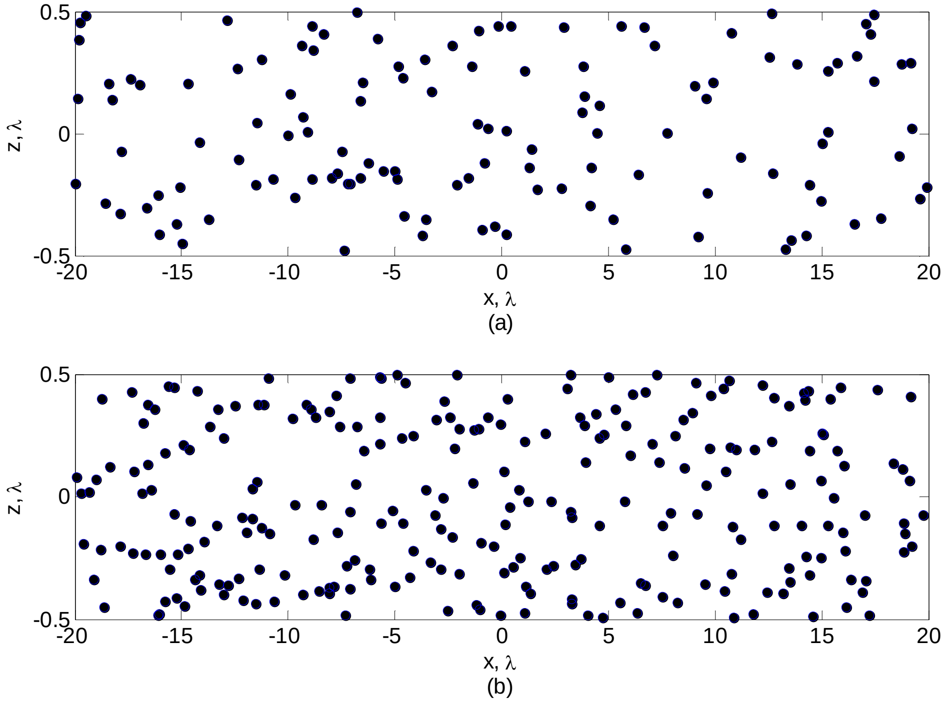

(a)

(b)

Fig. 2.5: Two realizations of discrete random media of L=40λ by d=1 using Metropolis algorithm with (a) f = 0.1 and (b) f =0.2

To obtain the pair distribution function from the realizations of discrete random media, we first generate the different realizations of discrete random media using Metropolis shuffling algorithm [9] and then compute the pair distribution function. Let the separation of the cylinders be counted in intervals of Δr. For the nth interval, the center separations of the particles are between $r_{sn} = b + (n-1)\Delta r$ and $r_{un} = b + n\Delta r$. Since a pair of cylinders are considered in uncorrelated positions when their separation is greater than 5*b* (i.e., $g(r)+1$ when $r > 5b$), and they cannot interpenetrate, the interval Δr is determined by

$$\Delta r = \frac{4b}{M} \tag{2.56}$$

where M is the total number of intervals and determines the resolution of the Monte Carlo pair distribution function. For each realization we count the *N*(*N*-1) pairs of separation. In the counting process, for the *j*th particle, *j* = 1,2,3,…, *N*, we calculate its separation with the *l*th particle (l = 1,2,3,…, *N* and $l \neq j$). Let $r_x = x_l - x_j$ and $r_z = z_l - z_j$. Then, if $r_x < 0.5$, replace r_x with $r_x - 1$ and if $r_x < -0.5$, replace r_x with $r_x + 1$. Do the same for r_z , with the appropriate replacements. Then we compute the separation r_d where $r_d = \sqrt{(r_x^2 + r_z^2)}$ and find out the interval where r_d falls. That will increase by one the counting of separation for that interval.

Let C_n be the number of counts of pair separations that fall in the nth interval. Then, $\frac{C_n}{N(N-1)}$ is the probability of finding a particle at the nth interval of separation. Thus, using the definition of the pair distribution function and the conditional probability

$$\frac{C_n}{N(N-1)} = \int_{nth} d\bar{r}p(\bar{r} \,|\, 0) \tag{2.57}$$

where $p(\bar{r} \,|\, 0)$ is the conditional probability of finding a particle at $\bar{r}$ given a particle at the origin. Since

$$p(\bar{r} \,|\, 0) = \frac{g(r)}{A} \tag{2.58}$$

We have

$$\frac{C_n}{N(N-1)} = \int_{r_{sn}}^{r_{un}} dr 2\pi r \frac{g(r)}{A} = \frac{g(\tilde{r}_n)}{A} \pi (r_{un}^2 - r_{sn}^2) \tag{2.59}$$

where $\tilde{r}_n$ is a weighted position in the nth interval. For example, $\tilde{r}_n = \sqrt{(r_{un}^2 + r_{sn}^2)/2}$. Thus,

$$g(\tilde{r}_n) = \frac{< C_n >}{n_o (N-1) \pi (r_{un}^2 - r_{sn}^2)} \tag{2.60}$$

where angular bracket refers to average over realizations.

2.3 Scattering Matrix Method

2.3.1 Description and Derivation

Scattering matrix method (SMM) is a well-established and efficient technique for analyzing the scattering response to layered media such as layered cylindrical or spherical geometries, waveguide junctions, and frequency selective surfaces. In [72-74], it has been applied to characterize cascaded microstrip step discontinuities and symmetric stubs. In this thesis, scattering matrix technique serves as the core of the formulation for solving scattering from multilayer rough surfaces and embedded objects. This approach is especially well suited for sensitivity analysis because it is possible to evaluate the effect of a change in one layer without repeating the entire computation [75]. Many other techniques [7, 76, 77] for analyzing layered structures solve the problem in entirety without employing cascading matrices which describe individual layers. Practical limitations associated with these approaches are increasing computational complexity with an increasing number of layers; a complete new analysis is required whenever a change is made in any layer. This section discusses scattering matrix formulation for plane wave propagation through layered media. SMM has been advantageously employed for handling wave propagation across interfaces and/or any discontinuities, with both propagating and evanescent modes included and sequential scattering features taken into account by cascading process. In general, the scattered field due to any scattering objects, such as planar interface, rough surface, waveguide junction, etc. can be expressed using plane wave solution which consists of spatial harmonics up to infinite orders. Through the truncation of a plane wave solution to a finite order, the scattered solution can then be cast into reflection and transmission matrices. The generalized scattering matrix, S_i, of the composite scattering system *i*, consisting of four submatrices of reflection and transmission, is given by

$$S_i = \begin{bmatrix} [R_i] & [\tilde{T}_i] \\ [T_i] & [\tilde{R}_i] \end{bmatrix} \tag{2.61}$$

where the tilde sign represents its reciprocal counterpart. The reflection and transmission sub-matrices describe the reflected and transmitted coefficients from the scattering system for a set of input vectors. Consider, for example, a rectangular waveguide with TE_{p0} excitation with unit amplitude from the left to a junction. If the amplitude of the nth mode of the reflected wave to the left is A_n, the (n, p) entry of the reflection matrix, $R_{n,p}$ is A_n. Similarly, if the amplitude of the mth mode of the wave transmitted to the right is B_m, $T_{m,p}$ is B_m. Consider another example for scattering from a rough surface. When the amplitude of incident wave is unity, $R_{i,j}$ and $T_{i,j}$ represent reflection and transmission coefficients into the angle θ_i due to a plane wave incident from the angle θ_j. The general form of reflection and transmission matrices can be written as follows:

$$[R] = \begin{bmatrix} R_{11} & R_{12} & \cdots & R_{1n} \\ R_{21} & R_{22} & \cdots & R_{2n} \\ \vdots & \vdots & \ddots & \vdots \\ R_{n1} & R_{n2} & \cdots & R_{nn} \end{bmatrix} \qquad (2.62) \qquad [T] = \begin{bmatrix} T_{11} & T_{12} & \cdots & T_{1n} \\ T_{21} & T_{22} & \cdots & T_{2n} \\ \vdots & \vdots & \ddots & \vdots \\ T_{n1} & T_{n2} & \cdots & T_{nn} \end{bmatrix} \qquad (2.63)$$

For a rough surface or a buried cylinder, the elements of the generalized scattering matrix are obtained by solving the electromagnetic problem using extended boundary condition method or T-matrix method. The next paragraph details the derivation of generalized scattering matrix technique for cascading two sets of scattering matrices to form a composite scattering matrix. This can be generalized to handle a cascade of N systems through recursion. The derivation given in this chapter is performed through direct substitution between inputs and outputs. An alternate derivation of generalized scattering matrix using signal flow graph can be found in [75]. Suppose an incident wave is impinging upon two scattering systems separated by a distance, L, with their scattering behaviors characterized by S_1 and S_2. Fig. 2.6 shows input and output parameters for two cascaded systems on which the following derivation is based. The following matrix relations (2.64) and (2.65) based on the scenario in Fig. 2.6 hold.

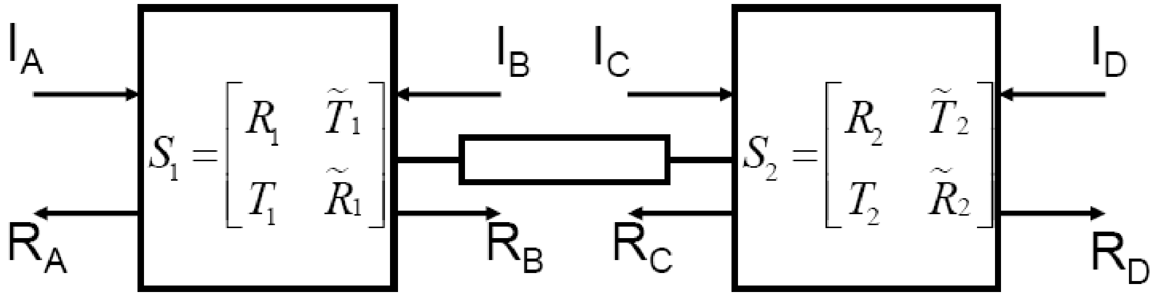

Fig. 2.6: Cascading two systems with scattering matrices S_1 and S_2

$$\begin{bmatrix} [R_A] \\ [R_B] \end{bmatrix} = \begin{bmatrix} [R_1] & [\tilde{T}_1] \\ [T_1] & [\tilde{R}_1] \end{bmatrix} \begin{bmatrix} [I_A] \\ [I_B] \end{bmatrix} \tag{2.64}$$

$$\begin{bmatrix} [R_C] \\ [R_D] \end{bmatrix} = \begin{bmatrix} [R_2] & [\tilde{T}_2] \\ [T_2] & [\tilde{R}_2] \end{bmatrix} \begin{bmatrix} [I_C] \\ [I_D] \end{bmatrix} \tag{2.65}$$

To account for wave propagation over a distance L, each mode is multiplied by phase shifting elements, exp(γL) where $\gamma = ik_x$.

$$\begin{bmatrix} [I_B] \\ [I_C] \end{bmatrix} = \begin{bmatrix} [0] & [\phi] \\ [\phi] & [0] \end{bmatrix} \begin{bmatrix} [R_B] \\ [R_C] \end{bmatrix} \tag{2.66}$$

$$[\phi] = \begin{bmatrix} e^{\gamma_1 L} & 0 & \cdots & 0 \\ 0 & e^{\gamma_2 L} & \cdots & 0 \\ \vdots & \vdots & \ddots & \vdots \\ 0 & 0 & \cdots & e^{\gamma_n L} \end{bmatrix} \tag{2.67}$$

Multiplying (2.64) and (2.65) out together with (2.66) gives the following equations.

$$[R_A] = [R_1][I_A] + [\tilde{T}_1][I_B] = [R_1][I_A] + [\tilde{T}_1][\phi][R_C] \tag{2.68}$$

$$[R_B] = [T_1][I_A] + [\tilde{R}_1][I_B] = [T_1][I_A] + [\tilde{R}_1][\phi][R_C] \tag{2.69}$$

$$[R_C] = [R_2][I_C] + [\tilde{T}_2][I_D] = [R_2][\phi][R_B] + [\tilde{T}_2][I_D] \tag{2.70}$$

$$[R_D] = [T_2][I_C] + [\tilde{R}_2][I_D] = [T_2][\phi][R_B] + [\tilde{R}_2][I_D] \tag{2.71}$$

Equations (2.69) and (2.70) are solved together to obtain the expressions for [R$_B$] and [R$_C$].

$$[R_B] = (I - [\tilde{R}_1][\phi][R_2][\phi])^{-1}([T_1][I_A] + [\tilde{R}_1][\phi][\tilde{T}_2][I_D]) \tag{2.72}$$

$$[R_C] = (I - [R_2][\phi][\tilde{R}_1][\phi])^{-1}([R_2][\phi][T_1][I_A] + [\tilde{T}_2][I_D]) \tag{2.73}$$

where I is an identity matrix. Substituting (2.72) into (2.68) leads to the following matrix expressions.

$$\begin{aligned}\left[R_A\right] &= \left\{[R_1]+[\tilde{T}_1][\phi](I-[\tilde{R}_1][\phi][R_2][\phi])^{-1}[R_2][\phi][T_1]\right\}[I_A] \\ &+\left\{[\tilde{T}_1](I-[\tilde{R}_1][\phi][R_2][\phi])^{-1}[\phi][\tilde{T}_2]\right\}[I_D]\end{aligned} \tag{2.74}$$

$$\begin{aligned}\left[R_D\right] &= \left\{[T_2][\phi](I-[R_2][\phi][\tilde{R}_1][\phi])^{-1}[T_1]\right\}[I_A] \\ &+\left\{[\tilde{R}_2]+[T_2][\phi](I-[\tilde{R}_1][\phi][R_2][\phi])^{-1}[\tilde{R}_1][\phi][\tilde{T}_2]\right\}[I_D]\end{aligned} \tag{2.75}$$

Therefore, the generalized composite scattering matrix of two cascaded systems is given by

$$\begin{bmatrix}[R_A]\\ [R_D]\end{bmatrix}=\begin{bmatrix}[R_i] & [\tilde{T}_i]\\ [T_i] & [\tilde{R}_i]\end{bmatrix}\begin{bmatrix}[I_A]\\ [I_D]\end{bmatrix} \tag{2.76}$$

$$\begin{aligned}S_i &= \begin{bmatrix}[R_i] & [\tilde{T}_i]\\ [T_i] & [\tilde{R}_i]\end{bmatrix} \\ &= \begin{bmatrix}[R_1]+[\tilde{T}_1][\phi](I-[\tilde{R}_1][\phi][R_2][\phi])^{-1}[R_2][\phi][T_1] & [\tilde{T}_1][\phi](I-[\tilde{R}_1][\phi][R_2][\phi])^{-1}[\tilde{T}_2] \\ [T_2][\phi](I-[R_2][\phi][\tilde{R}_1][\phi])^{-1}[T_1] & [\tilde{R}_2]+[T_2][\phi](I-[R_2][\phi][\tilde{R}_1][\phi])^{-1}[\tilde{R}_1][\phi][\tilde{T}_2]\end{bmatrix}\end{aligned} \tag{2.78}$$

This completes the derivation of SMM. The matrix inversion in (2.78) accounts for the multiple scattering and multiple bounces of modes between individual systems. Scattering matrices are truncated to a finite size where the number of modes used in the modal solution to scattered field is selected to ensure solution convergence. The next section provides the scattering matrix solutions to layered rough surfaces and buried cylinder problems.

2.3.2 Overview of Scattering Matrix Solution for Layered Rough Surfaces

This section outlines the main contribution of this thesis which is the application of SMM for solving scattering from layered rough surface with or without buried objects. First, the generalized scattering matrix expression for scattering from layered rough surfaces with an arbitrary dielectric profile depicted in Fig. 2.1 is provided. The composite scattering coefficients from cascading scattering matrices of two rough interfaces and of dielectric profiles can be computed recursively as shown below:

$$[R_{composite}]=[R_{f_1}]+[\widetilde{T}_{f_1}][\phi^{+}_{d1,top}][R_k]\left([I]-[\phi^{+}_{d1,top}][\widetilde{R}_{f_1}][\phi^{+}_{d1,top}][R_k]\right)^{-1}[\phi^{+}_{d1,top}][T_{f_1}] \tag{2.79}$$

$$[R_k]=[R_{p1}]+[\widetilde{T}_{p1}][\phi^{+}_{d1,bottom}][R_j]\left([I]-[\phi^{+}_{d1,bottom}][R_{p1}][\phi^{+}_{d1,bottom}][R_j]\right)^{-1}[\phi^{+}_{d1,bottom}][T_{p1}] \tag{2.80}$$

$$[R_j]=[R_{f_2}]+[\widetilde{T}_{f_2}][\phi^{+}_{d2,top}][R_{p2}]\left([I]-[\phi^{+}_{d2,top}][\widetilde{R}_{f_2}][\phi^{+}_{d2,top}][R_{p2}]\right)^{-1}[\phi^{+}_{d2,top}][T_{f_2}] \tag{2.81}$$

where [I] is the identity matrix, the subscripts f_1 and f_2 denote the rough surface profile $f_1(x)$ and $f_2(x)$, and the subscripts *p1* and *p2* denote the inhomogeneous stratified dielectric profiles $\varepsilon_1(z)$ and $\varepsilon_2(z)$ respectively. $[R_k]$ and $[R_j]$ are the intermediate reflection matrices which couple the bottom stratified dielectric medium $\varepsilon_2(z)$ to $\varepsilon_1(z)$, taking into account the presence of f_2. The matrices $[\phi^{+}_{d2,top}]$ ($[\phi^{+}_{d2,bottom}]$) and $[\phi^{+}_{d1,top}]$ ($[\phi^{+}_{d1,bottom}]$) are the phase shifting matrices of the top (bottom) dielectric thin layers in the inhomogeneous dielectric profiles described by $\varepsilon_2(z)$ and $\varepsilon_1(z)$, respectively, whose layer thicknesses are also set to be Δd_2 and Δd_1. Similarly, the scattering matrix solution to scattering from a buried cylinder in layered rough surfaces can be expressed as follows.

$$[R_{composite}]=[R_{f_1}]+[\widetilde{T}_{f_1}][\phi^{+}_{d_1}][R_k]\left([I]-[\phi^{+}_{d_1}][\widetilde{R}_{f_1}][\phi^{+}_{d1}][R_k]\right)^{-1}[\phi^{+}_{d_1}][T_{f_1}] \tag{2.82}$$

$$[R_k]=[R_{sc}]+[T_{sc}][\phi^{+}_{d_2}][R_{f_2}]\left([I]-[\phi^{+}_{d_2}][R_{sc}][\phi^{+}_{d2}][R_{f_2}]\right)^{-1}[\phi^{+}_{d_2}][T_{sc}] \tag{2.83}$$

where [I] is the identity matrix, the subscripts f_1, f_2, and *k* denote the rough surface profile $f_1(x)$, $f_2(x)$ and the intermediate reflection matrix which couples the bottom rough interface to the buried cylinder, and $[\phi^{+}_{d_j}]$ is

$$\left[\phi^{+}_{d_j}\right]=\begin{bmatrix} e^{+ik_1 d_j\cos\phi_1} & 0 & \cdots & 0 \\ 0 & e^{+ik_1 d_j\cos\phi_1} & \cdots & 0 \\ \vdots & \vdots & \ddots & \vdots \\ 0 & 0 & \cdots & e^{+ik_1 d_j\cos\phi_n} \end{bmatrix} \tag{2.84}$$

d_j is the layer thickness (i.e. d_1 = the layer thickness between the mean value of the top rough interface and the center of the cylinder, d_2 = the layer thickness between the center of the cylinder and the mean value of the bottom rough interface) and ϕ_m is the m^{th} Floquet mode scattering angle. For the discrete random media problem, the scattering matrix solution is obtained by replacing $[R_{sc}]$ with $[R_{DRM}]$ and the matrix expression is given by

$$[R_k]=[R_{DRM}]+[T_{sc}][\phi_{d_2}^{+}][R_{f_2}]\Big([I]-[\phi_{d_2}^{+}][\widetilde{R}_{DRM}][\phi_{d2}^{+}][R_{f_2}]\Big)^{-1}[\phi_{d_2}^{+}][T_{sc}] \tag{2.85}$$

The details of derivation of the above matrix for a rough surface or a buried cylinder will appear in chapters to follow.

CHAPTER 3

Scattering from Layered Rough Surfaces and its Application in Remote Sensing of Subsurface Soil Moisture

Following the review of the scattering matrix method (SMM), we derive the reflection and transmission matrices of a rough surface through the application of the extended boundary condition method (EBCM) in this Chapter. In EBCM, the matrix filling process is facilitated using Fast Fourier Transform (FFT). Upon constructing these reflection/transmission matrices of individual rough surfaces, the solution to scattering from layered rough surfaces is sought by recursively cascading these matrices based on SMM. Scattering coefficients are obtained by computing incoherent powers from the resulting Floquet modes of the overall system. Subsequently, a thorough validation assessment for the proposed method (EBCM/SMM) is made and bi-static scattering coefficients are validated against existing analytical and numerical solutions. A benchmarking study of EBCM/SMM and MoM for computational efficiency is also conducted. In numerical simulations, field-collected soil moisture data are used to investigate the penetration capability at different frequencies and to address the potential of low frequency radar systems in estimating deep soil moisture. In particular, soil moisture profiles during dry ground, wet ground, and wet subsurface layer conditions are examined. The results show that both backscattering coefficients and co-polarized phase difference at low frequencies are sensitive to subsurface roughness and deep soil moisture. Also, much larger depth sensitivity can be achieved using co-polarized phase difference than scattering coefficients.

3.1 Extended Boundary Condition Method (EBCM) and Scattering Matrices of a Rough Surface

The formulation of scattering from a single rough surface based on EBCM is discussed in [9, 64, 65]. The interactions between different layers of rough surfaces can be incorporated using SMM [64]. In this dissertation, the review on the formulation of 2D scattering from a rough surface for TE waves (h – pol) is provided. The solution for TM waves can be obtained using the concept of duality. In view of the duality theorem, all of the expressions for TE polarization case are modified to obtain the solution for TM polarization in a sense that electric fields and current densities are replaced by magnetic ones and $\mu_{0,1}$ are replaced by $\varepsilon_{0,1}$. Note that this is a mathematical substitution and does not require that the physical media be replaced. EBCM assumes periodic boundary conditions as depicted in Fig. 3.1.

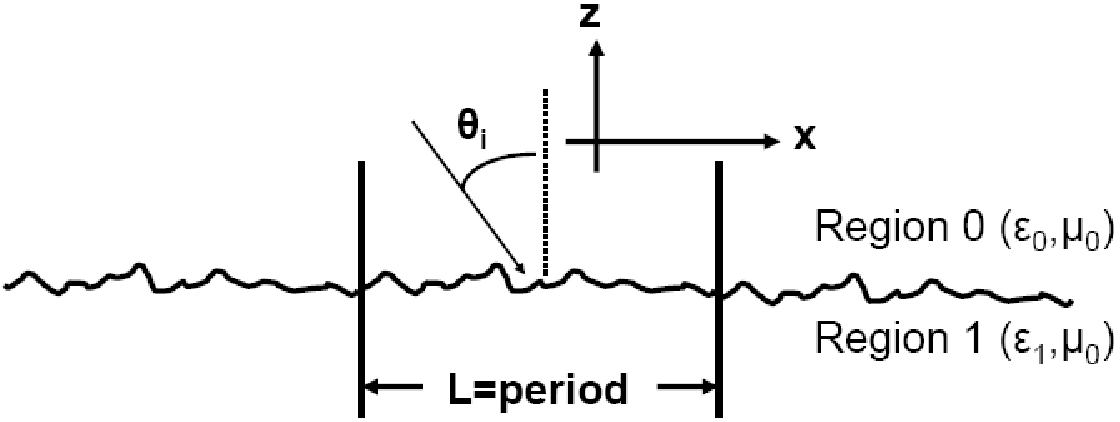

Fig. 3.1: The concept of periodic boundary condition in scattering from a rough surface

The length or period of rough surfaces is denoted by L. In this coordinate system, the surface height profiles are functions of x only and satisfy:

$$f(x) = f(x + nL), \quad \forall n \in \mathrm{N}$$

where N is the set of natural numbers. Suppose a plane wave with an arbitrary propagation direction $\overline{k_i}$ in the xz plane is incident upon the multilayer interfaces and its electric field is given by

$$E_i = \hat{e}E_o e^{i\bar{k}_i \cdot \bar{r}} = \hat{y}E_{iy}$$

where $\overline{k_i} = k_{xi}\hat{x} - k_{zi}\hat{z}$. Based on extinction theorem and using the scalar Green's function in regions 0 and 1, we have the total electric fields, E_{0y} , E_{1y} in regions 0 and 1 as follows.

Region 0:

$$E_{iy}(r) - \int_{f_1(x)} dx' g_{0L}(r,r')\hat{n}_1 \cdot \nabla'_s E_{0y}(r') - E_{0y}(r')\hat{n}_1 \cdot \nabla'_s g_{0L}(r,r')\} = \begin{cases} E_{0y}(r), z > f_1(x) \\ 0, z < f_1(x) \end{cases} \quad (3.1)$$

Region 1:

$$\int_{f_1(x)} dx' g_{1L}(r,r')\hat{n}_1 \cdot \nabla'_s E_{1y}(r') - E_{1y}(r')\hat{n}_1 \cdot \nabla'_s g_{1L}(r,r')\} = \begin{cases} E_{1y}(r), z < f_1(x) \\ 0, z > f_1(x) \end{cases} \quad (3.2)$$

where $g_{jL}(r,r')$ is the periodic Green's function and

$$g_{jL}(r,r') = \frac{i}{2L}\sum_{n=-\infty}^{\infty}\frac{1}{k_{jnz}}\exp(ik_{nx}(x-x'))\exp(ik_{jnz}\,|z-z'|) \quad (3.3)$$

$$k_{nx} = k_{xi} + \frac{2\pi n}{L} \quad (3.4)$$

$$k_{jnz} = \sqrt{k_j^{\ 2} - k_{nx}^{\ 2}} \quad (3.5)$$

Equation (3.3) can be interpreted as the field generated by a periodic array of line currents of progressive phases. The array produces a discrete spectrum of plane waves propagating along directions described by $\vec{K} = k_{nx}\hat{x} + k_{jnz}\hat{z}$. The discrete spatial harmonics are called Floquet modes. When k_{jnz} is real, the corresponding Floquet mode is propagating. When k_{jnz} is purely imaginary, the corresponding Floquet mode is non-propagating. The number of propagating waves is finite and depends on the period-over-wavelength ratio (L/λ_j) and the incidence angle.

The nth mode is propagating if it belongs to set S defined by

$$S = \left\{ n; \frac{-L}{2\pi}(k_j + k_{xi}) < n < \frac{L}{2\pi}(k_j - k_{xi}) \right\} \tag{3.6}$$

Substituting the periodic Green's function (3.3) into (3.1) and (3.2), the following equations are obtained where $|z - z^{'}| = z - z^{'}$ when $z > f_1(x)$ and $|z - z^{'}| = -(z - z^{'})$ when $z < f_1(x)$ for all x.

Region 0:

$$E_{oy}(r) = E_{iy}(r) + \sum_{n=-\infty}^{\infty} b_{01n} \exp(i(k_{nx}x + k_{onz}z)), \; z > f_{1,\max} \tag{3.7}$$

$$0 = E_{iy}(r) + \sum_{n=-\infty}^{\infty} a_{01n} \exp(i(k_{nx}x - k_{onz}z)), \; z < f_{1,\min} \tag{3.8}$$

Region 1:

$$E_{1y}(r) = \sum_{n=-\infty}^{\infty} b_{11n} \exp(i(k_{nx}x + k_{1nz}z)), \; z > f_{1,\max} \tag{3.9}$$

$$0 = \sum_{n=-\infty}^{\infty} a_{11n} \exp(i(k_{nx}x - k_{1nz}z)), \; z < f_{1,\min} \tag{3.10}$$

where

$$b_{j\ln} = \frac{-i}{2Lk_{jnz}} \int_{f_j(x)} \{ \hat{n}_l \cdot \nabla'_s E_{jy}(r') \exp(-i(k_{nx}x' + k_{jnz}z')) - E_{jy}(r') \hat{n}_l \cdot \nabla'_s \exp(-i(k_{nx}x' + k_{jnz}z')) \} \sqrt{1 + (f_l'(x'))^2}\, dx' \tag{3.11}$$

$$a_{j\ln} = \frac{-i}{2Lk_{jnz}} \int_{f_j(x)} \{ \hat{n}_l \cdot \nabla'_s E_{jy}(r') \exp(-i(k_{nx}x' - k_{jnz}z')) - E_{jy}(r') \hat{n}_l \cdot \nabla'_s \exp(-i(k_{nx}x' - k_{jnz}z')) \} \sqrt{1 + (f_l'(x'))^2}\, dx' \tag{3.12}$$

where $f^{'}(x')$ is the spatial derivative of $f(x')$. In addition, the surface fields are expanded in terms of their Fourier series with unknown coefficients as follows:

$$E_{1y}(x, f_1(x)) = \sum_{m=-\infty}^{\infty} \alpha_m \exp(ik_{mx}x) \tag{3.13}$$

$$\sqrt{1 + f_1'^2(x)}\, \hat{n}_1 \cdot \nabla E_{1y}(x, f_1(x)) = \sum_{m=-\infty}^{\infty} \beta_m \exp(ik_{mx}x) \tag{3.14}$$

The incident wave can also be decomposed into its Floquet modes by recalling that $\overline{E}_i = \hat{e}E_o e^{i\overline{k}_i \cdot \overline{r}} = \hat{y}E_{iy}$ and assuming $|E_{iy}| = 1$ (the magnitude of $E_{iy} = 1$). Then, using (3.8),

$$a_{01n} = \begin{cases} 0, \forall n \neq 0 \\ 1, n = 0 \end{cases} \tag{3.15}$$

Substituting (3.11), (3.12), (3.13), and (3.14) into (3.7) through (3.10) and imposing boundary conditions at z = *f₁(x)* result in the following matrix equations.

$$\sum_{m=-\infty}^{\infty} U_{nm}{}^{(1e,+)}\alpha_m + U_{nm}{}^{(2e,+)}\beta_m = a_{01n} \tag{3.16}$$

$$\sum_{m=-\infty}^{\infty} Q_{nm}{}^{(2,-)}\alpha_m + Q_{nm}{}^{(1,-)}\beta_m = 0 \tag{3.17}$$

where Q_{nm} and U_{nm} can be regarded as elements of operators/matrices representing interactions between half spaces. By truncating the infinite summations of (3.16) and (3.17), they can be cast into a system of matrix equations as follows:

$$\begin{bmatrix} \overline{\overline{U}}^{(1e,+)} & \overline{\overline{U}}^{(2e,+)} \\ \overline{\overline{Q}}^{(2,-)} & \overline{\overline{Q}}^{(1,-)} \end{bmatrix} \begin{bmatrix} \overline{\alpha} \\ \overline{\beta} \end{bmatrix} = \begin{bmatrix} \overline{a} \\ \overline{0} \end{bmatrix} \tag{3.18}$$

where

$$U_{nm}{}^{(1e,+)} = \frac{k_{nx}k_{mx} - k_o{}^2}{2k_{onz}{}^2} I_0{}^+, \quad U_{nm}{}^{(2e,+)} = \frac{-i}{2k_{onz}}\left[\left(\frac{k_o}{k_1}\right)^2\right]\frac{k_1 Y_1}{k_o Y_o} I_o{}^+ \quad Q_{nm}^{(2,-)} = \frac{k_{nx}k_{mx} - k_1^2}{2k_{1nz}{}^2} I_1^-, \quad Q_{nm}{}^{(1,-)} = \frac{i}{2k_{1nz}} I_1{}^-$$

$$I_o{}^+ = \frac{1}{L}\int_0^L e^{i[2\pi(m-n)\frac{x'}{L}]}(e^{ik_{onz}f_1(x')})dx' \qquad I_1{}^- = \frac{1}{L}\int_0^L e^{i[2\pi(m-n)\frac{x'}{L}]}(e^{-ik_{1nz}f_1(x')})dx'$$

and Y_j is the intrinsic admittance in the region *j*. Hence, $\overline{\alpha}$ and $\overline{\beta}$ can be obtained by inverting the matrix. We also note that $I_o{}^+$ and $I_1{}^-$ are the discrete Fourier transform of $e^{ik_{jnz}f_1(x')}$. It may be tempting to compute the matrix elements by directly applying Fast Fourier Transform (FFT) to the integrand. However, this simplistic approach cannot accurately determine the values of these Fourier-type integrals due to the oscillatory nature of the integrand. We employ a fast FFT-based integral evaluation approach formulated in [44]. The filling of matrix elements involves the computation of the following Fourier-type integrals:

$$I_s = \frac{1}{L}\int_0^L e^{i2\pi s\frac{x'}{L}}(e^{ik(s)f(x')})dx' \tag{3.19}$$

In principle, these integrals can be computed numerically for each *s* but the direct computation of these integrals in the matrix filling process is extremely time-consuming when there are several thousands or more integrals to be evaluated for each value of *k*. In addition, for very large values of *k(s)*, the term $e^{ik(s)f(x')}$ in the integrand oscillates rapidly, which may lead to a loss of accuracy unless a very fine integration step is used. The following FFT-based algorithm is applied to speed up the matrix filling process. Consider (3.19) and rewrite it as follows:

$$I_s = \delta_{s,0} + J_s \tag{3.20}$$

where

$$J_s = \frac{1}{L}\int_0^L e^{i2\pi s\frac{x'}{L}}(e^{ikf(x')} - 1)dx' \tag{3.21}$$

Then, we compute J_s by expanding $e^{ikf(x')}$ in powers of $kf(x')$ using Taylor series and integrating the resulting series term by term.

$$J_s = \sum_{n=1}^{N} \frac{(ik)^n}{n!} A_{sn} \tag{3.22}$$

$$\begin{aligned} A_{sn} &= \frac{1}{L}\int_0^L e^{i2\pi s\frac{x'}{L}} f^n(x')dx' \\ &\cong \frac{1}{l'}\sum_{l=0}^{l'-1} e^{i2\pi s\frac{l'}{l}} f^n(x_l) = \frac{1}{l'} fft(f^n(x_l), l') \end{aligned} \tag{3.23}$$

where $x_l = l\Delta x$ with $\Delta x = \frac{L}{l'}$ and l' is the number of FFT point. To fully exploit the computational efficiency of FFT operation, the length of a rough surface is set to be of powers of two. The test of convergence shows $l'=2^{13}$ or higher gives solution convergence. Values of A_{sn} do not depend on *k* and they need to be calculated only once for each surface profile. The number N of powers of *f(x)* that must be kept in the Taylor series expansion (3.22) depends on the roughness of rough surface profile. In [44], it is indicated that for h = 0.05λ, 10 terms (N=10) ensures solution accuracy. For h=0.1λ, 18 terms are used for obtaining convergent results.

As soon as $\overline{\alpha}$ and $\overline{\beta}$ of (3.18) are retrieved, the upward-propagating and downward-propagating field amplitudes can be found, which will be used later for the cascade of scattering matrices. They are found from

$$-\begin{bmatrix} \overline{\overline{U}}^{(1e,-)} & \overline{\overline{U}}^{(2e,-)} \\ \overline{\overline{Q}}^{(2,+)} & \overline{\overline{Q}}^{(1,+)} \end{bmatrix} \begin{bmatrix} \overline{\alpha} \\ \overline{\beta} \end{bmatrix} = \begin{bmatrix} \overline{b} \\ \overline{A} \end{bmatrix} \tag{3.24}$$

where $\overline{b}$ is the reflected wave and $\overline{A}$ is the transmitted wave. $\overline{\overline{U}}^{(1e,-)}$ and $\overline{\overline{U}}^{(2e,-)}$ are identical to $\overline{\overline{U}}^{(1e,+)}$ and $\overline{\overline{U}}^{(2e,+)}$ after replacing $I_0{}^{+}$ by $I_0{}^{-}$ where $I_o{}^{-} = \frac{1}{L}\int_0^L e^{i[2\pi(m-n)\frac{x'}{L}]}(e^{-ik_{onz}f_1(x')})dx'$. Similarly, $\overline{\overline{Q}}^{(2,+)}$ and $\overline{\overline{Q}}^{(1,+)}$ are identical to $\overline{\overline{Q}}^{(2,-)}$ and $\overline{\overline{Q}}^{(1,-)}$ after replacing I_1^{-} by I_1^{+} where $I_1^{+} = \frac{1}{L}\int_0^L e^{i[2\pi(m-n)\frac{x'}{L}]}(e^{ik_{1nz}f_1(x')})dx'$.

For TM polarization, duality can be applied, where $\alpha_m \rightarrow \gamma_m$, $\beta_m \rightarrow \eta_m$, $U_{nm}{}^{(je)} \rightarrow U_{nm}{}^{(jh)}$ and the expressions for $U_{nm}{}^{(jh)}$ can be obtained from those of $U_{nm}{}^{(je)}$ by replacing $Y_j \rightarrow Z_j$ where Z_j is the inverse of Y_j.

In general, for any arbitrary rough surface profile, $f_j(x)$, the generalized scattering matrix based on extended boundary condition method can be efficiently computed using the following relationship.

$$\begin{bmatrix} [S_{11}] & [S_{12}] \\ [S_{21}] & [S_{22}] \end{bmatrix} = \begin{bmatrix} [R_{f_j}] & [\widetilde{T}_{f_j}] \\ [T_{f_j}] & [\widetilde{R}_{f_j}] \end{bmatrix} = -\begin{bmatrix} \overline{\overline{U}}^{(1e,-)} & \overline{\overline{U}}^{(2e,-)} \\ \overline{\overline{Q}}^{(2,+)} & \overline{\overline{Q}}^{(1,+)} \end{bmatrix} \begin{bmatrix} \overline{\overline{U}}^{(1e,+)} & \overline{\overline{U}}^{(2e,+)} \\ \overline{\overline{Q}}^{(2,-)} & \overline{\overline{Q}}^{(1,-)} \end{bmatrix}^{-1} \tag{3.25}$$

Equation (3.25) is derived upon substituting (3.24) into (3.18) after isolating $\begin{bmatrix} \overline{\alpha} \\ \overline{\beta} \end{bmatrix}$ in (3.24) and relating the incident waves to the reflected and transmitted waves. Since $[R_{f_j}]$ and $[T_{f_j}]$ are not reciprocal for a rough surface (i.e., $R_{f_j,ij} \neq R_{f_j,ji}$ and $T_{f_j,ij} \neq T_{f_j,ji}$), we then define $[\widetilde{R}_{f_j}]$ and

$[\widetilde{T}_{f_j}]$ as reflection and transmission matrices filled with $R_{f_j,ji}$ and $T_{f_j,ji}$, respectively. Here, the subscript f_j denotes the j^{th} rough surface profile. More specifically, for the present problem, f_1 denotes the top rough interface and f_2 denotes the bottom rough interface. The matrix inversion in (3.25) is performed by partitioning. Reflection and transmission matrices can be individually computed by invoking block-wise inversion based on the following inversion formula:

$$\begin{bmatrix} A & B \\ C & D \end{bmatrix} = \begin{bmatrix} (A-BD^{-1}C)^{-1} & -(A-BD^{-1}C)^{-1}BD^{-1} \\ -D^{-1}C(A-BD^{-1}C)^{-1} & D^{-1}+D^{-1}C(A-BD^{-1}C)^{-1}BD^{-1} \end{bmatrix} \tag{3.26}$$

The expressions for reflection/transmission matrices are given as follows:

$$\left[R_{f_j}\right] = -\left\{\overline{\overline{U}}^{(1e,-)} \cdot [K] - \overline{\overline{U}}^{(2e,-)}\left[\left[\overline{\overline{Q}}^{(1,-)}\right]^{-1}\overline{\overline{Q}}^{(2,-)}[K]\right]\right\} \tag{3.27}$$

$$\left[T_{f_j}\right] = -\left\{\overline{\overline{Q}}^{(2,+)} \cdot [K] - \overline{\overline{Q}}^{(1,+)}\left[\left[\overline{\overline{Q}}^{(1,-)}\right]^{-1}\overline{\overline{Q}}^{(2,-)}[K]\right]\right\} \tag{3.28}$$

$$\left[\tilde{T}_{f_j}\right] = \left\{\begin{array}{l} \overline{\overline{U}}^{(1e,-)}[K]\overline{\overline{U}}^{(2e,+)}\left[\overline{\overline{Q}}^{(1,-)}\right]^{-1} \\ -\overline{\overline{U}}^{(2e,-)}\left[\left[\overline{\overline{Q}}^{(1,-)}\right]^{-1} + \left[\overline{\overline{Q}}^{(1,-)}\right]^{-1}\overline{\overline{Q}}^{(2,-)}[K]\overline{\overline{U}}^{(2e,+)}\left[\overline{\overline{Q}}^{(1,-)}\right]^{-1}\right] \end{array}\right\} \tag{3.29}$$

$$\left[\tilde{R}_{f_j}\right] = \left\{\begin{array}{l} \overline{\overline{Q}}^{(2,+)}[K]\overline{\overline{U}}^{(2e,+)}\left[\overline{\overline{Q}}^{(1,-)}\right]^{-1} \\ -\overline{\overline{Q}}^{(1,+)}\left[\left[\overline{\overline{Q}}^{(1,-)}\right]^{-1} + \left[\overline{\overline{Q}}^{(1,-)}\right]^{-1}\overline{\overline{Q}}^{(2,-)}[K]\overline{\overline{U}}^{(2e,+)}\left[\overline{\overline{Q}}^{(1,-)}\right]^{-1}\right] \end{array}\right\} \tag{3.30}$$

where $[K] = \left[\overline{\overline{U}}^{(1e,+)} - \overline{\overline{U}}^{(2e,+)}\left[\overline{\overline{Q}}^{(1,-)}\right]^{-1}\overline{\overline{Q}}^{(2,-)}\right]^{-1}$. We note that in total two matrix inversion operations and fifteen matrix multiplication operations are performed to obtain all reflection/transmission matrices of a rough surface. Through the block-wise matrix decomposition, the matrix structure of individual reflection/transmission matrices can be better understood. In addition, compared to (3.25), the computational complexity reduces from $O((2\mathrm{P})^2) + O((2\mathrm{P})^3)$ to $O(15P^2) + O(2(P)^3)$ where P = the total number of Floquet modes = 2N+1. The first term accounts for matrix multiplication and the second term is for matrix inversion. Since matrix inversion still constitutes a more significant factor contributing to the CPU runtime, it is advantageous to perform block-wise matrix inversion.

3.2 Scattering Matrices of a Stratified Soil Profile

Any inhomogeneous dielectric profile can be accurately modeled as a stack of many piecewise homogeneous dielectric thin layers provided the thickness of each layer is very small compared to the wavelength [64]. Therefore, a dielectric profile is first discretized into a stack of homogeneous dielectric thin layers. The reflection and transmission matrices are then obtained for each planar dielectric interface. Finally, the overall reflection and transmission matrices of an inhomogeneous dielectric profile are computed by applying the generalized scattering matrix technique where each reflection and transmission matrix of individual dielectric interfaces are recursively cascaded from the bottom dielectric interface to the top interface. The reflection and transmission matrices of a planar dielectric interface obey Fresnel's law and their expressions are given by:

$$[R^{VV}_{i,i+1}] = diag\{\frac{\varepsilon_{i+1}k_{iz} - \varepsilon_i k_{(i+1)z}}{\varepsilon_{i+1}k_{iz} + \varepsilon_i k_{(i+1)z}}\} \quad (3.31) \qquad [T^{VV}_{i,i+1}] = diag\{\frac{2\varepsilon_{i+1}k_{iz}}{\varepsilon_{(i+1)}k_{iz} + \varepsilon_i k_{(i+1)z}}\} \quad (3.32)$$

$$[R^{HH}_{i,i+1}] = diag\{\frac{k_{iz} - k_{(i+1)z}}{k_{iz} + k_{(i+1)z}}\} \quad (3.33) \qquad [T^{HH}_{i,i+1}] = diag\{\frac{2k_{iz}}{k_{iz} + k_{jz}}\} \quad (3.34)$$

Upon obtaining the individual reflection and transmission matrices of each dielectric interface, the generalized reflection and transmission matrices of a stratified dielectric profile, denoted by $[\overline{\overline{R}}_{i,i+1}]$ and $[\overline{\overline{T}}_{i,i+1}]$, can be derived by tracing the propagation of each Floquet mode from the region *i* to the region *i*+1 where the index *i* goes from 0 (the top layer of a stratified dielectric profile) to N-1 (the bottom layer of a stratified dielectric profile) as shown in Fig. 3.2.

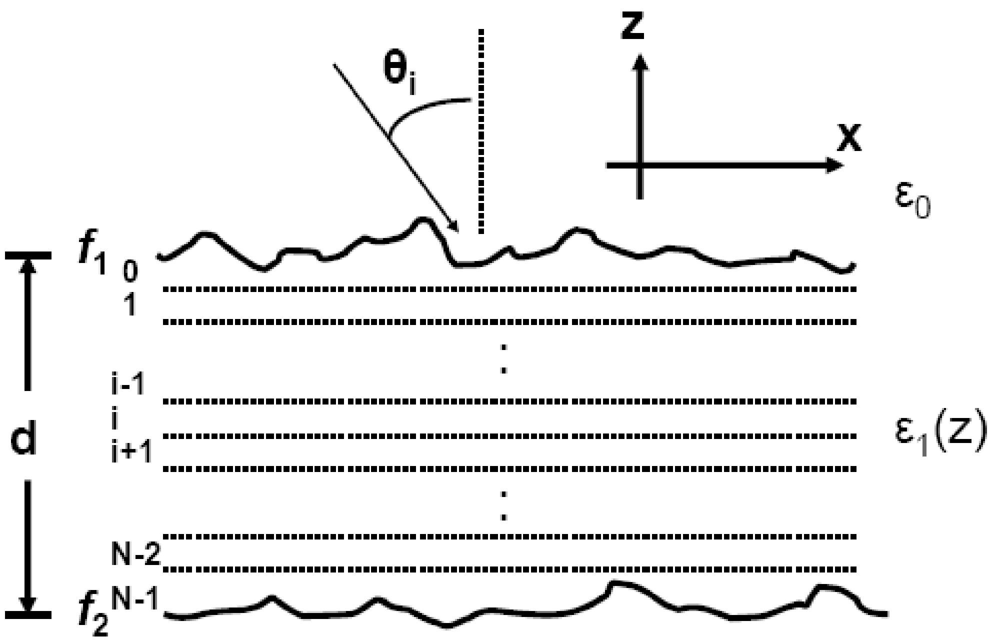

Fig. 3.2: The detail of an inhomogeneous dielectric profile between each two rough interfaces

The difference between $[\quad]$ and $[\overline{\overline{\quad}}]$ is that $[\quad]$ is the matrix notation for a single interface only whereas $[\overline{\overline{\quad}}]$ is the matrix notation for a dielectric profile from the bottom layer of the profile to the designated layer. The subscript *i*,*i*+1 denotes the interface between the layer *i* and the layer *i*+1. $[\overline{\overline{R}}_{i,i+1}]$ and $[\overline{\overline{T}}_{i,i+1}]$ are computed as follows:

$$[\overline{\overline{R}}_{i,i+1}] = [R_{i,i+1}] + [T_{i+1,i}][\phi^{+}_{\Delta d,i}][\overline{\overline{R}}_{i+1,i+2}]\left([I] - [\phi^{+}_{\Delta d,i}][R_{i+1,i}][\phi^{+}_{\Delta d,i}][\overline{\overline{R}}_{i+1,i+2}]\right)^{-1}[\phi^{+}_{\Delta d,i}][T_{i,i+1}] \quad (3.35)$$

$$[\overline{\overline{T}}_{i,i+1}] = [T_{i+1,i+2}]\left([I] - [\phi^{+}_{\Delta d,i}][R_{i+1,i}][\phi^{+}_{\Delta d,i}][\overline{\overline{R}}_{i+1,i+2}]\right)^{-1}[\phi^{+}_{\Delta d,i}][T_{i,i+1}] \quad (3.36)$$

and $[\phi^{+}_{\Delta d,i}]$ is

$$\left[\phi^{+}_{\Delta d,i}\right] = \begin{bmatrix} e^{+ik_i\Delta d\cos\phi_{i,1}} & 0 & \cdots & 0 \\ 0 & e^{+ik_i\Delta d\cos\phi_{i,2}} & \cdots & 0 \\ \vdots & \vdots & \ddots & \vdots \\ 0 & 0 & \cdots & e^{+ik_i\Delta d\cos\phi_{i,n}} \end{bmatrix} \quad (3.37)$$

where Δd is the thickness of each thin dielectric layer which is set to be uniform for all dielectric layers within the profile and $\phi_{i,m}$ is the m$^{\text{th}}$ Floquet mode scattering angle in the i^{th} layer. Essentially, $[\overline{\overline{R}}_{i,i+1}]$ and $[\overline{\overline{T}}_{i,i+1}]$ relate the amplitudes of reflected and transmitted Floquet modes to the amplitudes of incident ones at z = $-d_i$, accounting for the effects of reflections, transmissions, and multiple bounces of Floquet modes at all the interfaces located below the i^{th} layer. By recursively cascading each reflection and transmission matrix of individual dielectric interface from the bottom dielectric interfaces all the way to the top interface, the overall reflection and transmission matrices of an inhomogeneous dielectric profile, denoted by $[R_p]$ and $[T_p]$, are acquired. To couple the scattering matrices of a stratified dielectric profile to those of rough surfaces, the reflection and transmission matrices in a reciprocal direction, denoted by $[\widetilde{R}_p]$ and $[\widetilde{T}_p]$, must also be obtained. These matrices can be computed using (3.35) and (3.36) after swapping the index i and the index i+1 in the subscript (i.e., $[\overline{\overline{R}}_{i+1,i}]$ and $[\overline{\overline{T}}_{i+1,i}]$).

3.3 Computation of the Scattering Coefficients and Co-polarized Phase Difference

Once the composite matrix computed using (2.79)-(2.81) is obtained, the column vector of reflected waves $[b]$ from the system due to the column vector of an incident wave, $[A]$, is given by

$$[b] = [R_{composite}][A] \tag{3.38}$$

The relationship between bi-static scattering cross section and upward-propagating reflected field is given by:

$$\sigma_{2D} = \frac{Lk}{2\pi\cos\theta_i}\cos^2\theta_s\,|\,b_m\,|^2 = \frac{L}{\lambda}\frac{\cos^2\theta_s}{\cos\theta_i}\,|\,b_m\,|^2 \tag{3.39}$$

where L is the length of the rough surface, θ_i is the angle of incidence, and θ_s is the scattering angle. The derivation for (3.39) can be found in [44]. In addition, the phase statistics of layered rough surface scattering can also be collected using the present method. The co-polarized coherent phase difference, $\phi_c = \phi_{hh} - \phi_{vv}$, which has been shown to exhibit a strong dependence on both the target parameters (roughness and moisture content) and the radar parameters (incidence angle and frequency) [78] can be computed as:

$$\phi_c = \phi_{hh} - \phi_{vv} = \tan^{-1}\left(\frac{\mathrm{Im} < b_{hh} b_{vv}^{*} >}{\mathrm{Re} < b_{hh} b_{vv}^{*} >}\right) \tag{3.40}$$

where b_{hh} is the reflected waves from the overall system in HH polarization and b_{vv} is those in VV polarization. The coherent phase difference is the phase difference between HH and VV polarizations at which the pdf of co-polarized phase difference attains its maximum.

3.4 Comparison of Results, Validation, and Computational Efficiency

3.4.1 Validation with an Analytical Solution

For the purpose of validation, numerical simulations of the limiting case of two-interface rough surface scattering shown in Fig. 3.3 are first performed here for rough surfaces whose analytical small perturbation method (SPM) solutions exist ($kh_1, kh_2 < 0.3$ and $kl_1, kl_2 < 3$). The dielectric constants of each layer (ε_1 and ε_2), the surface statistics (kh_1, kl_1, kh_2, kl_2) and the layer thickness (d) are given in Table 3.1.

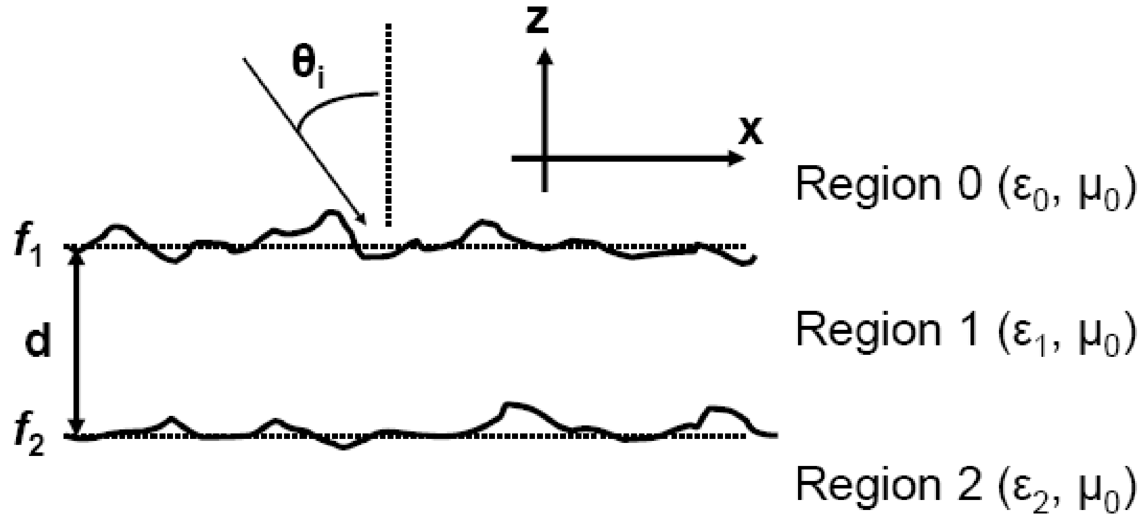

Fig. 3.3: Geometry of scattering from two-rough-interface surfaces used for validation with SPM and MoM

Table 3.1
The simulation parameters for scattering from two-interface rough surfaces for the purpose of validation with SPM

ε_1	ε_2	kh_1	kl_1	kh_2	kl_2	d	θ_i	L
4	7	0.15	1.5	0.05	1.5	3λ	45^o	25λ

These choices of surface parameters ensure that their analytical SPM solutions are valid. The number of Floquet modes used in the simulation is 101. The rough surfaces are generated using Gaussian spectra.

To validate the simulated results, the existing analytical SPM solution to multilayer rough surface scattering as described in [1] is used. In [1], the 1st order SPM solution to scattering from a two-rough-interface geometry is provided for two statistically independent rough surfaces:

$$\sigma_{hh} = k_o \frac{\cos^2\theta_s}{\cos\theta_i}(|\alpha_1^h|^2 W_1(\overline{k}^s_\perp - \overline{k}^i_\perp) + |\alpha_2^h|^2 W_2(\overline{k}^s_\perp - \overline{k}^i_\perp)) \tag{3.41}$$

$$\sigma_{vv} = k_o \frac{\cos^2\theta_s}{\cos\theta_i}(|\alpha_1^v|^2 W_1(\overline{k}^s_\perp - \overline{k}^i_\perp) + |\alpha_2^v|^2 W_2(\overline{k}^s_\perp - \overline{k}^i_\perp)) \tag{3.42}$$

where $W_1(\overline{k}_\perp)$ and $W_2(\overline{k}_\perp)$ are the spectral densities of the top and bottom rough boundaries respectively and $\alpha_1^h, \alpha_1^h, \alpha_2^v$, and α_2^v correspond to the 1st order coefficients from the small perturbation method. They are determined by imposing boundary conditions on both top and bottom rough interfaces simultaneously. This will translate to an 8 by 8 matrix inversion as formulated in [1]. The solution presented in this paper for bi-static scattering coefficient using the Monte Carlo simulation with 300 independent samples is validated against analytical SPM solution in Figs. 3.4-3.5. The coherent components are present in the plots as evidenced by the pronounced peak at 45^{o} which is the specular direction (absent in 1st order SPM). In general, numerical results are in excellent agreement with analytical SPM solutions for cases where SPM approximation is valid. When the rms height of the bottom interface is $kh_2 = 0.2$ in Fig. 3.5, there is a discrepancy between the numerical result and the SPM solution mostly in VV polarization over the range of scattering angles from 20^{o} to 80^{o}. Since the analytical SPM solution developed in [1] is only based on the first order term of perturbation series, this suggests the higher-order surface scattering effects due to layered rough surfaces are more important in VV polarization than in HH polarization. The solution presented here can accurately capture the effects of all orders of multiple scattering due to rough surfaces and multiple bounces between layers for surfaces which are not required to satisfy the small slope or small roughness approximation.

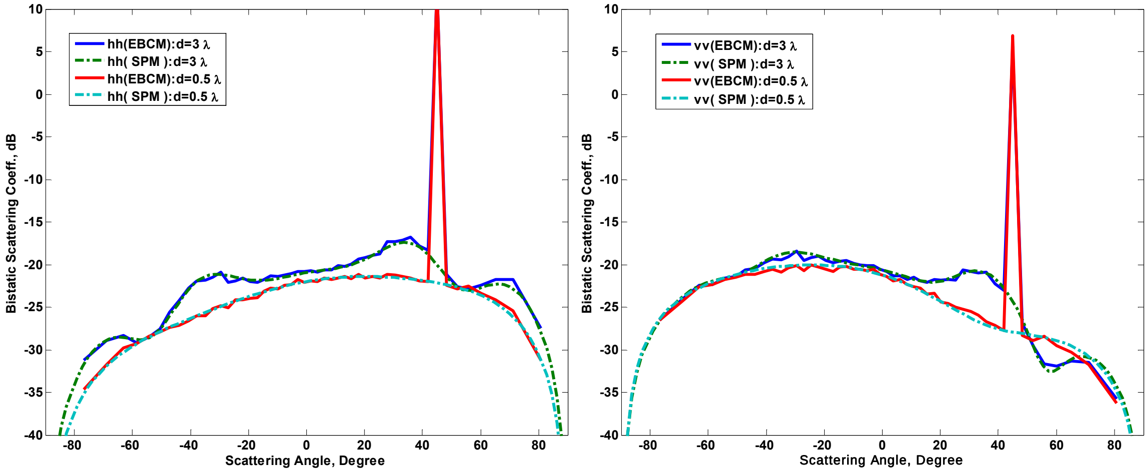

Fig. 3.4: Bi-static scattering coefficients for the scattering from two-rough-interface surfaces (Table 3.1) for different values of layer thickness

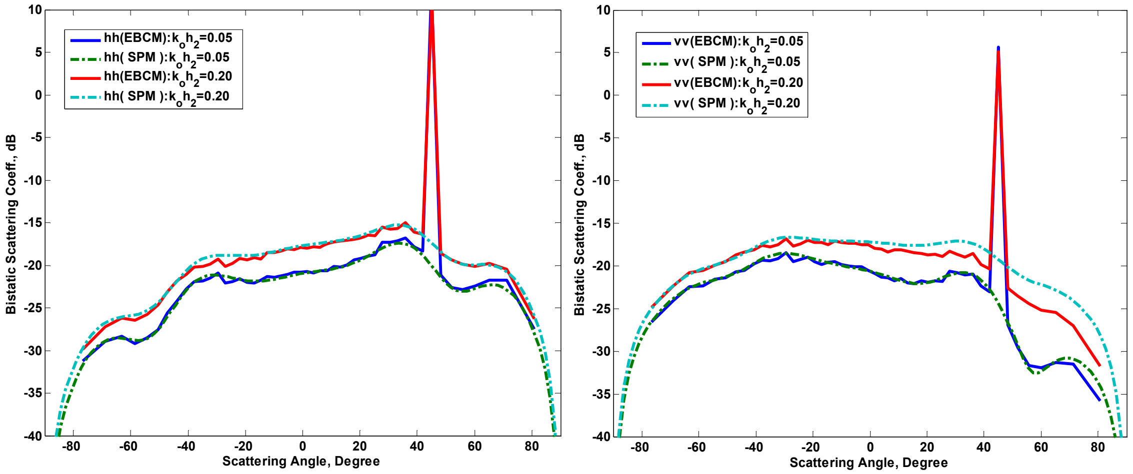

Fig. 3.5: Bi-static scattering coefficients for the scattering from two-rough-interface surfaces (Table 3.1) for different values of the rms heights of bottom interface

The next validation of this method is to verify the scattering matrix technique by examining bi-static scattering coefficient from a 4-point piece-wise homogeneous profile underneath a rough surface. The problem geometry is depicted in Fig. 3.6.

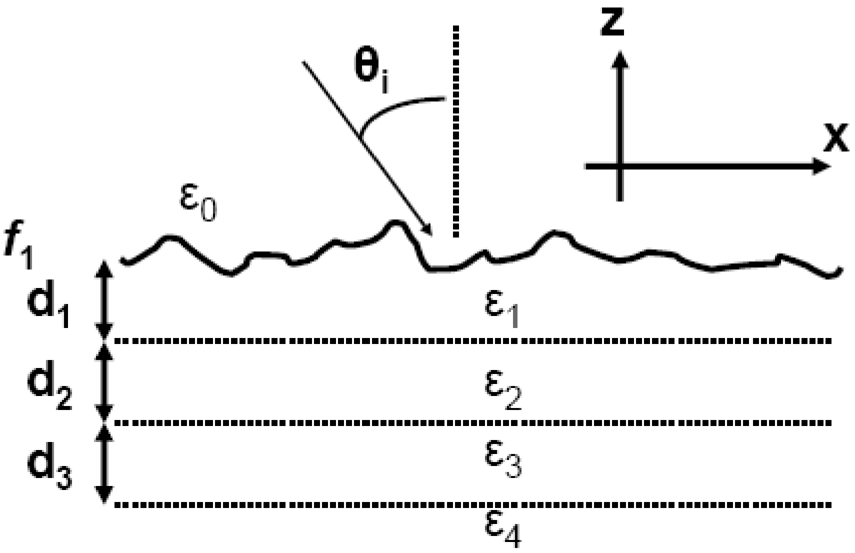

Fig. 3.6: Geometry of scattering from a 4-point piece-wise homogenous profile underneath a rough surface

The analytical SPM solution for this scenario is based on [1].

$$\sigma_{hh} = k_o \frac{\cos^2\theta_s}{\cos\theta_i}\left(|\alpha_{profile}{}^{h}|^2\, W_1(\overline{k}^{s}{}_{\perp} - \overline{k}^{i}{}_{\perp})\right) \tag{3.43}$$

$$\sigma_{vv} = k_o \frac{\cos^2 \theta_s}{\cos \theta_i} (|\alpha_{profile}^{\ v}|^2 W_1(\bar{k}^s_{\perp} - \bar{k}^i_{\perp})) \tag{3.44}$$

where $W_1(\bar{k}_{\perp})$ is the spectral density of the top ground rough boundary and $\alpha_{profile}^{\ h}$ and $\alpha_{profile}^{\ v}$ correspond to the 1st order coefficients from the small perturbation method. The simulation parameters are given in Table 3.2.

Table 3.2
The simulation parameters for scattering from a 4-point piece-wise homogeneous profile underneath a rough surface for the purpose of validation with SPM

ε_1	ε_2	ε_3	ε_4	$k_o h_1$	$k_o l_1$	d_1	d_2	d_3	θ_i	L
2	5	8	10	0.1	1.0	0.5λ	$1\ \lambda$	$0.5\ \lambda$	35^o	30λ

In Fig. 3.7 and Fig. 3.8, two scenarios of scattering from a 4-point piece-wise homogeneous profile where the rms height of the ground interface and the incidence angle are varied are examined. In both figures, numerical results are in excellent agreement with analytical SPM solutions for cases where SPM is valid. On the border of the SPM's validity domain, kh =0.3, the results produced by EBCM are slightly smaller than those of SPM.

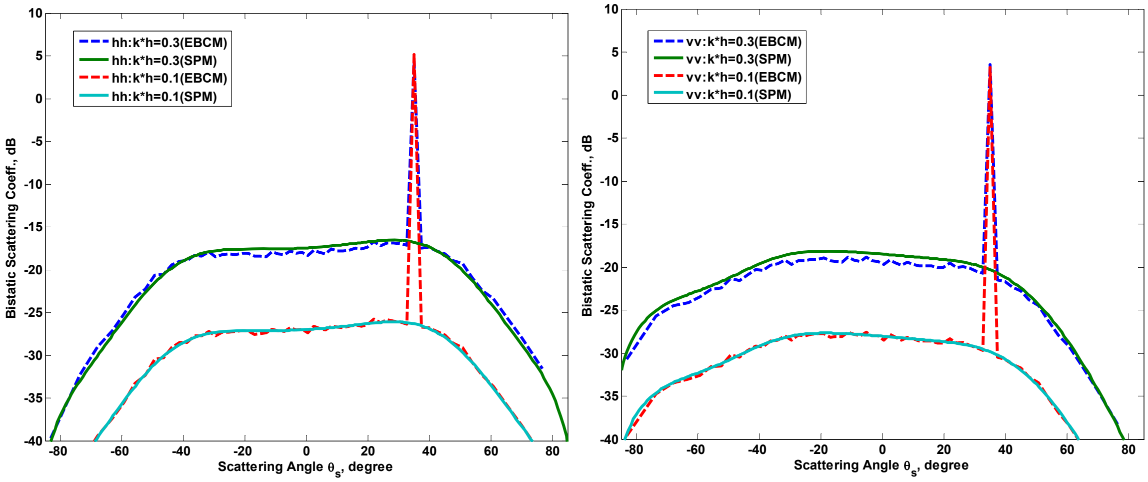

Fig. 3.7: Bi-static scattering coefficients for the scattering from a 4-point piecewise homogenous profile (Table 3.2) for different values of the rms heights of the roughness of the ground interface

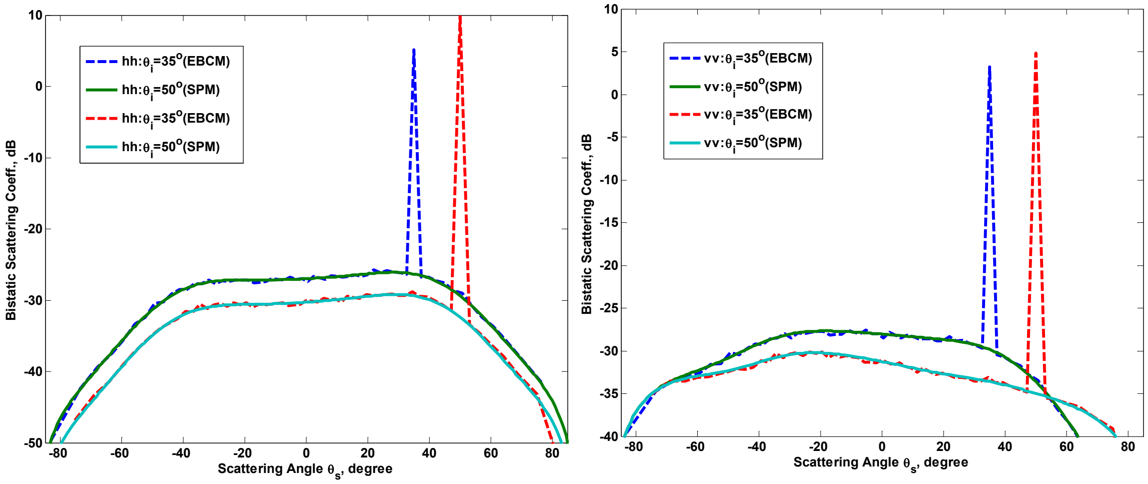

Fig. 3.8: Bi-static scattering coefficients for the scattering from a 4-point piecewise homogenous profile (Table 3.2) for different values of the incidence angle

3.4.2 Validation with Method of Moments (MoM)

The simulation results are further validated against those based on MoM. The formulation for two-interface layered rough surfaces based on MoM with pulse basis functions and delta testing functions is described in [7]. Starting from an integral equation approach, the solutions for the scattered fields in any region can be obtained by imposing boundary conditions on both interfaces and applying pulse basis functions and point matching. Appendix A summarizes the MoM solution to scattering from layered rough surfaces based on [7]. To reduce the edge diffraction effects due to a truncated sample of rough surface, a tapered windowing function is applied to the field illuminating the surface. The windowing function falls off smoothly to a negligible level at the ends of the truncated surface. The edges are hence not directly illuminated and the edge diffraction of a truncated surface sample is greatly suppressed [79-81]. This technique is known as the tapered illumination source.

For layered rough surface scattering, the tapered illumination becomes less useful in suppressing edge diffractions, as the effect of edge diffraction from subsurface interface is left completely untreated. Therefore, the length of surface sample for the numerical simulation of layered rough surface scattering has to be set to be a large number, i.e., $L=50\lambda$ in an attempt to further reduce the edge diffraction effect. In EBCM/SMM, the use of periodic boundary condition minimizes the edge diffraction effect and it suffices to set the length of surface sample to be L=30λ which translates to a major computational advantage over MoM. Also, the tapered illumination source in MoM does not exactly represent the actual incident field and leads to a loss of angular resolution. As the incidence angle moves toward the grazing angle, the length of a truncated rough surface must be increased to realistically model the incident field. This gives a practical upper limit on the modeled incidence angle of about 80° in [79]. These issues must be kept in mind in the following validation results.

In Fig. 3.9, the simulation results of bi-static scattering coefficients based on EBCM and MoM for different roughness regimes are examined. The simulation parameters are given in Table 3.3.

Table 3.3
The simulation parameters for scattering from two- rough-interface surfaces for the purpose of validation with MoM

ε_1	ε_2	l_1	l_2	d	θ_i	L	λ
3+i0.1	5	0.5 λ	0.5 λ	2 λ	35^o	30 λ	1 m

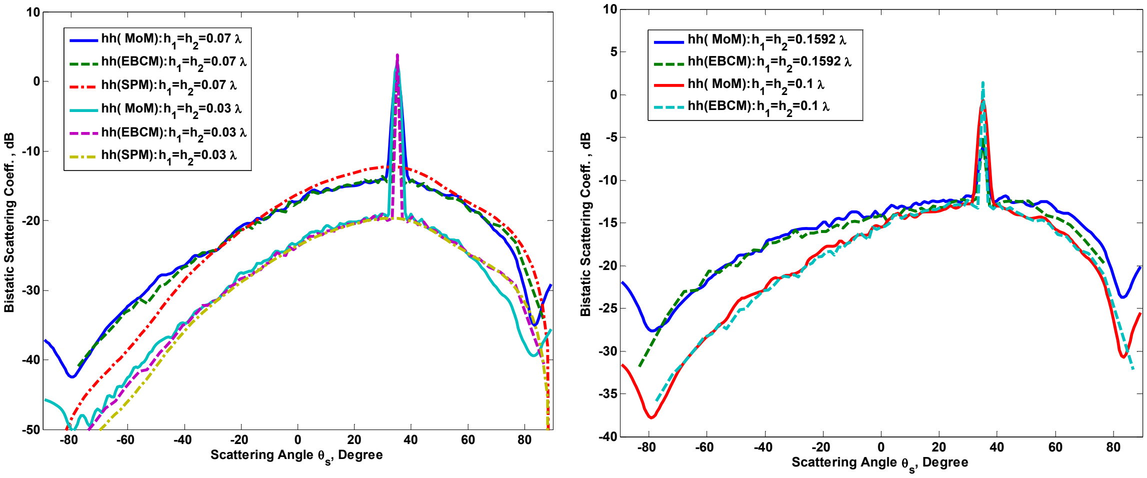

Fig. 3.9: Bi-static scattering coefficients for the scattering from two-rough-interface rough surfaces in HH polarization based on SPM, MoM and EBCM (Table 3.3): a small-moderate roughness regime (the right) and a moderate roughness regime (kh =1)

In Fig. 3.9, the plot on the left shows the bi-static scattering coefficient based on SPM, EBCM, and MoM for small-to-moderate roughness regime in HH polarization for non-grazing angles. For h_1=h_2=0.03λ (kh_1=kh_2=0.19) where SPM is valid, we observe the SPM, EBCM, and MoM curves of bi-static scattering coefficient are in excellent agreement. For h_1=h_2=0.07λ (kh_1=kh_2=0.44) where the roughness parameters drift out of the validity domain of SPM, the SPM curve shows discrepancy from those of EBCM and MoM which are consistent with each other. On the right plot in Fig. 3.9, the results of bi-static scattering coefficient based on EBCM and MoM are shown for moderate roughness regime up to ($kh_1=kh_2=1$) in HH polarization. Both the EBCM and MoM curves are in very good agreement for both $h_1=h_2=0.1\lambda$ and $h_1=h_2=0.16\lambda$. This shows that EBCM can easily handle a moderately rough surface. As roughness increases, EBCM may experience the problem of ill-conditioning and needs to be regularized [82]. However, for a natural surface of the rms heights of up to 5 cm, EBCM is capable of modeling electromagnetic scattering up to L band without any need for regularization. It is also important to point out that the magnitudes of specular returns based on EBCM are greater than those calculated using MoM. The application of tapered incident waves in MoM results in a loss of resolution and the specular peak is likely to get smeared out. It is also evident from Fig. 3.9 that the bi-static scattering behaviors toward the grazing angle based on MoM are inaccurate with a tapered illumination source.

3.4.3 Computational Efficiency

To compare EBCM with MoM, we note that EBCM introduces the concept of testing surfaces in order to simplify integral equations [64]. In EBCM, the integral equations are imposed not on the surface of the scatterer, but some other testing surfaces away from the actual surface of scatterer. The testing surfaces in EBCM are chosen such that the fields are expandable in Floquet modes in the case of periodic rough surfaces. In MoM, the basis functions used to represent the surface fields sit exactly on the surface of the scatterer. In general, EBCM results in much simpler equations with fewer unknown coefficients to be determined than those of MoM. On the other hand, EBCM suffers from the problem of ill-conditioning when the surface corrugation is too deep whereas MoM does not. In addition, the computational time for the evaluation of each matrix element using EBCM with the FFT-based matrix filling algorithm is still larger than that of MoM with pulse basis functions and point matching since, in MoM, the computation of each matrix element is just a functional evaluation of Hankel functions.

Compared to the single surface case, both memory requirement and computational time for MoM are significantly increased for a layered rough surface problem. Without applying any acceleration algorithms, the MoM has the memory requirement of $O(K^2)$ and computational complexity of $O(K^3)$, respectively, where the total number of unknowns is $K=2MN$, N is the total number of sample points per interface (i.e., $L = 50\lambda$ and $N = 500$ with 10 unknowns per wavelength) and M is the number of rough interfaces. The number of unknowns in EBCM is determined by the number of Floquet modes used to represent the induced current densities on the ground rough surface and is denoted by P (i.e. $L = 30\lambda$ and $P = 70$ with at least 2 Floquet modes per wavelength). As mentioned before, EBCM has many fewer unknowns to be determined than those of MoM (i.e. $P << N$). By applying SMM, the number of unknowns for scattering from layered rough surfaces remains the same as that of a single rough surface case. The effect of multiple scattering and bounces due to layered rough surfaces is taken into account using the generalized scattering matrix technique where each additional surface requires invoking an additional matrix inversion. Therefore, without the use of any efficient acceleration algorithms, the extended boundary condition method with scattering matrix technique requires $O((2P)^2)$ memory and $O(M(2P)^3)$ operations to solve, where P is the total number of Floquet modes, which is typically smaller than K for a single surface and does not increase with number of surfaces.

Much research effort has been devoted to facilitate the MoM solution to rough surface scattering. Acceleration algorithms such as Steepest Descent Fast Multipole Method [32] and Forward-Backward Method with Spectral Acceleration [6, 7] have been applied to expedite both matrix filling and matrix inversion processes of MoM for rough surface scattering. The algorithm in [7] is reported to improve both the MoM's memory requirement and computational complexity to $O(K)$. In this dissertation, the following benchmarking study is conducted to make an assessment of MoM and EBCM/SMM for their computational efficiencies. To compare the computational runtime between MoM and the proposed method based on EBCM/SMM, we performed a numerical study using MoM and EBCM/SMM for an example two-rough-interface scenario. The surface length of 50λ is considered and the angle of incidence is 35°. The two-rough-interface geometry with simulation parameters is given in Fig. 3.10.

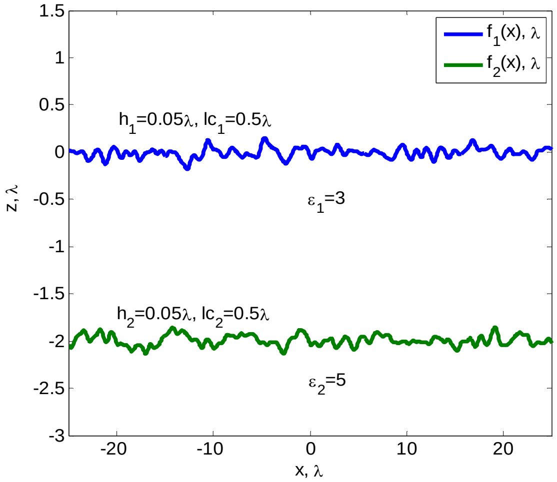

Fig. 3.10: The example two-interface scattering medium considered for the benchmarking study of MoM and EBCM/SMM

Both media are lossless so the power conservation law can be employed to verify the accuracy of the proposed method. The power conservation law is given as follows:

$$r_0 + t_2 = 1 \tag{3.45}$$

$$r_0 = \frac{1}{P_{inc}} \sum_n P^r{}_n = \sum_n \frac{\cos\theta_{s,n0}}{\cos\theta_i} \frac{|b_{no}|^2}{|a_o|^2} \quad (3.46) \qquad t_2 = \begin{cases} \sum_n \sqrt{\varepsilon_2} \frac{\cos\theta_{s,n2}}{\cos\theta_i} \frac{|A_{n2}|^2}{|a_o|^2}, & pol = HH \\ \sum_n \frac{1}{\sqrt{\varepsilon_2}} \frac{\cos\theta_{s,n2}}{\cos\theta_i} \frac{|A_{n2}|^2}{|a_o|^2}, & pol = VV \end{cases} \quad (3.47)$$

where $\theta_{s,ni} = \sin^{-1}(\frac{k_{nx}}{k_i})$ denotes the scattering angles in the i^{th} region, b_{n0} and A_{n2} are upward-propagating (reflected) amplitude in the 0th region (an air half space) and down-propagating (transmitted) amplitude in the 2^{nd} region (subsurface layer), a_o is the incident Floquet mode, and r and t are the reflectivity and transmissivity, respectively. Even if waves undergo multiple bounces and multiple scattering processes in a two-interface medium, the total reflected and transmitted energy should still sum to one. The validation of power conservation relation is critical in ensuring the accuracy of solutions. Fig. 3.11 displays the behavior of the computed sum of the reflected and transmitted energy as a function of the number of Floquet modes from the two-interface medium for different number of terms for both polarizations. According to the power conservation law, the total energy should be summed to one from lossless scattering systems.

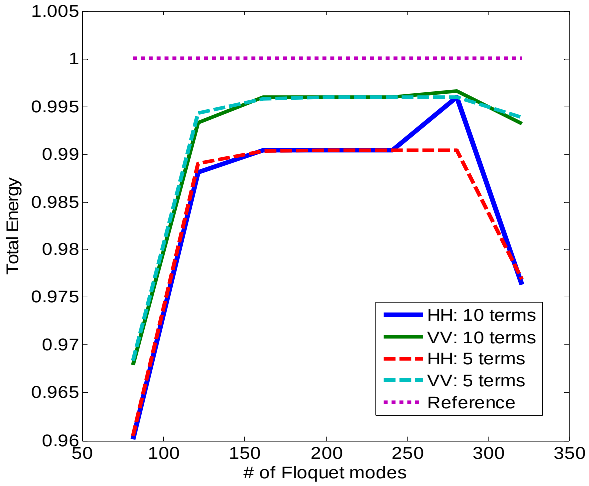

Fig. 3.11: Total energy computed from the two-interface medium

Fig. 3.11 shows that, in all cases, the power conservation law is satisfied within 5% for both polarizations. When the total number of Floquet modes used is below 150, it appears that total energy deviates more rapidly from the unity reference line. In addition, when there are excessively many evanescent Floquet modes considered in simulation, the large matrix size renders the matrix structure more susceptible to ill-conditioning, leading to a potential breakdown of the unity energy requirement.

Next, the bistatic scattering coefficients using MoM and EBCM/SMM are compared. In the MoM scheme, direct inversion and an iterative fast algorithm based on quasi-minimal residual (QMR) method [83] are examined for their computational runtime. The use of QMR method reduces the memory requirement to $O(\mathrm{K})$ and the computational requirement $O(\mathrm{K}^2)$ with smoother convergence behaviors than other iterative methods, such as, BiConjugate Gradient (BiCG) method. The tolerance for QMR method is specified to be $1\mathrm{x}10^{-7}$ and the maximum number of iterations is set to be 50. It is determined that the maximum number of iterations for QMR method has to be set above 40 for reasonable solution accuracy.

In the ECBM scheme, the matrix filling process is accelerated through FFT operation and direct matrix inversion is employed. The number of FFT points is set to be 2^{13} to ensure the accuracy of integral evaluation and different numbers of terms for the Taylor series expansion are examined. Fig. 3.12 shows both HH- and VV-polarized bistatic scattering coefficients using MoM with both direct inversion scheme and QMR method and EBCM/SMM with a fast FFT-based matrix filling algorithm with 5 and 10 terms collected in the Taylor series expansion. We observe that the MoM results with direct inversion and QMR method are almost identical and the EBCM results using 5 and 10 terms in its Taylor series expansion also converge. However, the bistatic scattering coefficients based on MoM and EBCM are not in good agreement for a single realization of the two-interface medium as expected. The discrepancy stems from various sources including the use of tapered Gaussian illumination source in MoM whereas an incident plane wave is used in EBCM, the truncated surface boundary in MoM and the application of periodic boundary condition in EBCM, the use of different basis functions to represent induced currents. Nonetheless, the scattering coefficients based on MoM and EBCM roughly trace out similar curves and they statistically converge to the same ensemble averages as evidenced by Fig. 3.9.

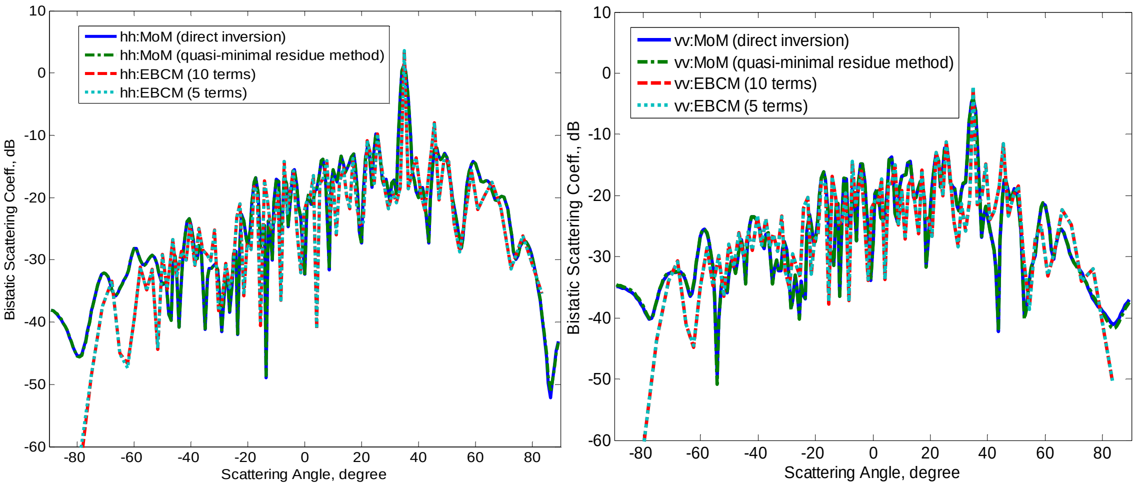

(a) (b)

Fig. 3.12: Bi-static scattering coefficients for the example two-interface scattering medium (Fig. 3.9) using MoM with direct inversion and quasi-minimal residue method and EBCM/SMM with a fast FFT-based matrix filling algorithm with 5 and 10 terms collected in the Taylor series expansion: (a) HH polarization (b) VV polarization

Fig. 3.13 shows total CPU times required to solve the two-interface scattering problem using MoM and EBCM/SMM for both polarizations against sample points (MoM) and total number of Floquet modes (EBCM) when the numerical simulation is run on a PC with 3.4 GHz intel Pentium processor and 2047 MB RAM. All of these results satisfy power conservation law within 1%. Since MoM and EBCM are different in their formulations with different types of basis functions, it is very difficult to define a fair speed benchmark for these two methods. In the benchmarking study, the comparison between MoM and EBCM for speed is made for different values of sample points (MoM) and Floquet modes (EBCM) in an attempt to assess their CPU time requirements for solving an identical scattering medium. The direct inversion in MoM is the most time consuming case and its CPU time grows as about the third power with increasing sample points. The QMR method significantly expedites the matrix inversion. In EBCM/SMM, the number of terms summed in the Taylor series expansion in the matrix filling process evidently constitutes the major factor contributing to CPU time. Clearly, EBCM/SMM is much faster than the MoM scheme with direct matrix inversion. Even though it is unclear if EBCM/SMM is a better alternative to the MoM with fast iterative algorithms, these results show that it offers a very efficient and competitive solution to forward modeling in scattering from layered rough surfaces. When EBCM/SMM is applied in 3D regime, the computational advantage due to the use of the recursion and cascade of this method will be even more significant than 2D case.

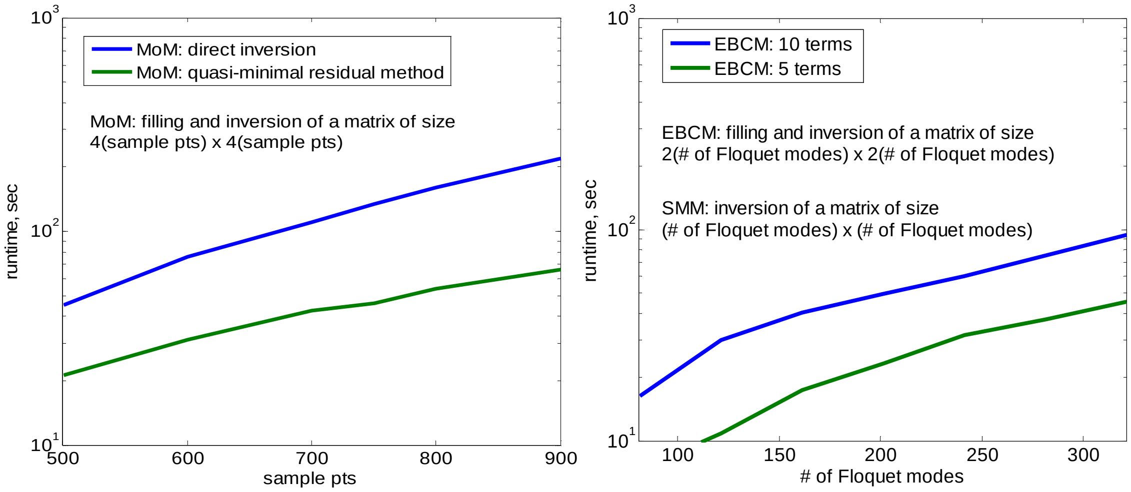

(a) **(b)**

Fig. 3.13: CPU runtime of (a) MoM with direct inversion and quasi-minimal residue method and (b) EBCM/SMM with a fast FFT-based matrix filling algorithm for computing both HH- and VV- polarized scattering responses to the two-interface medium (Fig. 3.9)

3.5 Numerical Results

A sensitivity study of backscattering coefficients in HH and VV polarizations and co-polarized phase difference for a two-rough-interface problem (Fig. 3.3) is first performed. The simulation parameters are given in Table 3.4 where $m_{v,j}$, S_j, and C_j are the soil moisture content, the mass fraction of sand and of clay in region j, respectively.

Table 3.4
The simulation parameters for scattering from two-rough-interface surfaces for purpose of sensitivity study

$m_{v,1}$	S_1	C_1	$m_{v,2}$	S_2	C_2	h_1	l_1	h_2	l_2	d
5 %	0.66	0.10	20%	0.36	0.40	3 cm	50 cm	3 cm	50 cm	30 cm

A semi-empirical model which describes the dielectric behaviors of soils as a function of volumetric moisture content in the range from 0.3 to 1.3 GHz was developed by Peplinski, et al. in [84, 85]. This model provides expressions for the real and imaginary parts of the relative dielectric constant of a soil medium in terms of the soil's textural composition (sand, silt, and clay fractions), the bulk density and the volumetric moisture content of the soil, and the dielectric constant of water at the specified frequency and physical temperature. Using the Peplinski model, these three soil parameters, $m_{v,j}$, S_j, and C_j, will translate to unique complex dielectric constants at 137 MHz and 435 MHz which are the frequencies of interest in this study, as proposed in conceptual soil moisture missions [22].

Fig. 3.14 and Fig. 3.15 show backscattering coefficients for different soil moisture of subsurface layer at 137 MHz and 435 MHz, respectively.

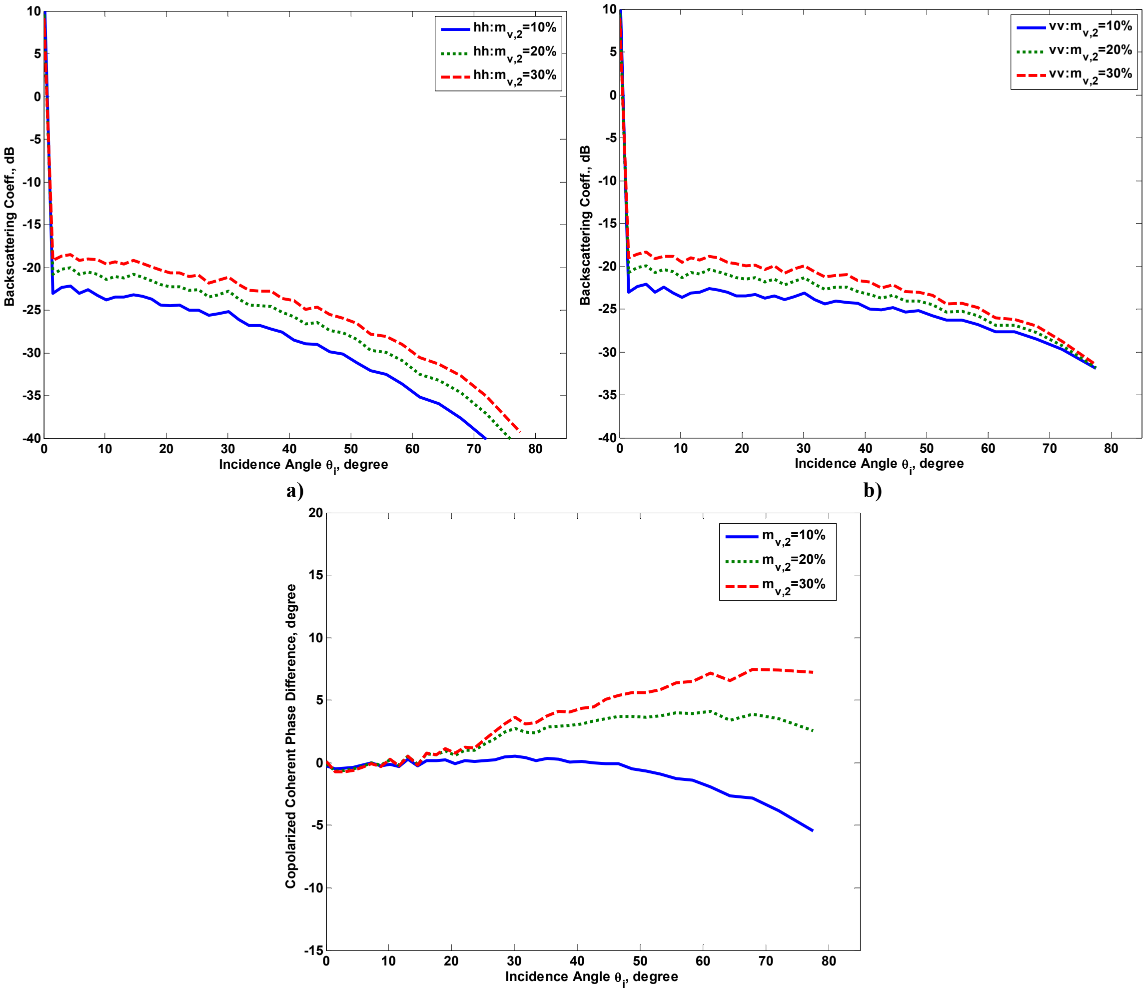

a) b)

c)

Fig. 3.14: Scattering parameters for different values of subsurface moisture contents at 137 MHz for a two-rough-interface problem (Table 3.4): a) backscattering coefficient in HH polarization (upper right figure) b) backscattering coefficient in VV polarization (upper left figure) c) co-polarized phase difference as a function of incidence angle (lower middle figure)

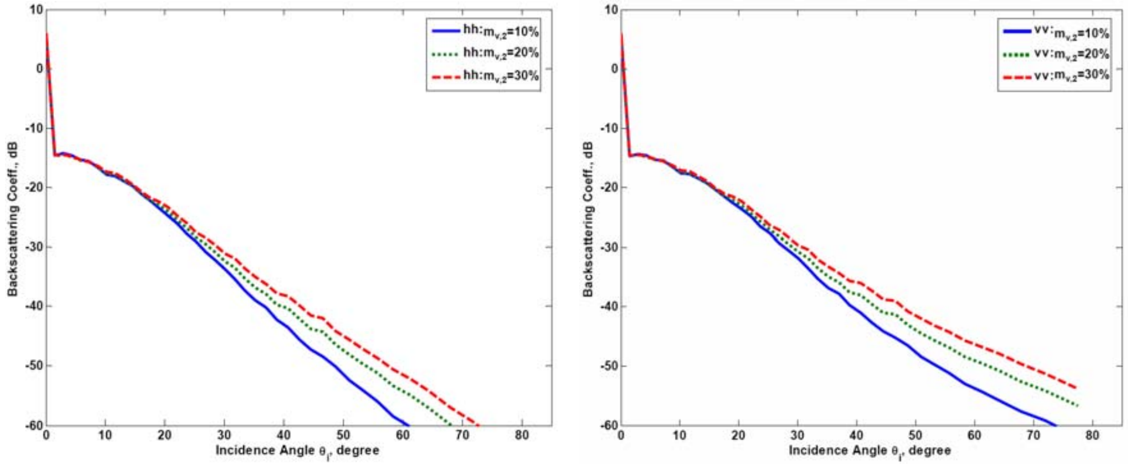

a) b)

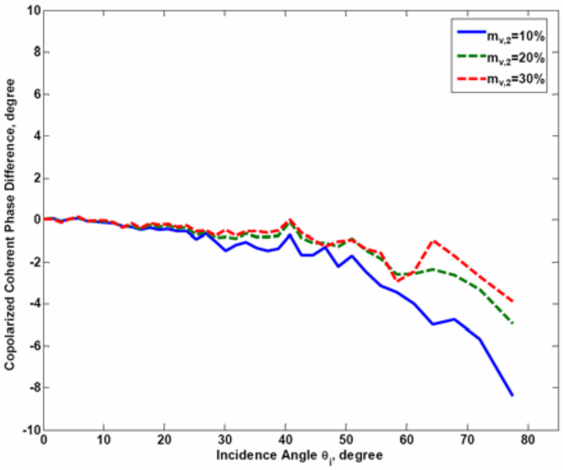

c)

Fig. 3.15: Scattering parameters for different values of subsurface moisture contents at 435 MHz for a two-rough-interface problem (Table 3.4): a) backscattering coefficient in HH polarization (upper right figure) b) backscattering coefficient in VV polarization (upper left figure) c) co-polarized phase difference as a function of incidence angle (lower middle figure)

Clearly, backscattering coefficients at 137 MHz are more sensitive to changes in subsurface moisture than those at 435 MHz. They also increase as the subsurface moisture increases. At 137 MHz, backscattering coefficients in HH and VV polarizations experience an increase of about 3-4 dB over the incidence angle range from 10^o and 50^o when the subsurface moisture increases from 10% to 30%. Co-polarized phase difference exhibits more sensitivity to the subsurface moisture when the incidence angle becomes larger. It is worth noting that co-polarized phase difference is zero at normal incidence because there is no distinction between HH and VV polarizations at normal incidence. At 435 MHz, it is evident from Fig. 3.14 that backscattering coefficients and co-polarized phase difference shows less sensitivity to subsurface moisture content than those at 137 MHz.

Next, the sensitivity to subsurface roughness at 137 MHz and 435 MHz is examined in Fig. 3.16 and Fig. 3.17 where the rms height of the bottom interface is varied from 1 cm to 5 cm.

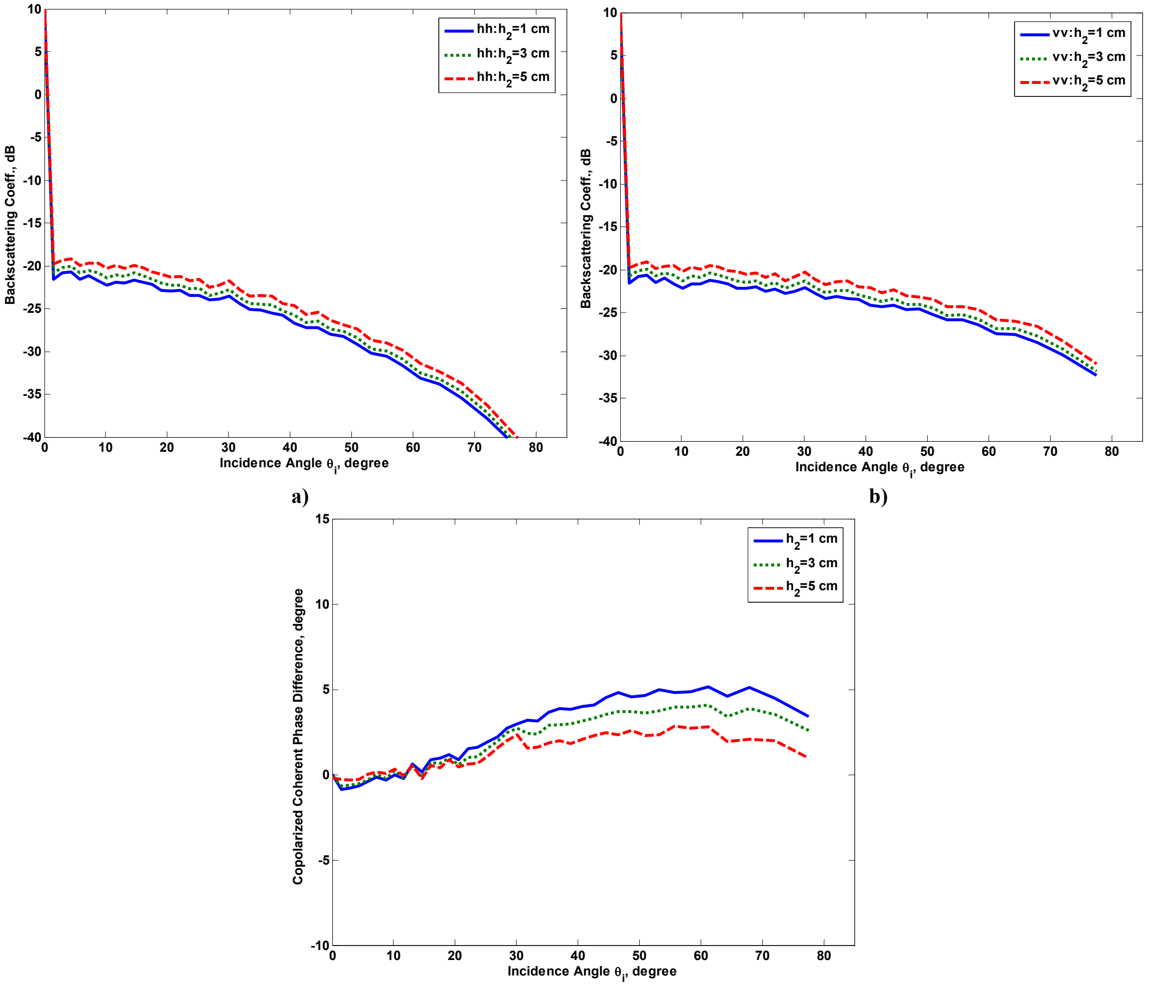

a)

b)

c)

Fig. 3.16: Scattering parameters for different values of subsurface rms height at 137 MHz for a two-rough-interface problem (Table 3.4): a) backscattering coefficient in HH polarization (upper right figure) b) backscattering coefficient in VV polarization (upper left figure) c) co-polarized phase difference as a function of incidence angle (lower middle figure)

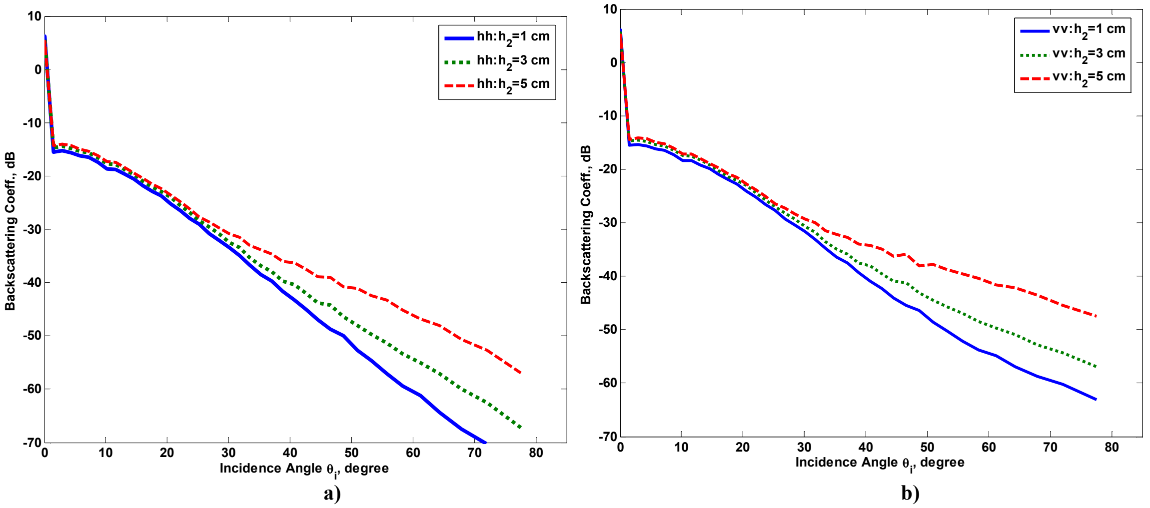

a)

b)

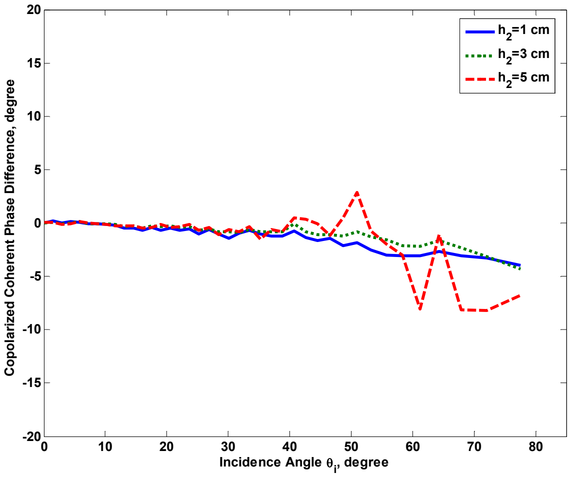

c)

Fig. 3.17: Scattering parameters for different values of subsurface rms height at 435 MHz for a two-rough-interface problem (Table 3.4): a) backscattering coefficient in HH polarization (upper right figure) b) backscattering coefficient in VV polarization (upper left figure) c) co-polarized phase difference as a function of incidence angle (lower middle figure)

At 137 MHz, backscattering coefficients in both HH and VV polarizations show only slight sensitivity to subsurface roughness (about 1.5 dB). The maximum deviation in co-polarized phase difference is about 3 degrees when the incidence angle is above 40° which may not be very useful when there is some phase calibration errors involved. At 435 MHz, however, backscattering coefficient seems to show much sensitivity to subsurface roughness for the incidence angles greater than 40°. Under a close examination of Fig. 3.17, however, the scale of backscattering coefficients for which the incidence angle is above 40° is typically around or below the noise floor of most practical systems. Thus, backscattering coefficients at 435 MHz do not provide a reliable measure to detect subsurface roughness. At h_2 = 5 cm, co-polarized phase difference shows mild fluctuations around 0° when the incidence angle is above 45°. When the subsurface interface is moderately rough and the incidence angle approaches the grazing angle, the effect of multiple scattering in subsurface layer may become so strong at this frequency that it results in a significant difference between HH and VV polarizations as suggested by strong sensitivity of co-polarized phase difference to subsurface roughness. We note that even though the subsurface layer is 30 cm below the ground surface, P-band radars can still penetrate and show sensitivity to subsurface layer features.

Finally, the effect of moisture profile variation in depth on backscattering coefficients and co-polarized phase difference is also studied. The dielectric profiles are assumed to be linear and they differ in the slopes of the linear variations. The specifications of dielectric profiles are given in Table 3.5 where $m_{v,i}$ and $m_{v,f}$ are the soil moisture contents of the top and bottom discrete thin layer in the top layer.

Table 3.5
The simulation parameters for scattering from two-rough-interface surfaces separated by the dielectric profiles

profile	$m_{v,i}$	$m_{v,f}$	variation
1	3%	5%	Linear
2	3%	10%	Linear
3	3%	15%	Linear

The dielectric profile is located in the top layer, typically a sand layer. Fig. 3.18 and Fig. 3.19 show scattering properties for different dielectric profiles at 137 MHz and 435 MHz.

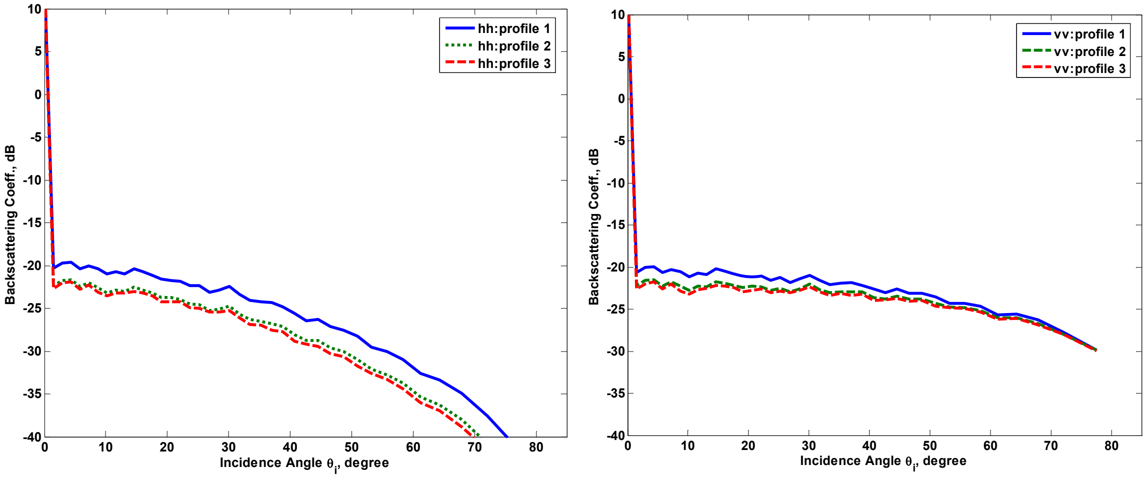

a) b)

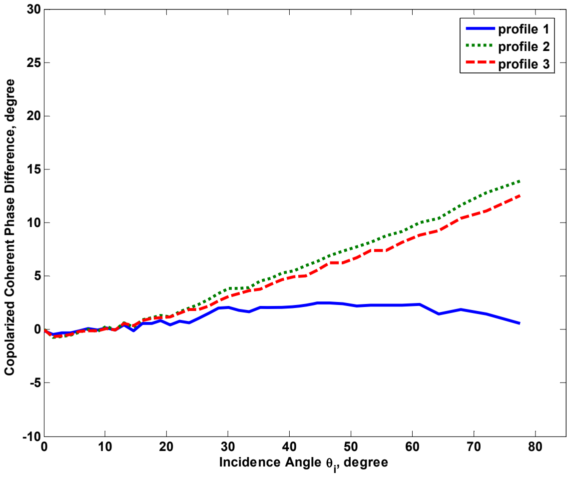

c)

Fig. 3.18: Scattering parameters for different linear dielectric profiles in the sand layer at 137 MHz for a two-rough-interface problem (Table 3.4 and Table 3.5): a) backscattering coefficient in HH polarization (upper right figure) b) backscattering coefficient in VV polarization (upper left figure) c) co-polarized phase difference as a function of incidence angle (lower middle figure)

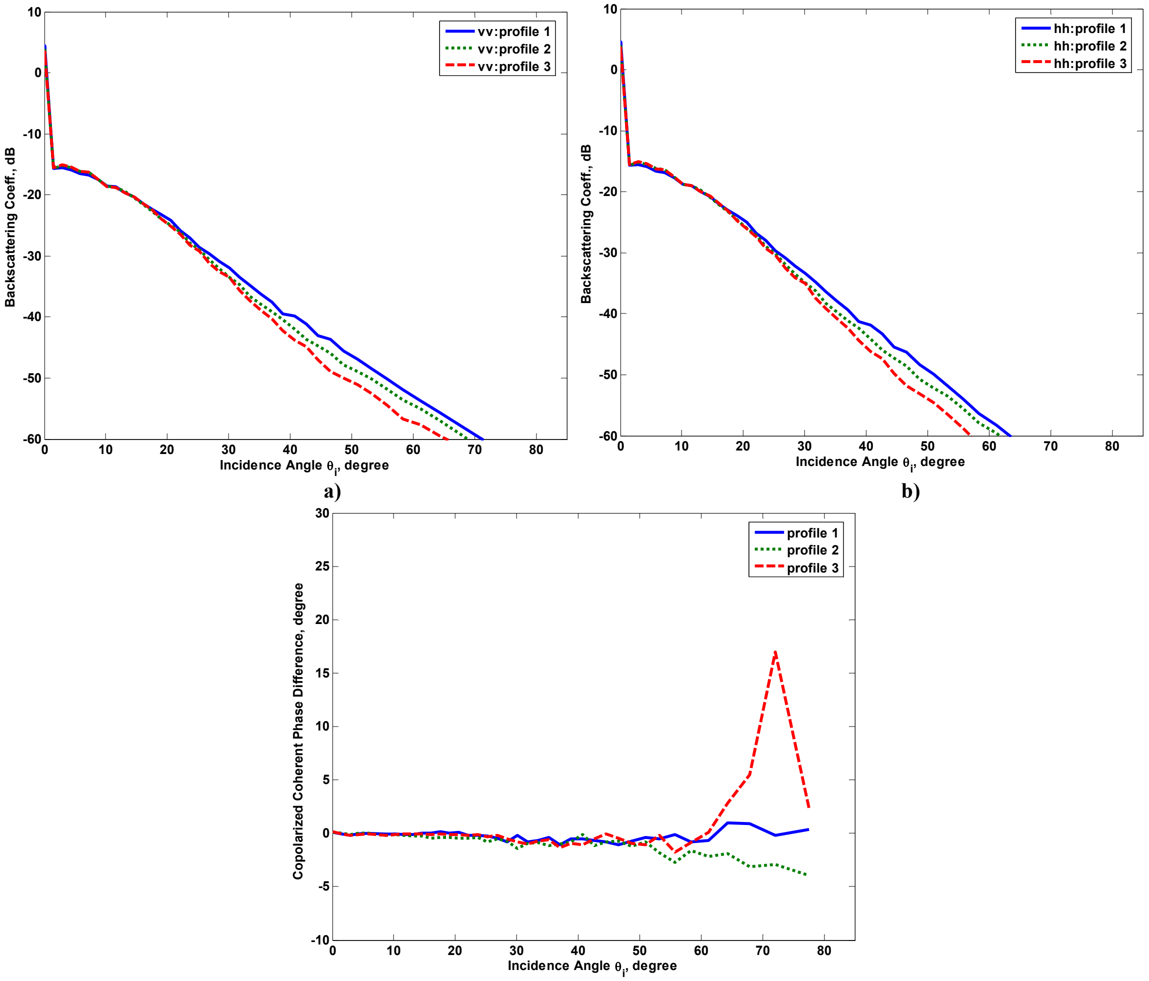

a)

b)

c)

Fig. 3.19: Scattering parameters for different linear dielectric profiles in the sand layer at 435 MHz for a two-rough-interface problem (Table 3.4 and Table 3.5): a) backscattering coefficient in HH polarization (upper right figure) b) backscattering coefficient in VV polarization (upper left figure) c) co-polarized phase difference as a function of incidence angle (lower middle figure)

In Fig. 3.18, backscattering coefficients at 137 MHz show a difference of about 2-3 dB between profile 1 and profile 3. As the gradients of the moisture variation become steeper, backscattering coefficients are more insensitive to moisture profiles. It has been suggested [26] that the reason behind the insensitivity of backscattering coefficients to inhomogeneous moisture profiles is due to the tapered impedance matching nature of profile. The natural soil moisture variation is typically gradual, resulting in slowly tapered impedance matching and hence a much less reflective mechanism. At 435 MHz (Fig. 3.19), backscattering coefficients show even less sensitivity to moisture profiles due to weaker penetration capability at this frequency. On the other hand, co-polarized phase difference at 137 MHz exhibits very strong sensitivity to moisture profiles. At 435 MHz, however, co-polarized phase difference is only sensitive to moisture profiles when the incidence angle is near the grazing angle but that is where the backscattered signal levels are extremely small and not reliably measurable.

Next, numerical simulations are carried out for scattering from multilayer rough surfaces with dielectric profiles during three distinct conditions of dry surface, wet surface, and hypothetical wet sub-layer. To obtain the backscattering coefficients and co-polarized phase difference due to realistic soil moisture profiles, the in-situ data collected in September 2003 by the USDA Southwest Watershed Research Center in Tucson, Arizona are used. The measurements were conducted at the Walnut Gulch Experimental Watershed (WGEW) in southern Arizona in support of the Microwave Observatory of Subcanopy and Subsurface (MOSS) project tower radar deployment. WGEW, which surrounds the town of Tombstone, is in the transition zone between the Sonoran and Chihuahuan Deserts. The climate is classified as semi-arid, with mean annual temperature at Tombstone of 17.7^{o}C and mean annual precipitation of 350 mm. The precipitation regime is dominated by the North American Monsoon with slightly more than 60% of the annual total falling during July, August, September and about one third falling during the six months October through March, mostly as rainfall. A shrub test site, Lucky Hills, was selected on sub-watersheds within the WGEW to evaluate and test the MOSS soil moisture radar technology. The soils in Lucky Hills are predominately sandy and gravelly loams (66% sand, 24% silt, and 10% clay). The subsurface rough layer is located about 30 cm below the ground. The layer beneath this subsurface interface mostly contains clay which is heavier than sandy soil and easily saturated (36% sand, 24% silt, and 40% clay).

The soil moisture profile for both the dry and wet ground conditions measured on August, 25 and September, 25, 2005 during a MOSS field experiment are provided in Fig. 3.20.

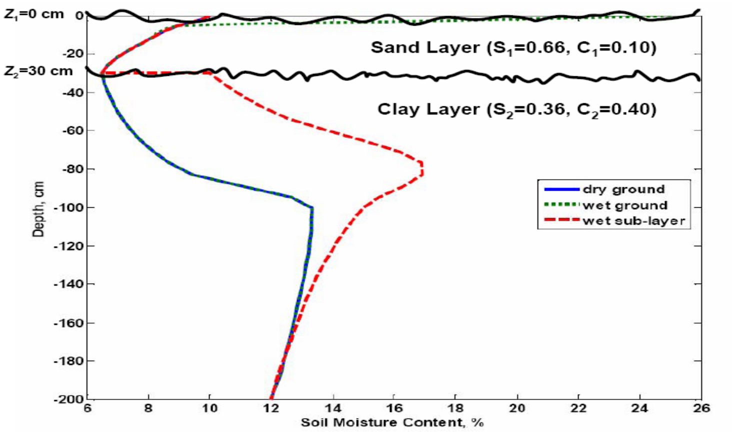

Fig. 3.20: The soil moisture profiles for the dry, wet surface conditions, and a wet subsurface layer

In addition, in order to study the sensitivity of scattering coefficients and co-polarized phase difference to subsurface anomalies at various frequencies, a synthetic soil profile with a fairly saturated subsurface layer is investigated and is labeled as ‘wet sub-layer’ in Fig. 3.20. The dielectric constant profiles are computed at the MOSS tower radar’s operating frequencies of 137 MHz (VHF band), 435 MHz (P band), and 1 GHz (L band) using the Peplinski model. Note that 137 MHz is outside the range for which the Peplinski et al., relations are derived. In the absence of other models, the same one was used to compute the complex dielectric constants at 137 MHz. However, to partially account for the modeling error where at low frequencies the model tend to overestimate the soil loss, an additional factor of 0.5 is multiplied with the imaginary part of complex dielectric constant at 137 MHz. This factor is arbitrary yet is deemed to be a reasonable scaling given the approximation factor of 2 in the frequencies.

As shown in Fig. 3.20, the rough surface profiles, $f_1(x)$ and $f_2(x)$, are located at z = 0 cm and z = - 30 cm. The simulation parameters given in Table 3.6 are used where (h_1, l_1), (h_2, l_2), are the roughness statistics (both the root-mean-squared height and correlation length) for the top and subsurface interfaces.

Table 3.6
The simulation parameters for scattering from two-rough-interface surfaces separated by the actual field-derived dielectric profiles

S_1	C_1	S_2	C_2	h_1 (cm)	l_1 (cm)	h_2 (cm)	l_2 (cm)	d(cm)	N
0.66	0.10	0.36	0.40	3	50	3	50	30	200

In addition, the inhomogeneous dielectric profiles ε₁(z) and ε₂(z) are each discretized into stacks of 50 piecewise homogeneous thin layers, resulting in Δd_1 = 0.6 cm (d_1 = 30 cm) and Δd_2 = 3.4 cm (d_1 = 170 cm), respectively. The backscattering coefficients and co-polarized coherent phase difference due to this actual field-derived medium are investigated and the sensitivity of scattering coefficients to different ground conditions at 137 MHz (VHF band), 435 MHz (P band), and 1 GHz (L band) is studied.

The simulation plots are given in Fig. 3.21 – Fig. 3.23. The backscattering coefficients for the dry and wet grounds at 435 MHz (Fig. 3.22) and 1 GHz (Fig. 3.23) show more sensitivity than those at 137 MHz (Fig. 3.21) as expected because the difference in moisture variation between the dry and wet grounds occurs only 2-3 cm in depth on the surface.

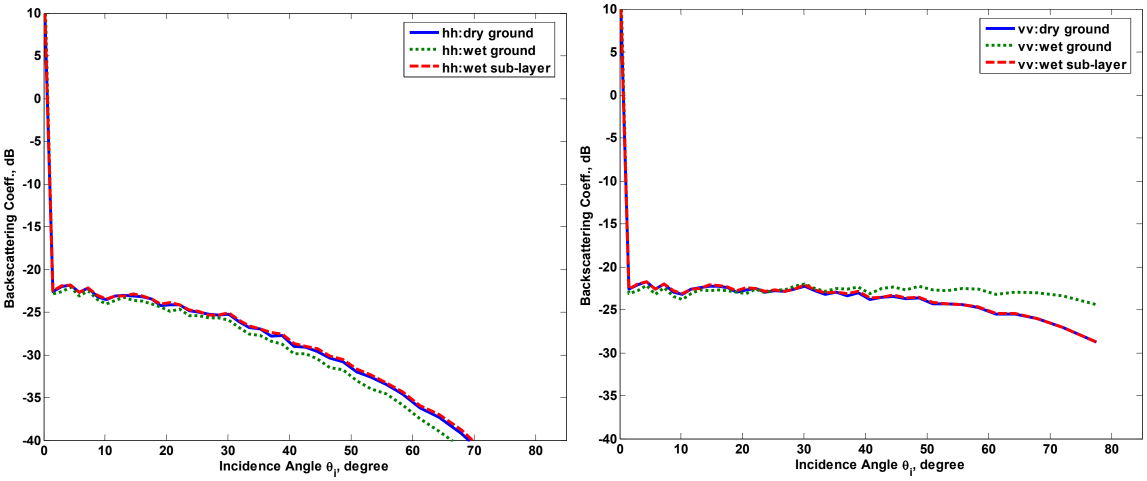

a) b)

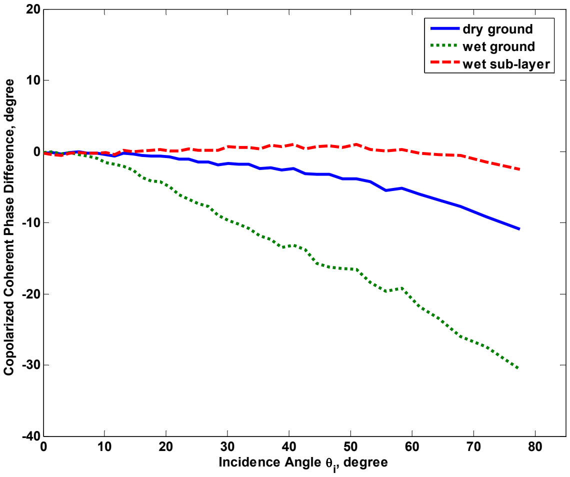

c)

Fig. 3.21: Scattering parameters for different dielectric profiles shown in Fig. 3.20 at 137 MHz (Table 3.6): a) backscattering coefficient in HH polarization (upper right figure) b) backscattering coefficient in VV polarization (upper left figure) c) co-polarized phase difference as a function of incidence angle (lower middle figure)

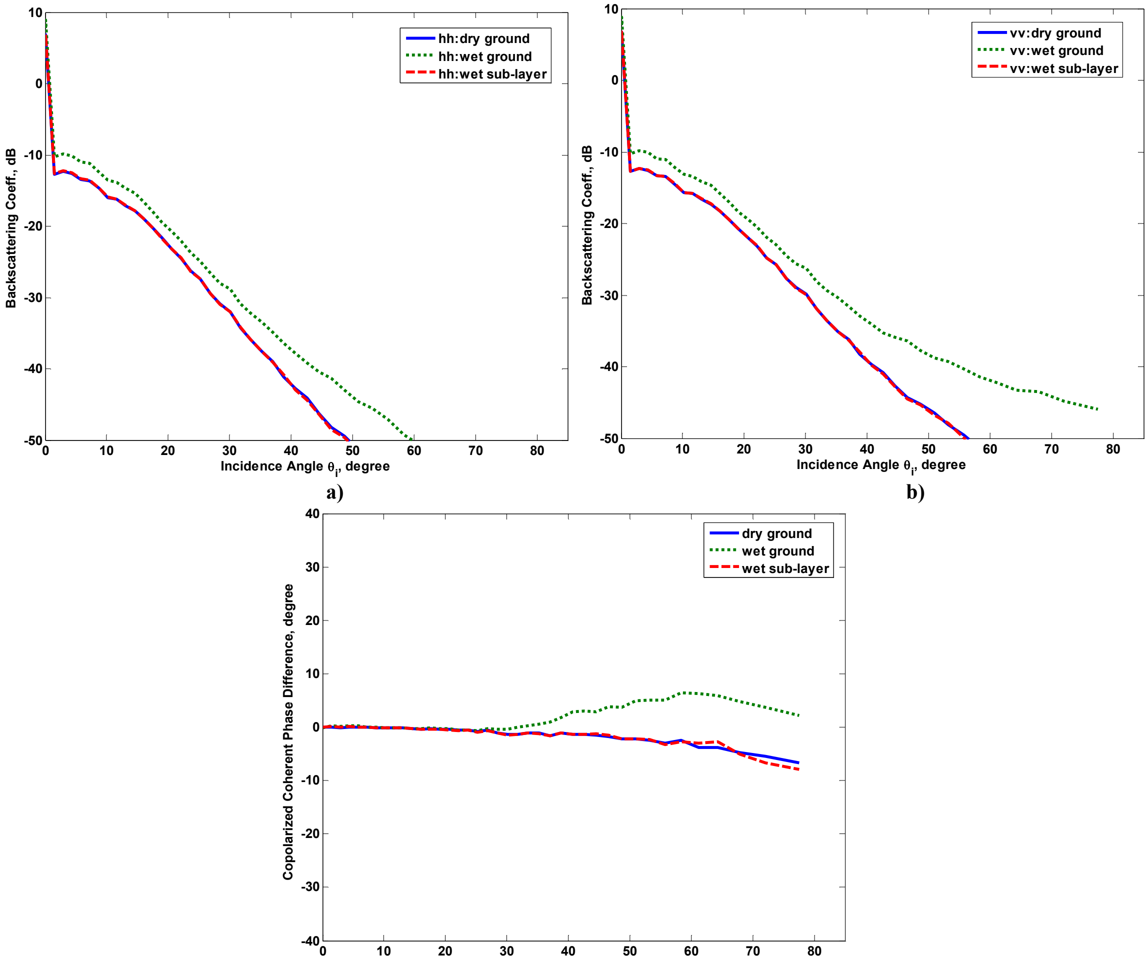

B

c)

Fig. 3.22: Scattering parameters for different dielectric profiles shown in Fig. 3.20 at 435 MHz (Table 3.6): a) backscattering coefficient in HH polarization (upper right figure) b) backscattering coefficient in VV polarization (upper left figure) c) co-polarized phase difference as a function of incidence angle (lower middle figure)

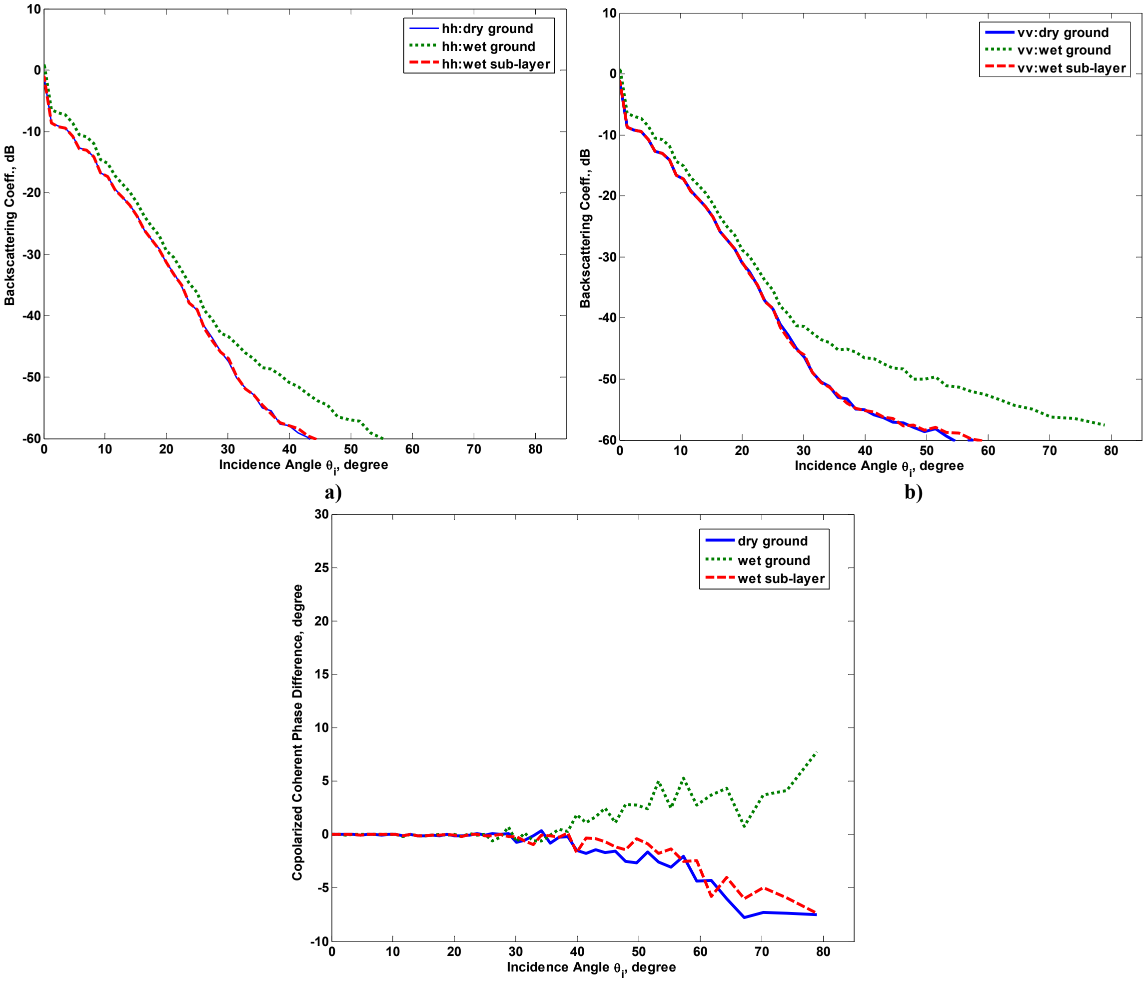

a)

b)

c)

Fig. 3.23: Scattering parameters for different dielectric profiles shown in Fig. 3.20 at 1 GHz (Table 3.6): a) backscattering coefficient in HH polarization (upper right figure) b) backscattering coefficient in VV polarization (upper left figure) c) co-polarized phase difference as a function of incidence angle (lower middle figure)

At 137 MHz, backscattering coefficients may not be able to provide a highly sensitive measure to detect the shallow spatial changes in moisture variation (5% in this case) since the perturbation in total backscattering coefficient is very small. However, co-polarized phase difference is quite sensitive to even this small spatial change in surface moisture. It also shows much sensitivity to the dry and wet ground conditions at 435 MHz and 1 GHz in the case of this shallow moisture variation.

In assessing the penetration capabilities of radar systems at 137 MHz, 435 MHz, and 1 GHz, we study and compare the scattering parameters for dry ground against those for wet sub-layer at these three frequencies of interest. Because the relatively large amount of loss present in the top layer can potentially mask the subsurface effects and significantly overshadow the effect of subsurface moisture variation, the usefulness of low frequency radar system is especially addressed here. The subsurface layer is typically mildly wet and does not give rise to a strong reflective mechanism. The tapered impedance matching nature of profile in the sand layer further prevents scattered fields due to subsurface wet layer from exiting the medium. The detection of subsurface moisture content is therefore quite challenging. In Fig. 3.22 and Fig. 3.23, backscattering coefficients and co-polarized phase difference at 435 MHz and 1 GHz are essentially indistinguishable between the dry ground and wet subsurface layer. At 137 MHz, although backscattering coefficients for the wet subsurface layer do not exhibit a large change from those for the dry ground, the sensitivity is larger than at the two higher frequencies. On the other hand, the information of co-polarized phase difference can detect even the slight variation in subsurface moisture content. Co-polarized phase difference shows a difference of about 5^o-8^o over the incidence angle from 50^o to 70^o between the dry ground and this slightly wet subsurface layer compared to practically no change for the higher frequencies. In practice, when the dielectric contrast between the ground and subsurface layer is typically larger than that used in this conservative simulation scenario, the dynamic range of variations in co-polarized phase difference will be much wider. This indicates that considerably larger sensitivity and penetration depth can be achieved using co-polarized phase difference, even for as small as a 5% moisture content change, than scattering coefficients. Low frequency polarimetric radars hence carry great promise in retrieving the subsurface moisture contents. Additionally, if the surface is covered by treed vegetation, it can be shown that coherent (double-bounce) reflections dominate the backscattering cross sections. This mechanism will be quite sensitive to the subsurface moisture content with a much larger dynamic range of variations for the cross sections.

3.6 Chapter Conclusion

A solution to scattering from multilayer rough interfaces separated by arbitrary dielectric profiles using EBCM/SMM is presented. The reflection and transmission matrices of rough interfaces are constructed using EBCM, which requires the assumption of periodic boundary conditions where the finite-length rough surface is extended periodically with period L. The reflection and transmission matrices of inhomogeneous dielectric profiles are constructed by first modeling the inhomogeneous dielectric profile as a stack of piecewise homogeneous dielectric thin layers and then recursively cascading reflection and transmission matrices of individual dielectric interfaces from the bottom dielectric interface to the top interface. Finally, the interactions between profiles and rough surfaces are accounted for by applying the generalized scattering matrix technique. In numerical simulations, the bi-static scattering coefficients are validated by comparing the simulation results with the existing analytical SPM and numerical MoM solutions to scattering from two-rough-interface structures and SPM solution to scattering from a 4-point piecewise dielectric profile. The comparison results are in excellent agreement.

Next, moisture profiles corresponding to the dry ground, wet ground, and wet subsurface layer conditions, based on the in-situ data collected by the USDA Southwest Watershed Research Center in Tucson, Arizona, are used to generate new results and study the sensitivities of measurements to various parameters. Numerical simulation results show that at low frequencies backscattering coefficients in both polarizations can still be altered due to subsurface moisture even if the ground surface is lossy and the deep soil moisture does not constitute a strongly reflective medium. In general, co-polarized coherent phase difference exhibits a strong dependence on the changes in subsurface soil moisture and provides a better measure in penetrating into deep soil layers than scattering coefficients. Therefore, co-polarized phase difference carries tremendous promise in inverting soil moisture content.

The proposed method in this paper can also be generalized to analyze three-dimensional scattering from two-dimensional multilayer rough surfaces. There already exists a 3D version of extended boundary condition method to scattering from a 2D periodic rough surface [86]. In addition, 3D scattering matrix approach is also widely utilized to handle layered geometries, which involves proper mode conversions between TE and TM polarizations. However, the 3D implementation of the method proposed in this thesis is by no means a trivial task, as the problem will be vectorial in nature and polarization conversions between TE and TM will take place. Future works on this topic include the implementation of this method to analyzing the three-dimensional scattering from multilayer rough surfaces in inhomogeneous stratified media and comparison with field radar data. These data exist from the Arizon experiments but since they do not have absolute calibration, they are not applicable yet.

CHAPTER 4

Backscattering Enhancement from Layered Rough Surfaces and Surface Plasmon Resonance

Based on the development of the EBCM/SMM technique for solving scattering from layered rough surfaces in Chapter 3, in this chapter we analyze backscattering enhancement due to surface plasmon resonance from two-rough-interface structures. Backscattering enhancement due to surface plasmon resonance is a manifestation of multiple scattering processes. This chapter explores the capability of this method in modeling coherent multiple scattering phenomena. Surface plasmon resonance is a charge-density oscillation associated with surface plasmon waves at the interface, which decay evanescently into both media and propagate along the interface. In a planar interface geometry, these surface plasmon waves stay bound to the surface. When the surface geometry becomes irregular, such as a periodic or rough surface, these surface plasmon waves become localized at protrusions and crevices of the rough surface, leading to the excitation of surface plasmon waves. When surface plasmon waves are excited and they traverse along the surface in opposite directions, they may constructively interfere with each other, coupling into propagating modes and producing an enhanced backscattered peak.

The proposed technique is an ideal candidate for solving backscattering enhancement from layered rough surfaces since it fully accounts for all multiple orders of scattering and multiple bounces due to wave interactions between rough interfaces. It is important to point out that this approach is especially well suited for sensitivity analysis because it is capable of evaluating the effect of a change in one layer without repeating the entire computation. Other techniques [44-47] for analyzing layered structures solve the problem in entirety without employing cascading matrices for individual layers which typically require much more computational time than the proposed technique. Finally, although the issue of ill conditioning may arise from EBCM when the surface corrugation is too deep, it nevertheless poses as a trivial problem because backscattering enhancement due to surface plasmon resonance takes place in a small roughness regime.

4.1 The Wavenumbers of Surface Plasmon Waves for a Dielectric Coated Metal

The mechanisms of backscattering enhancement due to the excitations of surface plasmon waves from a single rough surface are discussed in [87]. Here, the derivation for the wavenumbers of surface plasmon waves for two layers is presented. An electromagnetic wave incident upon a rough surface from angle θ_i results in surface plasmon waves propagating in opposite directions. The inward coupling of the incident wave by means of the roughness into surface plasmon waves may be expressed by the pair of grating equations in which the waves correspond to the 1st diffracted orders:

$$+k_{sp} = k_o \sin\theta_i + k_1 \qquad\qquad -k_{sp} = k_o \sin\theta_i - k_2 \tag{4.1}$$

where k_1 and k_2 are wavenumbers available in the surface-roughness spectrum. The quantity $+/-k_{sp}$ denotes the wavenumber of the forward (+) or backward (-) surface wave. The surface plasmon waves, once excited, may now couple to a propagating wave escaping from the surface at angle θ_s. This outward coupling of the surface plasmon waves into propagating scattered waves may be similarly described by the grating equations:

$$k_o \sin\theta_s = +k_{sp} - k_3 \qquad\qquad k_o \sin\theta_s = -k_{sp} + k_4 \tag{4.2}$$

where k_3 and k_4 are again among the wavenumbers contained in the roughness spectrum. In the backscattering direction with $\theta_s = -\theta_i$, equations (4.1) and (4.2) are identical and require that $k_1 = -k_4$

and k_2=-k_3. Physically, as described in [43], backward scattering can be understood as the propagating part of backward leaky surface plasmon modes excited by an incident wave impinging on a rough surface. Similarly, forward scattering is due to the forward-propagating leaky surface plasmon modes. The enhancement in the backscattering direction is induced by a series of scattering processes where the wavenumbers of incident waves and scattered waves coincide with each other. In essence, both forward and backward plasmon waves with the same wave-numbers but with opposite signs constructively interfere with each other, giving rise to backscattering enhancement. Equations (4.1) and (4.2) then describe the pair of time-reversed scattering processes that give rise to the predicted backscattering effect. The following section describes the formulation leading to the computation of the wavenumbers of surface plasmon waves for a dielectric-coated metal.

We consider TM electromagnetic waves for a dielectric-coated metal in the following two-layer geometry in Fig. 4. 1.

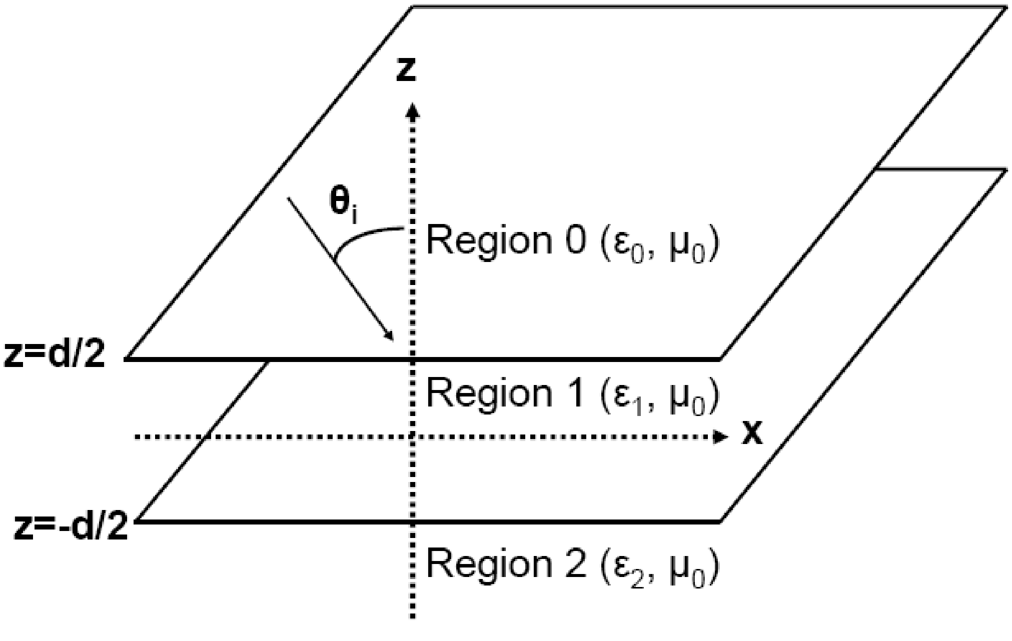

Fig. 4.1: The two-layer geometry for the computation of the wavenumbers of surface plasmon waves for a dielectric-coated metal.

The time-harmonic expression for TM waves is given as follows:

$$H_y(z,x,t) = H_y^j(z,x)e^{-i\omega t} \tag{4.3}$$

where $H_y^j(z,x)$ indicates surface waves, which are evanescent along z and traversing along x and the subscript j denotes the region. In region 0,

$$H_y^0(z,x) = Ae^{ik_x x}e^{-\alpha_{0z}z} = Ae^{ik_x x}e^{-\sqrt{k_x^2-k_0^2}\,z} \tag{4.4}$$

In region 1,

$$\begin{aligned} H_y^1(z,x) &= B_1 e^{ik_x x}e^{-\alpha_{1z}z} + B_2 e^{ik_x x}e^{\alpha_{1z}z} \\ &= B_1 e^{ik_x x}e^{-\sqrt{k_x^2-k_1^2}\,z} + B_2 e^{ik_x x}e^{\sqrt{k_x^2-k_1^2}\,z} \end{aligned} \tag{4.5}$$

In region 2,

$$H_y^2(z,x) = Ce^{ik_x x}e^{\alpha_{2z}z} = Ce^{ik_x x}e^{\sqrt{k_x^2-k_2^2}\,z} \tag{4.6}$$

By imposing the boundary condition at z = d/2 and z = -d/2,

$$H_y^0(z=d/2,x) = H_y^1(z=d/2,x) \tag{4.7}$$

$$\frac{\partial}{\partial z}H_y^0(z,x)_{z=\frac{d}{2}} = \frac{1}{\varepsilon_1}\frac{\partial}{\partial z}H_y^1(z,x)_{z=\frac{d}{2}} \tag{4.8}$$

$$H_y^1(z=-d/2,x) = H_y^2(z=-d/2,x) \tag{4.9}$$

$$\frac{1}{\varepsilon_1}\frac{\partial}{\partial z}H_y^1(z,x)_{z=\frac{d}{2}} = \frac{1}{\varepsilon_2}\frac{\partial}{\partial z}H_y^2(z,x)_{z=\frac{d}{2}} \tag{4.10}$$

This then translates into a system of four equations and four unknowns which can be cast into a matrix equation and solved simultaneously.

$$\begin{bmatrix} e^{-\alpha_{0z}\frac{d}{2}} & -e^{-\alpha_{1z}\frac{d}{2}} & -e^{\alpha_{1z}\frac{d}{2}} & 0 \\ -\alpha_{0z}e^{-\alpha_{0z}\frac{d}{2}} & \frac{1}{\varepsilon_1}\alpha_{1z}e^{-\alpha_{1z}\frac{d}{2}} & -\frac{1}{\varepsilon_1}\alpha_{1z}e^{\alpha_{1z}\frac{d}{2}} & 0 \\ 0 & -e^{\alpha_{1z}\frac{d}{2}} & -e^{-\alpha_{1z}\frac{d}{2}} & e^{-\alpha_{2z}\frac{d}{2}} \\ 0 & -\frac{1}{\varepsilon_1}\alpha_{1z}e^{\alpha_{1z}\frac{d}{2}} & \frac{1}{\varepsilon_1}\alpha_{1z}e^{-\alpha_{1z}\frac{d}{2}} & -\frac{1}{\varepsilon_2}\alpha_{2z}e^{-\alpha_{2z}\frac{d}{2}} \end{bmatrix} \begin{bmatrix} A \\ B_1 \\ B_2 \\ C \end{bmatrix} = \begin{bmatrix} 0 \\ 0 \\ 0 \\ 0 \end{bmatrix} \tag{4.11}$$

The following dispersion relation for surface plasmon waves is obtained after the matrix equation is solved.

$$(-\alpha_{oz}+\frac{1}{\varepsilon_1}\alpha_{1z})(-\frac{1}{\varepsilon_2}\alpha_{2z}+\frac{1}{\varepsilon_1}\alpha_{1z})e^{-\alpha_{1z}d}-(-\alpha_{oz}-\frac{1}{\varepsilon_1}\alpha_{1z})(-\frac{1}{\varepsilon_2}\alpha_{2z}-\frac{1}{\varepsilon_1}\alpha_{1z})e^{\alpha_{1z}d}=0 \tag{4.12}$$

It is worth noting that if ε_2 and ε_1 are equal, the dispersion relation can be simplified to $(-\alpha_{oz}-\frac{1}{\varepsilon_1}\alpha_{1z})=0$, leading to the known expression of the surface plasmon mode for a planar interface

$$k_{sp}=k_o\{\sqrt{\frac{\varepsilon_m\varepsilon_d}{\varepsilon_m+\varepsilon_d}}\} \tag{4.13}$$

By the same token, the dispersion relation can be derived for TE surface waves and its expression is given as:

$$(-\alpha_{oz}+\alpha_{1z})(-\alpha_{2z}+\alpha_{1z})e^{-\alpha_{1z}d}-(-\alpha_{oz}-\alpha_{1z})(-\alpha_{2z}-\alpha_{1z})e^{\alpha_{1z}d}=0 \tag{4.14}$$

The dispersion relations in (4.12) and (4.14) can be solved graphically to determine the wavenumbers of surface plasmon modes. Using the simulation parameters ε_1=3 and ε_2=-18+i0.55 and enforcing the positivity constraint on α_{jz}, the wavenumbers, $q_{sp}=k_{sp}/k_{o}$, are plotted against the layer thickness for both TE and TM polarizations in Fig. 4.2 (a) and (b).

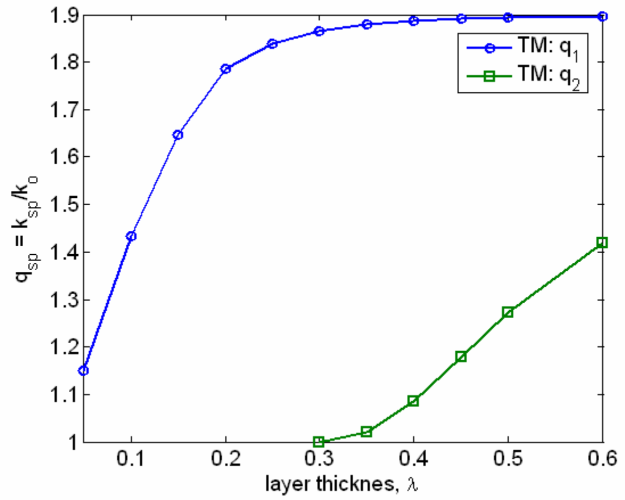

(a)

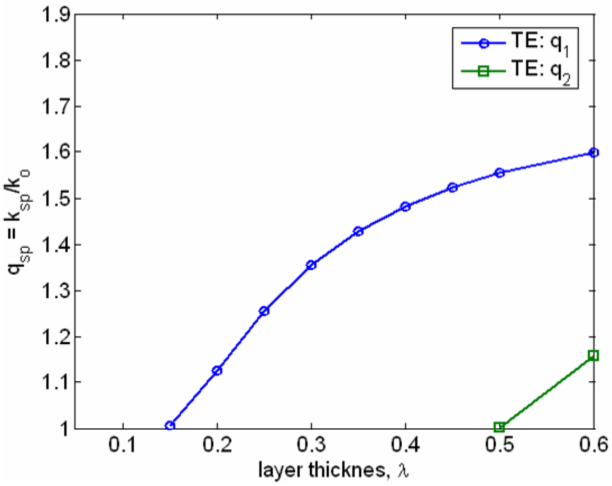

(b)

Fig. 4.2: The wavenumbers of surface plasmon waves as function of d for (a) TM and (b) TE polarizations

From d=0.05λ to d=0.25λ, only one valid solution q_1 exists for TM surface plasmon modes because the dielectric slab is too thin to support multiple guided modes. When the layer thickness exceeds d=0.30λ, the second guided surface mode q_2 comes into existence. The presence of multiple guided surface plasmon waves leads to the appearance of satellite peaks. A discussion regarding satellite peaks can be found in [44] where the solution to scattering from a free standing metal is derived based on the small perturbation method (SPM) up to the forth order and satellite peaks can be seen from the results based on SPM. The idea behind satellite peaks is that a bounded layered structure supports two or more guided waves and therefore satellite peaks are also generated in addition to the enhanced backscattering peak. For TE polarization, there only exists a single solution from d=0.15λ to 0.50λ. Below d=0.15λ, TE surface waves do not exist on this structure. When the layer thickness exceeds d=0.50λ, the second TE guided mode q_2 is induced.

The presence of two surface plasmon waves can give rise to two satellite peaks at the angles, $\theta_s^{\pm}$. The locations of satellite peaks given the wavenumbers of two guided waves, q_1 and q_2, can be found from [44]:

$$\theta_s^{\pm} = \sin^{-1}(-\sin(\theta_i) \pm [q_2 - q_1]) \qquad (4.15)$$

Substituting q$_1$ and q$_2$ from our graphical solution in Fig. 4.2 into (4.15) gives the locations of satellite peaks, $\theta_s^{\pm}$. Table 4.1 (a) lists the values of $\theta_s^{\pm}$ in TM polarization for different values of layer thickness from d=0.30λ to d=0.50λ when the incidence angle is 5°. Table 4.1 (b) gives the locations of satellite peaks for d =0.60λ for both TM and TE polarizations.

Table 4.1
(a) The locations of satellite peaks at $\theta_i = 5^o$ for different values of d in TM polarization

$d(\lambda)$	q_1	q_2	θ_s^+	θ_s^-
0.30	1.8647	1.0000	51.04°	-72.15°
0.35	1.8785	1.0208	50.40°	-70.88°
0.40	1.8862	1.0840	45.65°	-62.79°
0.45	1.8905	1.1777	38.73°	-53.13°
0.50	1.8930	1.2729	32.20°	-45.01°

(b) The locations of satellite peaks at $\theta_i = 5^o$ for d = 0.6λ for TM and TE polarizations

Pol.	q_1	q_2	θ_s^+	θ_s^-
TM	1.8954	1.4178	18.58°	-29.54°
TE	1.5993	1.1585	20.71°	-31.87°

4.2 Criteria for Backscattering Enhancement

4.2.1 Backscattering Propagating Floquet Mode

To capture backscattering enhancement using the EBCM/SMM approach, one of the Floquet modes must be propagating in the backscattering direction for the scenario of a single rough interface. For a two-interface problem, e.g., that of a metallic rough surface coated with a dielectric layer, one of the Floquet modes traveling inside the top layer must propagate exactly in the same direction as the transmitting direction of the coherent wave which corresponds to the backscattering direction in the top layer where backscattering enhancement takes place. Its transmitted angle obeys the Snell's Law of Transmission. From (3.5), it follows that this requirement is met if

$$X^2 + 2k_{xj}X - (k_j - k_{zj} - k_{xj})^2 = 0 \qquad (4.16)$$

where $X = \frac{2\pi n}{L}$, $k_{zj} = k_j \cos\theta_j , k_{xj} = k_j \sin\theta_j$ and j is the subscript denoting the region of a dielectric medium which lies above the metallic rough surface. The angle θ_j is the angle in region j at which the transmitted wave in the dielectric medium impinges upon the metallic medium. From (4.16),

$$X = \frac{2\pi n}{L} = \frac{-2k_{xj} - \sqrt{(2k_{xj})^2 - 4(k_j - k_{zj} - k_{xj})}}{2} \tag{4.17}$$

Based on the computed value of *X*, since n is an integer which ranges from –*N* to *N* (where 2*N*+1 is the total number of Floquet modes in simulation), we can then determine a set of *L*'s corresponding to different *n*'s which satisfies the condition of backscattering propagating Floquet mode. The value of *L* should also be set to be much greater than the correlation length of rough surface (i.e. $L > 40l_c$).

4.2.2 The Minimum Number of Floquet Modes for Surface Plasmon Resonance

Both modes, q_1 and q_2, must be captured in the discrete spectrum of plane waves employed in EBCM. The next paragraph describes the method for choosing the number of Floquet modes used in simulation in order to capture two guided surface waves. In the context of EBCM, the discrete spectrum of Floquet modes must account for the presence of surface plasmon wave k_{sp} which travels along the rough surface in the x direction. Using (3.4), the minimum number of Floquet modes required to capture surface plasmon waves can be computed and is given by

$$N_{\min} = \min\left(\frac{(k_{sp} + k_{xi})L}{2\pi}, \frac{(k_{sp} - k_{xi})L}{2\pi}\right) = \frac{(k_{sp} - k_{xi})L}{2\pi} \tag{4.18}$$

To properly determine *L* and *N*, the number of Floquet modes is first arbitrarily selected (preferably a large number). Then, *L* is computed based on (4.17). Subsequently, the condition from equation (4.18) is used to verify if the total number of Floquet modes, 2*N*+1, is greater than $2N_{min}+1$. If this condition fails, the total number of Floquet modes is increased. The value of N_{min}

is chosen based on the wavenumber of surface plasmon waves for a planar dielectric-coated metal. In the case of multilayer rough surfaces, the actual position of surface plasmon resonance is slightly shifted due to the presence of small roughness. In general, if N is chosen to be large with at least 4 Floquet modes per wavelength (i.e., $L = 30\lambda$ and $P = 70$ where 2*P+1 is the total number of Floquet modes), the condition in (4.18) is easily satisfied.

4.3 Comparison with MoM Results

Numerical simulations of scattering from two-interface rough surfaces are performed for validation and comparison. The dielectric constant of the lossless dielectric layer is $\varepsilon_1 = 3$. The metallic half space with a rough interface has a dielectric constant $\varepsilon_2 = -18.5 + i0.55$ (i.e., the dielectric constant of silver at λ = 633 nm). The angle of incidence is 10°. The simulation parameters given in Table 4.2 are used. The number of realizations of the surface profiles used for computing scattering coefficients is 500.

Table 4.2
The simulation parameters for backscattering enhancement from two-interface rough surface

ε_1	ε_2	kh_1	kl_1	kh_2	kl_2	kl_2	d	L
3	-18+i0.55	0.05	1.0	0.05	1.0	1.0	0.1λ	28.6843λ

The largest wavenumber of surface plasmon wave which has been determined in Table 4.1 is $k_{sp} = 1.8930\ k_o$. Using (4.18), the minimum number of Floquet modes, $2N_{min}+1$, is 100. The number of Floquet modes used in the simulation is 121. The choice of 121 Floquet modes ensures surface plasmon waves are accounted for as well as enough propagating and evanescent waves are being considered in the numerical simulation. First, for the validation purpose, the simulation results of backscattering enhancement based on EBCM/SMM and MoM [7] for different values of incidence angles are examined. The simulation results are given in Fig. 4.3.

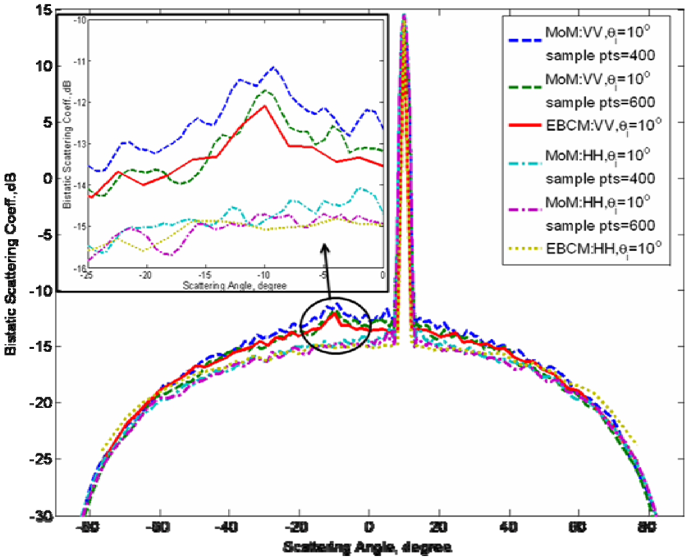

Fig. 4.3: Bistatic scattering based on EBCM and MoM from dielectric coated silver with rough interfaces for incidence angles of 10° for the purpose of validation

In MoM, the solutions for scattered fields in any region are obtained by imposing boundary conditions on both interfaces and applying pulse basis functions and point matching. To reduce the edge diffraction effect due to a truncated sample of rough surface, a tapered windowing function is applied to the field illuminating the surface. In an attempt to further reduce the edge diffraction effect from the subsurface interface, the length of surface sample for the numerical simulation based on MoM is set equal to L=40λ. In addition, both the uses of coarse and dense grids [9] are examined with a grid of 10 and 15 points per free-space wavelength respectively to discretize the surface. They correspond to 400 and 600 sample points for a surface length of 40λ, respectively. In both MoM and EBCM, matrices are inverted using a direct matrix inversion technique. To give an idea of the computational speed of EBCM/SMM and MoM, the completion of the Matlab numerical simulation for a single realization of two-interface rough surface scattering for both polarizations based on EBCM/SMM takes around 75 seconds whereas that based on MoM takes around 86 seconds and 267 seconds for coarse and dense grids, respectively, on a PC with Pentium-4 2-GHz processor and 1.5 GB RAM.

In Fig. 4.3, the HH-polarized bistatic scattering coefficients based on EBCM/SMM are in good agreement with those based on MoM for an incidence angle of 10°. For the VV-polarized bistatic scattering coefficients using a coarse grid (i.e., 400 sample points for a surface length of 40λ), although backscattered enhanced peaks are present in the simulation plots based on both EBCM/SMM and MoM, the magnitudes of backscattered enhanced peaks for an incidence angle of 10^o simulated using MoM are slightly greater than those simulated using EBCM/SMM. However, when a dense grid is employed with 600 sample points for a surface length of 40λ, then there is good agreement between the bistatic backscattering coefficients based on EBCM/SMM and MoM. The explanation for this observation is that the application of a coarse grid in MoM is not suitable for analyzing backscattering enhancement when a dielectric medium is very dense. The dielectric constant of silver, ε_2= -18+i0.55 requires a dense discretization due to rapid spatial variation of surface fields in a lossy dielectric medium with high permittivity.

A denser grid translates into much higher computational cost, making MoM an undesirable numerical technique for analyzing backscattering enhancement. The diffraction of surface plasmon waves at truncated surface edges employed in MoM may also lead to undesirable effects because surface plasmon waves can propagate over a large distance on a weakly rough surface. On the other hand, the choice of basis functions employed in EBCM/SMM makes it less susceptible to the problem of high spatial variation of surface fields and hence more computationally efficient. The periodic boundary condition used in EBCM/SMM also reduces the diffraction of surface plasmon waves at the rough surface edge.

4.4 Numerical Results

In this section, backscattering enhancement due to surface plasmon resonance is analyzed using the proposed technique. The simulation parameters in Table 4.2 with an angle of incidence equal to 5^o are employed in this numerical study. To investigate the scattering patterns of backscattering enhancement due to the subsurface characteristics and to clarify the sensitivity of enhanced backscattered peak to various physical parameters, several parameters are varied while others are kept fixed. In order to examine clearly any defining features of bistatic scattering response, the total number of realizations over which the average is computed is 2500. The simulation plots are given in Fig. 4.4 – 4.9. To highlight and emphasize the differences in the magnitudes of enhanced backscattered peaks for various cases, a linear scale is employed and coherent specular returns are removed in the following plots. In Fig. 4.4, the TM or VV polarized backscattering coefficients from the dielectric-coated silver for scattering with and without enhanced peaks are plotted. We observe that the enhanced backscattered peak vanishes as the angle of incidence moves toward the grazing angle. This observation is consistent with the characteristics of backscattering enhancement observed in [43, 44].

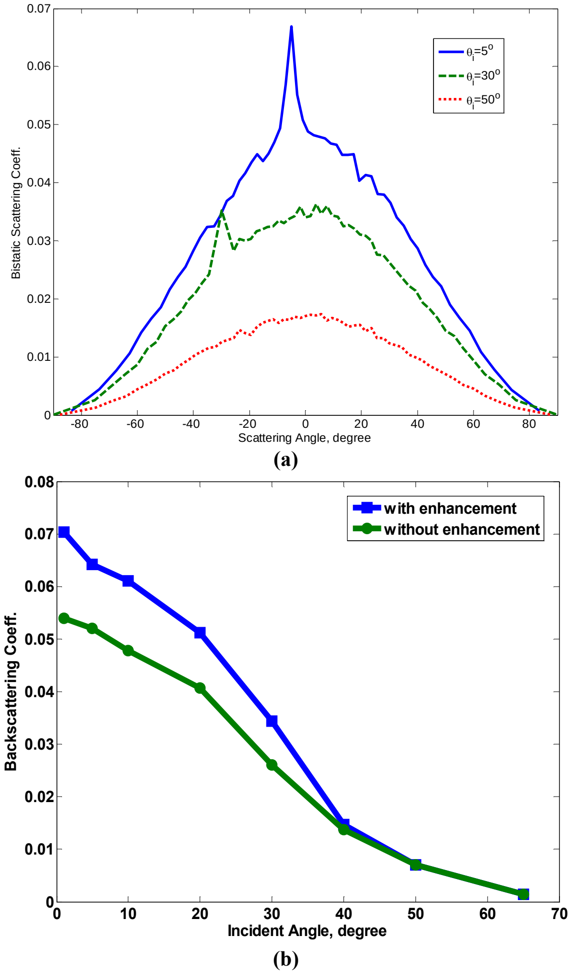

Fig. 4.4:(a) Bistatic scattering from dielectric-coated silver with rough interfaces for different angles of incidence (b) and the backscattering coefficients for scattering with and without enhancement

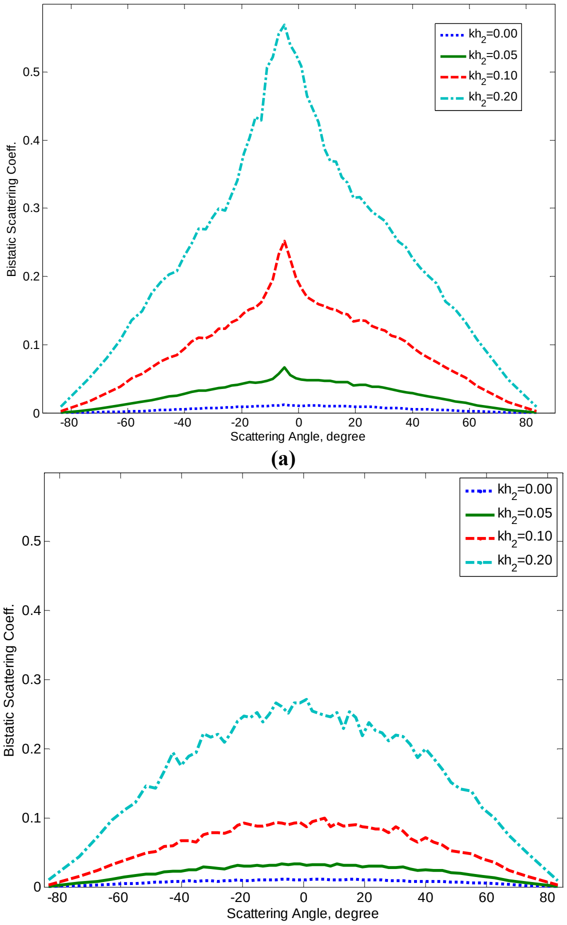

(a)

(b)

Fig. 4.5: Bistatic scattering from dielectric coated silver with rough interfaces for different roughness parameters of the bottom metallic rough surface for (a) VV polarization and (b) HH polarization. In (a), the enhancement increases with surface roughness in the roughness regime examined in this paper. In addition, the width of an enhanced peak gets widened as surface roughness increases. In (b), backscattering enhancement is not observed for HH polarization.

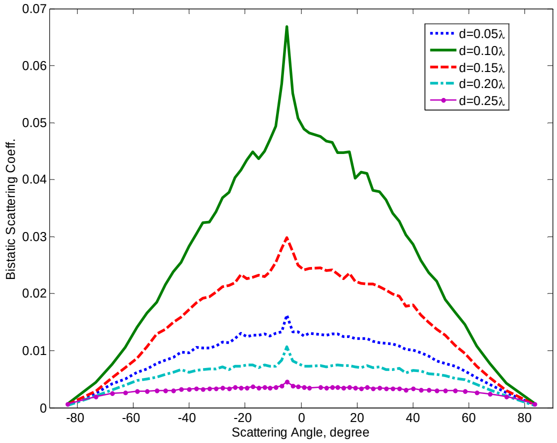

(a)

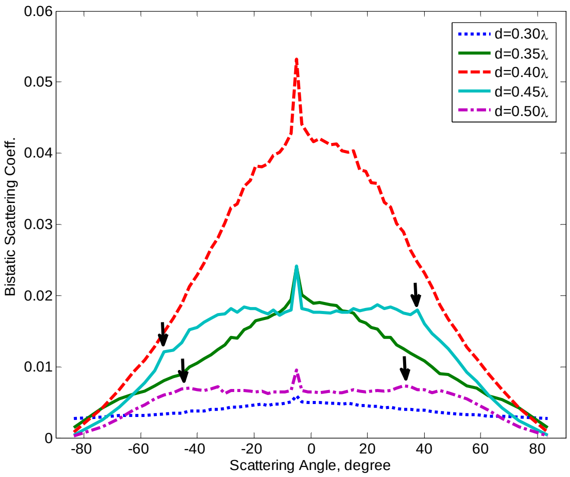

(b)

Fig. 4.6: (a) Bistatic scattering from dielectric coated silver with rough interfaces for different layer thicknesses from d=0.05λ to d=0.25λ for VV polarization (TM). In (b), bistatic scattering from dielectric coated silver with rough interfaces for different layer thicknesses from d=0.30λ to d=0.50λ for VV polarization (TM). The appearance of satellite peaks are evident for d=0.45λ and d=0.50λ as indicated by the peak-like features.

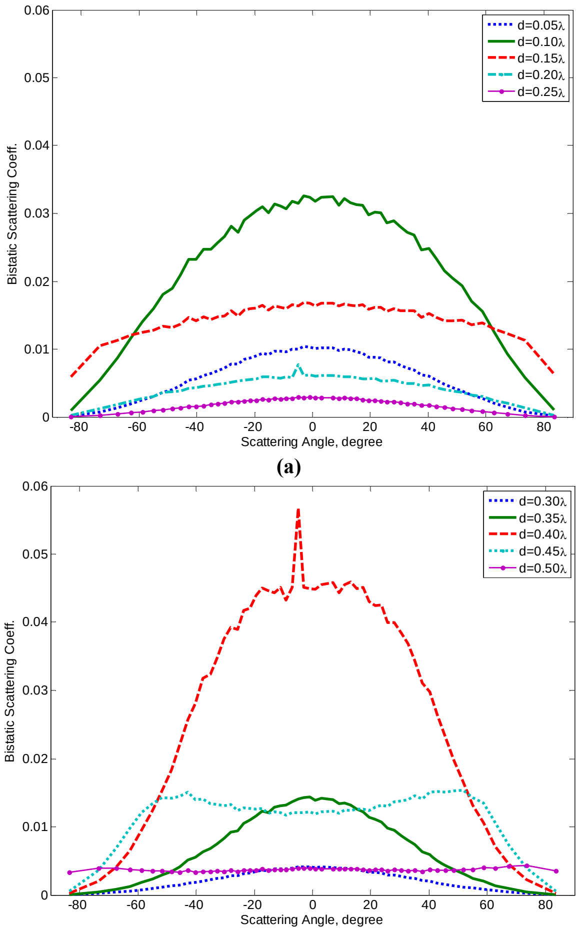

(a)

(b)

Fig. 4.7: (a) Bistatic scattering from dielectric coated silver with rough interfaces for different layer thicknesses from d=0.05λ to d=0.25λ for HH polarization (TE). In (b), bistatic scattering from dielectric coated silver with rough interfaces for different layer thicknesses from d=0.30λ to d=0.50λ for HH polarization (TE).

In Fig. 4.5, the curves of VV- and HH-polarized bistatic scattering coefficients are plotted for different root-mean-squared heights of the bottom metallic rough surface. Since all scattered waves reflect from the metallic half space and the dielectric layer is lossless, a slight increase in the root-mean-squared height of the bottom metallic interface will result in a significant increase in the bistatic scattering coefficients as evidenced by Fig. 4.5. In HH polarization (Fig. 4.5 (b)), backscattering enhancement is not present, indicating lack of TE surface waves for d =0.1λ, whih leads to absence of backscattering enhancement regardless of surface roughness. In VV polarization (Fig. 4.5 (a)), we observe that no backscattering enhancement occurs in the case of a flat metal. Surface roughness is a critical mechanism for the strength of backscattering enhancement. When the surface geometry is irregular, surface plasmon modes are converted back into volume electromagnetic waves, which propagate away from the surface through the mechanism of surface roughness. Surface plasmon waves are slow waves since they propagate along the interface while staying tightly bound to the surface. When the interface is rough, surface plasmon waves no longer stay tightly bound to the interface and begin coupling into propagating waves. The slow-wave nature of surface plasmon propagation effectively enhances surface scattering and therefore the effect of backscattering enhancement becomes more pronounced as surface roughness increases. Moreover, the angular width of the enhanced backscattered peak increases as the bottom metallic interface becomes rougher and the enhancement-to-background ratio remains roughly constant (~1.4). In [43], it is explained that this broadening is a direct consequence of the multiple scattering effect and the broadening of surface plasmon resonance which is either due to an increase in ohmic losses in the metal or to an increase in wave dissipation (also known as radiative damping) induced by higher coupling to other surface plasmon modes and to propagating modes when roughness increases. In other words, the broadening is attributed to an increased efficiency with which the roughness of rough surfaces scatters surface plasmon modes into propagating waves and into other surface plasmon modes.

In Figs. 4.6 and 4.7, the curves of VV- and HH-polarized bistatic scattering coefficients parametrized with different layer thicknesses from d = $0.05\lambda_o$ to d = $0.50\lambda_o$ are shown. For both polarizations, the enhancement initially increases with layer thickness from d=$0.05\lambda_o$ to d=$0.10\lambda_o$ but then decreases from d=$0.10\lambda_o$ to d=$0.25\lambda_o$. We note that VV-polarized surface waves give rise to backscattering enhancement for all d's whereas HH-polarized surface waves only lead to backscattering enhancement for d = $0.2\lambda_o$ and $0.4\lambda_o$ in the range studied. This suggests VV- (TM) and HH-polarized (TE) surface waves have different mode conversion efficiencies with TM surface waves coupling into propagating waves more efficiently than TE surface waves. Fig. 4.6 (b) also indicates the locations of satellite peaks for d= $0.45\lambda_o$ and d=$0.50\lambda_o$. From Table 4.1 (a), the locations of satellite peaks are given as follows: $\theta_s^+ = 38.73^o$ and $\theta_s^- = -53.13^o$ for d= $0.45\lambda_o$, $\theta_s^+ = 32.20^o$ and $\theta_s^- = -45.01^o$ for d=$0.50\lambda_o$. In Fig. 4.6 (b), clear peak-like features can be observed at 37.6^o and -52^o for d=$0.45\lambda_o$, which agree very well with the theoretical predictions in Table 4.1 (a). These features are manifestations of satellite peaks. For d=$0.50\lambda_o$, small hump-like features present at -45^o and 32.7^o also coincide with the theoretical locations of satellite peaks. For $0.30\lambda_o$ <d<$0.40\lambda_o$, the theoretical locations of satellite peaks are relatively near the grazing angles. The contribution due to single or multiple scattering processes is more prominent around the backscattering direction with the use of Gaussian surface spectrum. Therefore, with a significantly diminished effect of multiple scattering processes when the scattering angle is far away from the backscattering direction, no satellite peaks are observed for $0.30\lambda_o$ <d<$0.40\lambda_o$ in VV polarization.

To clearly demonstrate the appearance of satellite peaks, bistatic scattering coefficients of both VV and HH polarizations are plotted for d=$0.60\lambda_o$ in Fig. 4.8. At -5^o, pronounced enhanced backscattered peak is present for TM polarization whereas only a small backscattering enhancement effect is observed for TE polarization. Two satellite peaks are clearly evident at $+21.5^o$ and -32.7^o for TM polarization. They are in good agreement with the theoretical locations indicated in Table 4.1 (b) which are $\theta_s^+ = 18.6^\circ$ and $\theta_s^- = -29.5^\circ$. For TE polarization, we are unable to uniquely identify the location of satellite peaks. This again reflects the fact that TM surface waves are more susceptible to multiple scattering processes which induce the appearance of satellite peaks than TE surface waves through surface roughness. Gaussian surface roughness spectrum typically results in satellite peaks with extremely narrow-width peaks (~1-2°) and small peak to background ratios because it does not couple surface plasmon waves into propagating waves as effectively as other power spectra such as West and O'Donnell spectrum [88, 89].

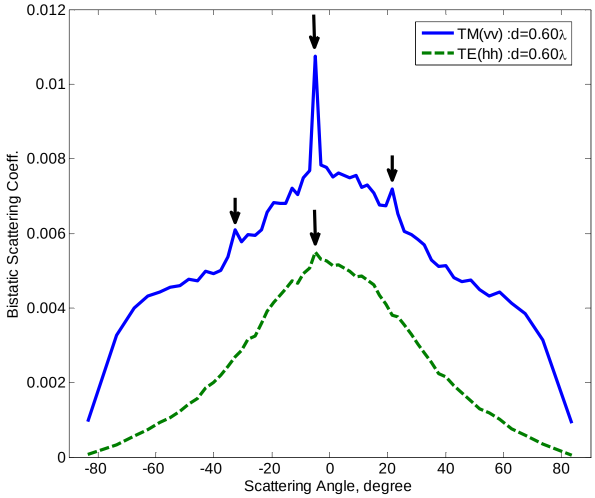

Fig. 4.8: Bistatic scattering from dielectric coated silver with rough interfaces for different layer thicknesses for d=0.6λ for VV polarization (TM) and HH polarization (TE)

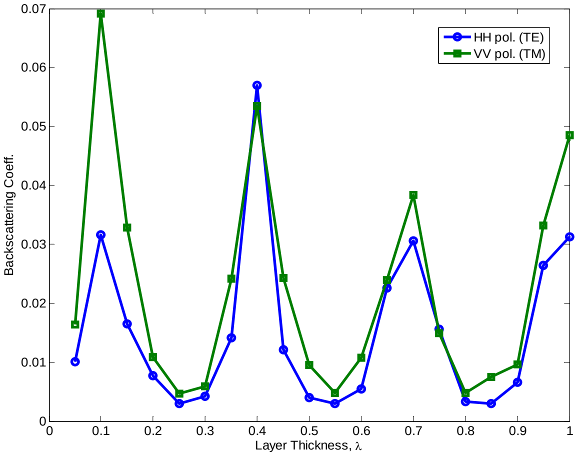

Fig. 4.9: Backscattering coefficient is plotted against layer thickness from d=0.05λ to d=0.60λ for both HH and VV polarizations. The periodic fluctuation is due to the interference effect of layered media and the period is $\lambda_1/2$ where λ_1 is the medium wavelength in the dielectric region.

In Fig. 4.9, both VV- and HH-polarized backscattering coefficients are plotted against layer thickness from d=0.05λ_o to d=1.00λ_o and clearly exhibits periodic oscillations with a period of $\lambda_1/2$ where λ_1 is half of the medium wavelength in the dielectric region. More specifically, it exhibits minima for thickness obeying

$$d = \frac{\lambda(2m+2)}{4\sqrt{\mathrm{Re}\{\varepsilon_1\}}} = \frac{\lambda_1}{2}(m+1) \tag{4.19}$$

and maxima for thickness obeying

$$d = \frac{\lambda(2m+1)}{4\sqrt{\mathrm{Re}\{\varepsilon_1\}}} = \frac{\lambda_1}{2}(m+\frac{1}{2}) \tag{4.20}$$

where m = 0, 1, 2, 3, … The periodic behavior is due to the constructive interference effect of layered media. For VV polarization from d=0.05λ_o to d=0.25λ_o, the amplitude fluctuation of the backscattering coefficient is the greatest (~9 dB). This large amplitude variation is attributed to the surface plasmon resonance effect. For HH polarization, however, the amplitude fluctuation for a very thin slab case with d varying from 0.05λ_o to 0.25λ_o is considerably smaller than that of VV polarization. This is due to a lack of HH-polarized surface plasom waves when d < 0.15λ_o. When d > 0.25λ_o, it is observed that backscattering coefficients of VV polarization tend to be larger than that of HH polarization. This reconfirms the fact that the effect of surface plasmon resonance is more prominent in VV polarization than in HH polarization. These features are useful for designing enhanced coupling efficiency from layered media. Fig. 4.9 also shows that backscattering enhancement is very sensitive to layer thickness even if it is below the half wavelength diffraction limit. Surface plasmon waves are capable of capturing very fine features of a target because evanescent waves contain information regarding sub-wavelength characteristics. Hence, backscattering enhancement holds promise in the retrieval of sub-wavelength layer thickness and hence super-resolution. Finally, it is also worth noting that 2D formulation does not account for cross-polarized fields, which would allow enhancement to be observable in both HV and VH polarizations.

4.5 Chapter Conclusion

An accurate solution to backscattering enhancement from multilayer rough interfaces based on EBCM/SMM is presented, which includes all orders of scattering. The multilayer rough surface interactions are accounted for by applying the generalized scattering matrix technique. The criteria for backscattering enhancement based on this method are also discussed. First, the consideration of backscattering propagating Floquet modes must be factored in the selection of L, the surface period. Second, the total number of Floquet modes must be chosen to be greater than the minimum total number of Floquet modes derived based on surface plasmon resonance criterion. In numerical simulation, the scattering from a dielectric coated silver rough surface is considered. It is observed that the enhanced backscattered peak disappears as the incidence angle moves towards the grazing angle. In addition, backscattering enhancement requires the rough surface geometry for coupling surface plasmon waves into radiated energy. Numerical results are validated against those based on MoM and it is observed that MoM gives poorer results for VV than for HH due to the use of a single coarse grid. Numerical analysis of backscattering enhancement due to surface plasmon resonance based on MoM may call for high computational cost due to the need for a dense grid.

In numerical simulations with EBCM/SMM, it is demonstrated that the angular width of the enhanced backscattered peak increases as the metallic interface becomes rougher. Furthermore, TM surface waves couple into propagating waves through the mechanism of roughness more efficiently than TE surface waves. The appearance of satellite peaks can be demonstrated when multiple guided surface waves are supported by the structure for TM polarization. The amplitude of enhanced backscattered peaks shows a great deal of sensitivity to layer thickness and it can be very useful in the retrieval of the thickness of a very thin layer well below the diffraction limit. Finally, the proposed numerical method accounts for all orders of scattering and provides rigorous solutions for backscattering enhancement and satellite peaks.

This proposed approach can easily be generalized to handle N-layer structures and is especially well suited for sensitivity analysis since it is capable of evaluating the effect of a change in one layer without repeating the entire computation.

CHAPTER 5

Scattering from Buried Objects in Layered Rough Surfaces and Mode Matching Technique

Using the formulation of EBCM/SMM in Chapter 3, we propose a technique which incorporates a buried object in layered rough surfaces by employing the T-matrix method. A T-matrix relates the incident field to the scattered field of an object, both of which are expanded in terms of cylindrical harmonics in two dimensions. To perform mode matching between layered rough surfaces and a buried object, the cylindrical-to-spatial harmonics (plane wave) transformation is applied to the T-matrix of a buried object. This harmonic transformation is derived through the use of the recurrence formula and Fourier integral representation for Hankel functions. When the T-matrix of a buried circular cylinder is transformed into the reflection/transmission matrices, these matrices can then be cascaded with those of layered rough surfaces to account for the electromagnetic interaction between a buried cylinder and multiple rough interfaces. In this chapter, the derivation of mode matching technique for a buried cylinder and an interface is first presented. Then, the validation of this proposed hybrid method is conducted by comparing the numerical results to the analytical ones. Subsequently, numerical studies for scattering from a buried cylinder in layered rough surfaces are performed for sensitivity analysis. Then, this proposed method is generalized to handle scattering from a cluster of cylinders embedded in layered rough surfaces through the application of the recursive T-matrix method. This topic of research is important in radar community which deals with volume scattering from sea ice, snow, and root-zone soil moisture. At the end of this chapter, validation studies and numerical results for scattering from discrete random media in layered rough surfaces are presented and discussed.

5.1 Mode Matching Technique and its Formulation

Following the development of the plane wave solution for scattering from layered rough surfaces through matrix cascading processes presented in Chapter 2 and 3, the next goal is to devise a method capable of incorporating a buried object into a rough layer. The scattered field of a buried cylinder is first cast in terms of plane waves and then the scattering matrix technique is employed to account for wave interactions between rough surfaces and the buried cylinder. This section discusses how to compute the plane wave solution to scattering by a cylinder. The formulation of the scattering from a periodic array of cylinders is first discussed briefly [66, 67, 69] and then the approximation with an infinite separation distance between cylinders is incorporated into the formulation in order to remove coupling between periodic cylinders. The technique for solving the scattering from a periodic array of cylinders is based on the T-matrix and Lattice sum approach.

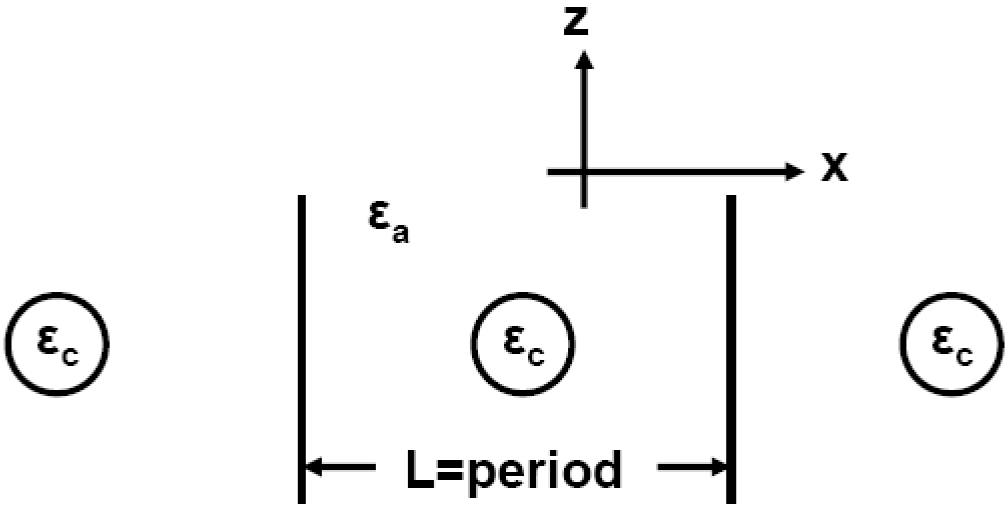

Fig. 5.1: The geometry of a periodic array of cylinders

The geometry of a periodic array of cylinders is illustrated in Fig. 5.1. The cylinders are situated in a background medium with dielectric constant ε_a. They are infinitely long along the y-direction and parallel to each other. For the cylinder problem, the polarization of an incident wave is defined as follows: a TM wave with E_y as the transverse component and a TE wave with H_y as the transverse component. In the following formulation, the transverse field component is expressed in terms of the wave function, ψ. In vector representation, the incident plane wave is expressed in cylindrical coordinate system (ρ_o, φ_o) centered at the origin of coordinate *O*.

$$\psi^i(x,y) = \Phi_{J,0}^T \cdot p_o \tag{5.1}$$

$$\Phi_{J,0} = [J_m(k_a\rho_o)e^{im\varphi_o}] \tag{5.2}$$

$$p_o = [i^m e^{im\alpha_o}] \;\; (m = 0, \pm 1, \pm 2, ...) \tag{5.3}$$

$\Phi_{J,0}$ and p_o are row vectors. The superscript T denotes the transpose of a matrix. K_o is the wavenumber of the background medium in which the array of cylinders is placed. The scattered field can be represented in terms of the local cylindrical coordinates (ρ_l, φ_l) with the center of *l*-th scatterer as the origin of coordinates:

$$\psi^s(x,y) = \sum_{l=-\infty}^{\infty} \Phi_{H,l}^T \cdot q_l^s \tag{5.4}$$

$$\Phi_{H,l} = [H_m^{(1)}(k_a\rho_l)e^{im\phi_l}] \tag{5.5}$$

$$\rho_l = \sqrt{(x-lL)^2 + y^2}\,, \cos\phi_l = \frac{x-lL}{\rho_l} \tag{5.6}$$

where q_l^s is the unknown amplitude vector of the wave scattered by the *l*-th circular cylinder. Applying Floquet theorem to the scattered field results in

$$\psi^s(x,y) = \sum_{l=-\infty}^{\infty} e^{ik_{xo}lL}\Phi_{H,l}^T \cdot q_o^s \tag{5.7}$$

where $k_{xa} = k_a \cos\alpha_o$ and α_o is the angle of incidence with respect to the x axis and α_o is the compliment of θ_i as shown in Fig. 3.1. The Floquet theorem reduces the problem to deriving the unknown amplitude, q_o^s.

To calculate q_o^s, the total field outside the cylinder is decomposed into the incident and scattered fields:

$$\psi(x,y) = \Phi_{J,l}^T \cdot p_o^s + \sum_{l=-\infty}^{\infty} e^{ik_{xo}lL} \Phi_{H,l}^T \cdot q_o^s \tag{5.8}$$

After applying the addition theorem to the Hankel function, $H_m^{(1)}(k_o\rho_l)e^{im\phi_l}$, the basis vector $\Phi_{H,l}(l \neq 0)$ is transformed to $\Phi_{J,0}$. After some rearrangement of (5.8), the following expression can be obtained:

$$\psi(x,y) = \Phi_{J,l}^T \cdot (p_o^s + \overline{L} \cdot q_o^s) + \Phi_{H,l}^T \cdot q_o^s \tag{5.9}$$

where

$$\overline{L} = [L_{mn}], \;\; L_{mn} = S_{n-m}(k_a L, k_{xa} L) \tag{5.10}$$

$$S_{n-m}(k_a L, k_{xa} L) = \sum_{l=1}^{\infty} H_{n-m}^{(1)}(k_a lL)[e^{ilk_{xa}L} + (-1)^{n-m} e^{-ilk_{xa}L}] \tag{5.11}$$

$S_{n-m}(k_o L, k_{xo} L)$ is called the lattice sum matrix of order (*n-m*). The above equation indicates that at the center of the array, the amplitude q_o^s of the scattered field is equal to the amplitude of scattered field when a plane wave with an equivalent amplitude vector $p_o + \overline{L} \cdot q_o^s$ is incident upon this cylinder. Through the application of T-matrix, q_o^s and p_o can be related as follows:

$$q_o^s = \overline{\overline{T}} \cdot p_o \tag{5.12}$$

$$\overline{\overline{T}} = (I - T \cdot \overline{L})^{-1} \cdot T \tag{5.13}$$

where *T* denotes the T-matrix of a single cylinder. Substituting q_o^s into (5.9) solves the scattering problem for a periodic array of cylinders. If we let the separation distance between cylinders approach infinity in the lattice-sum matrix which corresponds to the coupling between periodic cylinders, $[L]$ will become a zero matrix and

$$\overline{\overline{T}} = T \tag{5.14}$$

To perform mode matching between rough surfaces and cylinders, the scattered waves from cylindrical objects are decomposed into reflected and transmitted components. Expression (5.9) is cast in terms of spatial harmonics or Floquet modes in the periodic structure. By using the recursive relations for Hankel functions and an integral representation of the zeroth-order Hankel function, the scattered waves in the regions z > a and z < -a where a is the cylinder radius can be defined in terms of reflected and transmitted waves, which are expressed in terms of Floquet modes. The results are given as follows:

$$\Psi_l^r = r_{l0} e_l^+(x,z) \tag{5.15}$$

$$\Psi_l^T = f_{l0} e_l^-(x,z) \tag{5.16}$$

where

$$r_{l0} = u_l^T \cdot \overline{\overline{T}} \cdot p_0 \tag{5.17}$$

$$f_{l0} = \delta_{l0} + v_l^T \cdot \overline{\overline{T}} \cdot p_0 \tag{5.18}$$

$$u_l = \frac{2(-i)^m}{k_a L} \frac{e^{im\alpha_l}}{\sin\alpha_l}, \; v_l = \frac{2(-i)^m}{k_a L} \frac{e^{-im\alpha_l}}{\sin\alpha_l} \tag{5.19}$$

$$e_l^{\pm}(x,z) = e^{i(k_{xl}x \pm k_{zl}z)} \tag{5.20}$$

$$k_{xl} = k_a \cos\alpha_o + \frac{2l\pi}{L}, \; k_{zl} = \sqrt{k_a^2 - k_{xl}^2} \tag{5.21}$$

$$\cos\alpha_l = \frac{k_{xl}}{k_a}, \mathrm{Im}\{\sin\alpha_l\} \geq 0 \tag{5.22}$$

The quantity, δ_{l0}, describes the contribution of the incident wave in the transmitted wave region. In addition, r_{l0} and f_{l0} expresses the reflection and transmission coefficients for the *l*-th spatial harmonic from the incident wave of the zeroth (*l*=0) spatial harmonic. The separation distance, L, determines the scattering directions of Floquet modes from a periodic array of cylinders. The value of L is chosen to be the same as the period of the rough surface for proper mode matching between rough surfaces and cylinders.

5.2 Scattering Matrices of a Buried Cylinder

Reflection and transmission matrices of a periodic array of cylinders have been derived in [67, 69]. When the separation distance between cylinders is large and the interaction between cylinders becomes negligible, the scattering pattern of a periodic array of cylinders essentially resembles that of a single cylinder. We take advantage of this fact to effectively embed a cylinder in the layered rough surface geometry. The motivation for this approach mainly lies in the fast and efficient mode matching between a buried cylinder and rough surfaces. One of the key requirements in the application of scattering matrix technique is that scattering angles at which scattered waves propagate away from rough surfaces must be consistent with those from a buried cylinder. The conventional construction of the reflection and transmission matrices of a single cylinder requires the acquisition of the scattering patterns of a cylinder from all scattering angles. This can be accomplished by sweeping over all the scattering angles one angle at a time, which could be an extremely time-consuming process. By starting from a periodic array of cylinders and allowing the period to approach a large quantity, not only the construction of reflection and transmission matrices of a single cylinder becomes a fast and efficient one-step process without sweeping over all scattering angles, but also the solution of scattered field is expressed in terms of an infinite sum of Floquet modes spaced a distance of $\frac{2\pi n}{L}$ apart. Therefore, the requirement of mode matching between rough surfaces and a buried cylinder is automatically satisfied when the period of rough surfaces is set equal to that of the cylinders.

For a plane wave incident at angle θ_i with respect to the z axis, the direction of the m$^{\text{th}}$ Floquet mode is defined by the scattering angle ϕ_m such that

$$\sin\phi_m = \frac{m\lambda}{L} + \sin\theta_i \qquad (5.23)$$

where L is the spacing between cylinders and λ is the wavelength. In section 5.1, the scattered field of a periodic array of cylinders can be then transformed back into Floquet modes in the (x,z) coordinate system with an infinite sum of space harmonics with $k_{lx} = k_{xi} + \frac{2\pi l}{L}$ ($l = 0,\pm1,\pm2,...$). This calculation results in the column vectors with reflection and transmission elements $r_{l,n}$ and $t_{l,n}$, which relate the amplitude of the reflected and transmitted l^{th} Floquet mode to that of the incident n^{th} Floquet mode. These column vectors are arranged in a matrix to describe the reflection and transmission under the incidence of a sequence of Floquet modes with $k_{nx} = k_{xi} + \frac{2\pi n}{L}$ ($n = 0,\pm1,\pm2,...$). The reflection matrix $[R_c]$ and the transmission matrix $[T_c]$ of a periodic array of cylinders are given in (5.24)-(5.30)

$$\left[U\right] = \left[u_{mn}\right] = \frac{2(-i)^n}{k_a L \cos(\phi_m)} e^{in(\phi_n)} \tag{5.24}$$

$$\left[V\right] = \left[v_{mn}\right] = \frac{2(-i)^n}{k_a L \cos(\phi_m)} e^{-in(\phi_n)} \tag{5.25}$$

$$\left[P\right] = \left[p_{mn}\right] = i^m e^{in(\phi_n)} \tag{5.26}$$

$$[T^{TE}] = diag\{\frac{n_c J_m(k_c r) J_m^{'}(k_a r) - n_a J_m^{'}(k_c r) J_m(k_a r)}{n_a J_m^{'}(k_c r) H_m^{(1)}(k_a r) - n_c J_m(k_c r) H_m^{(1)'}(k_a r)}\} \tag{5.27}$$

$$[T^{TM}] = diag\{\frac{n_a J_m(k_c r) J_m^{'}(k_a r) - n_c J_m^{'}(k_c r) J_m(k_a r)}{n_c J_m^{'}(k_c r) H_m^{(1)}(k_a r) - n_a J_m(k_c r) H_m^{(1)'}(k_a r)}\} \tag{5.28}$$

$$[R_{sc}] = [U][T][P] \tag{5.29}$$

$$[T_{sc}] = [I] + [V][T][P] \tag{5.30}$$

where θ_i and ϕ_m are the incidence and Floquet mode angles, L is the spatial period of the cylinders, n_c and n_a are the indices of refraction of the homogenous cylinders and the surrounding material, k_c , k_a , and r are the wavenumbers of the cylinders and of the surrounding homogeneous material and the radius of the cylinder, respectively. The meaning of each matrix provided above is given in Table 5.1.

Table 5.1
Description of key matrices

$[U]$ and $[V]$	matrices which transform the mth order cylindrical wave into the upgoing and downgoing plane waves of the lth Floquet mode, respectively.
$[P]$	a matrix which transforms the downgoing nth Floquet mode into the mth order cylindrical wave
$[T]$	the T-matrix of the isolated single cylinder located at the origin
$[I]$	an identity matrix

Note that the period L is still present in equations (5.29) and (5.30) and it determines the number of Floquet modes considered in the scattering process. Since in reality scattering by a cylinder involves a continuous angular spectrum of plane waves, equations (5.29) and (5.30) are only valid when the period is large (i.e., L > 40λ) in order to ensure sufficiently many Floquet modes are included in numerical simulations. Finally, it is important to note that the resulting reflection and transmission matrices of a single cylinder, $[R_{sc}]$ and $[T_{sc}]$ are reciprocal (i.e., $R_{sc,ij} = R_{sc,ji}$ and $T_{sc,ij} = T_{sc,ji}$) where the subscript sc denotes a single cylinder.

5.3 Comparison of Results and Validation for Scattering from a Buried Cylinder below a Flat/Periodic Surface

The validation of the solution is performed by verifying the limiting case of the scattering from a cylinder beneath a rough surface as discussed in [90]. In [90], an analytical solution for a buried cylinder beneath a slightly rough surface is derived. The solution is obtained by employing the spectral, plane-wave representation of the fields and adding the successive reflections from the rough half-space boundary and the scattered fields from the cylinder. All of the multiple bounces are accounted for in the solution. First-order reflection and transmission coefficients from SPM are used for the rough surface scattering. The first test case considered in this paper is a buried cylinder beneath a flat surface. The second test case is a buried cylinder beneath a sinusoidal surface with a surface profile described by $f(x) = 0.0064\cos(\frac{2\pi}{0.4}x)$ used in [90]. The simulation parameters used together with a flat or sinusoidal surface are given in Table 5.2.

Table 5.2
The simulation parameters for scattering from a cylinder beneath a flat/periodic surface

ε_1	ε_c	d_1	a	θ_i	L
4+i0.01	2.25	1.3λ	0.16λ	45^o	40λ

In Fig. 5.2 and Fig. 5.3, the simulated results are compared against the SPM solution. They show very good agreement. In vv polarization, there is a small discrepancy in the forward direction between the simulated result and the SPM solution [90].

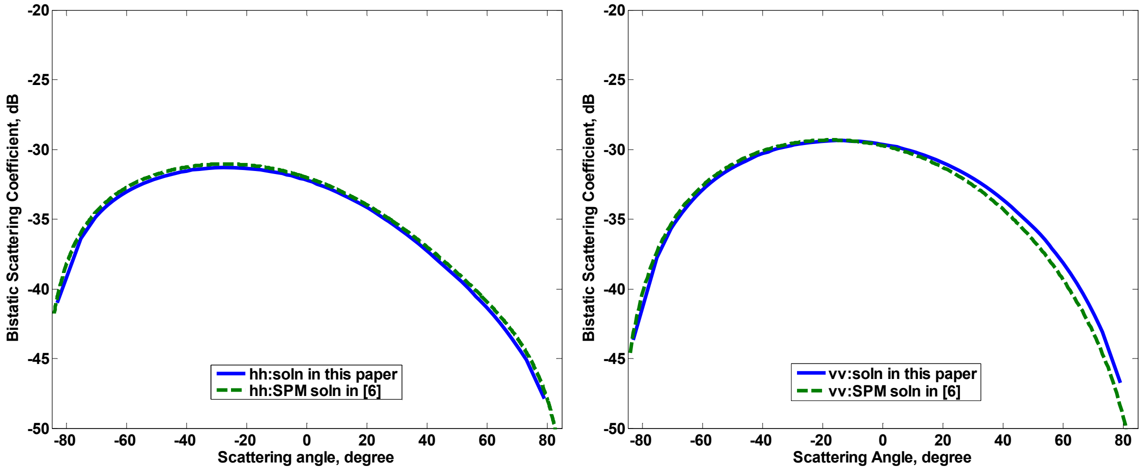

Fig. 5.2: Bistatic scattering coefficient for the scattering from a cylinder beneath a flat surface: the comparison of the proposed solution to that in the SPM solution in [90]

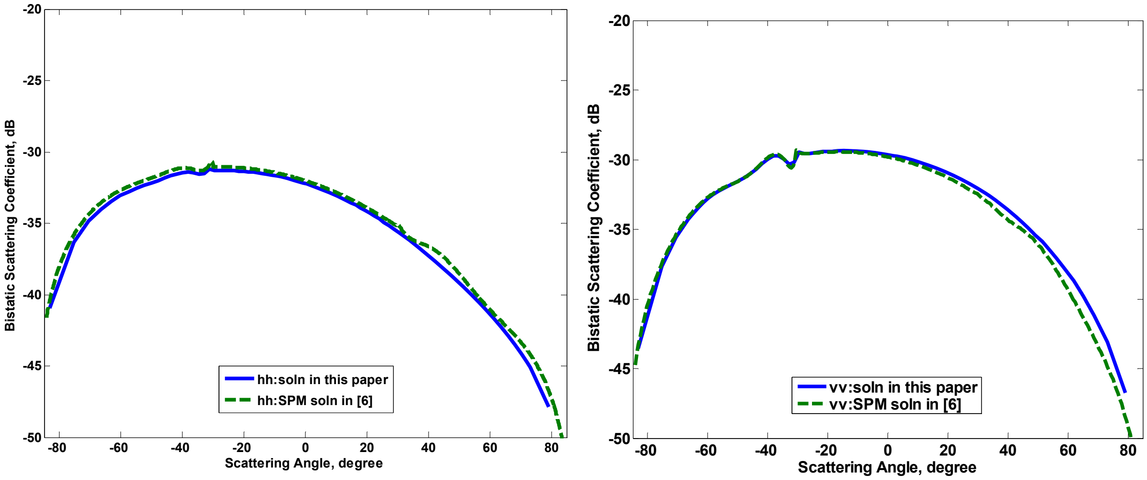

Fig. 5.3: Bistatic scattering coefficient for the scattering from a cylinder beneath a sinusoidal surface described by *f*(*x*)=0.0064cos(2π/0.4x) : the comparison of the proposed solution to the SPM solution in [90]

5.4 Numerical Results for Scattering from a Buried Cylinder in Layered Rough Surfaces

First, scattering from a buried cylinder beneath a single rough surface is simulated. The simulation parameters used in [90] are given in Table 5.3.

Table 5.3
The simulation parameters for scattering from a cylinder beneath a rough surface

ε_1	ε_c	h_f	l_f	d_1	a	θ_i	L
4+i0.01	2.25	0.01λ	0.2λ	1.3λ	0.16λ	60^o	40λ

The number of Floquet modes used is 161. This set of simulation parameters will result in 80 propagating modes in region 0 and 126 propagating modes in region 1, ensuring enough interactions between the buried cylinder and the rough surface are taken into consideration. The incoherent bistatic scattering coefficient is obtained using the Monte Carlo simulation with 300 independent samples. The simulated results of bistatic scattering coefficients parameterized by different correlation lengths are provided in Fig. 5.4. The distinctions between the scattering pattern of a buried cylinder beneath a rough surface and that beneath a flat surface are pronounced. The correlation length of a rough surface modifies the angular shape of a scattering pattern instead of significantly increasing the scattering coefficient.

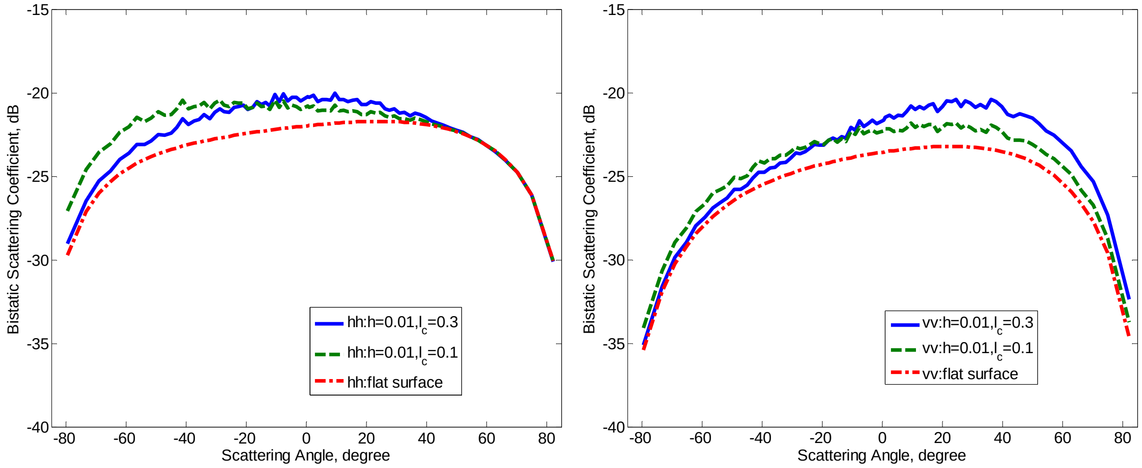

Fig. 5.4: Bistatic scattering coefficient for scattering from a cylinder beneath a rough surface for different values of correlation length

The numerical simulation of scattering from a cylinder buried in layered rough surfaces is then performed. The geometry is given in Fig. 5.5. The simulation parameters given in Table 5.4 are used.

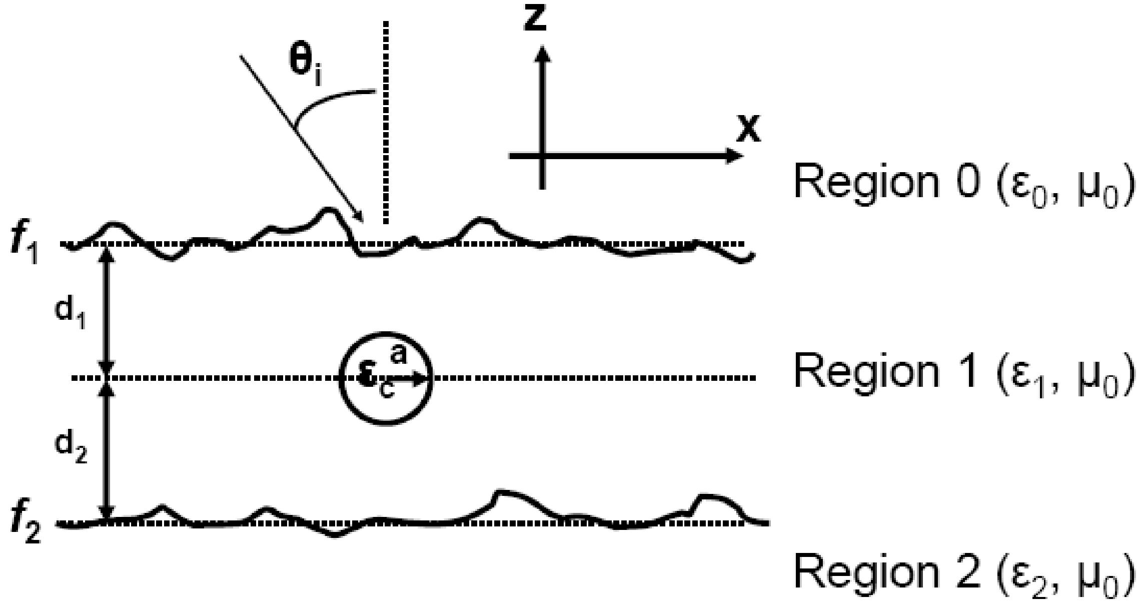

Fig. 5.5: Scattering from multilayer rough surfaces bounding a dielectric cylinder

Table 5.4
The simulation parameters for scattering from a cylinder buried in layered rough surfaces

ε_1	ε_2	ε_c	a	kh_f	kl_f	kh_b	kl_b	d_1	d_2	θ_i	L	N
4+i0.01	7	2.25	0.16λ	0.2	1.0	0.1	1.0	0.7λ	0.5λ	45^o	40λ	300

The number of Floquet modes used in the simulation is 161. The choice of 161 Floquet modes ensures enough propagating and evanescent waves are considered in the numerical simulation. In addition, the code is written in Matlab and the simulations are performed on a PC with Pentium-4 2-GHz processor and 1 GB RAM. It takes approximately thirty seconds for each realization.

First, to examine the effect that the cylinder has on the scattering pattern relative to the rough surface scattering, the bistatic scattering coefficients parameterized by various radii of a buried cylinder are provided in Fig. 5.6.

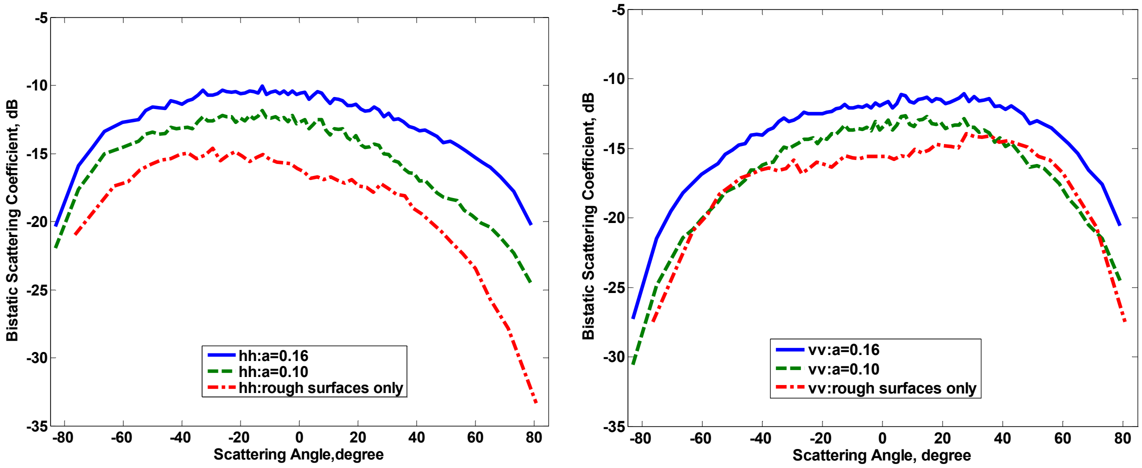

Fig. 5.6: Bistatic scattering coefficient for scattering from a cylinder beneath a rough surface for different values of the cylinder radius

When the radius of a cylinder shrinks to zero, only the effect of rough surface scattering is present in the total scattering pattern. It is observed in Fig. 5.6 that, in this example, the bistatic scattering coefficients in HH polarization shows greater sensitivity to the change in the size of a buried cylinder.

To investigate the scattering patterns due to the subsurface characteristics in the problem of a cylinder buried in layered rough surfaces and to clarify the sensitivity of bistatic scattering coefficient, several parameters are varied while others are kept fixed. The simulations results are given in Fig. 5.7 – Fig. 5.10.

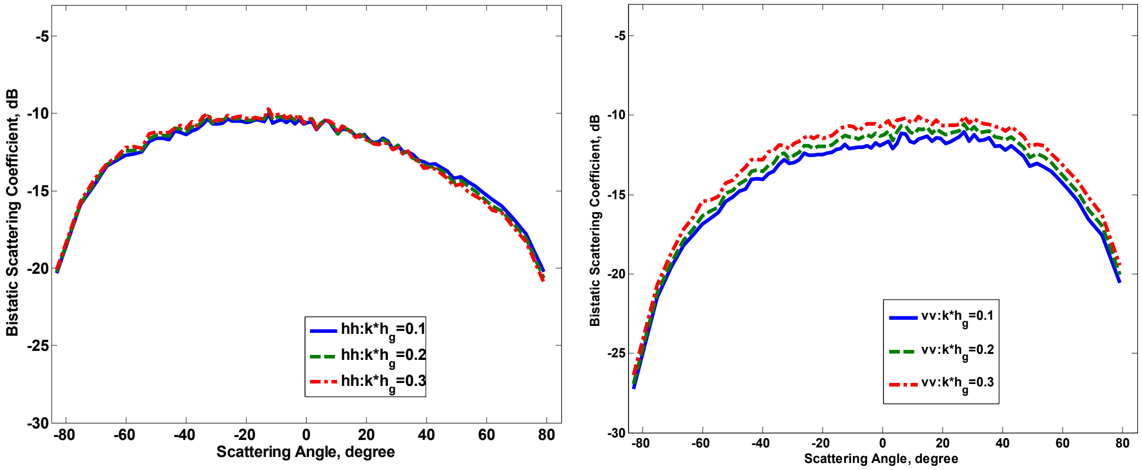

Fig. 5.7: Bistatic scattering coefficient for scattering from a buried cylinder buried in layered rough surfaces for different values of the subsurface root-mean-squared height, kh$_g$

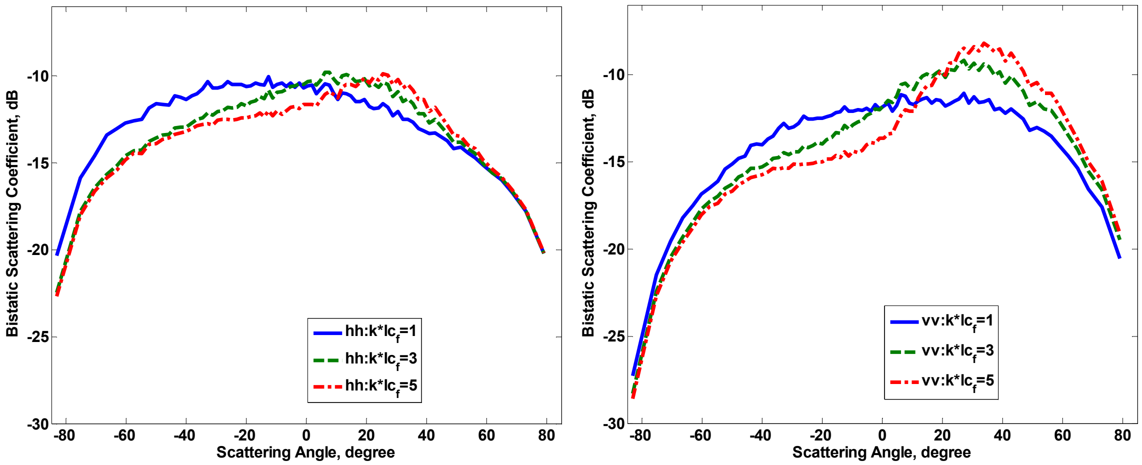

Fig. 5.8: Bistatic scattering coefficient for scattering from a buried cylinder buried in layered rough surface for different values of the correlation length of the top rough interface, klc$_f$

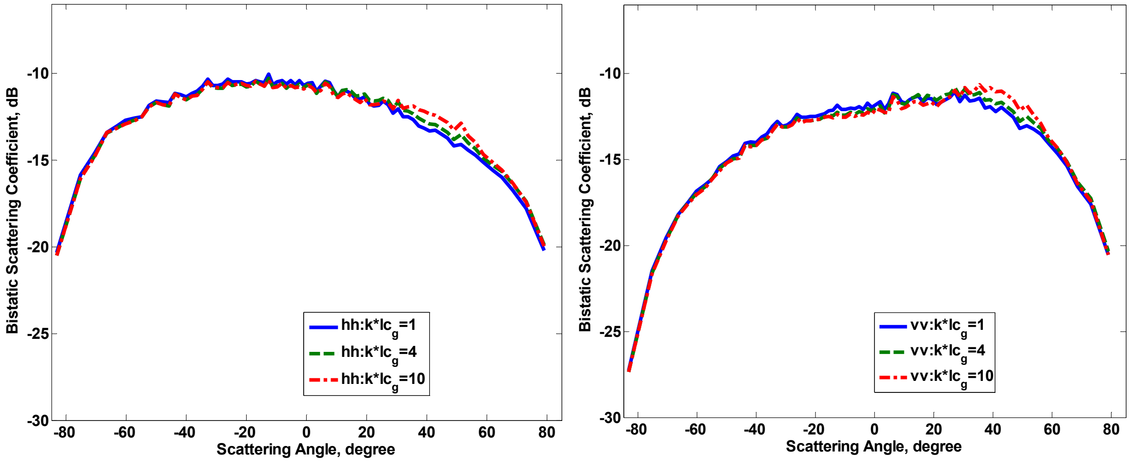

Fig. 5.9: Bistatic scattering coefficient for scattering from a buried cylinder buried in layered rough surfaces for different values of the correlation length of the bottom rough interface, klc$_g$

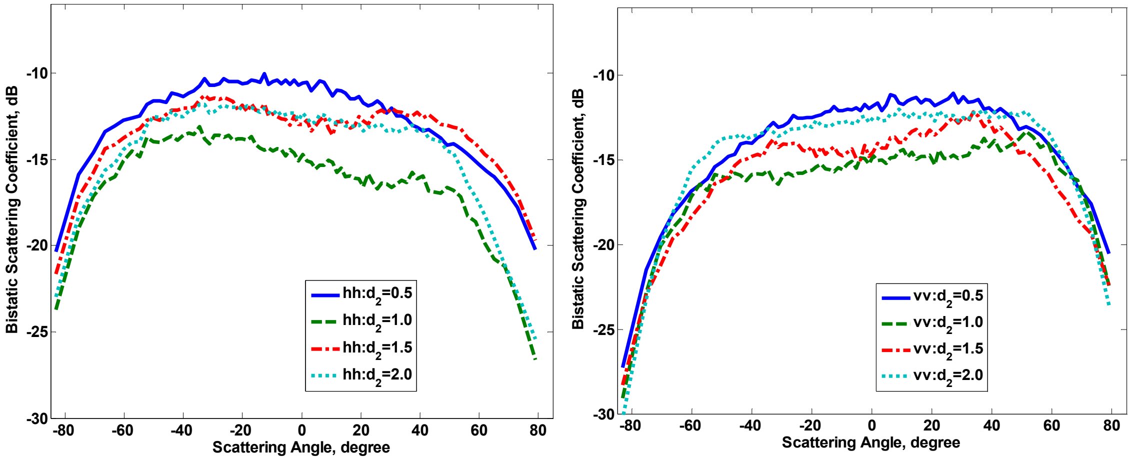

Fig. 5.10: Bistatic scattering coefficient for scattering from a buried cylinder buried in layered rough surfaces for different values of the layer thickness between the center of the cylinder and the mean value of the bottom rough interface, d$_2$

From Fig. 5.7 and Fig. 5.9, we observe that bistatic scattering coefficients in HH polarization are not very sensitive to either the root-mean-squared height or the correlation length of the bottom rough interface in a small roughness regime. In Fig. 5.8, the correlation length of the top rough interface modifies the angular dependence of bistatic scattering coefficients significantly. Therefore, in this example, it may suffice to model the bottom interface as a flat or slightly rough interface for HH polarization. The bistatic scattering coefficients in VV polarization, however, show more sensitivity to the root-mean-squared height of the bottom rough interface. A more significant change in the bistatic scattering coefficient in VV polarization is anticipated in moderate and large roughness regimes. Fig. 5.10 indicates that the bistatic scattering coefficients in both polarizations are strongly dependent on how far the cylindrical object is away from the bottom interface, d_2. The scattering behaviors are significantly altered when d_2 is changed.

5.5 Introduction to Volume Scattering in Layered Rough Surfaces

Building on the mode matching formulation for a buried cylinder and rough surfaces, we extend the T-matrix technique to analyze scattering from a cluster of cylinders embedded in layered rough surfaces. This area of research finds applications in volume scattering from sea ice or snow for depth retrieval of layered snow-covered ice, remote sensing of the root zone in vegetation canopies, forests or cultivated fields, and remore sensing of subsurface ground properties. These natural targets in remote sensing can usually be modeled as random media embedded in multi-layer rough surfaces where the characteristic parameters of these targets include the dielectric properties, scatterer size, shape, orientation, layer thickness, and roughness of the interface boundaries. The application of standard full-wave approaches, such as MoM and FDTD for analyzing scattering from discrete random media in layered rough surfaces can easily result in prohibitively large data structures and is typically very time-consuming. The objective of this section is to employ the hybrid technique based on EBCM/SMM, where the aggregate T-matrix of discrete random media is computed using the recursive T-matrix (RTM) technique, and the mode matching technique is then used to coherently account for multiple scattering between the discrete structures and rough surfaces.

In studying wave propagation through random media in layered rough surfaces, the vector radiative transfer (VRT) equation has been previously applied to account for the effects of multiple scattering, absorption, and transmission in [9, 91]. The VRT theory is an incoherent approach based on the principle of energy conservation which tracks the propagation of electromagnetic intensity through scattering media. Therefore, any coherent effects, such as interference, are neglected. Various analytical approaches for analyzing the discrete random medium problem based on a number of restrictive assumptions have also been developed. The treatment of multiple scattering from isotropic point scatterers in a tenuous medium was first given by Foldy [92], also known as the effective field approximation. For dense media, a higher-order method known as the quasi-crystalline approximation (QCA) was developed [9]. Together with the knowledge of pair distribution function, QCA has been widely employed to compute the effective propagation constants. On the contrary, the recursive T-matrix method has been considered one of the most computationally efficient and numerically accurate approaches for handling multiple scattering from a dense distribution of random scatterers [64, 93]. In this section, we generalized our approach for analyzing scattering from a cluster of scatterers embedded in layered rough surfaces through the application of the recursive T-matrix algorithm.

5.6 Aggregate T-Matrix for Discrete Random Media

The idea of using the T-matrix of a single scatterer for obtaining its reflection/transmission matrices to analyze a buried target in layered rough surfaces can be further extended to the concept of an aggregate T-matrix for a cluster of scatterers, which can be computed using recursive T-matrix algorithms. The recursive T-matrix methods have been extensively used for calculating the scattered field from multiple dielectric cylinders. T matrix approach represents fields using harmonic expansion and the recursion formula aggregates the effects of multiple scattering from a collection of cylinders. Equations (5.31) – (5.32) constitute the recursive relations for K scatterers:

$$\begin{aligned}\overline{T}_{n+1(n+1)} \cdot \overline{\beta}_{n+1,0} &= [\overline{I} - \overline{T}_{n+1(1)} \cdot \sum_{i=1}^{n} \overline{\alpha}_{n+1,i} \cdot \overline{T}_{i(n)} \cdot \overline{\beta}_{i,0} \cdot \overline{\alpha}_{0,n+1}]^{-1} \\ &\cdot \overline{T}_{n+1(1)} \cdot [\overline{\beta}_{n+1,0} + \sum_{i=1}^{n} \overline{\alpha}_{n+1,i} \cdot \overline{T}_{i(n)} \cdot \overline{\beta}_{i,0}]\end{aligned} \tag{5.31}$$

$$\overline{T}_{i(n+1)} \cdot \overline{\beta}_{i,0} = \overline{T}_{i(n)} \cdot \overline{\beta}_{i,0} \cdot [\overline{I} + \overline{\alpha}_{0,n+1} \cdot \overline{T}_{n+1(n+1)} \cdot \overline{\beta}_{n+1,0}] \tag{5.32}$$

where $n = 1, 2, ..., K$, $i = 1, 2, ..., n$, $\overline{T}_{i(n)}$ is the T-matrix for the i^{th} object in the presence of n scatterers, $\overline{\beta}$ and $\overline{\alpha}$ are the translational matrices used to translate T-matrices between different reference coordinate systems. Their expressions are given as follows:

$$\overline{\beta}_{i,j}^{m,n} = J_{n-m}(k_a r_{ij}) e^{i(n-m)\phi_{ij}} \tag{5.33}$$

$$\overline{\alpha}_{i,j}^{m,n} = H_{n-m}(k_a r_{ij}) e^{i(n-m)\phi_{ij}} \tag{5.34}$$

where i and j denotes the i^{th} and j^{th} scatterers and $r_{ij} = \sqrt{(x_i - x_j)^2 + (z_i - z_j)^2}$, $\phi_{ij} = \arctan(\frac{z_i - z_j}{x_i - x_j})$.

Subsequently, an aggregate T matrix for n scatterers can be defined such that

$$\overline{\tau}_{(n)} = \sum_{i=1}^{n} \overline{\beta}_{0i} \cdot \overline{T}_{i(n)} \cdot \overline{\beta}_{i0} \tag{5.35}$$

The recursion begins from the T-matrices, $\overline{T}_{i(1)}$, of the individual scatterers. Then, the $\overline{\beta}$ and $\overline{\alpha}$ of finite orders are computed to translate the T-matrices. These translational matrices and T-matrices are truncated with finite values P and M such that residual error is below acceptable levels. The value of P represents the number of harmonics used to expand the fields at the scattering origin (i.e., $x = z = 0$) and M represents the number of harmonics used to expand the fields in the objects' local coordinate systems (i.e., the locations of individual scatterers). In other words, P is the total number of harmonics used in the translation formula and M is the total number of harmonics approximating the field around each scatterer. Therefore, the number of harmonics P and M depend on the distances of scatterers from the scattering origin and the size of scatterers. The value of P increases with increasing separation distances of the scatterers from the scattering origin and the value of M increases with the size of scatterers. The choice of scattering origin is typically made to minimize P. The computational domain of discrete random media is set up to be L (extending from x= –L/2 to x = L/2) * d (extending from z = –d/2 and z = d/2) where d is the discrete random media's layer thickness and L is the horizontal length of the random media. The quantity L is a simulation parameter which is selected to be as large as possible. (i.e.,L > 40λ). In addition, the same L is used for rough surfaces and discrete random media to ensure proper mode matching between these two distributed scatterers. The natural choice for the scattering origin is the origin of the coordinate system (x = z = 0).

Although Equations (5.31)-(5.35) provide a rigorous solution to scattering from multiple scatterers, they may give rise to convergence problems in the addition formulas of recursive T-matrix algorithm for large M when the scattering origin and the object centers are very close, as reported in [93]. Therefore, in [93], the modified recursive T-matrix algorithm was proposed to overcome the convergence problem at the expense of a slight increase in computational cost. The modified recursive T-matrix algorithm is reformulated by enforcing $\overline{\beta}_{0i}\overline{\beta}_{i0} = I$ and avoiding the use of $\alpha_{p,q} = \beta_{p,o}\alpha_{o,q}$ which is the cause of the convergence problem. Then, the recursive T-matrix relation can be rewritten as follows:

$$\begin{aligned} \overline{T}_{n+1(n+1)} \cdot \overline{\beta}_{n+1,0} &= [\overline{I} - \overline{T}_{n+1(1)} \cdot \sum_{i=1}^{n} \overline{\alpha}_{n+1,i} \cdot \overline{T}_{i(n)} \cdot \overline{\beta}_{i,0} \cdot \overline{\beta}_{0,i} \overline{\alpha}_{i,n+1}]^{-1} \\ &\cdot \overline{T}_{n+1(1)} \cdot [\overline{\beta}_{n+1,0} + \sum_{i=1}^{n} \overline{\alpha}_{n+1,i} \cdot \overline{T}_{i(n)} \cdot \overline{\beta}_{i,0}] \end{aligned} \tag{5.36}$$

$$\overline{T}_{i(n+1)} \cdot \overline{\beta}_{i,0} = \overline{T}_{i(n)} \cdot \overline{\beta}_{i,0} \cdot [\overline{I} + \overline{\beta}_{0,i} \overline{\alpha}_{i,n+1} \cdot \overline{T}_{n+1(n+1)} \cdot \overline{\beta}_{n+1,0}] \tag{5.37}$$

$$\overline{\tau}_{(n)} = \sum_{i=1}^{n} \overline{\beta}_{0i} \cdot \overline{T}_{i(n)} \cdot \overline{\beta}_{i0} \tag{5.38}$$

Both conventional and modified recursive T-matrix algorithms have been tested for solution accuracy and convergence in this dissertation. Although the scattering origin is set to be at the origin and the random scatterers are occasionally situated very close to the scattering solution, both formulations still yield convergent solutions. It is also noted that not all valid scattering origins for a given problem give rise to the convergence problem. For a given collection of scatterers, there exists scattering origins where the conventional T-matrix recursions work adequately. Therefore, for the following numerical studies, the conventional recursive T-matrix method is employed.

Upon obtaining the aggregate T matrix for a dense medium, which consists of many densely packed cylinders, the aggregate T matrix is transformed into the corresponding reflection/transmission matrices using [5.24]-[5.30]. Hence, by applying the SMM, the solution to scattering from a discrete random medium can be sought. A caveat worth pointing out is that a discrete random medium is not reciprocal. The expressions for the reciprocal reflection/transmission matrices of a discrete random medium are given by

$$[\widetilde{R}] = [V][T][Q] \tag{5.39}$$

$$[\widetilde{T}] = [I] + [U][T][Q] \tag{5.40}$$

$$\left[Q\right] = \left[q_{mn}\right] = i^{m} e^{-in(\phi_n)} \tag{5.41}$$

It is also important to point out that the total number of spatial harmonics or plane waves, N, used in approximating the scattered field need not be the same as the number P. In the following simulation results, L = 40λ and P = 101 which is found to provide sufficient number of harmonics in the translation formula. To account for propagating and evanescent modes in simulation, N is set to be 201.

5.7 Comparison of Results and Validation for Scattering from a Half Space of Discrete Random Scatterers

To validate the proposed method for the discrete random medium problem, the case of scattering from a half space of discrete random media whose analytical solution [71] exists is verified. Using the simulation parameters given in Table 5.5, the simulation results of backscattering coefficients based on the proposed method are in agreement with the analytical ones based on SPF for various values of ε$_a$ and f_v where ε$_a$ is the dielectric constant of scatterers in random medium and f_v is the fractional volume of scatterers as demonstrated in Figs. 5.11 and 5.12. Therefore, the technique for analyzing electromagnetic interaction between an interface and a collection of scatterers through the use of recursive T-matrix algorithm and scattering matrix technique is fully validated. The numerical results based on the proposed method are Monte Carlo solutions denoted by MC. The analytical expressions for backscattering coefficients based on the strong fluctuation theory (SFT) are given by the following expressions:

$$\sigma_{hh} = | T_{01i}^{hh} T_{10i}^{hh} |^2 \, \frac{k_o^3 W_{hh}}{\cos\theta_i (2k_{1zi,hh}^{"})} \left| \frac{k_{zi}}{k_{1zi,hh}} \right|^2 \tag{5.42}$$

$$\sigma_{vv} = | T_{01i}^{vv} T_{10i}^{vv} |^2 \, \frac{k_o^3 W_{vv}}{\cos\theta_i (2k_{1zi,vv}^{"})} \left| \frac{k_{zi}}{k_{1zi,vv}} \right|^2 \tag{5.43}$$

$$W_{hh} = \left|\varepsilon_{g,hh}\right|^2 a^2 2 (f_v \left| \frac{(\varepsilon_a / \varepsilon_{g,hh} - 1)}{(\varepsilon_a / \varepsilon_{g,hh} + 1)} \right|^2 + (1 - f_v) \left| \frac{(\varepsilon_1 / \varepsilon_{g,hh} - 1)}{(\varepsilon_1 / \varepsilon_{g,hh} + 1)} \right|^2) \tag{5.44}$$

$$W_{vv} = \left|\varepsilon_{g,vv}\right|^2 \frac{a^2}{2} (f_v \left| (\varepsilon_a / \varepsilon_{g,vv} - 1) \right|^2 + (1 - f_v) \left| (\varepsilon_1 / \varepsilon_{g,vv} - 1) \right|^2) \tag{5.45}$$

$$\varepsilon_{g,vv} = \varepsilon_1 + f_v (\varepsilon_a - \varepsilon_1) \tag{5.46}$$

$$f_v \frac{(\varepsilon_a / \varepsilon_{g,hh} - 1)}{(\varepsilon_a / \varepsilon_{g,hh} + 1)} + (1 - f_v) \frac{(\varepsilon_1 / \varepsilon_{g,hh} - 1)}{(\varepsilon_1 / \varepsilon_{g,hh} + 1)} = 0 \tag{5.47}$$

Table 5.5
The simulation parameters for scattering from a half space of discrete random media

ε_1	ε_a	f_v	a	ε_a	d	P	M	L
2+i0.3	7+i0.5	0.1	0.07	3.6+i0.5	1λ	50	5	20 λ

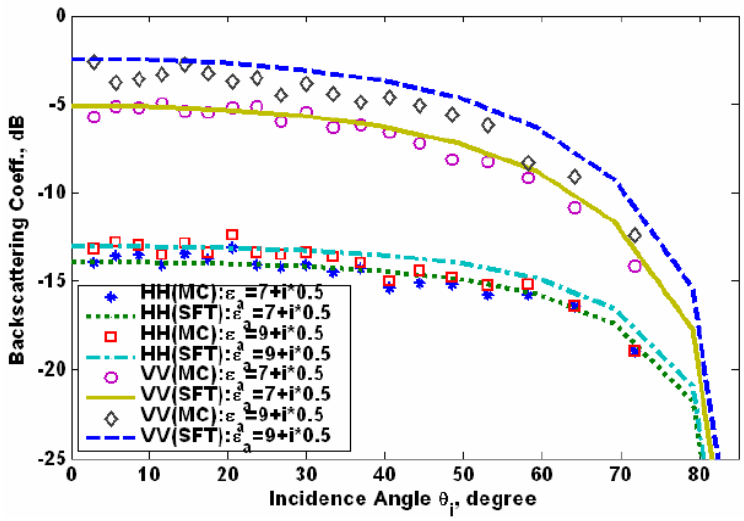

Fig. 5.11: Backscattering coefficients for scattering from a half space of discrete random scatterers for different values of ε_a based on SFT and MC (Table 5.5)

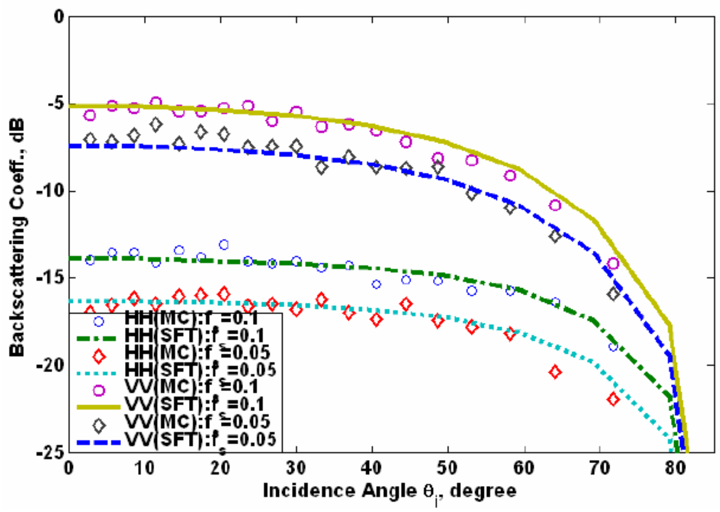

Fig. 5.12: Backscattering coefficients for scattering from a half space of discrete random scatterers for different values of f_s based on SFT and MC (Table 5.5)

5.8 Numerical Results for Scattering from Discrete Random Media in Layered Rough Surfaces

Next, numerical Monte-Carlo simulations are carried out for scattering from a slab of discrete random media with rough surfaces shown in Fig. 5.13.

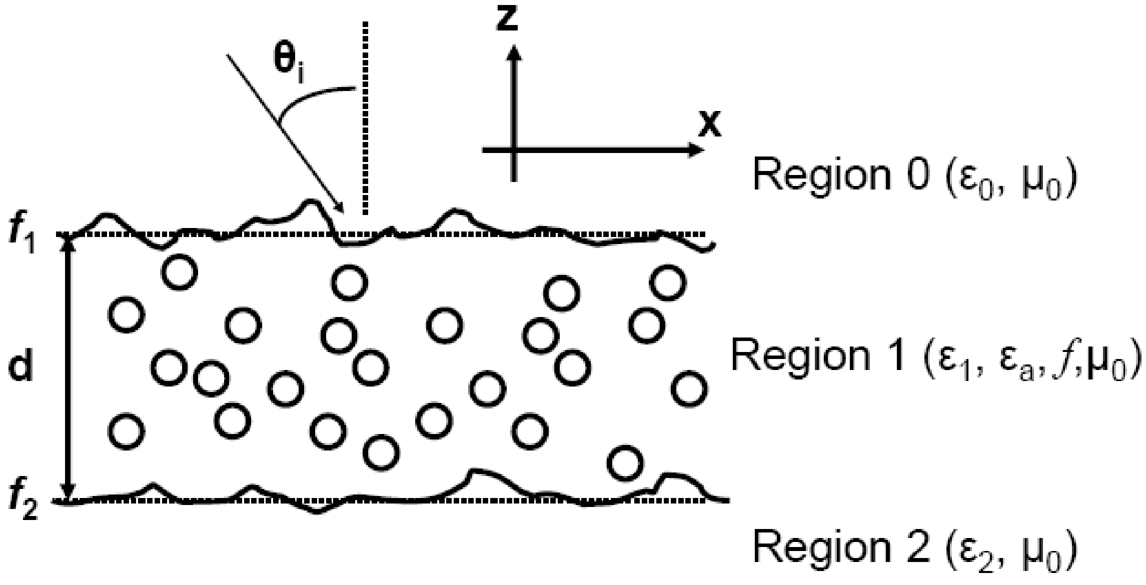

Fig. 5.13: Geometry of scattering from discrete random media in multilayer rough surfaces

The simulation parameters are given in Table 5.6. The random positions of discrete cylinders are determined using Metropolis shuffling algorithm [9]. We consider wave propagation in a layer of discrete random medium with and without rough surfaces above a dielectric layer. The thickness of this layer is 1λ. The horizontal length is 40λ. The total number of Floquet modes is set to be 201. This results in 80 propagating modes and 121 evanescent modes. The radii of all randomly distributed cylinders are 0.1λ. Since the cylinder size is a small fraction of a wavelength, the total number of harmonics used to expand the scattered field around a single scatterer is 7 and the total number of harmonics used in the translation formula is 101. Table 5.6 summarizes the dielectric and size properties of the discrete random medium and relevant simulation parameters.

Table 5.6
The simulation parameters for scattering from a layer of discrete random medium above a dielectric layer

ε_1	ε_2	f_v	a	ε_a	d	θ_i	P	M	N	L
2	5	0.1	0.1λ	3.6+i0.5	1λ	45°	101	7	201	40 λ

The primary objective is to study the effects of surface and volume scattering in layered discrete random media. The roughness statistics for top and subsurface interfaces are characterized by the rms heights (h_1, h_2) and correlation lengths (lc_1, lc_2). The correlation lengths for both top and subsurface interfaces are 0.5λ. It is also important to point out that the polarization is defined with respect to the axis of the cylinder. Therefore, HH-polarized scattered waves actually experience VV-polarized reflection upon a dielectric interface and vice versa.

The first numerical study examines the effects of the rms heights of both top and subsurface interfaces and the dielectric constant of surrounding background media on scattering coefficients while the rest of simulation parameters stay fixed. Fig. 5.14 shows the bistatic scattering coefficients for a layer of discrete random media with a flat and rough top interface for different values of ε_1. In Fig. 5.14 a), we observe the presence of two nulls for HH-polarized scattering coefficients for a flat slab and the locations of these nulls depend on ε_1. These nulls correspond to the Brewster's angles θ_B where $\theta_B=55^o$ and 63^o for $\varepsilon_1 = 2$ and 4, respectively. In addition, when $\varepsilon_1 = 4$, there is very small scattering due to very small dielectric contrast between the scatterers and the background medium. When the layer of discrete random medium is covered by a top rough surface, the nulls disappear due to rough surface scattering and the HH-polarized scattering coefficients increase in Fig. 5.14 (a). For VV-polarized scattering coefficients, the effect of rough surface scattering also results in greater scattering coefficients than a flat slab case in Fig. 5.14 (b). Fig. 5.15 shows the bistatic scattering coefficients for a layer of discrete random media with a flat and rough subsurface interface for different values of ε_1. In Fig. 5.15, the low dielectric contrast across the subsurface interface reduces the subsurface roughness effect on overall scattered intensity for $\varepsilon_1 = 4$. For $\varepsilon_1 = 2$, the effect of subsurface roughness is almost negligible in VV polarization compared to HH polarization, indicating a more significant effect of scatter darkening due to a higher extinction rate for VV polarization. In addition, we note that VV-polarized scattering coefficient is in general larger than HH-polarized scattering coefficient because there is greater transmission of horizontally polarized waves at the bottom boundary.

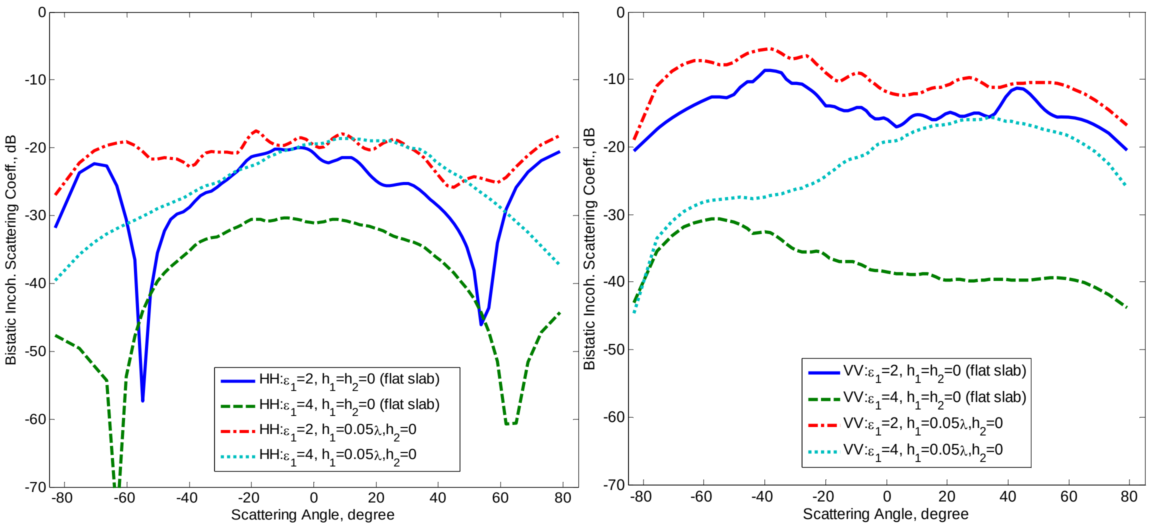

(a) **(b)**

Fig. 5.14: HH- (a) and VV- polarized (b) bistatic incoherent scattering coefficients for scattering from a layer of discrete random medium of different dielectric constants above a dielectric half space for different top surface roughness conditions

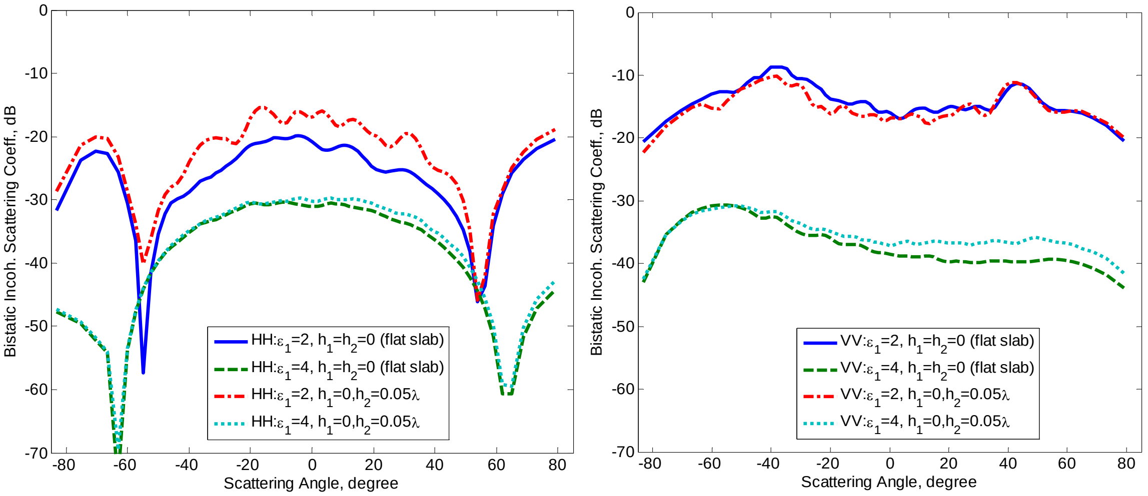

(a) **(b)**

Fig. 5.15: HH- (a) and VV- polarized (b) bistatic incoherent scattering coefficients for scattering from a layer of discrete random medium of different dielectric constants above a dielectric half space for different subsurface surface roughness conditions

Next, a numerical study is performed to investigate the effects of layer thickness on HH-polarized scattering coefficients in presence of top surface or subsurface roughness. The layer depth is comparable to a wavelength, resulting in oscillatory behaviors in the scattering coefficient due to constructive interference. Scattering coefficient is a strong function of layer depth. As the depth of the fractional volume increases, extinction increases as evidenced by an increase in the scattering coefficient. When the top surface becomes rough, it leads to a further increase in the scattered intensity. On the other hand, with subsurface roughness, the magnitude of increase in the scattering coefficient depends on the location of the subsurface interface. The larger the layer thickness, the more darkened the scatter due to subsurface roughness.

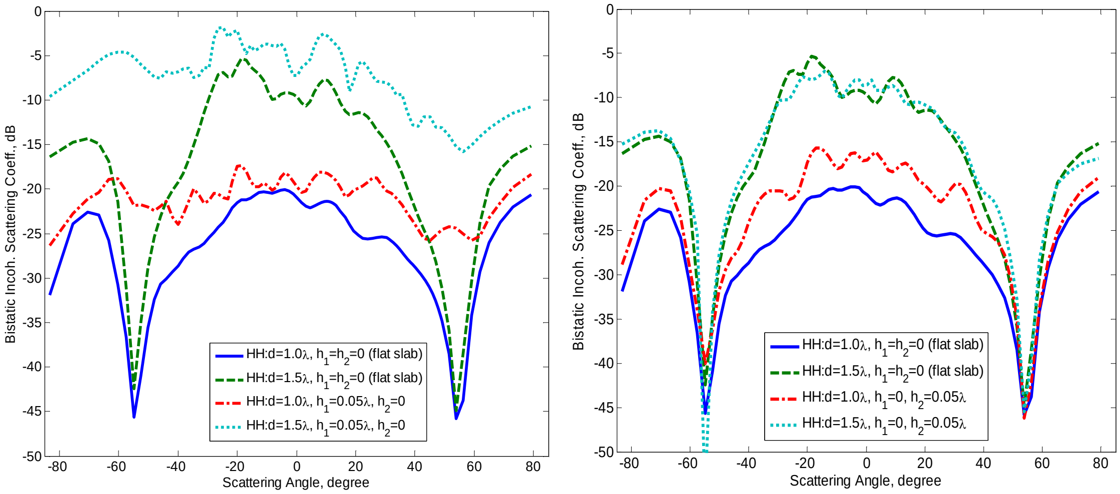

(a) **(b)**

Fig. 5.16: HH-polarized bistatic incoherent scattering coefficients for scattering from a layer of discrete random medium of different thicknesses above a dielectric half space for different (a) top surface and (b) subsurface roughness conditions

Figs. 5.17 and 5.18 show HH- and VV- polarized bistatic scattering coefficients for different values of the top surface (Fig. 5.17) and subsurface rms height (Fig. 5.18) and different volume fractions. We observe that when f increases from 0.1 to 0.2, HH-polarized scattering coefficient increases by 2-3 dB whereas VV-polarized scattering coefficient does not experience much of an increase. For $0.1< f <0.2$, the discrete random medium is considered slightly dense. The HH-polarized scattering coefficient clearly increases as f increases, indicating the mechanism of independent scattering still somewhat dominates. However, the little change in VV-polarized backscattering coefficient as the volume fraction increases from 0.1 to 0.2 suggests that for VV polarization the the effect of multiple scattering as a result of the packing of scatterers may not increase or even reduce the overall scattering strength. Above a certain volume fraction, scattering begins to diminish with increasing volume fractions. This behavior is consistent with the numerical results based on strong fluctuation theory [94]. In presence of top surface roughness, scattering coefficients increase by several dBs for both polarizations. However, when the subsurface interface is rough, the volume scattering strength strongly depends on the polarization state. For $0.1 < f < 0.2$, the effects of subsurface and volume scattering constructively sum together in HH polarization. For VV polarization, subsurface scattering enhances the effect of scatter darkening, resulting in a decrease in the bistatic scattering coefficient.

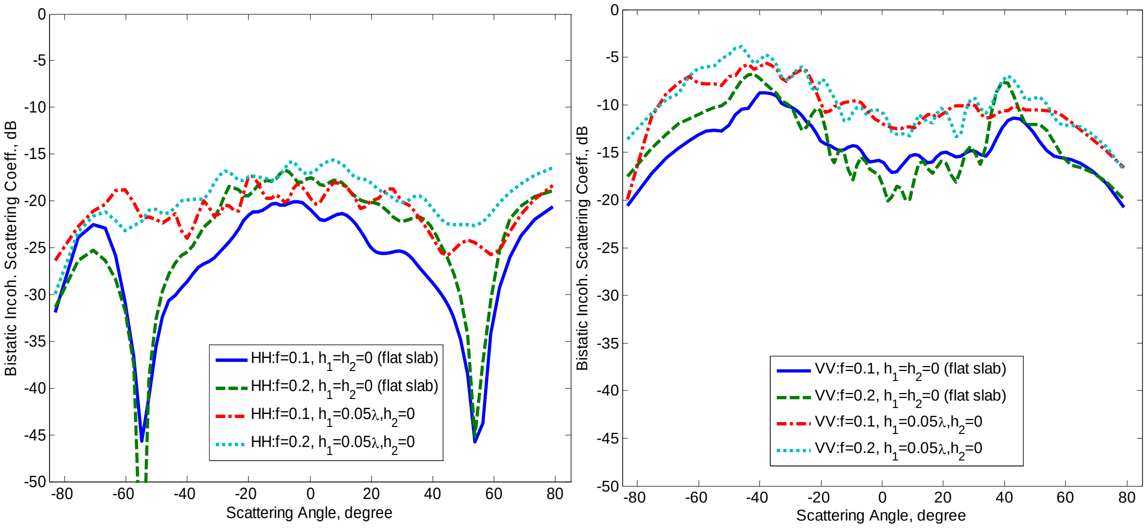

(a) **(b)**

Fig. 5.17: HH- polarized (b) bistatic incoherent scattering coefficients for scattering from a layer of discrete random medium of different volume fractions above a dielectric half space for different top surface roughness conditions

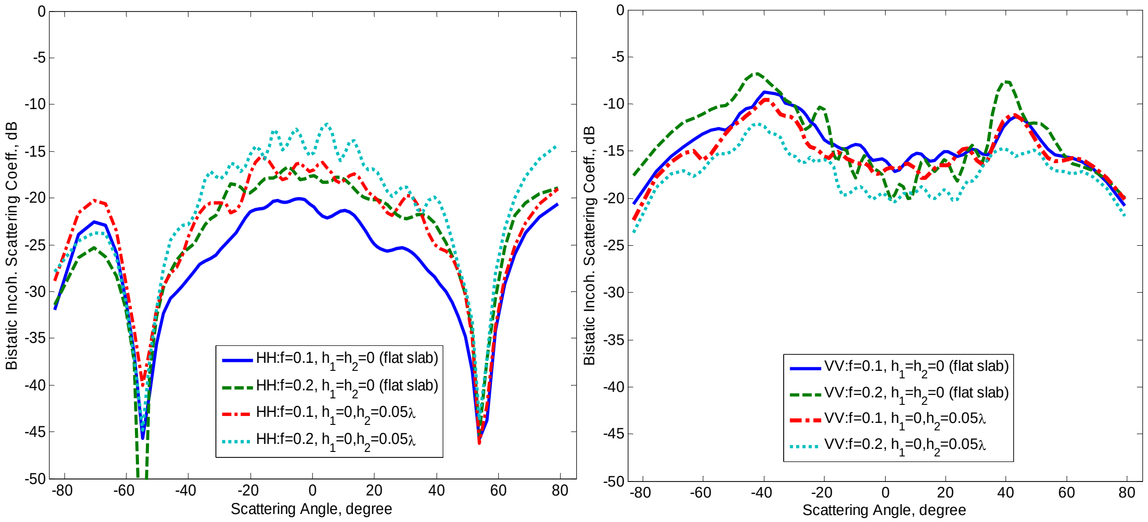

(a) **(b)**

Fig. 5.18: HH- (a) and VV- polarized (b) bistatic incoherent scattering coefficients for scattering from a layer of discrete random medium of different volume fractions above a dielectric half space for different subsurface surface roughness conditions

Figs. 5.19 and 5.20 show bistatic scattering coefficients for HH and VV polarizations for different values of the top surface (Fig. 5.19) and subsurface (Fig. 5.20) rms height and different cylinder sizes. The cylinder size is a significant factor contributing to the magnitude of volume scattering for HH polarization. When the cylinder radius decreases from 0.1λ to 0.05λ, the overall magnitude of the HH-polarized scattered intensity significantly decreases. On the other hand, although the magnitude of the VV-polarized scattered intensity does not experience as much a drastic drop as the HH-polarized scattered intensity for smaller cylinder size, its bistatic angular distribution is altered. We note for VV polarization, there is a peak of the bistatic scattering coefficient in the backscattering direction. This is a common characteristic of the cylinder scattering pattern. In addition, the sharpness of backscattering peak evidently depends on the cylinder radius. The other peak of the bistatic scattering coefficient occurs in the specular direction, demonstrating scattered waves tend to add coherently in the specular direction for a flat slab case. For HH polarization (VV on surface), the Brewster's angle effect prevents the formation of backscattering peaks and thus no backscattering peaks are observed. We also observe that surface roughness tends to broaden the angular widths of the backscattering and specular peaks.

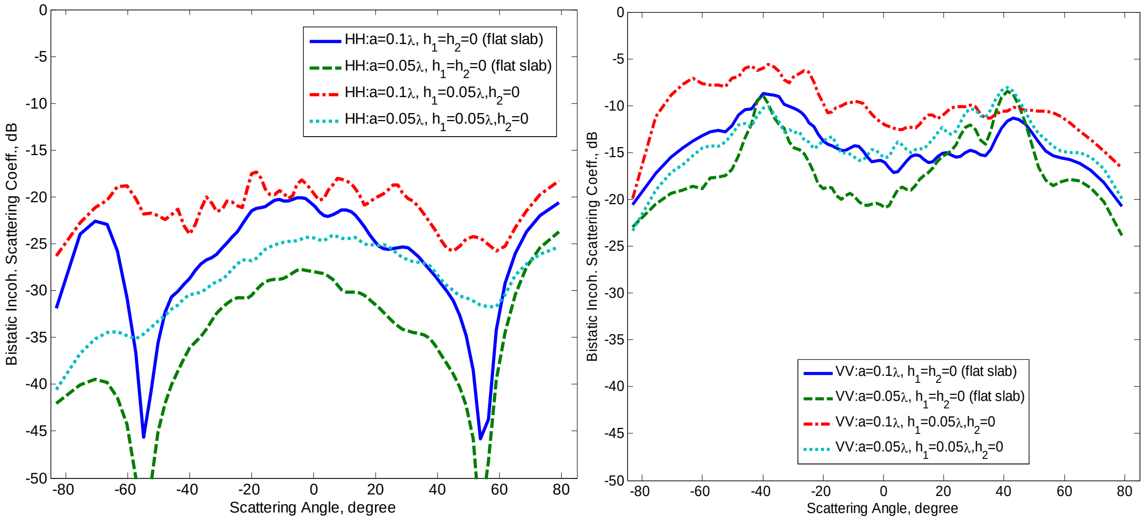

(a) **(b)**

Fig. 5.19: HH- (a) and VV- polarized (b) bistatic incoherent scattering coefficients for scattering from a layer of discrete random medium of different cylinder sizes above a dielectric half space for different top surface roughness conditions

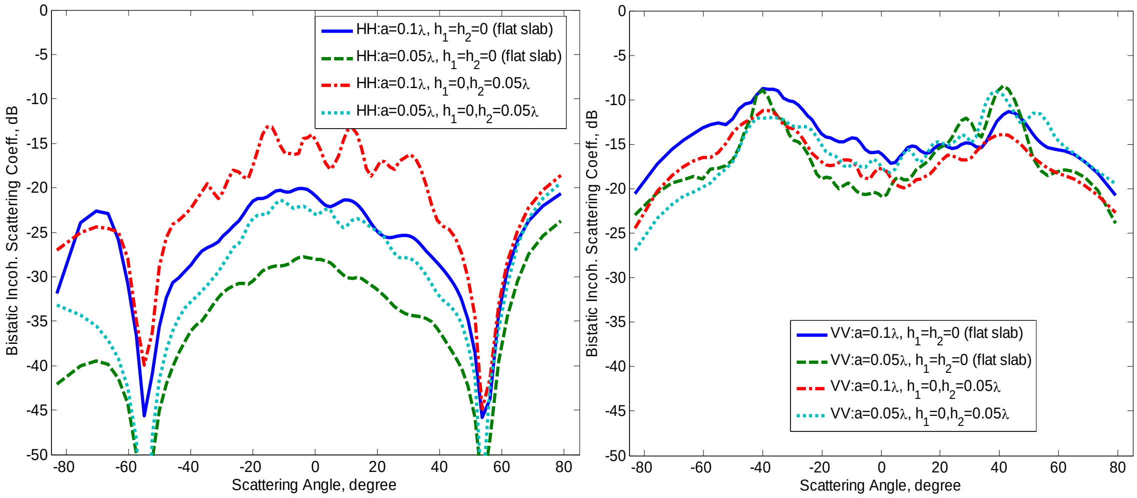

(a) **(b)**

Fig. 5.20: HH- (a) and VV- polarized (b) bistatic incoherent scattering coefficients for scattering from a layer of discrete random medium of different cylinder sizes above a dielectric half space for different subsurface surface roughness conditions

Finally, the sensitivity analysis for different values of subsurface dielectric constant is conducted. This study also focuses on the effect of subsurface roughness on scattering coefficient for different subsurface dielectric constant with or without subsurface roughness as shown in Fig. 5.21. In the backscattering direction, there is almost zero change to the HH-polarized scattering coefficient. On the other hand, VV-polarized scattering coefficient shows more sensitivity to subsurface dielectric constant. There is an increase of 3-4 dB in the VV-polarized backscattering coefficient for a flat slab case. The difference in the magnitude of sensitivity for different polarizations is due to greater transmission of horizontally polarized waves at the subsurface interface. When the bottom interface is rough, the increase in the VV-polarized bistatic scattering coefficient becomes more pronounced. Therefore, for VV polarization, subsurface roughness is a critical factor in enhancing the sensitivity.

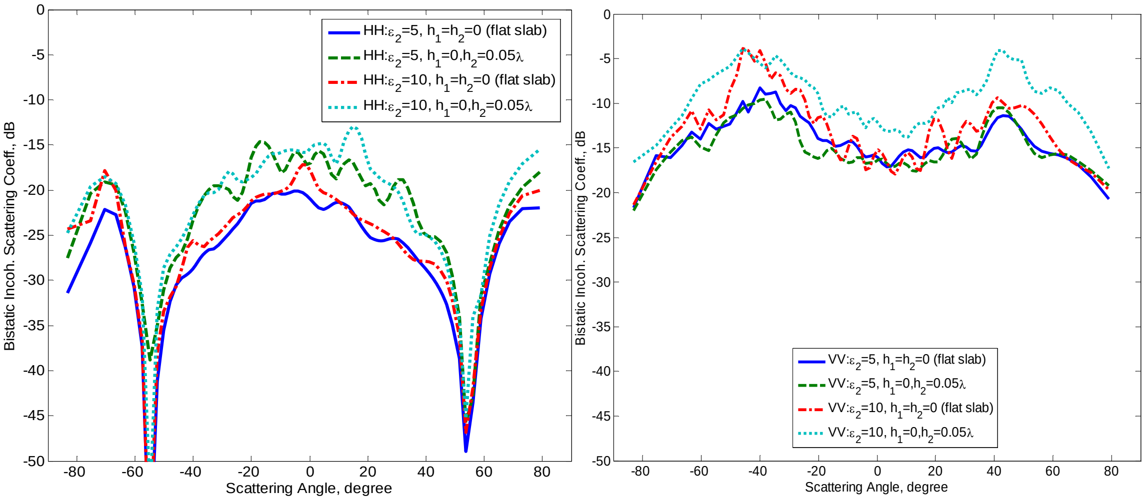

(a) **(b)**

Fig. 5.21: HH- (a) and VV- polarized (b) bistatic incoherent scattering coefficients for scattering from a layer of discrete random medium of different cylinder sizes above a dielectric half space for different subsurface surface roughness conditions

5.9 Chapter Conclusion

A solution to scattering from a cylinder buried in layered rough interfaces based on EBCM/SMM is presented. The reflection and transmission matrices of a rough interface as well as an isolated single cylinder are constructed using EBCM and recursive T-matrix algorithm, respectively, which require the assumption of periodic boundary conditions where the finite-length rough surface and the cylindrical object are extended periodically with period L. The coupling between cylinders in an arrangement of a periodic array is removed by incorporating a large separation distance between cylinders into the lattice-sum matrix of the recursive T-matrix formulation. Finally, the cylinder/rough surface interactions are accounted for by applying the generalized scattering matrix technique. In numerical simulations, the bistatic scattering coefficients are validated by comparing the simulation results with the existing solutions which are the limiting cases including scattering from two-interface rough surfaces without any buried object and from a buried cylinder beneath a single rough surface. The results are in good agreement. Numerical simulation results show that the use of HH polarization is more suitable for the detection of buried objects whereas VV polarization provides more sensitivity to roughness.

Also, the location of the bottom interface relative to the cylinder plays a crucial role in the bistatic scattering coefficient and can significantly alter the scattering response.

Subsequently, the proposed technique is employed to solve scattering from discrete random media embedded in layered rough surfaces. Through plane-wave decomposition and matrix cascading technique, the electromagnetic interactions between multiple scatterers, including rough surfaces and discrete random media is analyzed. Plane wave solution to the scattered fields due to individual distributed scatterers, such as a rough surface or a collection of random 2D particles, are then cast into reflection and transmission matrices in order to facilitate the application of scattering matrix approach. Various numerical results for scattering from a flat and rough layer of discrete random media above a dielectric half space are presented and discussed.

CHAPTER 6

A Multi-Frequency Inversion Technique for the Retrieval of the Subsurface Soil Properties Using VHF/UHF Radar Measurements

The characterization of subsurface structure and dielectric properties of soil media using microwave remote sensing technology holds promise in identifying soil stratigraphy, measuring soil moisture content, and assessing soil salinity. Using an existing forward model for scattering from layered rough surfaces based on the 1st order small perturbation method (SPM), a multi-frequency polarimetric inversion algorithm for the retrieval of subsurface soil properties using VHF/UHF band radar measurements is discussed in this chapter. The SPM forward solver is used as a proxy to reduce computational overhead inherent in any full-wave numerical method, such as those discussed in the preceding chapters.

When backscattering coefficients at an oblique incidence at multiple frequencies over VHF, UHF, and L bands are measured, the inversion scheme proposed in this chapter carries out the retrieval of the dielectric properties and roughness statistics of each distinct soil layer in a layer-stripping fashion. The dielectric constant of the top surface is first determined using an L-band inversion algorithm and then the top surface is mathematically stripped away. For the retrieval of subsurface properties, the dielectric constants as well as roughness statistics are estimated using an equivalent time-domain inversion technique with the minimization of a cost function defined in terms of the pulse shape of time delay echoes due to dual-polarized VHF/UHF band radar measurements. The core of this work lies in the use of virtual time-domain data realized using multi-frequency measurements. The proposed inversion scheme performs an inverse Cosine transform of radar measurements over the VHF/UHF bands to obtain synthetic time-domain data and subsequently exploits the information of the ensuing individual delay echoes representing successive reflections upon different rough surfaces.

Time-domain data have very attractive features, which can facilitate the inversion of material properties and roughness statistics of rough layers. They consist of a series of time echoes delayed at different times with each time-delayed echo representing a reflection upon a rough interface. The pulse shape of a time delayed echo is highly correlated with the dielectric contrast across an interface, rms height, and correlation length of the rough interface [47, 95, 96]. The time difference between delay echoes is linearly related to the layer thickness. The main objective of this research, formulated in order to set itself apart from previous inversion methods, is to account for subsurface roughness in the development of the inversion algorithm by characterizing it as a statistical unknown and then to simultaneously estimate the subsurface dielectric and roughness properties through pulse shape optimization. In this Chapter, numerical studies are first performed to investigate the accuracy of the proposed inversion technique in the absence of measurement, model, and calibration errors. Then, extensive error analysis is carried out to examine the performance of the proposed inversion method in the presence of errors. The robustness of this method against errors in the estimates of top surface parameters is also evaluated. We note that this Chapter presents a theoretical development of the inversion algorithm, with field demonstrations pending the future availability of radar data.

6.1 Multi-Frequency Polarimetric Radar Measurements at VHF/UHF and L Bands

The radar system on which the development of the following inversion algorithm is based envisions three frequency bands: VHF/UHF bands spanning the frequency range from 100MHz to 500 MHz and L band (i.e., 1.2 GHz). The L-band radar system is assumed to perform a single or a few measurements in the 1.2-1.4 GHz range, which are employed to invert the ground-surface dielectric properties. The multi-frequency radar system envisioned also covers both VHF and UHF bands to perform low frequency radar measurements from 100 MHz to 500 MHz with 15 uniform sample points for the retrieval of subsurface soil moisture. Fig. 6.1 depicts the idea of a multi-frequency radar system probing a layered soil medium. Radar data are acquired in HH and VV polarizations and with an incidence angle at center swath of 35°. This choice of an incidence angle is selected to be not near the grazing angle because low incidence angles maximize the soil contribution with respect to the contribution of vegetation as suggested in [56] and the inversion results are less affected by errors due to noise at low incidence angles than at high incidence angles. On the other hand, the distinction between HH and VV polarizations is more pronounced at high incidence angles than at low incidence angles. Therefore, the polarimetric nature of radar data can be more fully exploited and more independent information can be extracted at higher incidence angles. Consequently, an incidence angle of 35° is deemed to be a reasonable choice from the polarimetric perspective.

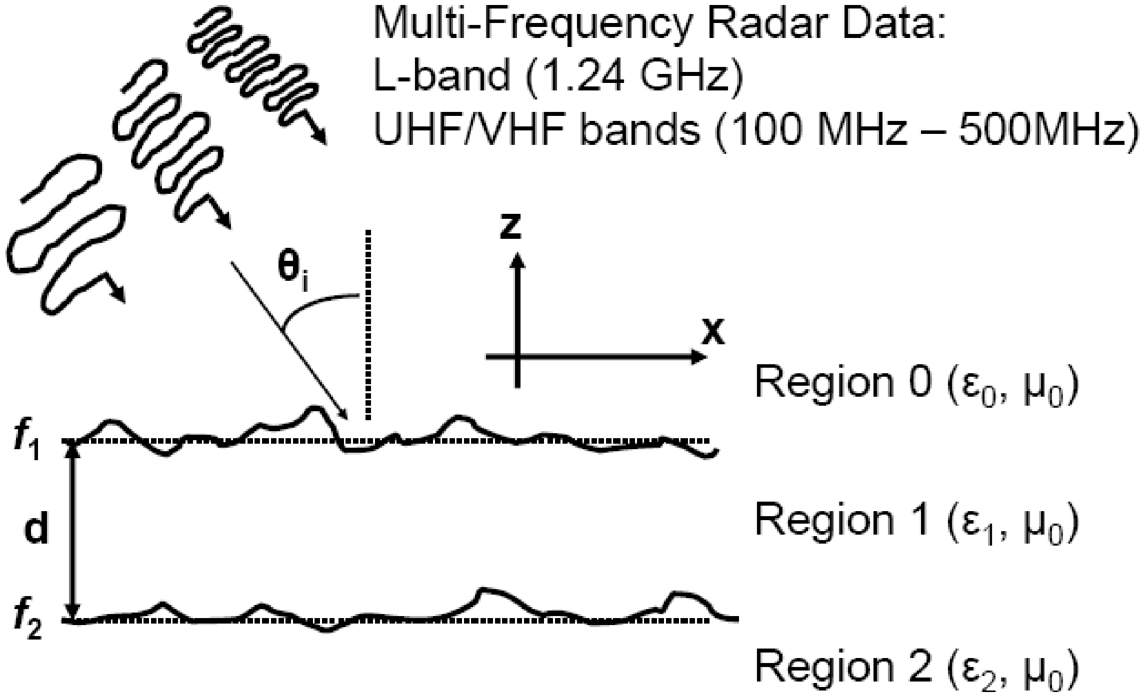

Fig. 6.1: Multi-frequency measurements to probe layered rough surfaces

Currently, a ground-based tower-mounted radar system has been developed to demonstrate the UHF and VHF SAR instrument proposed in Microwave Observatory of Subcanopy and Subsurface (MOSS) mission project [22]. The tower-mounted radar was designed to operate at 137 MHz (VHF), 435 MHz (UHF) and 1.2 GHz (L). This system is a pulsed polarmetric radar and uses a single log-periodic antenna (LPA) on both transmit and receive (T/R). A fast T/R switch is used to change the operating mode of the antenna between pulses. The LPA is a dual-polarized wide-band antenna covering the frequency range of 80-1200 MHz, with return loss of no worse than 10 dB across the band. The antenna beamwidth is several tens of degrees in all principal planes, requiring a beam-forming scheme to allow proper correspondence of the data to scattering target locations. The beam-forming method employed consists of synthesizing a large effective aperture by moving the antenna mounted on the tower vertically such that the focused beam resolution cell is about 10 m on the ground. The size of the synthetic aperture and sample spacing are scaled with wavelength. The antenna boresight is adjustable. The look angle of the focused beam can be controlled during post processing and is typically varied in the 25^{o}-65^{o} range. The transmitted signal is switched to allow dual (T/R) operation of the antenna and the transmitted signal has a finite bandwidth determined by the nominal pulse width and the switch transient characteristics. In this case, the effective bandwidth is in the range of 20-50 MHz.

In order to implement the proposed multi-frequency radar from 100 MHz to 500 MHz based on the design specifications of the tower-mounted radar system, the proposed radar system can employ both a log periodic antenna and a frequency swept source to scan over the required frequency band at a large number of frequencies and collect the data required to test the algorithms. Alternatively, the radar system can operate at three distinct frequencies at 137 MHz, 300MHz, and 435MHz with the bandwidths ranging from 50MHz to 100 MHz. This frequency coverage should provide an adequate number of frequency measurements for algorithm testing.

6.2 Forward Scattering Model and Construction of Synthetic Time-Domain Data from Multi-Frequency Measurements

A forward model for scattering from two-rough-interface surfaces based on the small perturbation method (SPM) has been developed in [1] where nine input parameters including five material parameters (Re{ε_1}, Im{ε_1}, Re{ε_2}, Im{ε_2}, *d*) and four parameters describing roughness statistics (h_1,lc_1,h_2,lc_2) in the problem scenario are mapped into backscattering coefficients, $\sigma_{hh,fi}$ and $\sigma_{vv,fi}$, at the frequency f_i.

$$\sigma_{hh} = 4\pi k_o^2 \cos^2\theta_s (|\alpha_1^h|^2 W_1(\bar{k}^s_\perp - \bar{k}^i_\perp) + |\alpha_2^h|^2 W_2(\bar{k}^s_\perp - \bar{k}^i_\perp)) \tag{6.1}$$

$$\sigma_{vv} = 4\pi k_o^2 \cos^2\theta_s (|\alpha_1^v|^2 W_1(\bar{k}^s_\perp - \bar{k}^i_\perp) + |\alpha_2^v|^2 W_2(\bar{k}^s_\perp - \bar{k}^i_\perp)) \tag{6.2}$$

where $W_1(\bar{k}_\perp)$ and $W_2(\bar{k}_\perp)$ are the spectral densities of the top and bottom rough boundaries, respectively, and $\alpha_1^h, \alpha_1^h, \alpha_2^v$, and α_2^v correspond to the 1st order coefficients from the small perturbation method. They are determined by imposing boundary conditions on both top and bottom rough interfaces simultaneously. This translates to an 8 by 8 matrix inversion.

At low frequencies from 100 MHz to 500 MHz, SPM is valid at the surface roughness scale for the most natural surfaces and gives appropriate scattering results. Using this analytical forward model based on SPM, virtual time-domain data can be constructed by taking the inverse Fourier transform of the band-limited frequency measurements. Given $\sigma_{hh,f1}$, $\sigma_{hh,f2}$,…, $\sigma_{hh,fn}$, $\sigma_{vv,f1}$, $\sigma_{vv,f2}$,…, $\sigma_{vv,fn}$, the virtual time-domain data can be synthesized through the use of the Discrete Cosine Transform given as follows:

$$\sigma_{pp}(t) = \sum_i^N w_i \sigma_{pp}(f_i)\cos(2\pi f_i t) \tag{6.3}$$

where *pp* is the polarization, i.e., *hh* or *vv,* and w_i's are the Hamming weights used to reduce the side-lobe level due to band-limited measurements. The reason behind obtaining synthetic time-domain information is that inversion of layer thickness is then greatly facilitated and performed using the information of the time difference between the 1st and 2nd time delay echoes. Although it is advantageous to consider the ratios of HH and VV backscattering coefficients to reduce the calibration errors and roughness effect for a single rough surface case, it is unclear if simple ratios between HH and VV scattering coefficients will effectively work for layered rough surfaces. Therefore, in this study, HH and VV backscattering coefficients are considered separately.

6.3 Recovery of Top Ground Parameters

The retrieval of soil moisture content and surface roughness from L-band radar observations of bare soil surfaces can be quantitatively performed using many existing techniques, such as those in [16, 54, 56]. L-band radar data yield useful information regarding soil moisture content and surface roughness of bare soil surfaces (the top few centimeters of soil-surface layer). At L band, the sensing or sampling depth, defined as the depth over which the sensor has retrieved a return signal yielding information or the thickness of the soil layer that gives the most significant contribution due to scattering, is in general in the range of 0.2 – 0.25λ for a slightly wet surface. At f = 1.2 GHz, the sensing depth is ~5-7cm, indicating that the soil moisture that L-band microwave sensor observes is only a weighted average of soil moisture content over 5-7 cm. Despite the fact that waves may still penetrate deep into the soil for a dry surface at L-band (i.e., 10 cm – 15 cm), L-band radar data typically are not influenced by the presence of a subsurface layer located around 30 cm or more away from the ground surface.

A frequency-domain inversion technique for the retrieval of top surface parameters using L band radar measurements is presented in this section. The input measurements are radar backscattering cross-sections at center frequencies of 1.24 GHz with a bandwidth of 80 MHz. The inversion parameters are ε_1', h_1 and lc_1. The premises on which this analysis rests are that at L band, waves can only penetrate several centimeters into the ground, the application of the forward model for scattering from a homogenous half space with a rough surface is valid provided the depth of subsurface layer is greater than from the sensing depth of L band, and the top layer is lossy. In most scenarios, the subsurface layer of interest is located 30cm-1m away from the ground and the attenuation of top surface is characterized by $\varepsilon_1'' = 0.3\sim0.5$ for dry soil and $\varepsilon_1'' = 0.8\sim1.1$ for wet soil [84, 85]. Here, an assessment of the impacts of attenuation and layer depth of top layer on inversion results is made.

The inversion algorithm for top surface parameters is described as follows. Backscattering coefficients from 1.20 GHz to 1.28 GHz with five uniform samples over the bandwidth are measured. These backscattering coefficients are represented by 5X1 column vectors, and the elements denoted by $\underline{\sigma}_{hh}$ and $\underline{\sigma}_{vv}$ for HH and VV polarizations. The cost function is then defined as:

$$C = \frac{\left\| \begin{bmatrix} \underline{\sigma}_{hh} \\ \underline{\sigma}_{vv} \end{bmatrix}_{stimulated} - \begin{bmatrix} \underline{\sigma}_{hh} \\ \underline{\sigma}_{vv} \end{bmatrix}_{measured} \right\|}{\left\| \begin{bmatrix} \underline{\sigma}_{hh} \\ \underline{\sigma}_{vv} \end{bmatrix}_{measured} \right\|} \tag{6.4}$$

Here, $\begin{bmatrix} \underline{\sigma}_{hh} \\ \underline{\sigma}_{vv} \end{bmatrix}_{stimulated}$ is computed using the forward model for scattering from a homogeneous half space with a rough surface. The vector $\begin{bmatrix} \underline{\sigma}_{hh} \\ \underline{\sigma}_{vv} \end{bmatrix}_{measured}$ is computed based on the two-layer SPM model. The unknown parameters are ε_1', ε_1'', h_1, and lc_1. The backscattering coefficients do not show much sensitivity to ε_1'', making this parameter very challenging to invert using L band radar data. Therefore, the parameters designed to be inverted are ε_1', h_1, and lc_1. A constrained Nelder-Mead simplex algorithm is used to seek a solution with the constrained ranges of ε_1' from 2 to 20, h_1 from 0.2 cm to 2.7 cm and lc_1 from 6 cm to 25 cm, all well within reasonable and naturally occurring bounds. The simulation parameters are given as follows: $\mathrm{Re}\{\varepsilon_1\}=6$, $\varepsilon_2= 15*(1+j1/10)$, $h_1=1\text{cm}$, $lc_1=10\text{cm}$, $h_2=2.5\text{cm}$, $lc_2=20\text{cm}$. Inversions are performed for different values of $\mathrm{Im}\{\varepsilon_1\}$ and d. The quality of inversion results depends on the depth of subsurface interface. To analyze how the layer thickness and attenuation of top layer affect the inversion based on the SPM forward model, the relative error between the actual and inverted results is examined. Relative error (*RE*) indicates the quality of an inverted result relative to the size of the actual result and is given by

$$RE = \frac{\Delta X}{X} \tag{6.5}$$

where ΔX = inverted value – actual value and X = actual value. When $\log_{10}$(RE) is used, $\log_{10}$(RE) = -1, -2, and -3 means 10% , 1%, and 0.1% error. Therefore, if 10% error is considered to represent a good inversion result, then points which lie below $\log_{10}$(RE) = -1 are those where inversion results are perceived to agree with actual results. In the following analysis, synthetic data sets are generated directly using the SPM forward model and thus any error is a result of modeling and inversion errors. The $\log_{10}$(RE) in ε_1', h_1, lc_1 are plotted in Fig. 6.2 against depth for different values of ε_1''.

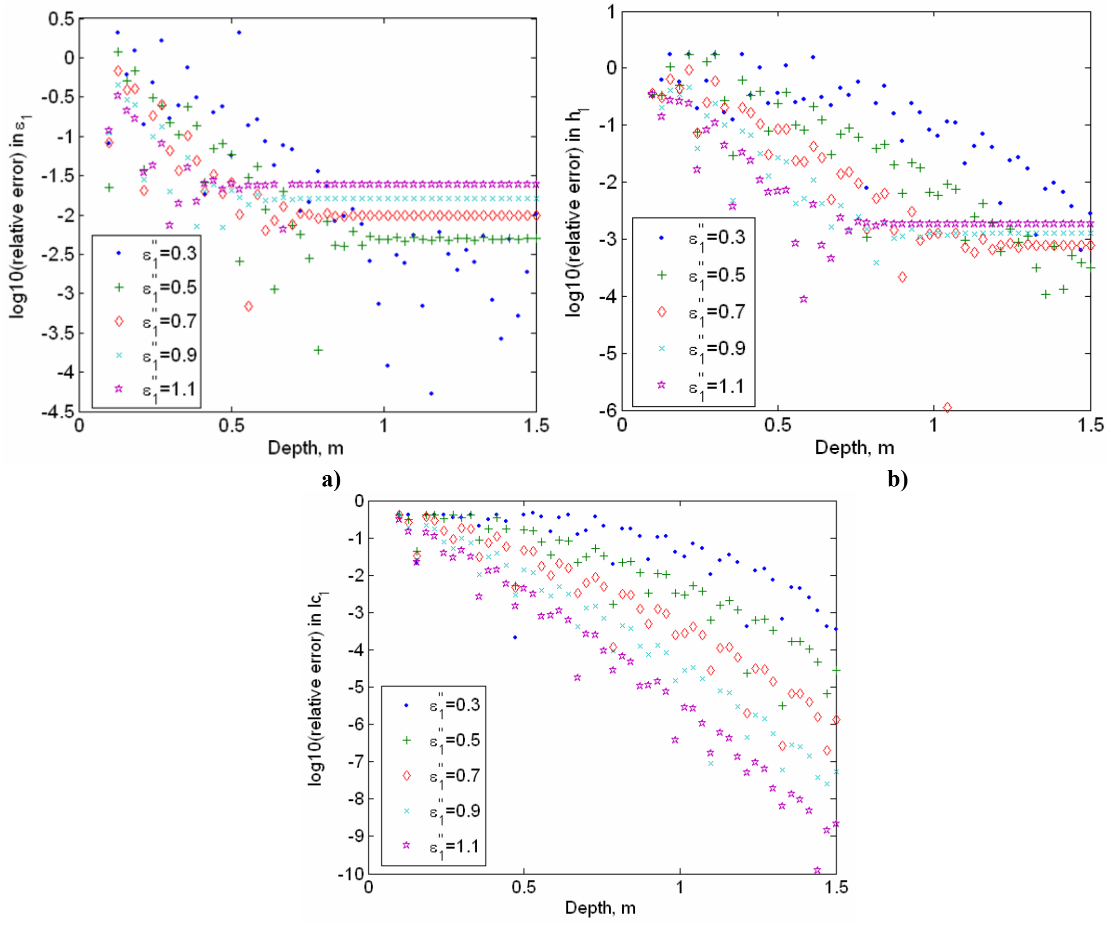

a)

b)

c)

Fig. 6.2: Relative errors between the inverted and the actual values of a) ε_1', b) h_1, and c) lc_1 against layer depth for different values of ε_1''

We anticipate that as layer thickness, d, increases and/or the attenuation of the top layer, proportional to ε_1'', increases, the effect of subsurface layer vanishes. The inverted value of l_{c1} gets more accurate as evidenced by a decrease in relative errors as the values of layer thickness and/or ε_1'' increase as shown in Fig. 6.2 (c). When we examine the behaviors of relative error in ε_1' and h_1 in Fig. 6.2 (a) and (b) for different values of layer thickness and ε_1'', we observe that although the relative errors are all kept under -1.5 dB which shows that the inverted and actual values are in good agreement, the observation where the relative error grows as ε_1'' increases when layer thickness exceeds a certain threshold (i.e., ~0.3-0.6 m) calls for further investigation. This observation can be understood through the examination of cost functions. The cost functions against ε_1' and h_1 for two different sets of d and ε_1' are plotted in Fig. 6.3. The global minima for both cost functions all fall at the point of $\varepsilon_1' = 6$ and $h_1 = 0.01$ m. We observe that for $\varepsilon_1'' = 0.3$, the cost function is smooth and there is only one minimum over the domain of interest. However, for $\varepsilon_1'' = 1.0$, the cost function becomes extremely nonlinear and there are multiple local minima over the domain of interest. These local minima are very closely clustered around the location of global minimum and the solution given by the Nelder Mead simplex algorithm may get stuck in a local minimum under these circumstances. This problem can be solved by resorting to a global optimization technique, but at a much greater computational expense. Despite the potential local minima problem, Nelder Mead optimization technique yields relative errors between the inverted and actual values in ε_1', h_1, lc_1 less than 1% for a wide range of scenarios.

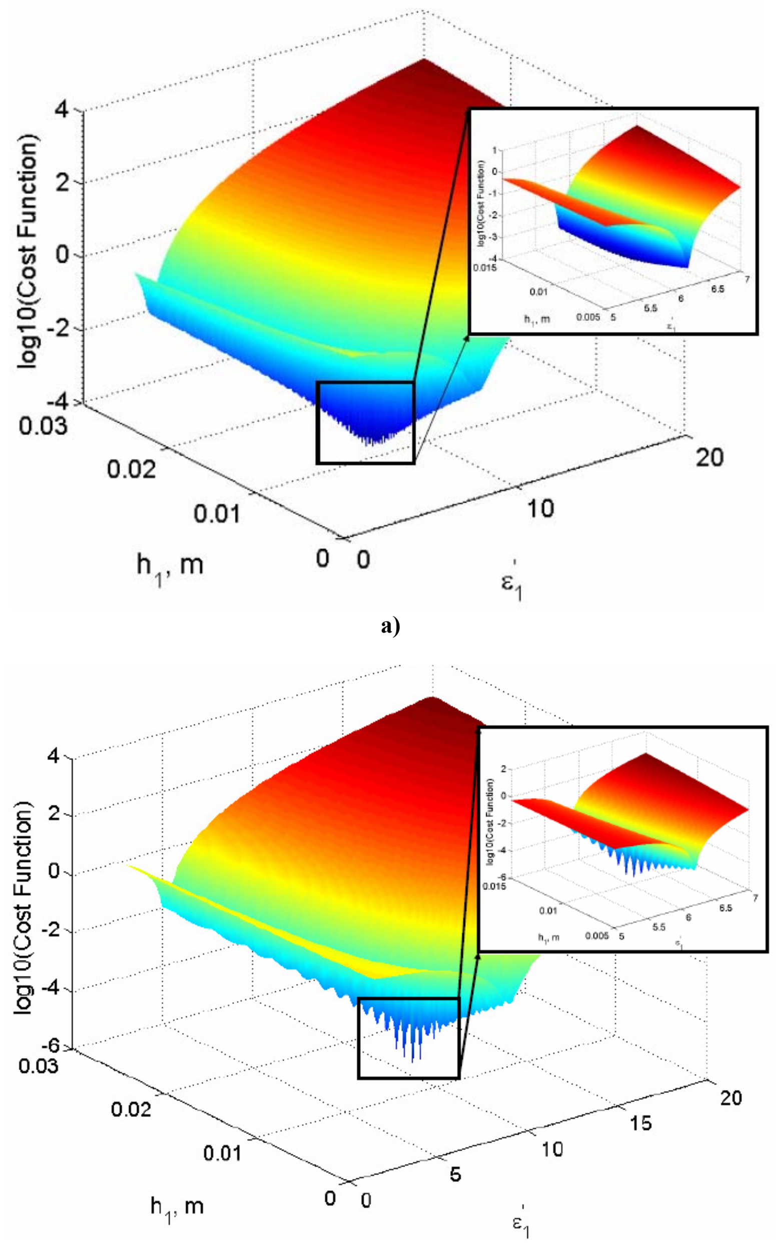

a)

b)

Fig. 6.3: Cost function against ε_1' and h_1 for different values of (a) $\varepsilon_1''= 0.3$ and (b) $\varepsilon_1''= 1.0$

For the retrieval of subsurface dielectric properties using VHF/UHF radar measurements, the inverted value of Re{ε_1} from L-band radar measurements can be fed into the inversion algorithm as a-priori information. The soil dielectric model by Peplinski et al.. in [84, 85] suggests that the real part of the ground soil dielectric, Re{ε_1}, at L-band is very similar to that at UHF/VHF bands. The picture is much more complicated for the value of Im{ε_1}. The value Im{ε_1} at L-band is significantly different from that at VHF/UHF band and generally exhibits great frequency variation. Therefore, Im{ε_1} must be modeled as an independent unknown or unknowns for the retrieval of subsurface soil moisture content from VHF- and UHF-band radar data. Nevertheless, the use of L-band radar measurements yield information regarding Re{ε_1}, h_1, and lc_1, leaving the remaining retrieved parameters as Im{ε_1}, Re{ε_2}, h_2, lc_2, and d. One may also use a frequency higher than L-band for the retrieval of top surface parameters.

6.4 Dielectric Soil Model at VHF/UHF Bands

Before the discussion of the subsurface inversion algorithm, the soil dielectric properties at VHF/UHF bands need to be characterized. The frequency dependence also needs to be accounted for, and the model be carefully parameterized with the number of independent unknowns properly specified for the development of the inversion method. The dielectric model for soils over the frequency range from 300 MHz to 1300 MHz has been developed in [84, 85]. The model relates the complex dielectric constant of a soil medium to the soil textural composition (sand, silt, and clay fractions), the bulk density and volumetric moisture content of the soil at a specified microwave frequency and physical temperature. In [84], it is shown that the real part of soil dielectric constant only exhibits very slight dependence on frequency from 300 MHz to 1.3 GHz. In Fig. 6.4, the real and imaginary parts of the relative soil dielectric constant are plotted against soil moisture content for f =100MHz, 200MHz, 300 MHz, 400 MHz, and 500 MHz based on this model. For the example in Fig. 6.4, the mass fraction of sand is 0.3, the mass fraction of clay is 0.2, and the ambient temperature is 17.7C.

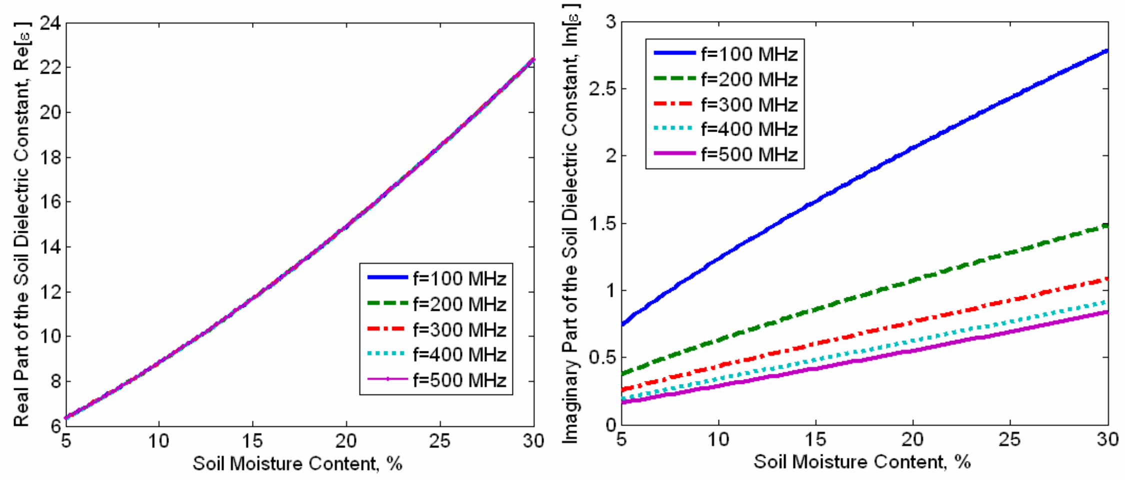

(a) **(b)**

Fig. 6.4: The (a) real and (b) imaginary parts of the relative soil dielectric constant are plotted against soil moisture content for different values of frequency

Evidently, over the frequency range from 100 MHz to 500 MHz, the real part of dielectric constant of a soil medium is frequency-independent. The real part of soil dielectric constant provides a good indicator of soil moisture content as demonstrated by their strong relationship. The imaginary part of the soil dielectric constant strongly depends on frequency and the soil dielectric model in [84, 85] clearly overestimates the imaginary part of the soil dielectric constant at lower frequencies (i.e., f=100 MHz and 200 MHz).

At microwave frequencies, there are in general two types of losses contributing to the value of dielectric constant: dielectric loss and conduction loss. The imaginary part of soil dielectric constant has a strong frequency variation from 300 MHz to 500 MHz and the frequency dependence becomes less pronounced as the operating frequency increases. In the absence of other studies for the lower frequencies, we extend this result down to 100 MHz and, for the sake of the retrieval of soil parameters, use the parameterization of dielectric model for soils as given below.

$$\varepsilon = \mathrm{Re}\{\varepsilon\} + j\,\mathrm{Im}\{\varepsilon\} = \mathrm{Re}\{\varepsilon\} + j(\varepsilon'' + \alpha\frac{f_c}{f}) \qquad (6.6)$$

where $\mathrm{Re}\{\varepsilon\}$ is the real part of dielectric constant of soil, ε'' is the dielectric loss, α is the conduction loss, f_c is the center frequency of the system and f is the operating frequency.

6.5 Sensitivity Analysis of Backscattering Coefficients for Different Subsurface Geophysical Parameters

A sensitivity analysis of backscattering coefficients for different values of various subsurface geophysical parameters is performed in order to make an assessment of the potential of inverting these parameters. Fig. 6.5 (a) shows the backscattering coefficients in both frequency domain and time domain for different values of $\mathrm{Re}\{\varepsilon_2\}$ in a particular scenario. It is evident that the frequency response of backscattering coefficients from 100 MHz to 500 MHz is a strong function of the dielectric property of subsurface layer. Figure 6.5 (b) shows the inverse Cosine transform of the frequency response using (6.3). In Fig. 6.4 (b), the second time delay echo due to the reflection upon the second interface is present at t~9.5 nsec and the pulse shapes of first and second time delay echoes show strong dependence on the dielectric property of the subsurface layer. Similar studies to test the sensitivity of backscattering coefficients against $\mathrm{Im}\{\varepsilon_2\}$, α, h_2, and lc_2 are made and graphically demonstrated in Figs. 6.6-6.9, respectively. Several observations are worth mentioning. It is evident from Figs. 6.6 (a) and (b) that backscattering coefficients at low frequencies in both frequency and time domains do not show much sensitivity to the loss in the subsurface layer, making an accurate estimation of $\mathrm{Im}\{\varepsilon_2\}$ extremely difficult, if not impossible, using radar measurements of HH and VV backscattering coefficients. For this reason, the imaginary part of the subsurface soil dielectric constant is approximated as $\mathrm{Im}\{\varepsilon_2\}=1/10*\mathrm{Re}\{\varepsilon_2\}$. This approximation is also employed in [56]. In Fig. 6.7, it is seen that backscattering coefficients show only slight sensitivity to the conduction loss of the ground layer and it is hence speculated that the retrieval of α in (6.6) will be more unreliable than that of other parameters and may be significantly influenced by noise. In Fig. 6.8 and Fig. 6.9, backscattering coefficients exhibit great sensitivity to subsurface roughness condition, including both h_2, and lc_2

and therefore, a reliable inversion algorithm should yield accurate estimates of subsurface roughness statistics.

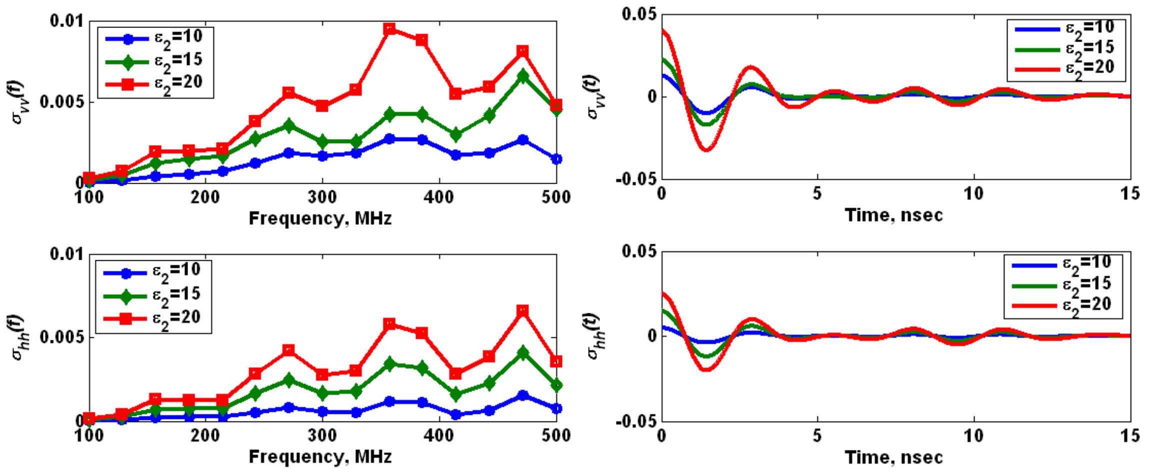

a) b)

Fig. 6.5: Sensitivity analysis of backscattering coefficients for different values of Re{ε_2} (a) in frequency domain and (b) in time domain for a two-rough-interface problem based on SPM: the incidence angle = 35°, ε_1=6+i(0.5+0.03*fc/f), d= 60 cm, h_1=1cm, lc_1=10cm, h_2=2.5cm, lc_2=20cm, and f_{min}=100 MHz, f_{max} = 500 MHz with 15-point uniform sampling

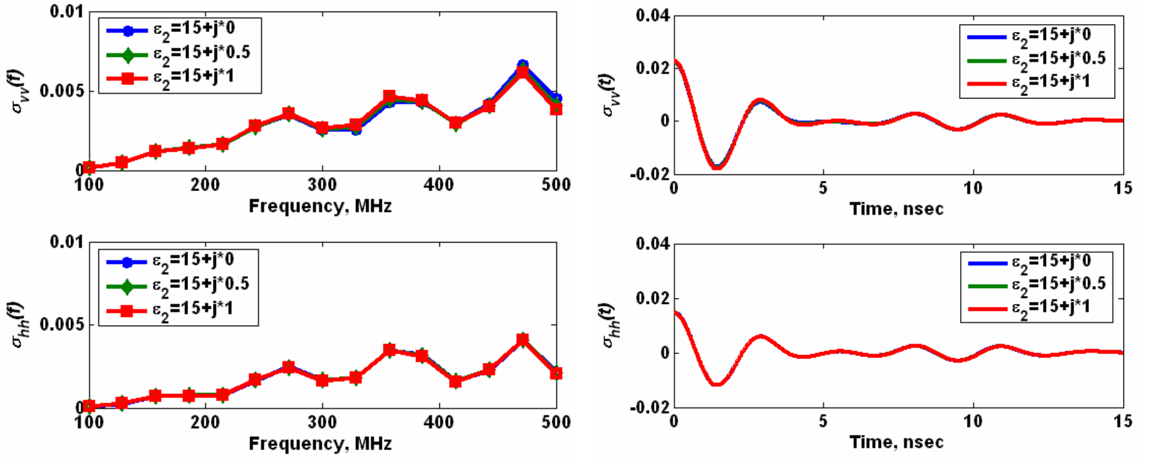

a) b)

Fig. 6.6: Sensitivity analysis of backscattering coefficients for different values of Im{ε_2} (a) in frequency domain and (b) in time domain for a two-rough-interface problem based on SPM: all other simulation parameters are the same as those in Fig. 6.5

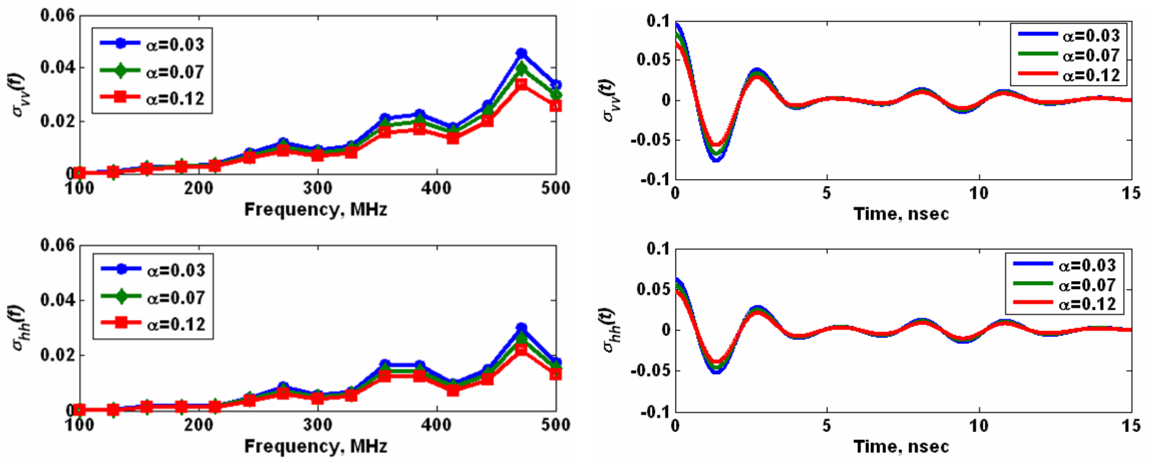

a) b)

Fig. 6.7: Sensitivity analysis of backscattering coefficients for different values of α (a) in frequency domain and (b) in time domain for a two-rough-interface problem based on SPM: all other simulation parameters are the same as those in Fig. 6.5

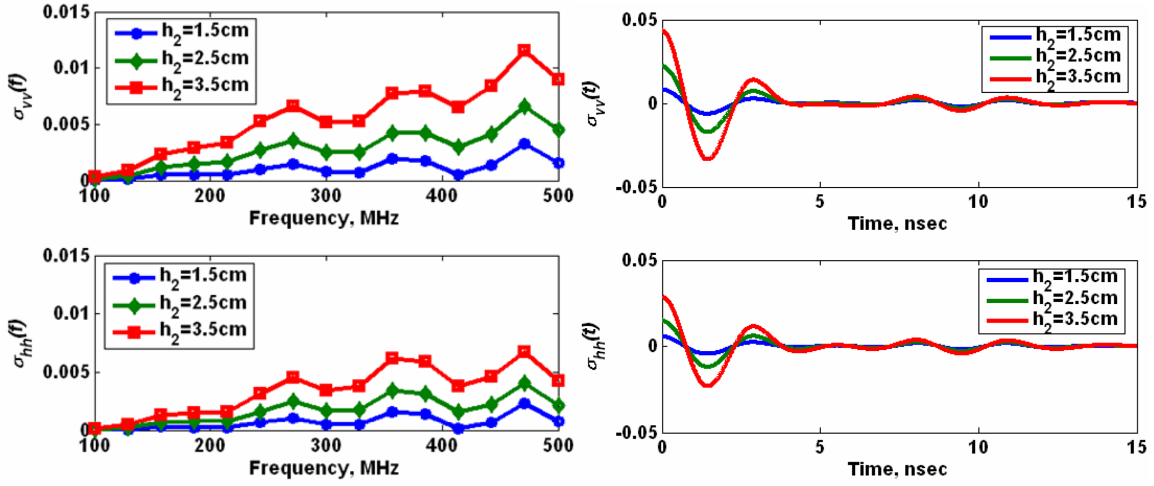

a) b)

Fig. 6.8: Sensitivity analysis of backscattering coefficients for different values of h₂ (a) in frequency domain and (b) in time domain for a two-rough-interface problem based on SPM: all other simulation parameters are the same as those in Fig. 6.5

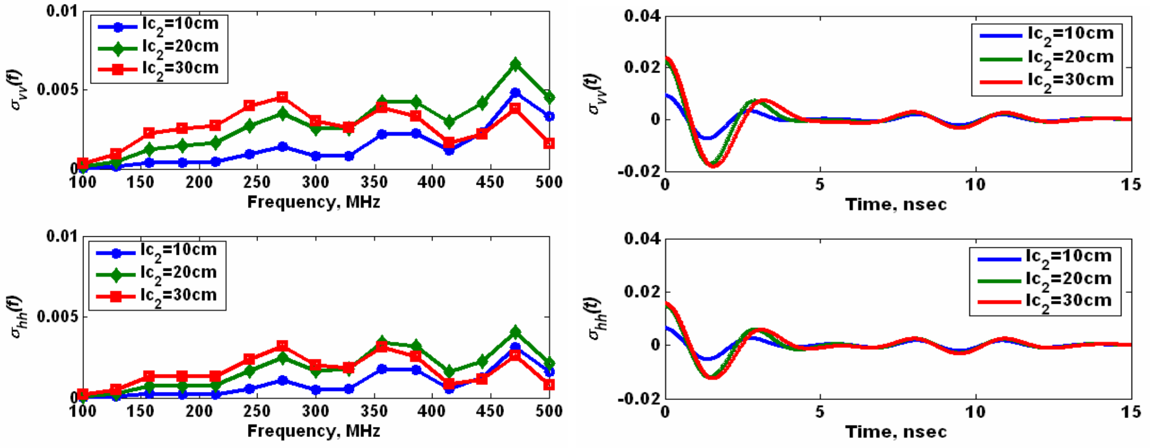

a) b)

Fig. 6.9: Sensitivity analysis of backscattering coefficients for different values of lc₂ (a) in frequency domain and (b) in time domain for a two-rough-interface problem based on SPM: all other simulation parameters are the same as those in Fig. 6.5

6.6 Retrieval Algorithm for Subsurface Geophysical Parameters

We first obtain measurements of the radar system at frequencies from 100 MHz to 500 MHz, denoted by $\begin{pmatrix} \sigma_{f_i}^{VV} \\ \sigma_{f_i}^{HH} \end{pmatrix}$, where $\sigma_{f_i}^{VV}$ and $\sigma_{f_i}^{HH}$ are the measured backscattering coefficients at VV and HH polarization, respectively. The top rough soil layer is characterized by a frequency-dependent complex soil dielectric constant given by (6.6). The roughness statistics of the top rough interface are described by the rms height, h_1, and the correlation length, $l_{c,1}$. In this dissertation, it is assumed that both top and subsurface interfaces have a Gaussian soil surface correlation function. In addition, as mentioned before, backscattering coefficients show very little sensitivity to the imaginary part of the subsurface soil dielectric constant. Hence, the imaginary part of the subsurface soil dielectric constant is approximated as one-tenth of its corresponding real part (i.e., $\mathrm{Im}\{\varepsilon_2\}=1/10*\mathrm{Re}\{\varepsilon_2\}$) [56]. The subsurface soil layer is characterized by a frequency-independent soil dielectric constant given by

$$\varepsilon_2 = \mathrm{Re}\{\varepsilon_2\} + j\,\mathrm{Im}\{\varepsilon_2\} = \mathrm{Re}\{\varepsilon_2\} + j\frac{1}{10}\mathrm{Re}\{\varepsilon_2\} \tag{6.7}$$

The roughness statistics of the subsurface rough interface are described by the rms height, h_2, and the correlation length, $l_{c,2}$.

Upon constructing synthetic time-domain data from sampled frequency measurements from 100 MHz to 500 MHz, the first step of retrieval algorithm for layer thickness is to extract the time difference between the peaks of time delay echoes to estimate the layer thickness. Then, after the real part of the ground soil dielectric constant is estimated from the inversion of ground surface parameters using the technique presented in section 6.5, the layer thickness of top layer can be computed using the relationship between the layer thickness and time separation between the 1st and the 2nd time delay echoes as given by

$$d = \frac{t_o c}{2\sqrt{\varepsilon_1^{'} - \sin^2(\theta_i)}} \tag{6.8}$$

where t_o is the time difference between the time delay echoes. Using synthetic time-domain data, the 1st and 2nd time delay echoes are first time-gated with a pulse width equal to two times the reciprocal of system bandwidth. The 1st time delay echo excludes any effects of multiple scattering and multiple bounces between top and bottom rough interfaces whereas the 2nd time delay echo represents the reflection upon the second rough interface. Both pulses yield information regarding subsurface geophysical parameters. The pulse shapes of both 1st and 2nd time delay echoes are then properly parameterized using a set of unknown coefficients, $\underline{C}$ for hh-polarized data and $\underline{D}$ for vv-polarized data with a set of known basis functions. In this work, the basis functions employed are dirac delta functions because the extraction of unknown coefficients is thus made straightforward and efficient. In other words, the unknown coefficients, $\underline{C}$ and $\underline{D}$, are basically the sampled points of the hh-polarized and vv-polarized 1st and 2nd time delay echoes, respectively. Issues concerning robustness to noise, data uncertainties, and run time for the optimization of cost function may demand a more sophisticated parameterization schemes which could require fewer unknown coefficients, such as spline basis functions.

Physical constraints on subsurface parameters can be imposed to facilitate the solution search for the inversion algorithm. The variability ranges of subsurface geophysical parameters for natural deep soil media, especially the subsurface roughness statistics, have not been fully investigated. Nevertheless, based on the ranges of geophysical parameters for bare soil surface in [56] for the purpose of inversion, the range of input roughness parameters and permittivities are given by Table 6.1. The range of dielectric constants at VHF/UHF bands corresponds to volumetric moisture contents from 3% to 35%. An additional physical constraint which can be imposed on the values of $\mathrm{Re}\{\varepsilon_2\}$ is based on the Fresnel law of reflection, where the reflection coefficients are negative if waves traveling in a less dense medium impinge upon a denser medium (i.e., $\mathrm{Re}\{\varepsilon_1\} < \mathrm{Re}\{\varepsilon_2\}$) and positive when the converse is true (i.e., $\mathrm{Re}\{\varepsilon_1\} > \mathrm{Re}\{\varepsilon_2\}$) as graphically shown in Fig. 6.10.

Table 6.1
Ranges of subsurface geophysical parameters where case #1 corresponds to a negative peak value of the second time delay echo and case #2 corresponds to a positive peak value of the second time delay echo

Parameter	Lower Bound	Upper Bound
$\mathrm{Re}\{\varepsilon_2\}$ for case #1	$\mathrm{Re}\{\varepsilon_1\}$	20
$\mathrm{Re}\{\varepsilon_2\}$ for case #2	3	$\mathrm{Re}\{\varepsilon_1\}$
h_2	0.2cm	2.7cm
lc_2	6cm	25cm
$\mathrm{Im}\{\varepsilon_1\}$	0	2
α	0	0.2

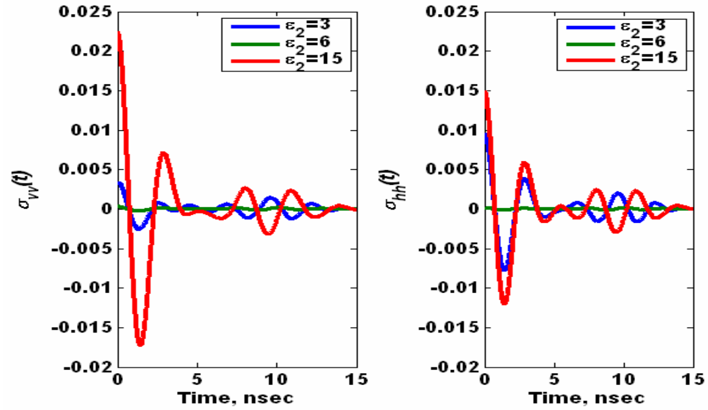

Fig. 6.10: Demonstration of a negative peak value of the second delay echo when Re{ε₁} < Re{ε₂} and a positive peak value of the second delay echo when Re{ε₁} > Re{ε₂} for a two-rough-interface problem based on SPM: all other simulation parameters are the same as those in Fig. 6.5

With the unknown coefficients for both polarizations extracted, the inversion of subsurface parameters can then proceed. The cost function is defined as follows.

$$\mathbb{C} = \frac{\left\| \begin{bmatrix} C \\ D \end{bmatrix}_{simulated} - \begin{bmatrix} C \\ D \end{bmatrix}_{measured} \right\|^2}{\left\| \begin{bmatrix} C \\ D \end{bmatrix}_{measured} \right\|^2} \qquad (6.9)$$

At this step of the inversion, $\mathrm{Re}\{\varepsilon_1\}$, h_1, and lc_1 have already been inverted and the value of layer thickness d has been retrieved using the measured value of time difference between the 1st and 2nd delay echoes. The remaining parameters to be retrieved are $\mathrm{Im}\{\varepsilon_1\}$, α ,$\mathrm{Re}\{\varepsilon_2\}$, h_2, lc_2, bearing in mind that we have taken $\mathrm{Im}\{\varepsilon_2\}= 1/10\ \mathrm{Re}\{\varepsilon_2\}$. The simulated coefficients $\begin{bmatrix} C \\ D \end{bmatrix}_{simulated}$ are computed with $\mathrm{Re}\{\varepsilon_1\}$, h_1, lc_1, and d as a-priori information. This reduction in the number of unknowns significantly facilitates the inversion for subsurface geophysical parameters through the initial stripping of top surface layer using L-band or higher frequency radar measurements. In the following section, an assessment of error propagation due to the estimation of top surface parameters is made to analyze how the deviation from the actual values of top surface parameters influences the retrieval of subsurface parameters. After the cost function has been properly defined, a nonlinear inversion method based on a constrained Nelder-Mead nonlinear simplex algorithm is employed to retrieve the medium parameters. Although Nelder-Mead nonlinear simplex algorithm is a local optimization method, it is relatively robust, numerically less complicated, and it usually finds an accurate solution in a relatively efficient manner (e.g., the inversion of five unknowns, Im$\{\varepsilon_1\}$, α ,Re$\{\varepsilon_2\}$, h_2, and lc_2, takes less than 1 min on a PC with Pentium-4 2-GHz processor and 1 GB RAM). Fig. 6.11 shows a flowchart for retrieving subsurface soil moisture and roughness statistics using radar measurements at L, UHF, and VHF bands.

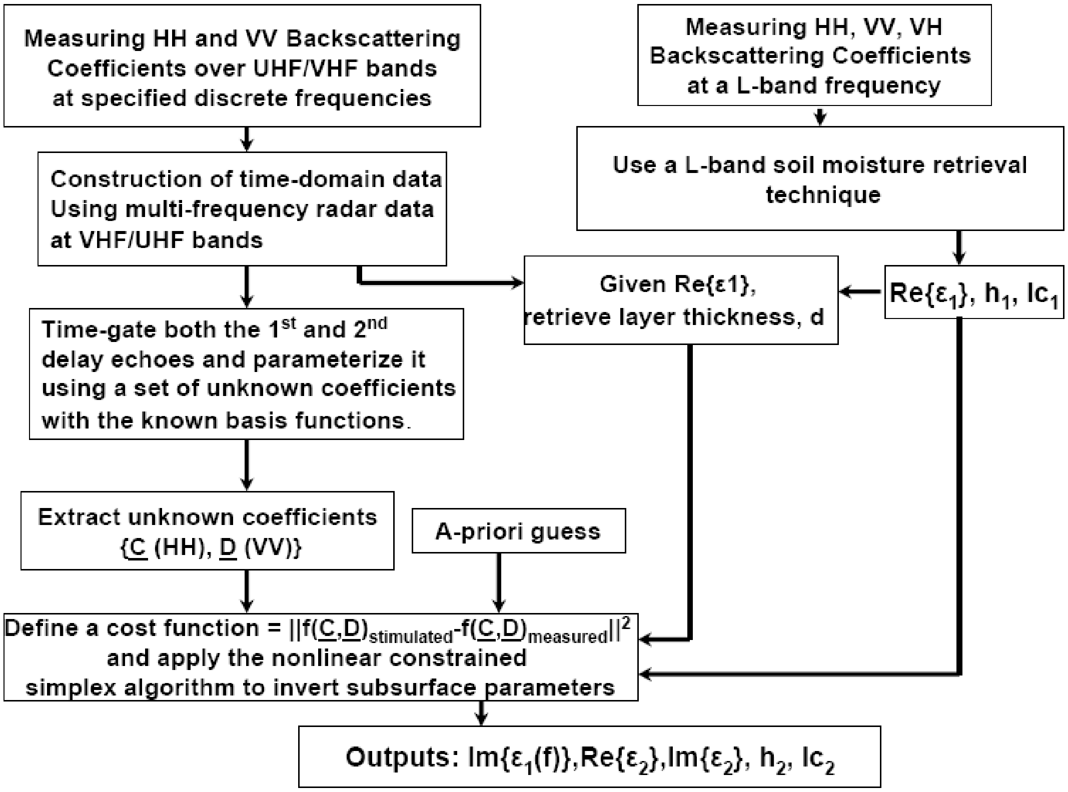

Fig. 6.11: Flowchart for retrieving subsurface geophysical parameters using radar measurements at L, UHF, and VHF bands

6.7 Numerical Simulations

6.7.1 Inversion Results

A preliminary numerical study of the proposed inversion algorithm in the absence of noise is carried out for the scenario of 2-interface rough surfaces. The actual simulation parameters (the 'truth') are given as follows: $\mathrm{Re}\{\varepsilon_1\}=6$, $\mathrm{Im}\{\varepsilon_1\}=0.5$, $\alpha=0.03$, $\varepsilon_2=\mathrm{Re}\{\varepsilon_2\}+j1/10*\mathrm{Re}\{\varepsilon_2\}$, $h_1=1$cm, $lc_1=10$cm, $h_2=2.5$cm, $lc_2=20$cm, d=60cm. In the first study, we assume that the top surface parameters, including $\mathrm{Re}\{\varepsilon_1\}$, h_1, and lc_1, have been perfectly inverted using a single or a few L-band radar measurements. Upon obtaining the values of $\mathrm{Re}\{\varepsilon_1\}$, h_1, and lc_1, the retrieval of subsurface geophysical parameters then proceeds. To study the robustness of the inversion algorithm, inversion is performed for different values of several subsurface geophysical parameters: $\mathrm{Re}\{\varepsilon_2\}$, h_2, and lc_2. The primary objective of this study is to evaluate the accuracy of the proposed subsurface inversion method. First, the inverted results for different values of $\mathrm{Re}\{\varepsilon_2\}$ while having the other parameters fixed are given in Table 6.2. Fig. 6.12 shows the actual value of $\mathrm{Re}\{\varepsilon_2\}$ versus the inverted value of $\mathrm{Re}\{\varepsilon_2\}$. It is evident from Fig. 6.12 that there is good agreement between the values of $\mathrm{Re}\{\varepsilon_{2,\mathrm{actual}}\}$ and $\mathrm{Re}\{\varepsilon_{2,\mathrm{inverted}}\}$ for all values of $\mathrm{Re}\{\varepsilon_2\}$. The simplex inversion algorithm is capable of successfully seeking a global solution where all of the inverted subsurface geophysical parameters except for $\alpha_{\mathrm{inverted}}$ are consistent with the actual values. From the sensitivity analysis, it is evident that backscattering coefficients do not show much dependency to α and hence the retrieved value of α is inaccurate. In addition, to study one particular case of error propagation from the estimate of h_1, 10% error is applied to the estimated value of h_1 and used to retrieve subsurface geophysical parameters. The reason behind choosing h_1 for the study of error propagation is that uncertainty in the retrieved value of h_1 is usually larger than that of $\mathrm{Re}\{\varepsilon_1\}$. The inverted values of $\mathrm{Re}\{\varepsilon_2\}$ are plotted and compared against the actual value of $\mathrm{Re}\{\varepsilon_2\}$ for $h_1 = 1$ cm and $h_1 = 0.9$ cm. In this numerical example, it is observed that the proposed inversion algorithm yields very accurate inversion results even with a 10 % estimation error in the a-priori value of h_1.

Table 6.2
The tabulated inversion results of subsurface geophysical parameters for different values of the real part of the subsurface soil dielectric constants

$Re\{\varepsilon_{2,actual}\}$	$Im\{\varepsilon_{1,inverted}\}$	$\alpha_{inverted}$	$Re\{\varepsilon_{2,inverted}\}$	$h_{2,inverted}$ (cm)	$lc_{2,inverted}$(cm)	$d_{,inverted}$(cm)
20	0.52	0.0068	19.76	2.52	19.56	60.07
17	0.52	0.0049	16.85	2.53	19.40	60.07
15	0.53	0.0000	14.98	2.54	19.20	60.06
13	0.51	0.0158	13.00	2.52	19.59	60.06
10	0.52	0.0096	10.07	2.57	18.94	60.14
9	0.56	0.0142	9.32	2.67	17.45	60.14
7	0.58	0.0571	7.23	2.53	18.22	60.33
6	0.60	0.0051	6.09	2.40	18.76	64.04
5	0.52	0.0017	5.00	2.51	19.48	60.02
3	0.50	0.0071	3.05	2.47	19.99	60.25

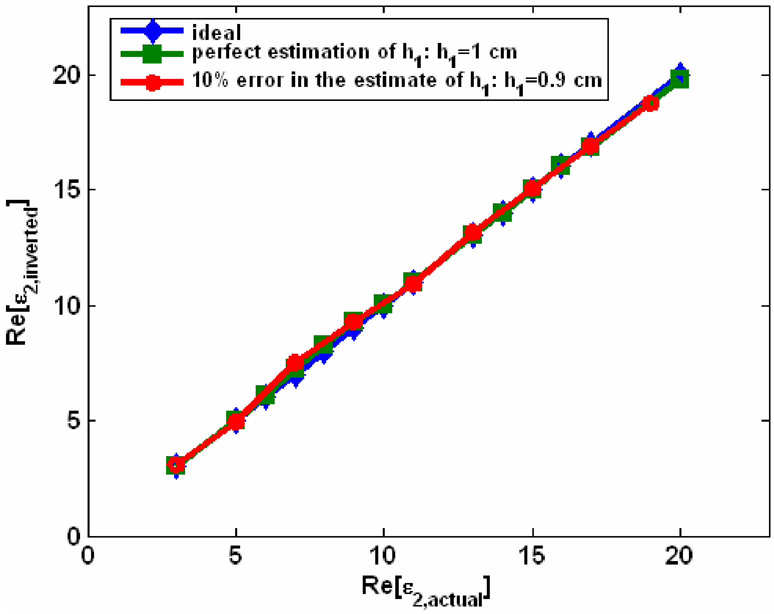

Fig. 6.12: Actual values of Re{ε_2} versus inverted values of Re{ε_2} for the ideal case, $h_{1,estimated}$=1cm, and $h_{1,estimated}$ =0.9cm

Next, inversion is performed for different values of h_2 and the inverted results for different values of h_2 are given in Table 6.3 while having the other parameters fixed. Fig. 6.13 shows the actual value of h_2 versus inverted value of h_2. It is clearly shown that there is good agreement between the values of $h_{2,actual}$ and $h_{2,inverted}$. When 10% error is applied to the estimated value of h_1 and fed into the inversion algorithm to retrieve subsurface geophysical parameters, the curve of $h_{2,inverted}$ versus $h_{2,actual}$ in Fig. 6.13 experiences a downward shift away from the curve of ideal case, demonstrating that a moderate error in the roughness of top interface propagates into $h_{2,\text{inverted}}$ and amplifies the magnitude of error in $h_{2,\text{inverted}}$ over the whole range of h_2.

Table 6.3
The tabulated inversion results of subsurface geophysical parameters for different values of the rms height of the subsurface interface

$h_{2,\text{actual}}$(cm)	Im{$\varepsilon_{1,\text{inverted}}$}	α_{inverted}	Re{$\varepsilon_{2,\text{inverted}}$}	$h_{2,\text{inverted}}$ (cm)	$lc_{2,\text{inverted}}$(cm)	$d_{,\text{inverted}}$(cm)
0.7	0.57	0.0014	16.35	0.75	17.31	60.22
0.9	0.58	0.0005	16.44	0.95	17.53	60.18
1.1	0.48	0.1034	16.02	1.10	21.21	60.18
1.3	0.52	0.0311	15.50	1.32	19.60	60.18
1.5	0.45	0.1298	15.87	1.48	22.01	60.14
1.7	0.53	0.0003	15.09	1.74	19.05	60.14
1.9	0.53	0.0039	15.06	1.94	19.18	60.14
2.1	0.51	0.0199	15.06	2.12	19.62	60.14
2.3	0.52	0.0021	14.98	2.33	19.25	60.06
2.5	0.53	0.0000	14.98	2.54	19.20	60.14
2.7	0.50	0.0060	15.01	2.70	20.01	60.06

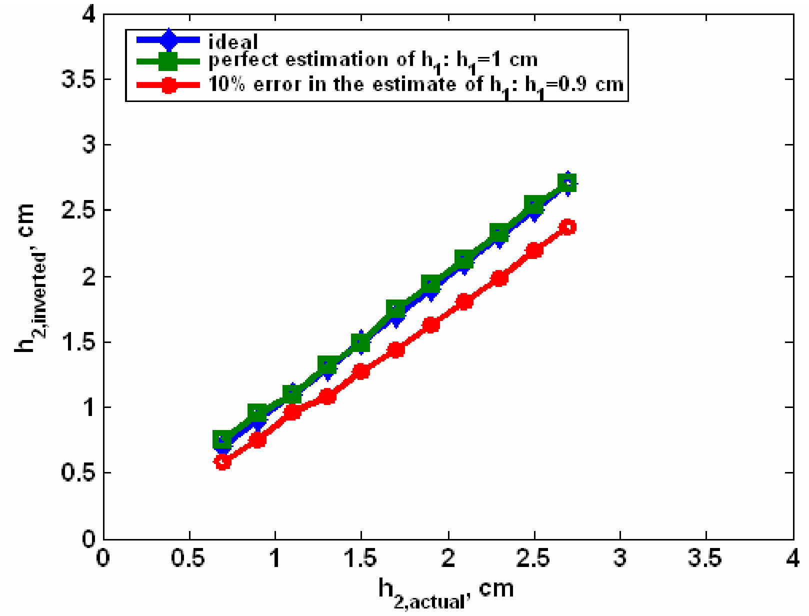

Fig. 6.13: Actual values of h_2 versus inverted values of h_2 for the ideal case, $h_{1,\text{estimated}}$=1cm, and $h_{1,\text{estimated}}$ =0.9cm

Finally, inversion is performed for different values of lc_2 and the inverted results for different values of lc_2 are given in Table 6.4 while having the other parameters fixed. Fig. 6.14 shows the actual value of lc_2 versus the inverted value of lc_2. In general, there is good agreement between the values of $lc_{2,\text{actual}}$ and $lc_{2,\text{inverted}}$ over the entire range of lc_2 under consideration. When

10% error is applied to the estimated value of h_1 and used to retrieve subsurface geophysical parameters, the curve of $lc_{2,inverted}$ versus $lc_{2,actual}$ slightly drifts away from the curve of ideal case especially for the scenarios of low correlation length (i.e., $lc_2 < 15$ cm), suggesting that with a moderate error in the estimated value of the rms height of top interface, inversion of correlation length for the bottom layer gets progressively more challenging as the slope (i.e., $\frac{h_2}{lc_2}$) of subsurface rough surface gets larger.

Table 6.4
The tabulated inversion results of subsurface geophysical parameters for different values of the correlation length of the subsurface interface

lc_{actual}(cm)	Im{$\varepsilon_{1,inverted}$}	$\alpha_{inverted}$	Re{$\varepsilon_{2,inverted}$}	$h_{2,inverted}$(cm)	$lc_{2,inverted}$(cm)	$d_{,inverted}$(cm)
0.07	0.50	0.0682	15.75	2.19	8.16	60.14
0.11	0.53	0.0014	15.19	2.91	9.22	60.06
0.15	0.46	0.0762	15.12	2.39	16.34	60.06
0.17	0.48	0.0556	15.07	2.46	17.67	60.06
0.20	0.53	0.0000	14.98	2.54	19.20	60.06
0.23	0.56	0.0585	17.20	2.54	22.89	60.14
0.27	0.51	0.0234	15.00	2.51	26.81	60.14
0.31	0.52	0.0023	14.98	2.49	30.43	60.18
0.33	0.51	0.0217	14.99	2.50	32.77	60.22

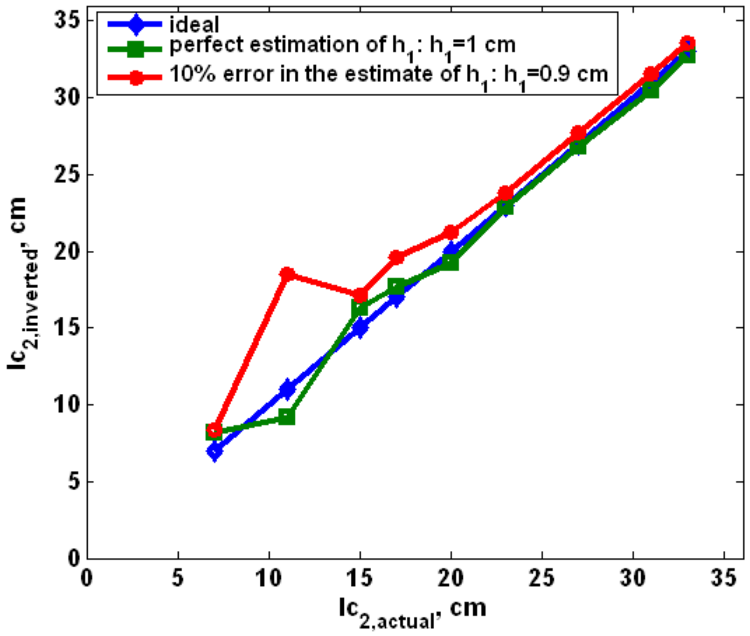

Fig. 6.14: Actual values of lc_2 versus inverted values of lc_2 for the ideal case, $h_{1,estimated}$=1cm, and $h_{1,estimated}$ =0.9cm

6.7.2 Error Propagation from the Estimation of Top Surface Parameters

Thorough numerical studies of error propagation are made to investigate the sensitivity of inverted subsurface geophysical parameters to the estimated errors in top surface parameters using L-band radar measurements. In Fig. 6.15, six subsurface geophysical parameters are inverted for different values of top surface parameters. The assessment of error propagation is scenario-dependent. As a result, a detailed quantitative discussion that includes all scenarios is not possible. However, useful conclusions can be drawn from the analysis of error propagation to understand how sensitivity of inversion is impacted by estimation inaccuracy in the values of Re{ε_1}, h_1, and lc_1.

Fig. 6.14 shows inverted values of subsurface geophysical parameters as a result of erroneous top surface parameters used as a-priori information with the green lines indicating the actual values. It is observed that the proposed inversion scheme is fairly robust to error propagation from the estimated values of surface roughness statistics, h_1 and lc_1. Layer thickness can be accurately computed regardless of any estimation errors in h_1 and lc_1 in Fig. 6.15 (b) and (c). The retrieval of the imaginary part of top soil dielectric constant and subsurface soil dielectric constant is relatively unaffected by the estimation error from h_1 and lc_1. As expected, the inversion quality of subsurface roughness statistics gets significantly undermined by slight estimation inaccuracy in top surface roughness statistics. Fortunately, the primary parameter of interest is subsurface soil dielectric constant. The retrieval of subsurface soil dielectric constant exhibits only slight sensitivity to the a-priori values of h_1 and lc_1. On the other hand, the retrieval of subsurface soil dielectric constant significantly depends on the estimated value of Re{ε_1} as demonstrated by Fig. 6.15 (a). Figure 6.15 (a) shows that the error in Re{ε_1} linearly affects the error in Re{ε_2}. It can be attributed to the fact that the resulting retrieved values of d and Im{ε_1} are strongly correlated to the a-priori value of Re{ε_1}. In addition, error in d also significantly impacts the retrieved values of subsurface parameters. The promising observation is that a 10% error in Re{ε_1} (i.e., varying from Re{ε_1}=5.4 to Re{ε_1}=6.6) results in a roughly 15% error in

Re{$\varepsilon_{2,\text{inverted}}$} (i.e., varying from Re{ε_2}=13 to Re{ε_2}=17). Therefore, the error amplification factor due to uncertainties in Re{ε_2} does not pose as a detrimental threat to inversion.

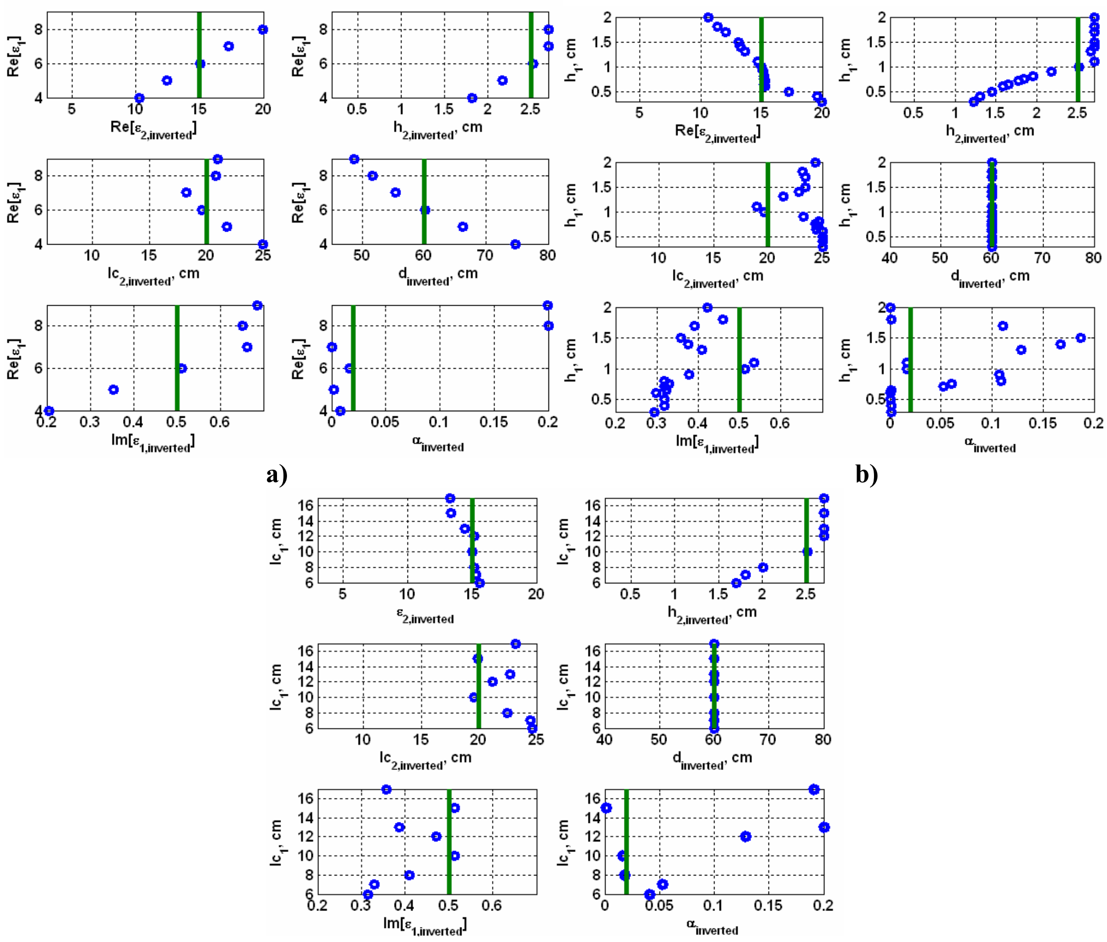

a) b)

c)

Fig. 6.15: Numerical studies of uncertainties and error propagation into the inverted values of subsurface geophysical parameters from the estimates of a) Re{ε_1}, b) h_1 , and c) lc_1

6.7.3 Analysis of Measurement, Model, and Calibration Errors

The impact of measurement, model, and calibration errors on the accuracy of subsurface soil dielectric constant using UHF and VHF band radar measurements is assessed in this subsection. Measurement, model, and calibration errors propagate through the inversion algorithm and impact the retrieved parameter accuracy. In this chapter, similar to the error analysis performed in [56], measurement, model, and calibration errors are lumped together and represented as a total error denoted by *C* in dB. Radar measurements are obtained by adding a zero-mean Gaussian random process with standard deviation of 0.2, 0.5, 1.0 dB to backscattering coefficients predicted by SPM. These correspond to errors of 4.7%, 12.2%, and 25.8%, respectively.

$$\sigma_{measured}(dB) = \sigma_{actual}(dB) + C(dB) \tag{6.10}$$

where C captures the error sources from measurement, model, and calibration.

The histograms of output inverted subsurface parameters, $\mathrm{Re}\{\varepsilon_2\}$, h_2, lc_2, and d are generated using Monte Carlo simulation with 1000 realizations and the results are provided for different C's with standard deviations of 0.2, 0.5, and 1 dB in Figs. 6.16-6.18. First, an increase in the standard deviation of C evidently raises the variance of output subsurface parameters. In addition, the use of a constrained inversion algorithm in the presence of random errors can result in exceptionally high incidence of inverted values capped at upper limits as evidenced by the appearance of spikes at h_2 = 2.7 cm of the probability density function of h_2 in Figs. 6.16-6.18. This indicates that the addition of random errors alters the cost function in such a way that absolute minima tend to be formed at the boundary points of the domain of interest. The actual value of h_2 is set to be 2.5 cm which is fairly close to its upper bound, $h_{2,upper}$= 2.7 cm and consequently the inversion from measurements corrupted by errors is strongly biased toward the upper bound for h_2. For low error cases, the probability density function of lc_2 resembles a Gaussian distribution. When the error becomes larger, the inverted lc_2 value frequently gets stuck at the upper limit of 25 cm. For $\mathrm{Re}\{\varepsilon_2\}$, the shape of probability density function changes drastically as the function of total error. For low error cases, the maximum of the probability density function centers around the mean, which is close to the actual value of $\{\varepsilon_2\}$. However, as the total errors get larger, multiple maxima show up in the probability density function of $\{\varepsilon_2\}$ (Fig. 6.18). Although the mean still corresponds to the actual value, the appearance of multiple peaks suggests that multiple local minima are formed around the actual value as a result of increasing total errors. Finally, the probability density function of the inverted values of layer thickness is discretely distributed due to the discrete nature of the peak detection process. In general, the retrieval of layer thickness is very robust to errors as evidenced by low standard deviations associated with the histograms for layer thickness in Figs. 6.16-6.18. Quantitatively, for std[C] = 1.0 dB (~25% measurement error), subsurface soil dielectric constant has a mean of 14.3 and a standard deviation of 2.5. This translates into about a 17.5% error off the measured mean. Subsurface rms height has a mean of 2.28 cm and a standard deviation of 0.39 cm with about a 17% error off the measured mean. Figures 6.16-6.18 demonstrate that the mean values of the inverted geophysical parameters are in fair agreement with the actual values for total errors of 0.2, 0.5, and 1.0 dB. Significant improvements are also anticipated when the retrieval process of layer thickness is made more robust to measurement errors. Any estimation inaccuracy in recovering layer thickness worsens the estimation results of Re{ε_2}, h_2, and lc_2 since the retrieval of layer thickness proceeds before the inversion of subsurface geophysical parameters.

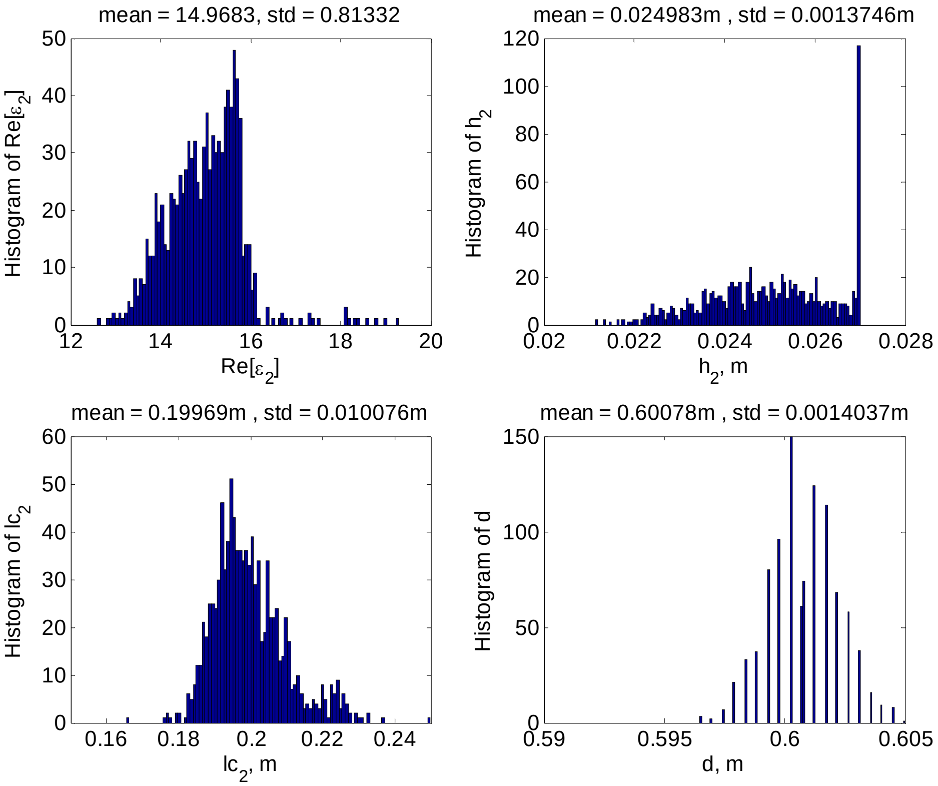

Fig. 6.16: Total error analysis and the histograms of inverted parameters for different total errors when error = 0.2 dB

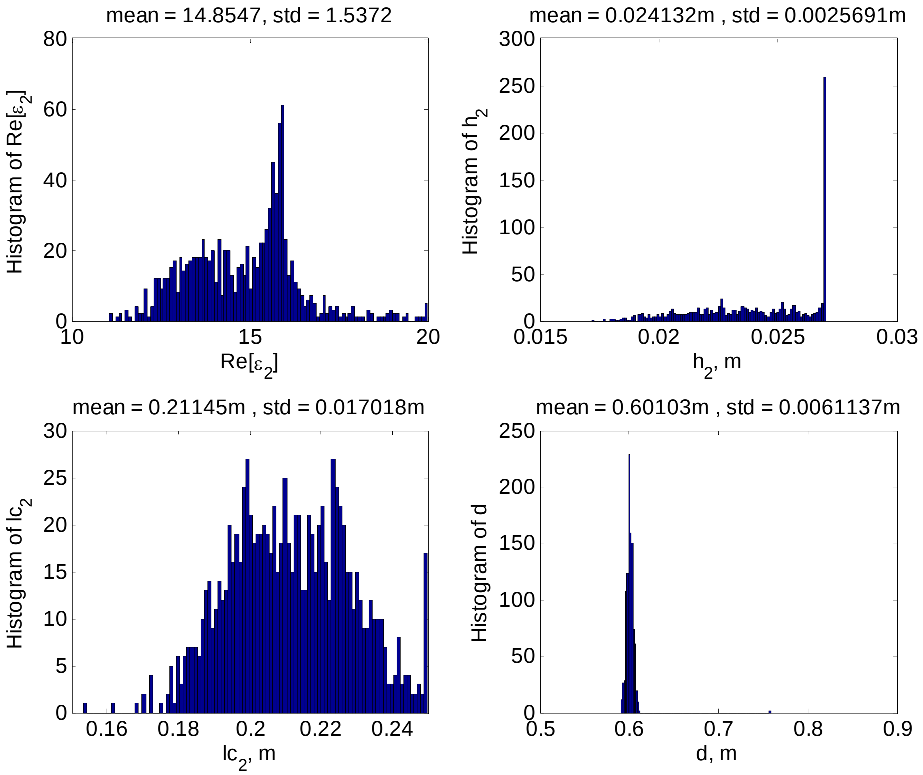

Fig. 6.17: Total error analysis and the histograms of inverted parameters for different total errors when error = 0.5 dB

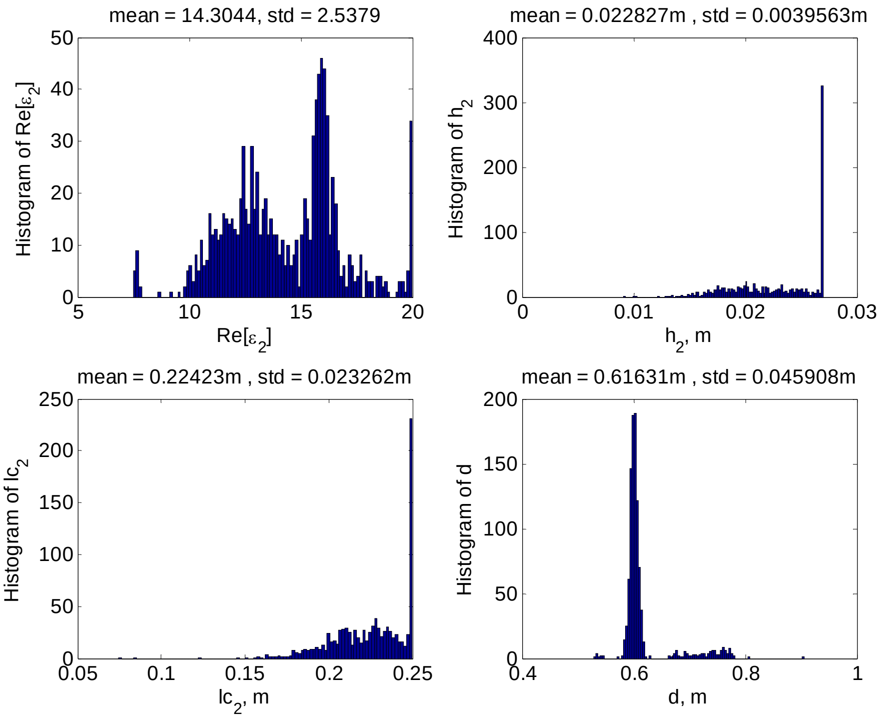

Fig. 6.18: Total error analysis and the histograms of inverted parameters for different total errors when error = 1.0 dB

In addition, error analysis is performed to investigate the sensitivity of inverted geophysical parameters to a change in the actual value of subsurface rms height, h_2. In the following analysis, the value of h_2 is set to be 1.5 cm while the rest of parameters stay intact. The histograms of output inverted subsurface parameters, $Re\{\varepsilon_2\}$, h_2, lc_2, and d are also generated using Monte Carlo simulations with 1000 realizations and the results are provided for different *C*s' with standard deviations of 0.2, 0.5, and 1 dB in Figs. 6.19-6.21. Figures 6.19-6.21 all show that the mean values of the inverted geophysical parameters are in good agreement with the actual values. In addition, the proposed inversion method is capable of detecting changes in subsurface roughness statistics even in the presence of large errors. The standard deviations associated with the inverted h_2 are much less than the previous case when h_2 is 2.5 cm (closer to the upper limit set at 2.7 cm). When the actual subsurface roughness is away from the upper limit, the inversion results are less prone to getting trapped at local minima on the domain boundary of the cost function. This demonstrates the scenario-dependent performance quality of the proposed nonlinear inversion method. The choice of variability ranges and the values of actual geophysical parameters usually have implications for the outcome of inversion using this local optimization technique.

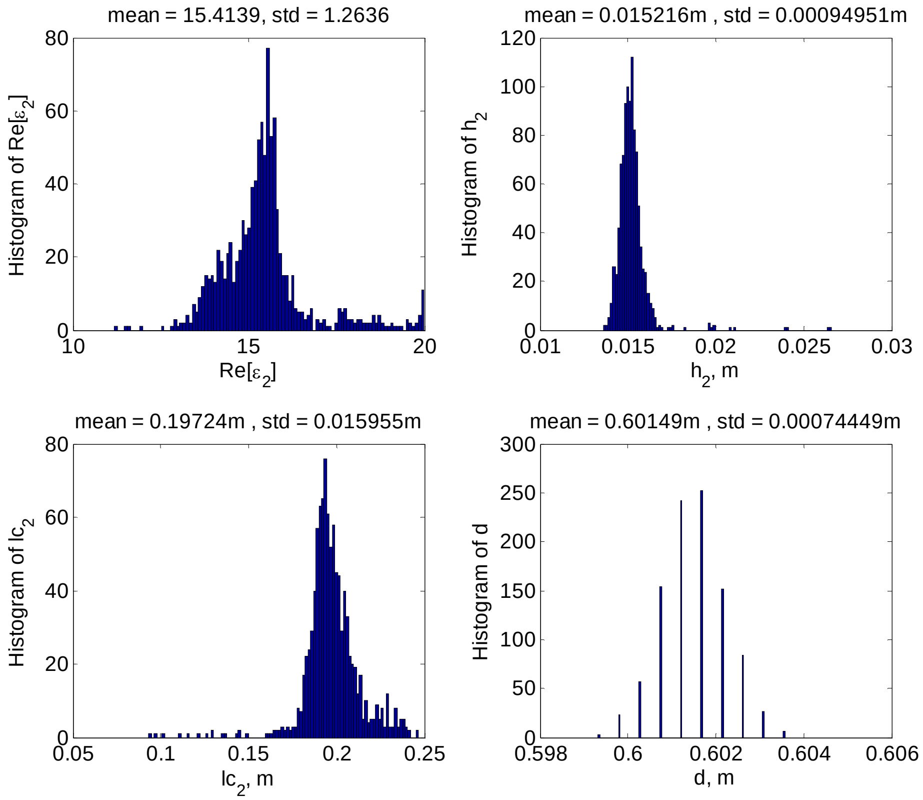

Fig. 6.19: Total error analysis and the histograms of inverted parameters for different total errors (h_2 =1.5 cm) when error = 0.2 dB

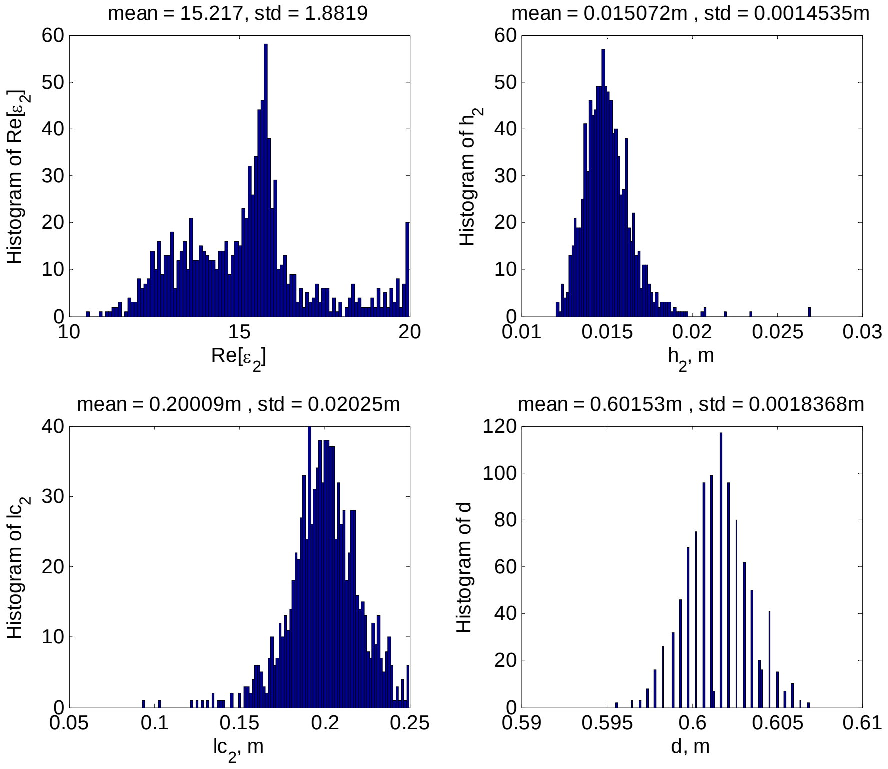

Fig. 6.20: Total error analysis and the histograms of inverted parameters for different total errors (h_2 = 1.5 cm) when error = 0.5 dB

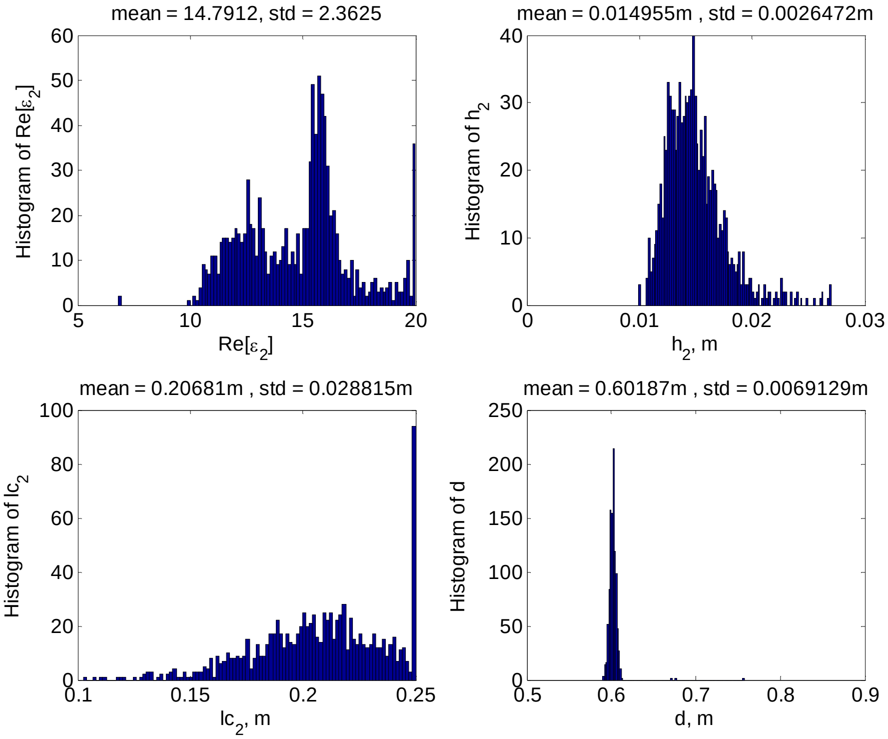

mean = 14.7912, std = 2.3625

mean = 0.014955m , std = 0.0026472m

mean = 0.20681m , std = 0.028815m

mean = 0.60187m , std = 0.0069129m

Fig. 6.21: Total error analysis and the histograms of inverted parameters for different total errors (h_2 = 1.5 cm) when error = 1.0 dB

6.8 Chapter Conclusion

A multi-frequency inversion algorithm for the retrieval of subsurface soil moisture content is presented. The near-surface parameters are estimated using L-band or higher radar measurements and the subsurface probing capability is achieved through the use of low frequency radar measurements at VHF and UHF. In the proposed algorithm, the dielectric constant of the top surface is first determined using L band radar measurements using a frequency-domain inversion technique. Subsequently, the top surface is mathematically stripped away. For the retrieval of subsurface properties, the dielectric constants as well as roughness statistics are estimated using a time-domain inversion technique together with a parameter optimization for the pulse shape of time delay echoes from VHF/UHF band radar observations. Numerical studies are performed to investigate the accuracy of the proposed inversion technique in both the absence and presence of measurement, model, and calibration errors, and to investigate the robustness of this method against errors in the estimates of top surface parameters. Numerical studies show that subsurface parameters except for the conduction loss of top layer, α, can all be successfully retrieved in the presence of slight estimation inaccuracy in top surface parameters. Measurement, model, and calibration errors do not significantly affect the reliability of the retrieved subsurface geophysical parameters and the proposed inversion method is robust to errors and uncertainties. Error analysis also demonstrates the capability of the proposed algorithm for detecting changes in subsurface roughness statistics even in the presence of large errors.

CHAPTER 7

Conclusion and Future Work

7.1 Conclusion

The primary objective of this thesis was to develop an accurate and efficient technique for two-dimensional scattering from layered rough surfaces with or without buried objects based on the extended boundary condition method (EBCM) and the scattering matrix method (SMM). Plane wave expansion/scattering matrix method has established itself as an efficient means of rigorously solving the scattered field and power distribution of periodic structures, for modeling reflection/transmission of stratified planar media, and periodic arrays of cylinders compared to other widely used (numerical) techniques such as FDTD, MoM, and FEM. The primary underlying contributions of this dissertation are to optimize EBCM for rough surface scattering through the application of fast FFT-based matrix filling algorithm, and to employ SMM to coherently solve the scattered field from a stack of multiple rough surfaces, in the possible presence of buried objects.

The proposed method has been tested and validated against both analytical and numerical solutions and then applied to study low frequency radar scattering from a field-derived soil moisture profile in order to evaluate the potential of retrieving subsurface soil moisture.

Given the capability of this technique for modeling coherent multiple scattering phenomena, we utilized this technique to study backscattering enhancement and satellite peaks due to surface plasmon resonance from multilayer rough surfaces. For weakly layered rough surfaces, this technique shows that multiple surface plasmon waves are excited, giving rise to multiple scattering of waves for both HH and VV polarizations. The appearance of backscattering enhancement is a result of scattered waves adding up in phase in the backscattering direction after undergoing multiple orders of scattering. Multiple guided surface waves also constructively interfere with each other and contribute to additional enhanced peaks in other scattering directions than the backscattering direction. These peaks are called satellite peaks. In this dissertation, a thorough sensitivity study of backscattering enhancement to the subsurface properties of layered media was conducted with numerous qualitative conclusions drawn based on the numerical results. The theoretical locations of satellite peaks were predicted and the locations of the demonstrated satellite peaks were in good agreement with the theory.

Following the formulation of EBCM/SMM for solving scattering from layered rough surfaces, the proposed method is generalized to incorporate a buried cylinder or a cluster of cylinders in layered rough surfaces. The scattering problem is reformulated through the characterization of cylinders and rough interfaces by their reflection and transmission responses. The reflection/transmission matrices of buried objects and rough interfaces are recursively cascaded using SMM to account for wave interactions between these scatterers. The capability of the proposed technique is further demonstrated by providing a solution to scattering from discrete random media in layered rough surfaces.

The last part of this dissertation focuses on the development of a multi-frequency inversion algorithm for the retrieval of subsurface soil moisture using VHF/UHF- and L-band radar measurements with a proposal of an envisioned platform and radar system. A pulse echo profile contains temporal information showing the process of wave propagation and scattering through layered media, and is useful in identifying contributions from different rough layers. Backscattering coefficients at multiple frequencies are synthetically generated using the analytical forward solver based on SPM. Top surface parameters are first recovered using L-band radar measurements because with a relatively low penetration depth at L band compared to VHF/UHF bands, the subsurface properties are not reflected in backscattering coefficients. Subsequently, the pulse echo profile is computed through the use of inverse Cosine transform using VHF/UHF band radar measurements. Each echo is parameterized and then these parameters are used to invert both the subsurface dielectric constant and subsurface roughness statistics. The performance of the proposed inversion algorithm is demonstrated by error propagation and error analysis. Numerical studies show good performance of the proposed method. Error analysis demonstrates the robustness of the proposed method to added noise by showing the average values of inversion results converge to the actual values. In addition, inversion results exhibit little sensitivity to the inversion results of top-layer roughness statistics.

7.2 Future Work

7.2.1 Numerical Solution to Three Dimensional Scattering from Layered Rough Surfaces

This dissertation focuses on 2D scattering from layered rough surfaces. The next natural step in continuation of this research is the development and implementation of a numerical solution to 3D scattering from layered rough surfaces using the proposed method based on EBCM/SMM. EBCM has been applied to scattering from 2D periodic surfaces and the matrix filling process can be expedited using 2D FFT. With proper TM and TE mode conversion accounted for, 3D SMM can be implemented to incorporate the effect of layer thickness. Iterative/accelerated matrix inversion algorithms can further be employed to reduce the computational runtime. After the development of a 3D numerical forward model for scattering from layered rough surfaces, an extensive sensitivity analysis for remote sensing of subsurface soil moisture can be carried out to study both co-polarized and cross-polarized scattering coefficients and co-polarized phase difference in response to the variation in subsurface dielectric constant and roughness statistics. In addition, backscattering Enhancement due to surface plasmon resonance from 2D layered rough surfaces also remains as an unexplored research topic due to its computational complexity associated with 3D numerical modeling. The MoM solution to 3D scattering from layered rough surfaces in [32] is not a good candidate for analyzing backscattering enhancement and demonstrating satellite peaks due to the application of tapered illumination source which tends to smear out the scattering response. Therefore, EBCM/SMM constitutes as an ideal method for studying backscattering enhancement of surface plasmon waves from 2D weakly rough surfaces.

7.2.2 Multi-frequency Inversion Algorithm for the Retrieval of Subsurface Soil Moisture With non-Uniform Frequency Sampling

The last part of this dissertation considers a multi-frequency inversion algorithm for the retrieval of subsurface soil moisture using uniform frequency samples over VHF/UHF bands. However, depending on the available measurement system, the VHF/UHF frequency range may not be uniformly sampled. Due to some practicality and feasibility constraints in spaceborne radar applications, the frequency content typically is well under-sampled and the sample locations are non-uniformly spaced. This may impact the analysis, and the reconstruction of time signal using non-uniform frequency samples poses as a nontrivial problem. Reference [97] presents an algorithm for reconstructing time signal from non-uniform frequency samples. Future investigation needs to be conducted to study the effect of non-uniform frequency sampling on the reconstruction quality of pulse echo profile and the inversion results. A feasibility assessment will be made to determine the minimum number and the locations of frequency samples required for desirable inversion results.

7.2.3 Validation with Experimental Results

The focus of dissertation is the theoretical development of scattering analysis for layered rough surfaces. Cross-validation with experimental data is the next step in this area of research. A prototype VHF/UHF tower radar for subsurface sensing has been deployed to collect backscattering radar measurements at 137MHz and 437 MHz in [22]. Radar calibration is being performed in order to process the collected radar data and the current challenge is to understand and possibly quantify measurement errors as well as calibration accuracies.

APPENDIX

APPENDIX A

Scattering from Layered Rough Surfaces based on Method of Moments (MoM)

This appendix summarizes an MoM formulation for 3 stratified homogenous regions, separated by 2 rough surfaces with point matching and pulse basis functions based on [7]. Starting from an integral equation approach, the solutions for the scattered fields in any regions can then be obtained by imposing boundary conditions on both interfaces and applying pulse basis functions and point matching to the induced currents.

$$\sum_n a_{mn}^{(1,1,1)} U_m^1 + b_{mn}^{(1,1,1)} \psi_m^1 = \psi_{inc} \tag{1}$$

$$\sum_n \rho_2 a_{mn}^{(2,1,1)} U_m^1 + b_{mn}^{(2,1,1)} \psi_m^1 + a_{mn}^{(2,1,2)} U_m^2 + b_{mn}^{(2,1,2)} \psi_m^2 = 0 \tag{2}$$

$$\sum_n \rho_2 a_{mn}^{(2,2,1)} U_m^1 + b_{mn}^{(2,2,1)} \psi_m^1 + a_{mn}^{(2,2,2)} U_m^2 + b_{mn}^{(2,2,2)} \psi_m^2 = 0 \tag{3}$$

$$\sum_n \rho_3 a_{mn}^{(3,2,2)} U_m^2 + b_{mn}^{(3,2,2)} \psi_m^2 = 0 \tag{4}$$

where

$$a_{mn}^{(a,b,c)} = \begin{cases} \omega^{(a,c)} \dfrac{idx}{4} H_0^{(1)}(k_a \,|\, \bar{r}_{m,b} - \bar{r}_{m,a} \,|), & for \quad (b = c, m \neq n) \quad or \quad b \neq c \\ \omega^{(a,c)} \dfrac{idx}{4} H_0^{(1)}(\dfrac{k_a \Delta l_{m,b}}{2e}), & for \quad (b = c, m = n) \end{cases} \tag{5}$$

$$b_{mn}^{(a,b,c)} = \begin{cases} -\omega^{(a,c)} \dfrac{ik_a dx}{4} \dfrac{H_1^{(1)}(k_a \,|\, \bar{r}_{m,b} - \bar{r}_{m,c} \,|)}{|\, \bar{r}_{m,b} - \bar{r}_{m,c} \,|} * (f_c^{'}(x_n)(x_n - x_m) - (f_c(x_n) - f_b(x_m)), & for \quad (b = c, m \neq n) \quad or \quad b \neq c \\ \dfrac{1}{2} - \omega^{(a,c)} \dfrac{f_b^{''}(x_m)}{4\pi} \dfrac{dx}{1 + f_b^{'}(x_m)^2}, & for \quad (b = c, m = n) \end{cases} \tag{6}$$

Equations (1)-(4) can be cast in a matrix.

$$\overline{\overline{Z}}\,\overline{I} = \overline{V} \tag{7}$$

where

$$Z=\begin{bmatrix} \overline{\overline{a}}^{(1,1,1)} & \overline{\overline{b}}^{(1,1,1)} & \overline{\overline{0}} & \overline{\overline{0}} \\ \rho_2\overline{\overline{a}}^{(2,1,1)} & \overline{\overline{b}}^{(2,1,1)} & \overline{\overline{a}}^{(2,1,2)} & \overline{\overline{b}}^{(2,1,2)} \\ \rho_2\overline{\overline{a}}^{(2,2,1)} & \overline{\overline{b}}^{(2,2,1)} & \overline{\overline{a}}^{(2,2,2)} & \overline{\overline{b}}^{(2,2,2)} \\ \overline{\overline{0}} & \overline{\overline{0}} & \rho_3\overline{\overline{a}}^{(3,2,2)} & \overline{\overline{b}}^{(3,2,2)} \end{bmatrix} \tag{8}$$

$$\overline{I}=\begin{bmatrix} \overline{U}_1 \\ \overline{\psi}_1 \\ \overline{U}_2 \\ \overline{\psi}_2 \end{bmatrix} \tag{9}$$

$$\overline{V}=\begin{bmatrix} \overline{\psi}^{inc} \\ \overline{0} \\ \overline{0} \\ \overline{0} \end{bmatrix} \tag{10}$$

Four unknown vectors to be sought, $\overline{U}_1$, $\overline{\psi}_1$, $\overline{U}_2$, and $\overline{\psi}_2$ are induced electric and magnetic currents on the surfaces $f_1(x)$ and $f_2(x)$. After the induced currents, $\overline{U}_1$ and $\overline{\psi}_1$, have been computed, the scattered field in region 0 can be determined using Hyugen's principle. Compared to the single surface case, both memory requirement and computational time are significantly increased for layered rough surfaces problem. Thus, an efficient algorithm to facilitate the solution is necessary. In [7], forward and backward method with spectral acceleration for scattering from layered rough surfaces is presented, which reduces the memory requirement and computational complexity from $O(K^2)$ and $O(K^3)$ to $O(K)$ and $O(K)$, respectively, where the total number of unknowns is $K=2(M-1)N$, N is the total number of sample points per interface and M is the number of layers.

BIBIOGRAPHY

[1] A. Tabatabaeenejad and M. Moghaddam, "Bistatic scattering from three-dimensional layered rough surfaces," *IEEE Transactions on Geoscience and Remote Sensing*, vol. 44, pp. 2102-2114, 2006.

[2] T. M. Elfouhaily and J. T. Johnson, "A new model for rough surface scattering," *IEEE Transactions on Geoscience and Remote Sensing*, vol. 45, pp. 2300-2308, 2007.

[3] D. Didascalou, M. Dottling, N. Geng, and W. Wiesbeck, "An approach to include stochastic rough surface scattering into deterministic ray-optical wave propagation modeling," *IEEE Transactions on Antennas and Propagation*, vol. 51, pp. 1508-1515, 2003.

[4] F. W. Millet and K. F. Warnick, "Validity of rough surface backscattering models," *Waves in Random Media*, vol. 14, pp. 327-347, 2004.

[5] Q. Li, C. H. Chan, and L. Tsang, "Monte Carlo simulations of wave scattering from lossy dielectric random rough surfaces using the physics-based two-grid method and the canonical-grid method," *IEEE Transactions on Antennas and Propagation*, vol. 47, pp. 752-763, 1999.

[6] A. Iodice, "Forward-backward method for scattering from dielectric rough surfaces," *IEEE Transactions on Antennas and Propagation*, vol. 50, pp. 901-911, 2002.

[7] C. D. Moss, T. M. Grzegorczyk, H. C. Han, and J. A. Kong, "Forward-backward method with spectral acceleration for scattering from layered rough surfaces," *IEEE Transactions on Antennas and Propagation*, vol. 54, pp. 1006-1016, 2006.

[8] D. Zahn, K. Sarabandi, K. F. Sabet, and J. F. Harvey, "Numerical simulation of scattering from rough surfaces: A wavelet-based approach," *IEEE Transactions on Antennas and Propagation*, vol. 48, pp. 246-253, 2000.

[9] L. Tsang, J. A. Kong, K.-H. Ding, and C. O. Ao, *Scattering of Electromagnetic Waves - Numerical Simulations*: New York: Wiley, 2001.

[10] F. D. Hastings, J. B. Schneider, and S. L. Broschat, "A Monte-Carlo FDTD Technique for Rough Surface Scattering," *IEEE Transactions on Antennas and Propagation*, vol. 43, pp. 1183, 1995.

[11] F. D. Hastings, J. B. Schneider, S. L. Broschat, and E. I. Thorsos, "An FDTD method for analysis of scattering from rough fluid-fluid interfaces," *IEEE Journal of Oceanic Engineering*, vol. 26, pp. 94-101, 2001.

[12] V. Galdi, P. Kosmas, C. M. Rappaport, L. B. Felsen, and D. A. Castanon, "Short-pulse three-dimensional scattering from moderately rough surfaces: A comparison

between narrow-waisted Gaussian beam algorithms and FDTD," *IEEE Transactions on Antennas and Propagation*, vol. 54, pp. 157-167, 2006.

[13] R. T. Marchand and G. S. Brown, "On the use of finite surfaces in the numerical prediction of rough surface scattering," *IEEE Transactions on Antennas and Propagation*, vol. 47, pp. 600-604, 1999.

[14] H. Braunisch, Y. Zhang, C. O. Ao, S. E. Shih, Y. E. Yang, K. H. Ding, J. A. Kong, and L. Tsang, "Tapered wave with dominant polarization state for all angles of incidence," *IEEE Transactions on Antennas and Propagation*, vol. 48, pp. 1086-1096, 2000.

[15] J. A. Roden, S. D. Gedney, M. P. Kesler, J. G. Maloney, and P. H. Harms, "Time-domain analysis of periodic structures at oblique incidence: orthogonal and nonorthogonal FDTD implementations," *IEEE Transactions on Microwave Theory and Techniques*, vol. 46, pp. 420-427, 1998.

[16] P. C. Dubois, J. van Zyl, and T. Engman, "Measuring soil moisture with imaging radars," *IEEE Transactions on Geoscience and Remote Sensing*, vol. 33, pp. 915-926, 1995.

[17] Y. Oh, K. Sarabandi, and F. T. Ulaby, "An empirical model and an inversion technique for radar scattering from bare soil surfaces," *IEEE Transactions on Geoscience and Remote Sensing*, vol. 30, pp. 370-381, 1992.

[18] U. Narayan, V. Lakshmi, and T. J. Jackson, "High-resolution change estimation of soil moisture using L-band radiometer and Radar observations made during the SMEX02 experiments," *Geoscience and Remote Sensing, IEEE Transactions on*, vol. 44, pp. 1545-1554, 2006.

[19] F. Lemaitre, J. C. Poussiere, Y. H. Kerr, M. Dejus, R. Durbe, P. de Rosnay, and J. C. Calvet, "Design and test of the ground-based L-band Radiometer for Estimating Water In Soils (LEWIS)," *Geoscience and Remote Sensing, IEEE Transactions on*, vol. 42, pp. 1666-1676, 2004.

[20] Z. Xiwu, P. R. Houser, J. P. Walker, and W. T. Crow, "A method for retrieving high-resolution surface soil moisture from hydros L-band radiometer and Radar observations," *Geoscience and Remote Sensing, IEEE Transactions on*, vol. 44, pp. 1534-1544, 2006.

[21] D. Entekhabi, E. G. Njoku, P. Houser, M. Spencer, T. Doiron, K. Yunjin, J. Smith, R. Girard, S. Belair, W. Crow, T. J. Jackson, Y. H. Kerr, J. S. Kimball, R. Koster, K. C. McDonald, P. E. O'Neill, T. Pultz, S. W. Running, S. Jiancheng, E. Wood, and J. van Zyl, "The hydrosphere State (hydros) Satellite mission: an Earth system pathfinder for global mapping of soil moisture and land freeze/thaw," *IEEE Transactions on Geoscience and Remote Sensing*, vol. 42, pp. 2184-2195, 2004.

[22] M. Moghaddam, Y. Rahmat-Samii, E. Rodriguez, D. Entekhabi, J. Hoffman, D. Moller, L. E. Pierce, S. Saatchi, and M. Thomson, "Microwave Observatory of Subcanopy and Subsurface (MOSS): A Mission Concept for Global Deep Soil Moisture Observations," *IEEE Transactions on Geoscience and Remote Sensing*, vol. 45, pp. 2630-2643, 2007.

[23] M. Moghaddam, S. Saatchi, and R. H. Cuenca, "Estimating subcanopy soil moisture with radar," *Journal of Geophysical Research-Atmospheres*, vol. 105, pp. 14899-14911, 2000.

[24] C. h. Kuo and M. Moghaddam, "Electromagnetic Scattering From Multilayer Rough Surfaces With Arbitrary Dielectric Profiles for Remote Sensing of Subsurface Soil Moisture," *IEEE Transactions on Geoscience and Remote Sensing*, vol. 45, pp. 349-366, 2007.

[25] D. J. Breckenfeld, "Soil Survey of Walnut Gulch Experimental Watershed, Arizona " *United States Department of Agriculture, Natural Resource Conservation Service and Agricultural Research Service in cooperation with Arizona Agricultural Experimental Station*, pp. 130, 1993.

[26] K. Sarabandi and T. Chiu, "Electromagnetic scattering from slightly rough surfaces with inhomogeneous dielectric profiles," *IEEE Transactions on Antennas and Propagation*, vol. 45, pp. 1419-1430, 1997.

[27] R. Azadegan and K. Sarabandi, "Analytical formulation of the scattering by a slightly rough dielectric boundary, covered with a homogenous dielectric layer," *Antennas and Propagation Society International Symposium, 2003. IEEE*, vol. 3, pp. 420-423 vol.3, 2003.

[28] G. Franceschetti, P. Imperatore, A. Iodice, D. Riccio, and G. Ruello, "Scattering from a layered medium with one rough interface: comparison and physical interpretation of different methods," *IGARSS '03. Proceedings.*, vol. 4, pp. 2912-2914 vol.4, 2003.

[29] K. Krishen, "Scattering of electromagnetic waves from a layer with rough front and plane back (small perturbation method by Rice)," *IEEE Transactions on Antennas and Propagation* vol. 18, pp. 573-576, 1970.

[30] A. Soubret, G. Berginc, and C. Bourrely, "Backscattering enhancement of an electromagnetic wave scattered by two-dimensional rough layers," *Journal of the Optical Society of America a-Optics Image Science and Vision*, vol. 18, pp. 2778-2788, 2001.

[31] I. M. Fuks and A. G. Voronovich, "Wave diffraction by rough interfaces in an arbitrary plane-layered medium," *Waves in Random Media*, vol. 10, pp. 253-272, 2000.

[32] M. El-Shenawee, "Polarimetric scattering from two-layered two-dimensional random rough surfaces with and without buried objects," *IEEE Transactions on Geoscience and Remote Sensing*, vol. 42, pp. 67-76, 2004.

[33] A. Ishimaru, "Backscattering enhancement: from radar cross sections, to electron and light localizations to rough surface scattering," *IEEE Transactions on Antennas and Propagation*, vol. 33, pp. 7-11, 1991.

[34] A. R. McGurn and A. A. Maradudin, "Localization Effects in the Elastic-Scattering of Light from a Randomly Rough-Surface," *Journal of the Optical Society of America B-Optical Physics*, vol. 4, pp. 910-926, 1987.

[35] A. A. Maradudin and E. R. Mendez, "Enhanced Backscattering of Light from Weakly Rough, Random Metal-Surfaces," *Applied Optics*, vol. 32, pp. 3335-3343, 1993.

[36] K. A. Odonnell, R. Torre, and C. S. West, "Observations of second-harmonic generation from randomly rough metal surfaces," *Physical Review B*, vol. 55, pp. 7985-7992, 1997.

[37] E. Betzig, A. Lewis, A. Harootunian, M. Isaacson, and E. Kratschmer, "Near-Field Scanning Optical Microscopy (Nsom) - Development and Biophysical Applications," *Biophysical Journal*, vol. 49, pp. 269-279, 1986.

[38] J. T. Johnson, L. Tsang, R. T. Shin, K. Pak, C. H. Chan, A. Ishimaru, and Y. Kuga, "Backscattering enhancement of electromagnetic waves from two-dimensional perfectly conducting random rough surfaces: A comparison of Monte Carlo simulations with experimental data," *IEEE Transactions on Antennas and Propagation*, vol. 44, pp. 748-756, 1996.

[39] A. A. Maradudin, T. Michel, A. R. McGurn, and E. R. Mendez, "Enhanced Backscattering of Light from a Random Grating," *Annals of Physics*, vol. 203, pp. 255-307, 1990.

[40] A. Y. Nikitin, F. Lopez-Tejeira, and L. Martin-Moreno, "Scattering of surface plasmon polaritons by one-dimensional inhomogeneities," *Physical Review B*, vol. 75, 2007.

[41] V. M. Shalaev, *Optical Properties of Nanostructured Random Media*: Springer Berlin/ Heidelberg, 2002.

[42] W. Johnstone, G. Stewart, T. Hart, and B. Culshaw, "Surface plasmon polaritons in thin metal films and their role in fiber optic polarizing devices," *Lightwave Technology, Journal of*, vol. 8, pp. 538-544, 1990.

[43] T. R. Michel, "Resonant Light-Scattering from Weakly Rough Random Surfaces and Imperfect Gratings," *Journal of the Optical Society of America a-Optics Image Science and Vision*, vol. 11, pp. 1874-1887, 1994.

[44] A. Madrazo and A. A. Maradudin, "Numerical solutions of the reduced Rayleigh equation for the scattering of electromagnetic waves from rough dielectric films on perfectly conducting substrates," *Optics Communications*, vol. 134, pp. 251-263, 1997.

[45] T. A. Leskova, E. I. Chaikina, G. Navarrete, and G. Martinez-Niconoff, "Resonance effects in the scattering of light from a rough metal surface with a thin coating," *Physical Review B*, vol. 59, pp. 11062-11068, 1999.

[46] R. M. Fitzgerald, A. Leskova, and A. A. Maradudin, "Transmission of Light through a Metal Film with Two Corrugated Surfaces," *SPIE*, pp. 5878, 2005.

[47] B. Baumeier, T. A. Leskova, and A. A. Maradudin, "Transmission of light through a thin metal film with periodically and randomly corrugated surfaces," *Journal of Optics a-Pure and Applied Optics*, vol. 8, pp. S191-S207, 2006.

[48] K. Oneill, R. F. Lussky, and K. D. Paulsen, "Scattering from a metallic object embedded near the randomly rough surface of a lossy dielectric," *IEEE Transactions on Geoscience and Remote Sensing*, vol. 34, pp. 367-376, 1996.

[49] C. Rappaport and M. El-Shenawee, "Modeling GPR signal degradation from random rough ground surface," presented at Geoscience and Remote Sensing Symposium, 2000. Proceedings. IGARSS 2000. IEEE 2000 International, 2000.

[50] G. F. Zhang, L. Tsang, and K. Pak, "Angular correlation function and scattering coefficient of electromagnetic waves scattered by a buried object under a two-dimensional rough surface," *Journal of the Optical Society of America a-Optics Image Science and Vision*, vol. 15, pp. 2995-3002, 1998.

[51] M. El-Shenawee and C. M. Rappaport, "Monte Carlo Simulations for clutter statistics in minefields: AP-mine-like-target buried near a dielectric object

beneath 2-D random rough ground surfaces," *IEEE Transactions on Geoscience and Remote Sensing*, vol. 40, pp. 1416-1426, 2002.

[52] Y. Zhang, Y. E. Yang, H. Braunisch, and J. A. Kong, "Electromagnetic wave interaction of conducting object with rough surface by hybrid SPM/MOM technique - Abstract," *Journal of Electromagnetic Waves and Applications*, vol. 13, pp. 983-984, 1999.

[53] J. T. Johnson and R. J. Burkholder, "A study of scattering from an object below a rough surface," *IEEE Transactions on Geoscience and Remote Sensing*, vol. 42, pp. 59-66, 2004.

[54] Y. Oh, "Quantitative retrieval of soil moisture content and surface roughness from multipolarized radar observations of bare soil surfaces," *IEEE Transactions on Geoscience and Remote Sensing*, vol. 42, pp. 596-601, 2004.

[55] P. J. van Oevelen and D. H. Hoekman, "Radar backscatter inversion techniques for estimation of surface soil moisture: EFEDA-Spain and HAPEX-Sahel case studies," *IEEE Transactions on Geoscience and Remote Sensing*, vol. 37, pp. 113-123, 1999.

[56] F. Mattia, G. Satalino, L. Dente, and G. Pasquariello, "Using a priori information to improve soil moisture retrieval from ENVISAT ASAR AP data in semiarid regions," *IEEE Transactions on Geoscience and Remote Sensing*, vol. 44, pp. 900-912, 2006.

[57] U. Spagnolini, "Permittivity measurements of multilayered media with monostatic pulse radar," *IEEE Transactions on Geoscience and Remote Sensing*, vol. 35, pp. 454-463, 1997.

[58] S. Lambot, E. C. Slob, I. van den Bosch, B. Stockbroeckx, and M. Vanclooster, "Modeling of ground-penetrating radar for accurate characterization of subsurface electric properties," *IEEE Transactions on Geoscience and Remote Sensing*, vol. 42, pp. 2555-2568, 2004.

[59] W. H. Weedon, "A Step-Frequency Radar Imaging System for Microwave Nondestructive Evaluation," *Progress in Electromagnetic Research*, pp. 121-146, 2000.

[60] E. Chapin, S. Hensley, and T. R. Michel, "Calibration of an across track interferometric P-band SAR," presented at Geoscience and Remote Sensing Symposium, 2001. IGARSS '01. IEEE 2001 International, 2001.

[61] S. Hensley, E. Chapin, A. Freedman, C. Le, S. Madsen, T. Michel, E. Rodriguez, P. Siqueira, and K. Wheeler, "First P-band results using the GeoSAR mapping system," presented at Geoscience and Remote Sensing Symposium, 2001. IGARSS '01. IEEE 2001 International, 2001.

[62] K. Wheeler and S. Hensley, "The GeoSAR airborne mapping system," presented at Radar Conference, 2000. The Record of the IEEE 2000 International, 2000.

[63] J. A. Kong, *Electromagnetic Wave Theory*, Second ed. New York: Wiley, 2000.

[64] W. C. Chew, *Waves and Fields in Inhomogeneous Media*. New York: IEEE Press, 1995.

[65] S. L. Chuang and J. A. Kong, "Scattering of Waves from Periodic Surfaces," *Proceedings of the IEEE*, vol. 69, pp. 1132-1144, 1981.

[66] H. Toyama and K. Yasumoto, "Electromagnetic scattering from periodic arrays of composite circular cylinder with internal cylindrical scatterers," *Progress in Electromagnetics Research-Pier*, vol. 52, pp. 321-333, 2005.

[67] K. Yasumoto, H. T. Jia, and H. Toyama, "Analysis of two-dimensional electromagnetic crystals consisting of multilayered periodic arrays of circular cylinders," *Electronics and Communications in Japan Part Ii-Electronics*, vol. 88, pp. 19-28, 2005.

[68] H. T. Jia, K. Yasumoto, and H. Toyama, "Reflection and transmission properties of layered periodic arrays of circular cylinders embedded in magnetized ferrite slab," *IEEE Transactions on Antennas and Propagation*, vol. 53, pp. 1145-1153, 2005.

[69] K. Yasumoto, H. Toyama, and T. Kushta, "Accurate analysis of two-dimensional electromagnetic scattering from multilayered periodic arrays of circular cylinders using lattice sums technique," *IEEE Transactions on Antennas and Propagation*, vol. 52, pp. 2603-2611, 2004.

[70] T. Kushta and K. Yasumoto, "Electromagnetic scattering from periodic arrays of two circular cylinders per unit cell," *Journal of Electromagnetic Waves and Applications*, vol. 14, pp. 853-854, 2000.

[71] P. R. Siqueira, K. Sarabandi, and F. T. Ulaby, "Numerical-Simulation of Scatterer Positions in a Very Dense Medium with an Application to the 2-Dimensional Born Approximation," *Radio Science*, vol. 30, pp. 1325-1339, 1995.

[72] T. S. Chu and T. Itoh, "Generalized Scattering Matrix-Method for Analysis of Cascaded and Offset Microstrip Step Discontinuities," *IEEE Transactions on Microwave Theory and Techniques*, vol. 34, pp. 280-284, 1986.

[73] R. Mittra and S. W. Lee, *Analytical Techniques in the Theory of Guided Waves*. NewYork: Macmillan, 1971.

[74] R. E. Collin, *Foundations for Microwave Engineering*. New York: McGraw-Hill, 1966.

[75] R. C. Hall, R. Mittra, and K. M. Mitzner, "Analysis of Multilayered Periodic Structures Using Generalized Scattering Matrix-Theory," *IEEE Transactions on Antennas and Propagation*, vol. 36, pp. 511-518, 1988.

[76] S. W. Lee, G. Zarrillo, and C. L. Law, "Simple Formulas for Transmission through Periodic Metal Grids or Plates," *IEEE Transactions on Antennas and Propagation*, vol. 30, pp. 904-909, 1982.

[77] J. T. Johnson, J. A. Kong, R. T. Shin, D. H. Staelin, K. Oneill, and A. W. Lohanick, "3rd Stokes Parameter Emission from a Periodic Water-Surface," *IEEE Transactions on Geoscience and Remote Sensing*, vol. 31, pp. 1066-1080, 1993.

[78] Y. Lasne, P. Paillou, G. Ruffie, and M. Crapeau, "Effect of multiple scattering on the phase signature of wet subsurface structures: Applications to polarimetric L- and C-band SAR," *IEEE Transactions on Geoscience and Remote Sensing*, vol. 43, pp. 1716-1726, 2005.

[79] R. M. Chen and J. C. West, "Analysis of Scattering from Rough Surfaces at Large Incidence Angles Using a Periodic-Surface Moment Method," *IEEE Transactions on Geoscience and Remote Sensing*, vol. 33, pp. 1206-1213, 1995.

[80] J. C. West, "On the control of edge diffraction in numerical rough surface scattering using resistive tapering," *IEEE Transactions on Antennas and Propagation*, vol. 51, pp. 3180-3183, 2003.

[81] Y. Oh and K. Sarabandi, "Improved numerical simulation of electromagnetic wave scattering from perfectly conducting random surfaces," *IEE Proceedings-Microwaves Antennas and Propagation*, vol. 144, pp. 256-260, 1997.

[82] C. H. Kuo and M. Moghaddam, "Scattering from multilayer rough surfaces based on the extended boundary condition method and truncated singular value decomposition," *IEEE Transactions on Antennas and Propagation*, vol. 54, pp. 2917-2929, 2006.

[83] K. Inan and V. B. Erturk, "Application of iterative techniques for electromagnetic scattering from dielectric random and reentrant rough surfaces," *IEEE Transactions on Geoscience and Remote Sensing*, vol. 44, pp. 3320-3329, 2006.

[84] N. R. Peplinski, F. T. Ulaby, and M. C. Dobson, "Dielectric properties of soils in the 0.3-1.3-GHz range (vol 33, pg 803, 1995)," *IEEE Transactions on Geoscience and Remote Sensing*, vol. 33, pp. 1340-1340, 1995.

[85] N. R. Peplinski, F. T. Ulaby, and M. C. Dobson, "Dielectric-Properties of Soils in the 0.3-1.3-Ghz Range," *IEEE Transactions on Geoscience and Remote Sensing*, vol. 33, pp. 803-807, 1995.

[86] J. T. Johnson, R. T. Shin, and J. A. Kong, "Scattering and thermal emission from a two dimensional periodic surface," *Progress in Electromagnetics Research-Pier*, vol. 17, 1997.

[87] A. A. Maradudin, A. R. McGurn, and E. R. Mendez, "Surface-Plasmon Polariton Mechanism for Enhanced Backscattering of Light from One-Dimensional Randomly Rough Metal-Surfaces," *Journal of the Optical Society of America a-Optics Image Science and Vision*, vol. 12, pp. 2500-2506, 1995.

[88] K. A. O'Donnell, C. S. West, and E. R. Mendez, "Backscattering enhancement from polariton-polariton coupling on a rough metal surface," *Physical Review B*, vol. 57, pp. 13209-13219, 1998.

[89] C. S. West and K. A. Odonnell, "Observations of Backscattering Enhancement from Polaritons on a Rough Metal-Surface," *Journal of the Optical Society of America a-Optics Image Science and Vision*, vol. 12, pp. 390-397, 1995.

[90] D. E. Lawrence and K. Sarabandi, "Electromagnetic scattering from a dielectric cylinder buried beneath a slightly rough surface," *IEEE Transactions on Antennas and Propagation*, vol. 50, pp. 1368-1376, 2002.

[91] L. Tsang, J. A. Kong, K.-H. Ding, and C. O. Ao, *Scattering of Electromagnetic Waves – Advanced Topics*. New York: Wiley, 2001.

[92] L. L. Foldy, "The Multiple Scattering of Waves .1. General Theory of Isotropic Scattering by Randomly Distributed Scatterers," *Physical Review*, vol. 67, pp. 107-119, 1945.

[93] A. Sahin and E. L. Miller, "Recursive T-matrix methods for scattering from multiple dielectric and metallic objects," *IEEE Transactions on Antennas and Propagation*, vol. 46, pp. 672-678, 1998.

[94] Y. Q. Jin and J. A. Kong, "Strong Fluctuation Theory for Electromagnetic-Wave Scattering by a Layer of Random Discrete Scatterers," *Journal of Applied Physics*, vol. 55, pp. 1364-1369, 1984.

[95] X. Feng and J. Ya-Qiu, "Multiparameter inversion of a layer of vegetation canopy over rough surface from the system response function based on the mueller matrix solution of pulse echoes," *Geoscience and Remote Sensing, IEEE Transactions on*, vol. 44, pp. 2003-2015, 2006.

[96] J. Ya-Qiu, C. Fei, and C. Mei, "Retrievals of underlying surface roughness and moisture from polarimetric pulse echoes in the specular direction through stratified vegetation canopy," *Geoscience and Remote Sensing, IEEE Transactions on*, vol. 42, pp. 426-433, 2004.

[97] G. Karlheinz and S. Harald, "Fast Local Reconstruction Methods for Nonuniform Sampling in Shift-Invariant Spaces," *SIAM Journal on Matrix Analysis and Applications*, vol. 24, pp. 899-913, 2003.